Temperature Profiles and Thermal Strain Analysis in Multi-fastener Carbon Fibre Reinforced Plastic -Aluminium Lap Joints

Jodi R. Miller

A thesis submitted to the University of Bristol in accordance with the requirements of the degree of Doctorate of Philosophy in the Faculty of Engineering and the Department of Aerospace Engineering

February 2004

Abstract

Temperature profiles of and combined thermal-mechanical induced strains for Carbon Fibre Reinforced Plastic (CFRP)-Aluminium multi-fastener double lap joints in a wingbox structure are examined. Two dimensional (2D) FE analyses for cases of full, empty, and half-full fuel tank scenarios are used to develop temperature profiles. The influence of conduction, convection, and radiation on temperature profiles is examined. Results show that the empty tank scenario produces the highest temperatures, with the joint region having the peak temperatures, and that convection and radiation must both be modelled in order to accurately estimate wingbox temperatures for the empty, and half-full tank scenarios. Analytical temperature prediction models, both at and away from the joint region, are developed for combined convection and radiation boundary conditions at both external surfaces of this unique finite geometry. For transient analyses, single and multiple layer models are designed using integral transforms and separation of variables, respectively. To show the joint region is critical in terms of induced strains, sequentially coupled thermal-stress analysis is performed using the resulting temperature profiles. Based on these results, and on the results of the temperature profiling, an experimental model is designed to study the effects of thermal and mechanical loading on a three-fastener double lap joint with CFRP skin and aluminium laps. To fully explore the joint region, three dimensional (3D) FE results are compared with experimental data. Mechanical tensile stress in the elastic range is applied at room temperature (295K) and at an elevated temperature (373K). Increasing temperature alters the strain patterns among the fasteners and generally decreases the peak radial strains at individual fasteners, but increases tangential strains. The effect of torque on the strain distribution in these multi-fastener double lap joints is examined by comparing finger-tight and operationally-tight (35Nm) torques at both temperatures. Increasing torque significantly reduces peak strains on individual fasteners and evens the strain distribution across the joint.

Acknowledgements

I would like to take this opportunity to thank everyone who helped me throughout my journey toward completion of this thesis. At the University of Bristol, I would like to thank Dr. Paul Weaver for his support and advise as my supervisor, Dr. Graham Hill for finally talking to me and for being so patient while I bogged down your machine and brain, Dr. Neil Taylor for always taking the time to make sure I was alright, Mr. John Burns for his endless computing assistance, all the workshop guys for their support and creativity, and all the other staff and students who helped along the way to make time in Bristol memorable. I would like to pass my appreciation to Airbus for their support and interest in this project, especially the Composite Wing Team for all their help and advice. I would like especially like to thank very close friends: Una Jean Paver for being there, letting me get away, introducing me to fine English Pub fare and wonderful South African wines, and for some of my best memories of my time in England; Pablo Tejera-Cuesta for your support and reminders to 'get this thing done', terrific lunches, teaching me to make croquettes, and for all the fun and laughter; Maggie Campbell for following me over there, taking such good care of me, organizing my life and continually keeping in touch. Thank you to my family who have been there through everything, and whose love and support has brought me to where I am today. Mom and Dad, thank you for all the phone calls, for listening and worrying, and for making me feel like no matter how many miles are between us, we are never far at heart. Jana, thanks for all our European adventures, for showing me the backpacker's way, for being the best little sister ever, and for all the good times we share. To the rest of my family, thank you for keeping in touch, for wonderful holidays at home, and for sending your love and support across the ocean. Most of all, I'd like to thank my husband, Derek, because without you, none of this would have been possible. Thank you for believing in me, even when I didn't, being so patient while I was away and all the time it's taken me to finish this, all the things you did to surprise me, hours and hours of phone calls, hugs when I needed them, untiring support....the list goes on and on. You mean the world to me. Thank you for making me so happy....for being you and for loving me.

Jodi

Author's Declaration

I declare that all work contained in this dissertation is original, was performed by the author, and was carried out in accordance with the Regulations of the University of Bristol. All references to related work are cited and are accurate to the best of the author's knowledge, and no part of this dissertation has been submitted for any other academic award. All views expressed in this dissertation are those of the author.

J. Miller

Jodi Miller

Table of Contents

List of Figures

List of Tables

Nomenclature

A = area (m^2)

B = Biot number = HL

c_p = specific heat (J/kg K)

d = fastener diameter (mm)

E = Young's Modulus (MPa)

g = gravitational acceleration constant (9.81 m^2/s) ; internal heat generation term

h = heat transfer coefficient (W/m^2K)

H = ratio of heat transfer coefficient (h) to thermal conductivity (k)

k = conductivity (W/mK)

L, L' = length (m) ; characteristic length = surface area/perimeter

n = number of fasteners in a multi-fastener joint ; number of experimental test runs

P = load (N)

q = heat flux (W/m^2)

R, r = hole radius

t = thickness ; time

T, T_s, T_∞ T_e T_f T_i = temperature (K), surface temperature, sink temperature, environmental temperature, film temperature, initial temperature

ΔT = temperature difference (degrees)

w = plate width for a single fastener joint ; fastener spacing (pitch) in a multi-fastener joint

x = distance through thickness (mm) ; experimental value

α = coefficient of thermal expansion (mm/K) ; thermal diffusivity (m^2/s)

β_m = mth eigenvalue

δ = characteristic length (m) = distance between heated bodies in natural convection

σ = Stefan-Boltzmann constant (1.308×10^{-23} J/K) ; stress (MPa)

ε = emissivity ; strain

μ = dynamic viscosity (poise) ; kinetic friction coefficient

ν = kinematic viscosity (m^2/s)

θ = angle from bearing plane ; Integral Transform temperature variable

ρ = density (kg/m^3)

Chapter 1 Introduction

1.1 Purpose

The purpose of this research is to study the effects of temperature on strain distribution in multi-fastener double lap hybrid joints. This decision is based on the increased use of Carbon Fibre Reinforced Plastics (CFRP) in aircraft design. CFRP is a complicated material, and with increased complexity of aircraft geometry and unique thermal and mechanical loading conditions, this investigation is a necessary first step in understanding this combination of material and design. The possible use of CFRP in the outer wingbox on the A380 and A400M aircraft provides motivation for this work. The possibility of a double-shear joint in the design connecting an aluminium inner wingbox to a CFRP wingbox via two aluminium laps makes this research novel and provides additional challenges. Gaining an understanding of this type of joint under unusual combined loading conditions requires breaking the problem into three main components. Firstly, a 2D finite element FE heat transfer analysis determines the thermal environment for a simplified wingbox stationed on a runway over the course of a very hot, dry, twelve-hour day. Secondly, a detailed examination of heat transfer through the joint region compares analytical and FE analyses. Finally, a study of the effects on the strain distribution around the fasteners for both thermal loading and combined thermal and mechanical loading within the elastic range is carried out using experimentation and 3D FE analyses.

1.2 Background

There has been a dramatic increase in the use of composites in primary aircraft structures in recent years. The composite CFRP is used extensively in the construction of fighter aircraft and in primary structures, such as the empennage, and parts of the fuselage on larger transport aircraft. Composites offer a significant reduction in weight, because they can be tailored specifically to meet anticipated load conditions, thereby reducing the amount of material needed to safely carry loads equal to that of purely isotropic materials. With the increased use of composites come new design concerns. One of these concerns is the behaviour of joint regions containing these materials. The use of composites in aircraft structures means that mechanically fastened joints become critical elements because of the difference in load transferability in comparison to isotropic materials. These joints are crucial to

overall aircraft integrity, making their design central to overall structural performance. This in turn, makes it essential to have a clear understanding of the behaviour of composites within such joints.

Composites are orthotropic, meaning that they have three mutually perpendicular axes with differing properties, unlike metals, which are largely isotropic, having the same properties along all axes. This is the key difference between composites and their metallic counterparts. Because composites are mostly orthotropic in nature, the effect of load conditions must be carefully examined to ensure adequate strength in the secondary loading axes. This is a problem not associated with isotropic materials. When composites are used, more thorough strain analyses are required to obtain a complete picture of the overall loading, including primary and secondary loads, on a given part. Within the joint regions themselves, complications arise due to contact stresses, friction, and clearance, as well as the resulting stress concentrations, and these may differ from those found in isotropic materials.

Along with complex mechanical loading conditions, aircraft are subject to unique temperature environments. When orthotropic material such as composites are used in these environments, additional complications occur due to the different thermal properties on each of the three axes; for example conductivity, which affect heat transfer, or coefficients of thermal expansion, which affect load distribution. Assumptions are often made to simplify the orthotropic problem to two directions: transverse and axial. Given the complex loading of multi-fastener joints in an aircraft, this simplification may not accurately represent desired conditions, particularly in strain analyses.

The background for the current problem is described by Figure 1.1, where the spanwise joint between the different wingbox types is identified as an area of concern.

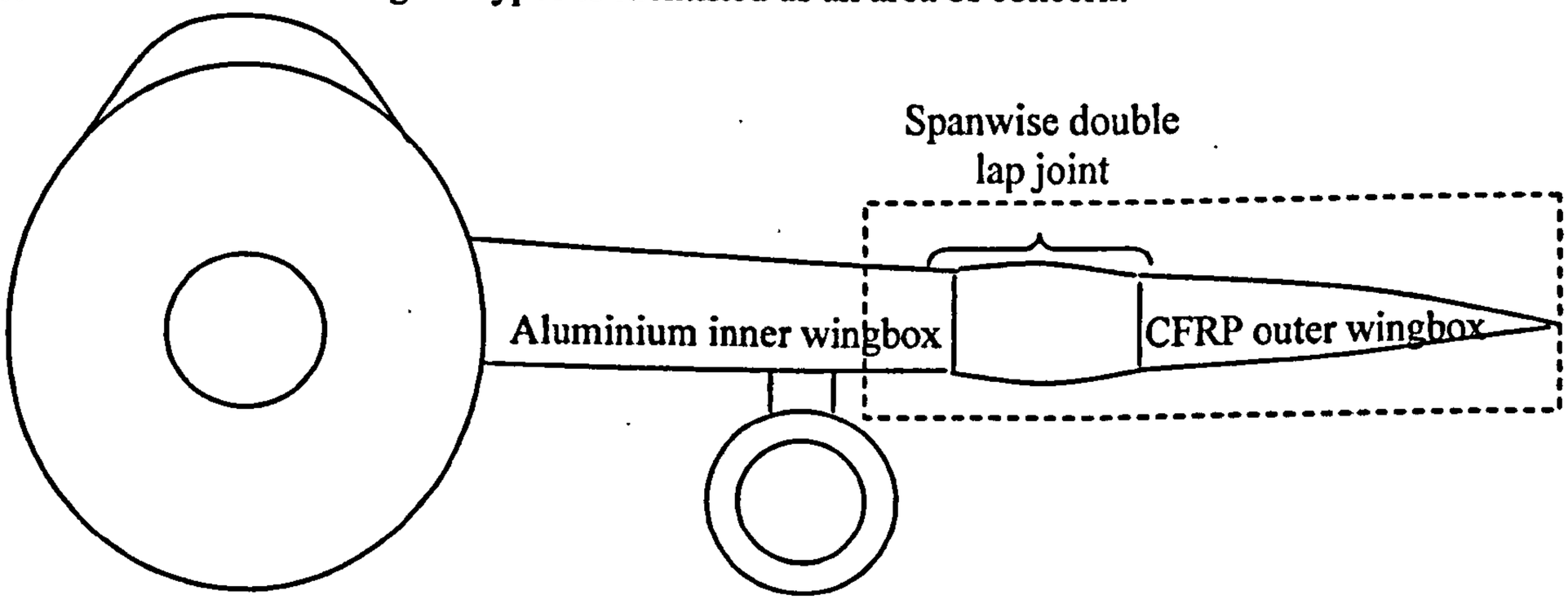

Figure 1.1. Description of primary area of concern in aircraft design.

From a mechanical standpoint, joints are critical in the transfer of the load. As such, joints require a thorough design investigation. Furthermore, from a thermal perspective, joint regions are of particular concern because of the interface of dissimilar materials, as well as differing material orientation, namely orthotropic and isotropic in this case. Thermal loading in these regions induces mechanical strains, which have an impact on overall strain patterns, especially when additional mechanical loading is involved.

Recognizing the importance of this area to aircraft integrity, and in order to use available literature and technology to further this novel investigation of combined thermal-mechanical behaviour on multi-fastener joints, the problem must be simplified. It is important to first understand a simplified wingbox, by approximating the spanwise geometry shown in Figure 1.2(a) with the rectangular wingbox given in Figure 1.2(b).

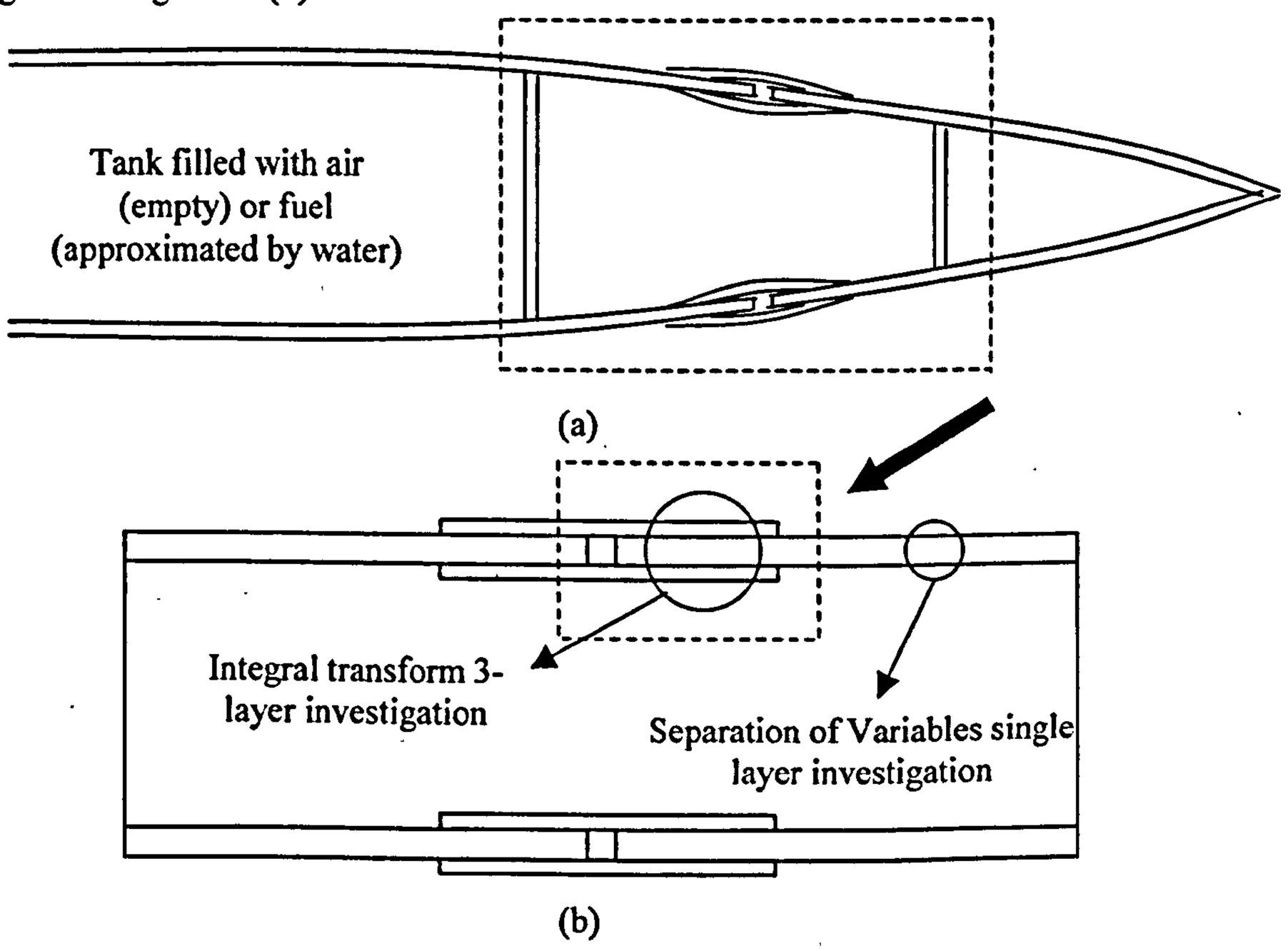

Figure 1.2. Simplification of spanwise joint geometry to rectangular wingbox structure.

This simplified wingbox is used for the heat transfer analyses in Chapter 2. To constrain the problem, conditions of a hot, dry, twelve-hour day with the aircraft resting on the tarmac are modelled. Furthermore, it is assumed that there is no wind and no cloud cover, creating a worst-case heat transfer state. In Chapter 3, 2D FE, based on the assumption that chordwise heat transfer does

not greatly influence spanwise through-thickness results, is used to model conduction, natural convection, and radiation through the wingbox for cases of full, half full, and empty fuel tanks. For three-layer and single layer conditions, analytical modelling is also performed in Chapter 3, as shown in Figure 1.2(b), using separation of variables and integral transform methods, respectively. These analytical modelling results are compared to the 2D FE results.

Having gained an understanding of the thermal environment of the wingbox, a study of the impact of these temperatures on the joint behaviour is undertaken. Macroscopic behaviour is of primary concern to understanding the entire joint behaviour. Failure analyses and associated microscopic level study is beyond the scope of the current work, and is left for future consideration. The model in Figure 1.2(b) is used to perform a sequentially coupled thermal-stress analysis confirming that the region of greatest impact is the top joint on the CFRP skin side in Chapter 4. This area is then targeted for detailed investigation, using a manufactured experimental specimen, similar to that shown in Figure 1.3.

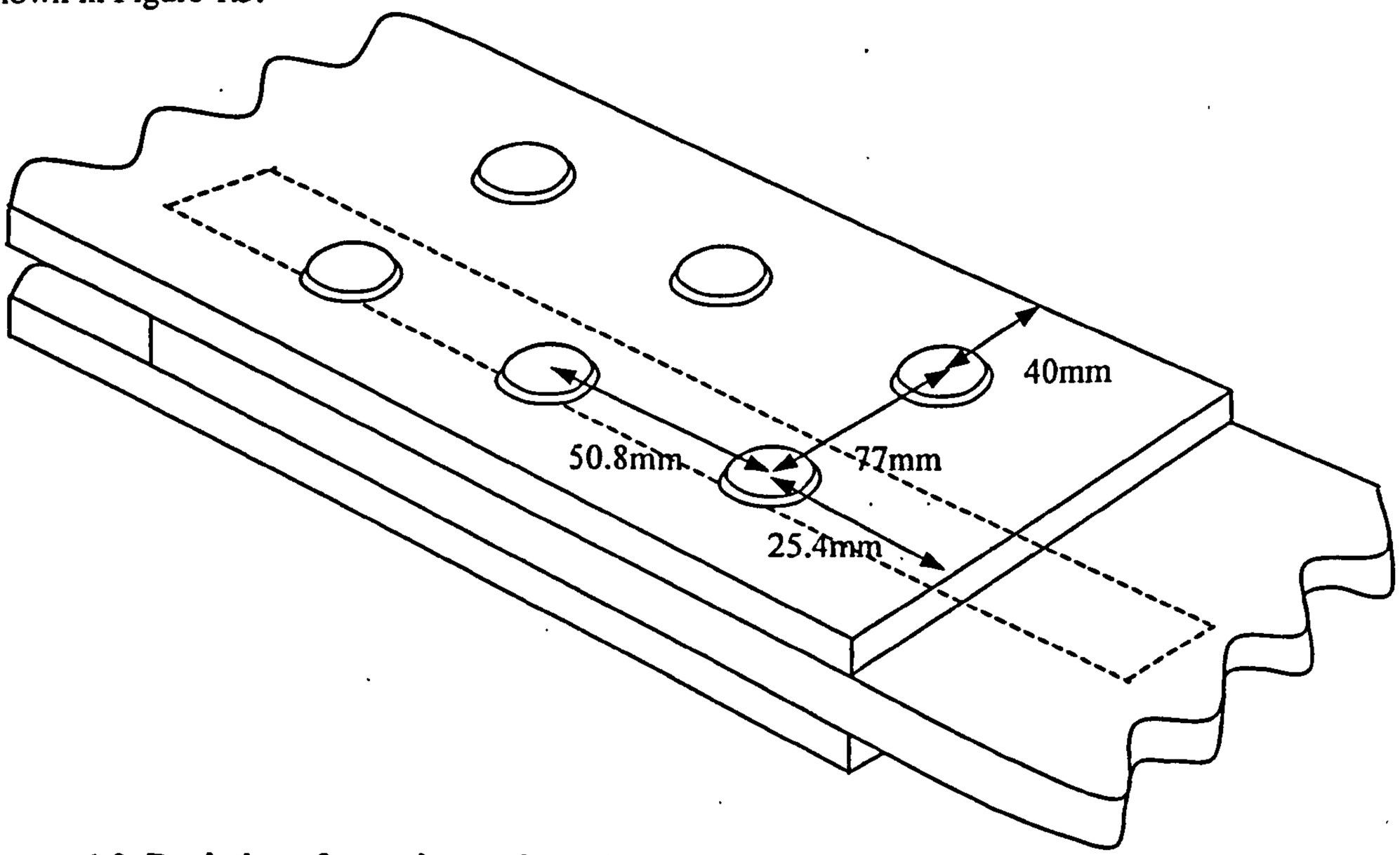

Figure 1.3. Depiction of experimental specimen design.

The specimen contains CFRP skin between two aluminium laps and uses protruded head bolts. Since the corresponding wing loading on the top joint is tensile, tensile mechanical testing is performed at 295K (room temperature) and 373K, based on the results of the heat transfer analyses.

Two different torque levels, finger-tight (1Nm) in Chapter 5 and full torque (35Nm) in Chapter 6, are considered.

To augment the results of the experimental study, and to provide confidence in the values, a 3D FE model is constructed as shown in Figure 1.4. To allow for sufficient mesh refinement, only a portion of the experimental specimen is modelled as depicted by the dashed lines in Figure 1.3, within the limits of computing ability. The FE results, based on experimental validation, can be used to simulate experiments and provide additional contact information, through the use of various boundary conditions.

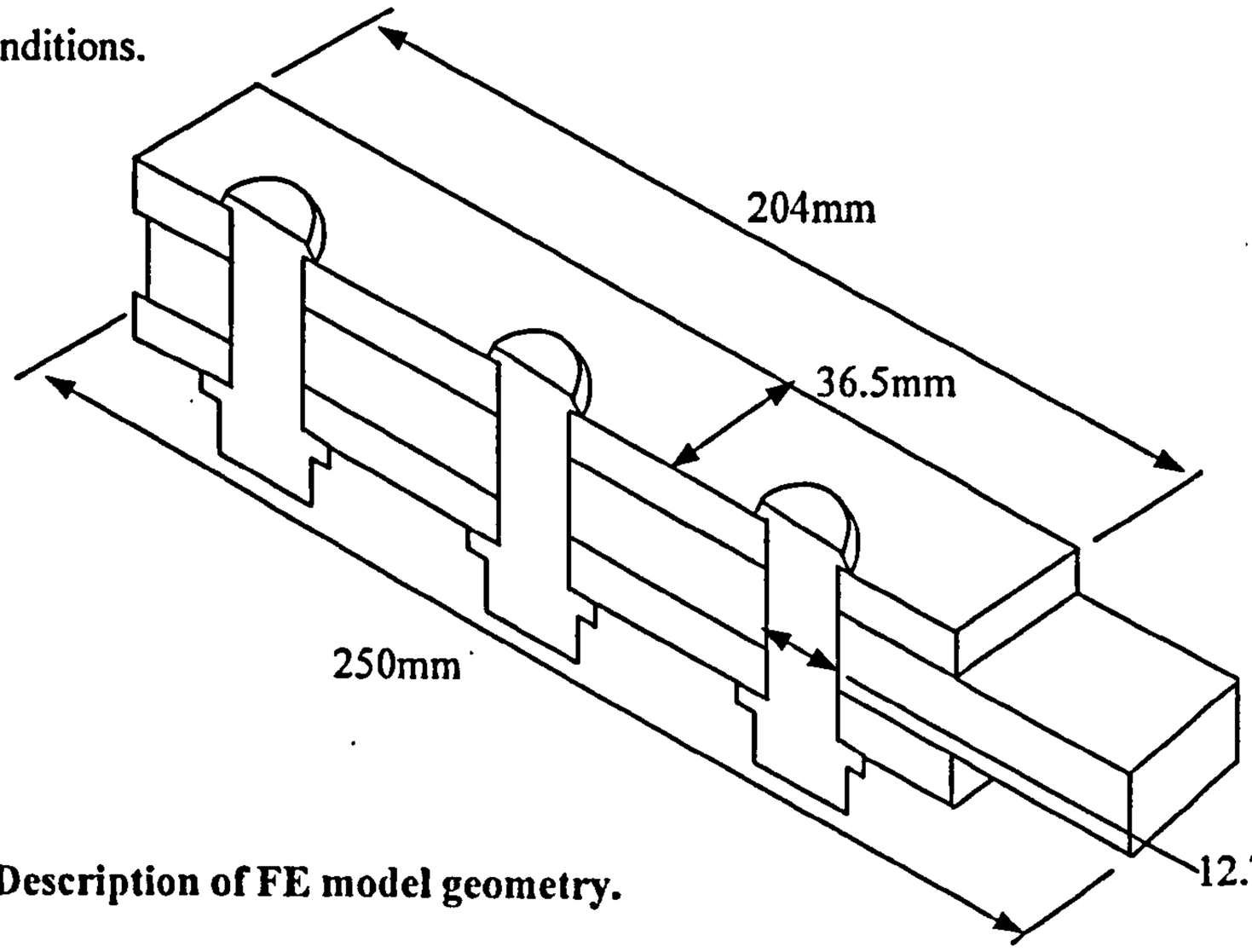

Figure 1.4. Description of FE model geometry.

The benefits of weight reduction and load tailoring make composites ideal for aircraft structures, despite the fact that the use of composites, especially in joint regions, creates a complex, non-linear design problem. This work examines areas of concern in a double shear joint design containing multiple fasteners and a CFRP-aluminium interface.

The flow diagram of the current problem can be formed by connecting Figure 1.1 that describes the global area of concern where the aluminium inner wingbox attaches, using a double lap aluminium joint, to a CFRP outer wingbox, followed by Figure 1.2 that shows a spanwise slice indicating the detail of the double lap configuration and the simplified rectangular wingbox used for heat transfer model; both single and triple layer analytical and FE models, as well as preliminary global stress analysis. Following this, Figure 1.3 shows the details for the 3D experimental specimen to study

thermal effects on strain distribution, combined with the FE results for the region detailed in Figure 1.4, the 3D FE model for strain and stress analyses.

1.3 Literature Review

The literature review includes information regarding heat transfer, bolted joints, and combined thermal and mechanical load conditions.

1.3.1 Heat Transfer

The background of heat transfer is described followed by 2D FE work, analytical work, and finally experimental work.

1.3.1.1 Background

The first step to understanding the temperature environment is performing a heat transfer analysis. The Fourier Heat Transfer Equation can be used to describe heat transfer problems:

$$\frac{\partial^2 T(x,t)}{\partial x^2} + \frac{g(x,t)}{k} = \frac{1}{\alpha}\frac{\partial T(x,t)}{\partial t} \text{ in } 0 \le x \le L, t > 0 \qquad (1\text{-}1)$$

Heat transfer is a function of three mechanisms: conduction, convection, and radiation. Heat can be transferred by a single mechanism, but in most real-life heat transfer problems, energy movement is a result of a combination of the three. The direction of energy flow and the heat transfer mechanisms observed in a problem are influenced by specific boundary conditions. Boundary conditions can be subdivided into linear conditions, including conduction and convection, and non-linear conditions, including radiation. The three potential heat transfer conditions in equation form, as defined by Ozisik [1] and Holman [2] are:

$$q = -k\frac{dT}{dx} \qquad (1\text{-}2)$$

$$q = h(T_s - T_\infty) \qquad (1\text{-}3)$$

$$q = \sigma\varepsilon(T_s^4 - T_\infty^4) \qquad (1\text{-}4)$$

Conduction, equation (1-2), heat transfer is generally the primary heat transfer mechanism through a solid material, while a combination of convection, equation (1-3), and radiation, equation (1-4), usually act to transport heat energy through a fluid to the solid's surface. Conduction is dependent on the thermal conductivity, k, convection on the heat transfer coefficient, h, and radiation on the emissivity, ε and Boltzmann's constant, σ. In the current wingbox problem, all three of the heat transfer mechanisms are observed. Externally, air is the fluid, and studying the effects of hot, sunny weather conditions on a stationary aircraft the largest contributing factor is a direct flux from the sun, followed by radiation to the sky or ground, and finally convection to the air. Through the skins, conduction is the mechanism of heat transfer, and is largely influenced by the material properties, especially in the joint region. Figure 1.5 illustrates the various mechanisms of heat transfer and their general role in the analyses of a simplified wingbox.

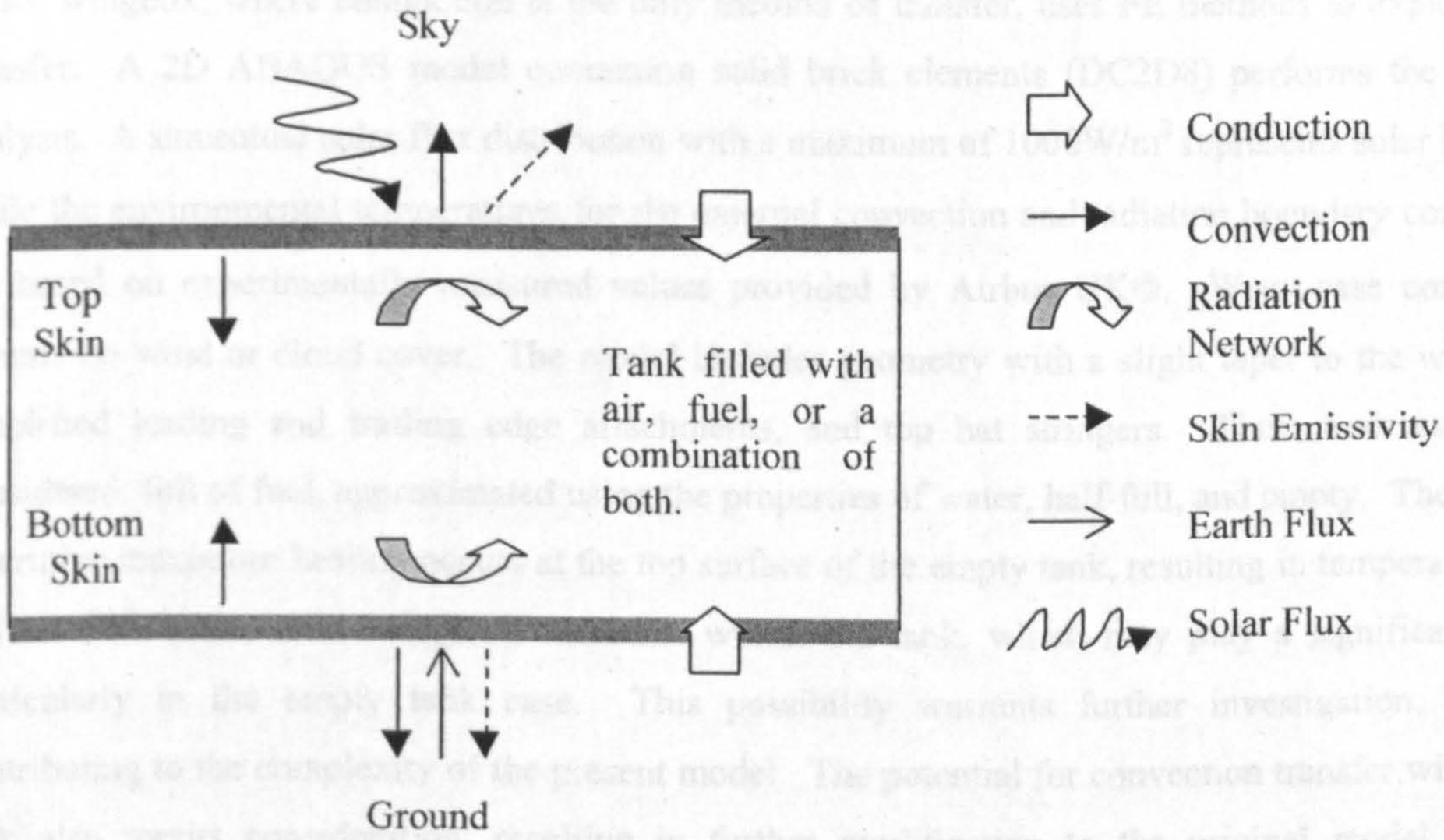

Figure 1.5. Thermal loading conditions on simplified wingbox structure.

Transient temperature analyses for box structures, especially structures constructed of composite materials and under a wide range of thermal conditions, are rare in open literature. The papers that exist either concentrate on steady state analysis [3] or exclude one or more of the modes of heat transfer. Models including natural convection within an enclosure and showing a temperature difference between the horizontal walls are few [4], [5], [6]. Most natural convection analyses in enclosures involve heat transfer between vertical walls, which is known to behave very differently from that of horizontal orientation [7]. Generally, the existing natural convection models are either

based on experimental results in relatively small enclosures, or involve an incomplete cavity subject to boundary conditions different from those of the current problem [8]. Radiation effects in an enclosure have been studied, but the results of these studies are too specific to be applied to a problem involving combined mechanisms of heat transfer [9]. No work in open literature combines the effects of transient natural convection and radiation within a horizontal box structure, and none of the independent studies on the mechanisms of heat transfer involve work on composite structures.

1.3.1.2 Two Dimensional (2D) FE

Numerical solution is used to complete the first step of study for heat transfer through the global wingbox structure, because of the complex geometry and boundary conditions, and because it allows for comparison with previous work [10]. An independent analysis [10] of tank temperatures for a CFRP wingbox, where conduction is the only method of transfer, uses FE methods to explore heat transfer. A 2D ABAQUS model containing solid brick elements (DC2D8) performs the current analysis. A sinusoidal solar flux distribution with a maximum of 1000W/m^2 represents solar heating, while the environmental temperatures for the external convection and radiation boundary conditions are based on experimentally measured values provided by Airbus UK©. Worst-case conditions assume no wind or cloud cover. The model includes geometry with a slight taper to the wingbox, simplified leading and trailing edge attachments, and top hat stringers. Three tank cases are considered: full of fuel, approximated using the properties of water, half-full, and empty. The results determine maximum heating occurs at the top surface of the empty tank, resulting in temperatures of 404K. The above model neglects radiation within the tank, which may play a significant role, particularly in the empty tank case. This possibility warrants further investigation, thereby contributing to the complexity of the present model. The potential for convection transfer within the tank also merits consideration, resulting in further modification to the original model design. Regions of dissimilar materials, such as a joint between aluminium and CFRP skins are suspect and extend the current study to include the joint region. Although a simplified model is used, it provides valuable insight into these considerations, while recognizing the need for further investigation.

Airbus UK© [11] performed studies on fuel heating when a CFRP skin is used in place of aluminium. Analyses use a Fortran program developed to study supersonic transport. This program uses experimentally determined flight data, to account for fuel flow through the tanks. The use of a CFRP skin leads to increased fuel temperatures, indicating the need for detailed investigations of the effects of CFRP, and justifying the current work presented in Chapter 2.

1.3.1.3 Analytical

Numerical methods for solving transient problems are a widely accepted form of solution, with different commercial packages, such as ABAQUS, NASTRAN and PATRAN, available for a variety of problems. However, a simple analytical method offers insight into the physical properties of a particular problem, while providing confidence in numerical results through the use of an independent method of solution. Despite advancements in computer technology, analytical solutions still play an integral role in gaining a solid understanding of a problem. In fact, the computer provides a more efficient means of obtaining analytical solutions, especially in the area of series approximations, giving the analytical approach a more practical and wider range of application in the design world.

In the current problem, analytical methods create a detailed model of the skin region, serve to validate the finite element results, and offer a practical understanding of the influence of heat energy. The current work is innovative in that it allows for both convection and radiation at both surfaces of a single layer, through the use of the integral transform technique, and at a multi-layered external surfaces, based on separation of variables, in transient analyses. The importance of unique boundary conditions at each respective surface is taken into consideration.

Ozisik [1] provides solution temperature profiles, in terms of space and time, based on an integral transform solution technique. Ozisik summarises other analytical solution techniques, and develops a range of formulae for infinite, semi-infinite, and finite boundary problems of transient heat transfer, subject to general boundary conditions. Although these solutions are formally complete, they lack specific developments for complex boundary conditions such as convection or radiation. Other analytical solutions for transient problems are generally limited to semi-infinite or infinite solids where exact, rather than series approximations, can be obtained [2]. Limited work has been done on plates with finite boundaries, and simplified boundary conditions of constant temperature or constant flux are generally the only conditions applied [12], [13], [14]. The present work, which considers combined convection and radiation conditions at both external surfaces of a slab with finite boundaries, is original and pioneering.

Transient analysis is an important component of the current problem, as the temperature load on the wingbox is influenced by many elements and is, therefore, in a constant state of change.

Heisler [2]charts are a popular method of attaining transient results. They use previously developed plots, based on experimental trend analyses for specific boundary conditions. They are, however, limited to identical boundary conditions at both external surfaces, and are generally given only as mid-surface temperatures. Ozisik's formulae have been used as benchmarks for supplementary analytical developments [15], [16]. Boley and Weiner [17] discuss different methods of heat conduction and analytical solutions, arriving at conclusions that support the work of Ozisik [1].

Most developments in this field have taken place in recent years, suggesting that the potential for analytical solutions in place of numerical analyses has not been fully explored. The difficulty with using an analytical approach to heat transfer problems arises from the fact that for any small alteration in problem definition, especially in boundary conditions, the analytical solution may change dramatically. De Monte [15] provides a good summary of different possible analytical methods that can be used to solve transient heat transfer problems, and outlines the strengths of these methods for specific applications. The error analysis performed is valuable in gaining an appreciation for the number of terms required to reach a desired level of accuracy using the closed-form analytical solution. Unfortunately, in the problem definition itself, a simplifying assumption of a first-order constant temperature boundary condition is made, thereby limiting the applicability of this work. In principle this work can be expanded, but the expansion to higher order boundary conditions is not as simple as De Monte implies.

Antonopoulos and Tzivanidis [16] have also carried out work on separation of variables for multi-layered specimens, using the solution principles Ozisik discusses. Analytical solutions exist for one-dimensional heat transfer through a composite structure subject to convection boundary conditions at its surfaces. The work provides important insight into analytical solutions in a composite region, dealing with third order convection boundary conditions. It does not, however, address radiation boundary conditions, which play a significant role in the current problem. Based on work by Zerkle and Sunderland [18], a linearised form of radiation boundary conditions are developed herein for use with the analytical model for convection and is presented in Chapter 3. Distinct and original, analytical modelling for more complex radiation and combined boundary conditions is explored in the current work.

Mantelli and Yavanovich [19], [20] have done the only work on heat transfer in bolted joints, using an analytical model to measure the contact resistance of bolted joints. They perform a parametric

heat transfer analysis. This work determines that microscopic contact conductance is not crucial, that radiation resistance is not important unless large gaps are present, but that thickness of the joint is a major consideration. Thermal interaction between fasteners occurs when the ratio of the fastener pitch to the washer radius is less than ten. However, this value is material dependent. This study suggests that in modelling the current bolted joint, assumptions of a smooth and even contact surface, and no gap radiation are permissible. It also validates the use of a primarily macroscopic level investigation.

1.3.1.4 Experimental

Airbus UK© [21] has performed environmental testing on a CFRP wingbox in Madrid. The solar intensity of this experiment can be approximated by a sinusoidal curve with a maximum of $900W/m^2$. The maximum temperature is found on the top surface, with a value of approximately 338K. Even allowing for experimental error, including wind gusts and lower solar intensity, a CFRP wingbox can undergo extreme heating conditions, justifying further investigation into thermal stresses introduced by such conditions. None of this previous work includes a joint region, necessitating further study, which is described in Chapter 4.

The effects of thermal environment on an aircraft are identified as a concern by Barzelay and Boison [22] who perform a number of experiments using aluminium to show the effects of heating unique aircraft geometry. The results show an increase in thickness causes a decrease in the thermal gradient due to improved heat flow, leading to lower thermal stresses. Barzelay and Boison [22] note that the thermal gradient increases with increased heating, which is intuitive since the rate of conduction is influenced only slightly by increases in temperature. With regard to aircraft-specific geometry, thermal stress generally causes tensile stresses, but in particular areas, such as over spars, compressive stresses are induced. This demonstrates the difficulty associated with geometry and joint regions, and justifies the need to study areas of dissimilar material in greater detail.

1.3.2 Bolted Joints

The literature review also includes bolted joints, which are broken down into multi-fastener and single fastener sections.

1.3.2.1 Multi- Fastener

Multi-fastener joints is further broken into experimental, analytical, 2D FE, and 3D FE sections.

1.3.2.1.1 Experimental

One of the most common methods of joining materials is using fasteners or bolts. Other methods, such as bonding, have been explored, but the customer perception of greater safety with the use of multiple fasteners still makes mechanical fasteners the most popular choice. Aircraft structures contain a large number of bolted and riveted connections. It is at these connections, or joint regions, where failure is generally initiated, making them a critical design concern. Generally the first indication of failure is better understood by studying the strain distributions in these critical areas. Although bolted joints are recognized to be extremely important in overall design, limited work has been done to study both thermal and mechanical influences on a multi-fastener joint. The novel aspect of the current work is that it does consider both thermal and mechanical loading conditions in a hybrid composite metallic joint containing multiple protruded head bolts. Despite the fact that multi-fastener joints are commonly used in larger structures, few studies have been conducted on effects associated with multiple fasteners, particularly in joints containing composite materials.

The regions associated with a bolted joint are described according to their position relative to the direction of mechanical loading. The plane where the fastener reacts with the hole itself to transmit the load is called the bearing plane, and is found at x=0°. The plane at 90° to the bearing plane, containing the smallest relative width in the specimen, is called the net tension plane. In multi-fastener joints this region is associated with bypass loading. Figure 1.6 depicts a general bolt hole region.

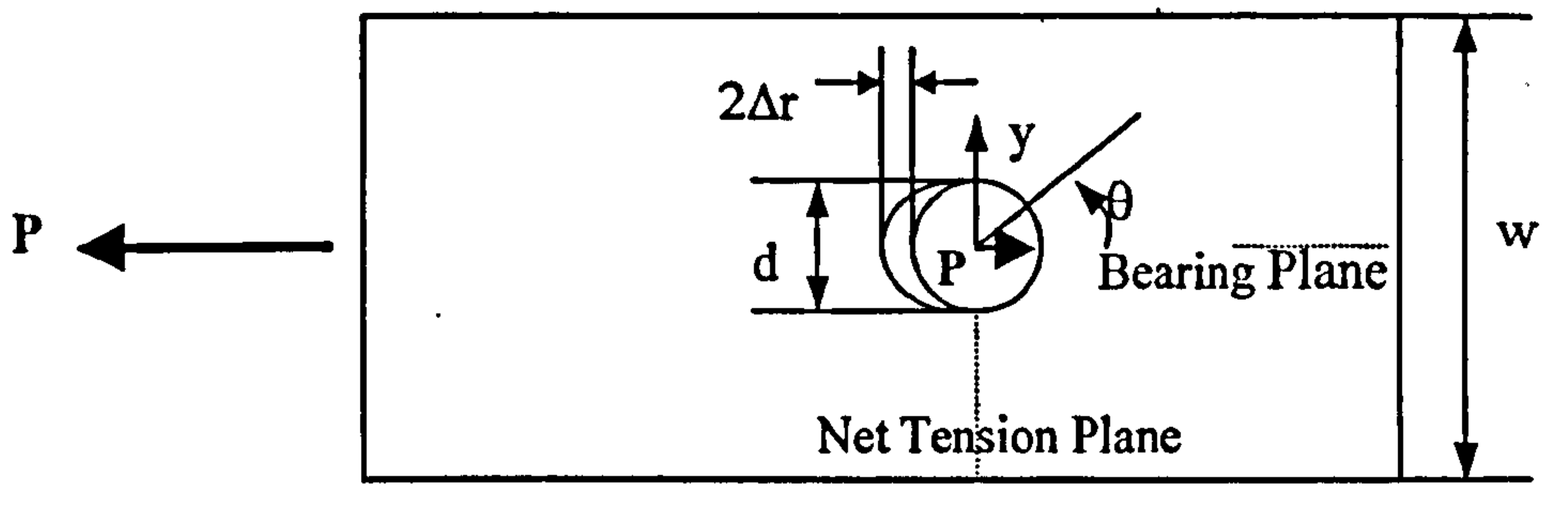

Figure 1.6. General description of bolt hole region.

As the fastener reacts with the surface of the hole in he bearing plane, a compressive stress is induced, in reference to tensile load. While in the net-tension plane, because the same load is distributed over a smaller cross-sectional area, a higher tensile stress is induced. Bearing plane failure is considered the "safer" of the two because the material generally yields or deforms prior to complete failure, unlike tensile failure, where no noticeable damage is observed before the part fails. Figure 1.7 represents stress concentrations at the bearing and net-tension planes.

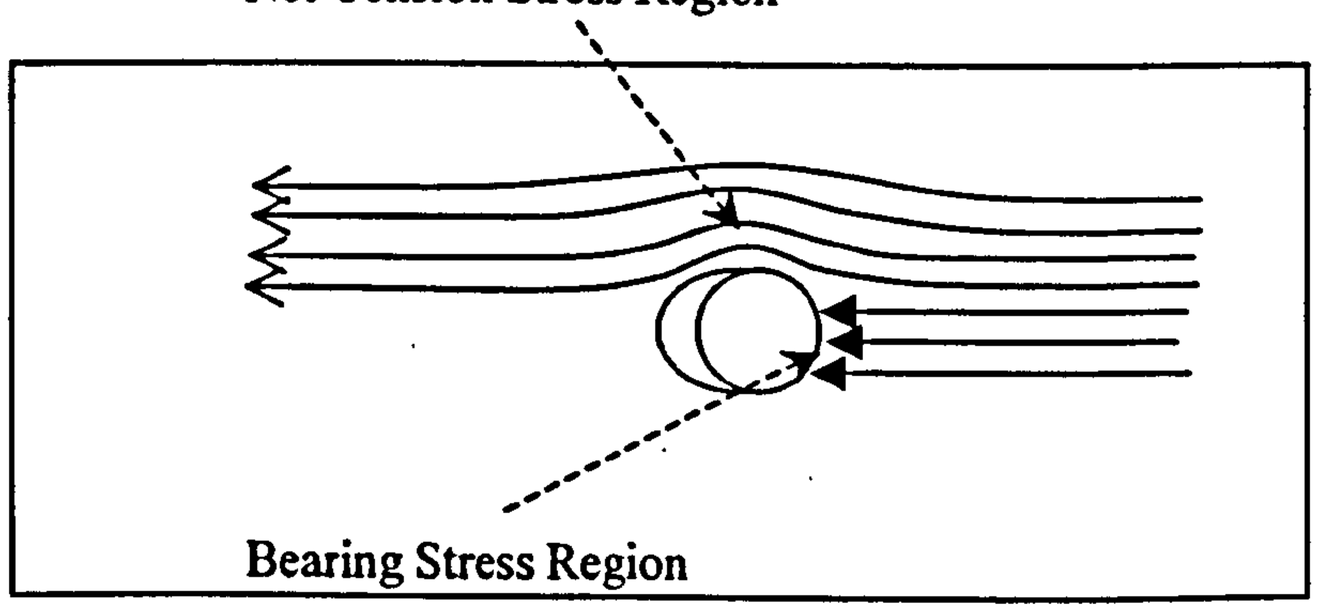

Figure 1.7. Net-tension and bearing stress description.

Hart-Smith has performed extensive studies on these regions [23], [24], [25]. In his article on bonded-bolted composite joints [23], Hart-Smith examines double and single stepped lap joints containing multi-rows of bolts. Hart-Smith's theory of bearing and bypass refers to stress concentration due to compressive contact (for a tensile load) at the hole/fastener interface as bearing, while bypass load is that which is not transmitted at that fastener, but rather transfers past the hole along the net-tension plane to react at other holes. Figure 1.8 illustrates the concept of bearing-bypass in multi-fastener joints, and the dashed boundary indicates that this hole is in the middle of a larger group of fasteners. This bearing-bypass concept is the primary difference in studying multi-

fastener and single fastener joints, since in a single fastener joint loads react at one fastener, as a result there is no bypass.

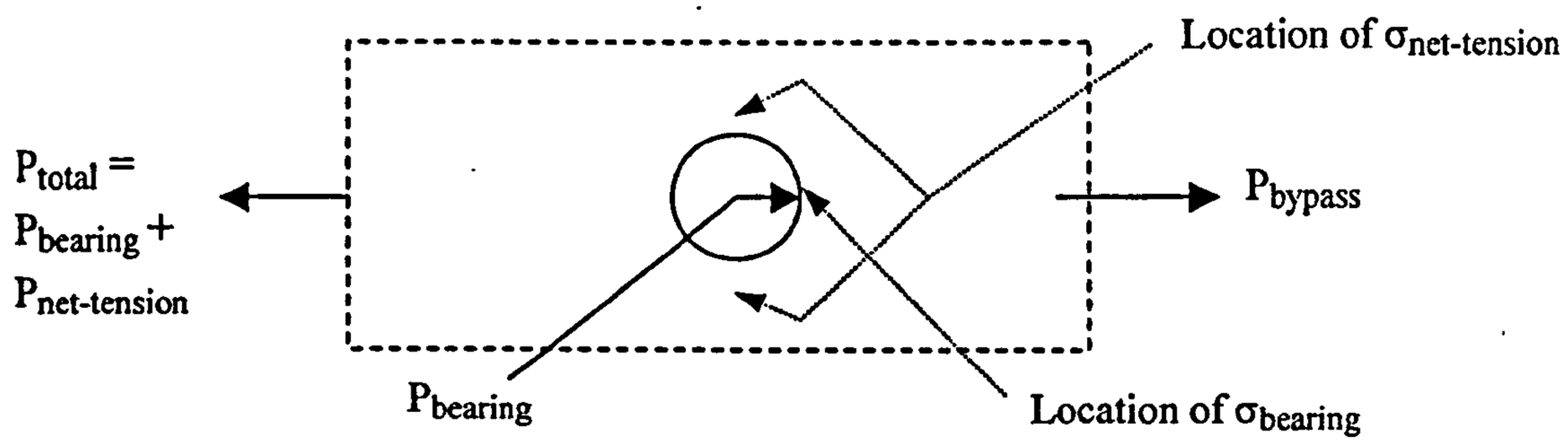

Figure 1.8. Illustration of bearing-bypass load.

Double lap strength can be predicted with fair accuracy using elastic stiffness, but due to eccentric loading, the single lap becomes significantly more non-linear. Based on failure results, the bonded joint containing no fasteners is actually the strongest design, but by only a slim margin over a bolted joint with no bonding. Stepping of the laps tends to equalise load distribution, reducing stress concentrations and increasing joint strength when compared to rectangular plates.

Studies of critical joints in aircraft structures [24] involve the manufacture and testing to tensile failure of 180 test specimens with quasi-isotropic and high 0° lay-ups. They include a number of different double lap configurations, tapered, uniform, and stepped designs. In all cases, both the laps and the central plate are made of composite, different from the current hybrid joint. The results show that both lay-ups have similar strength, possibly due to the fact that the increased stress concentration induced by greater deviation from isotropy nullify the benefits of additional in-plane strength acquired by increasing 0° plies. Softening or elongation of the bolt hole increases bypass strength by reducing stress concentrations at the net-tension plane. Torque significantly increases failure load, and wider joints tend to have a greater non-linear region with increased chance of bearing failure, where narrow specimens tend to fail at the tension plane. Single hole specimen examination shows that allowable strength of the central plate is always greater than that of the splice plates, even when all three are the same thickness. This indicates that the laps are critical in the double lap design. Some suggested design guidelines include: for unloaded (fastener-free) holes the minimum width should be 3d, where d is the hole diameter. For multi-row joints this value increases to 4d or 5d due to the increased requirement for bypass strength; bolt diameter should equal the thickness of the centre plate to prevent load shifting caused by bolt bending; larger nuts should be used to improve

clamp-up from the torque, reducing the chance of net-tension failure; and for multi-row joints the centre plate and the laps should be uniform thickness for best performance; however, single row joints commonly perform better than multi-row designs. Results suggest that bypass load at the first bolt in a multi-row joint should be maximised to improve joint efficiency by decreasing stress concentration. The key to designing CFRP joints is to restrict the bolt bearing, which leads to delamination at critical load locations. The determination of strain magnitude and distribution is, therefore, essential. Finally, the study notes that joint strength is sensitive to geometry and the material itself. However, minor changes in lay-up seem to have a lesser effect.

1.3.2.1.2 Analytical

Hart-Smith [25] has also suggested an analytical method for analysing bolted composite joints, to predict strength in geometries other than those of the standard test coupon. His method is based on adapting elastic stress concentration factors at loaded bolt holes in isotropic materials to fit orthotropic composite design. Single and multi-hole joints are compared, as well as eccentrically loaded holes in finite-width strips. However, these analyses are purely analytical with no experimental test data for confirmation of joint performance.

In Hart-Smith's work [25], experimental data is used within the analytical analyses. A coefficient based on experimental results, and is a function of bolt size, lay-up, and thickness, is used to reassess an isotropic joint of the same geometry. The difficulty with composites is that they are neither perfectly elastic nor plastic. Tensile loads are used since they are generally considered more critical to aircraft structures. The additional tensile load must go around the hole in the joint material, whereas compressive loads can be transferred directly by the fasteners. Results show that the ratio of bearing strength to net-tension strength affects the maximum joint strength and the optimum d/w and d/p. For a highly orthotropic lay-up, the optimum pitch is 2.5d, whereas for an isotropic lay-up, the optimum pitch is 3d. For an orthotropic lay-up, failure tends to be either bearing or net-tension, but for the isotropic lay-up a pitch of 5d is required to invoke bearing failure, and to compromise total joint strength. A minimum edge distance of 3d is suggested for composites, as compared to 2d for metals, reiterating the difficulty of composite joint design. When torque is introduced, there is considerable improvement in bearing strength, which shows agreement with previous work [24]. The strength of multi-row joints exceeds that of an optimum single row, but only slightly, demonstrating that strength increase is not directly proportional to the number of fasteners. This challenges the findings of Hart-Smith's previous work [23], [24], which indicates that the behaviour

and modelling of multi-fastener joints is not fully understood. Joint performance depends on lay-up, degree bunching (stacking similar plies together to discourage delamination), and resin content, which dictates 'psudo-plastic' behaviour.

Oplinger performs analytical and experimental work on the structural behaviour of mechanically fastened composite joints [26]. Oplinger selects the least squares boundary collocation as the analytical method, with FE for verification. Multi-fastener joints are simulated using generic single bolt models with specific boundary conditions to approximate bearing-bypass conditions, similar to that in Figure 1.8. In the analytical modelling, Oplinger uses a rigid pin with a cosinusoidal contact distribution. Experimentally, pin-bearing single fastener coupons are used to perform failure studies and Moire strain analyses. The optimum "pitch", which in this case is interchangeable with width, is material dependent and generally of the range 2d to 2.5d, which is in good agreement with the results from Hart-Smith [25]. Their results suggest that as long as the pitch is sufficient, the edge distance can be relatively short (2-2.5d). Multi-fastener joints with parallel and series arrangements as given in Figure 1.9 are also examined.

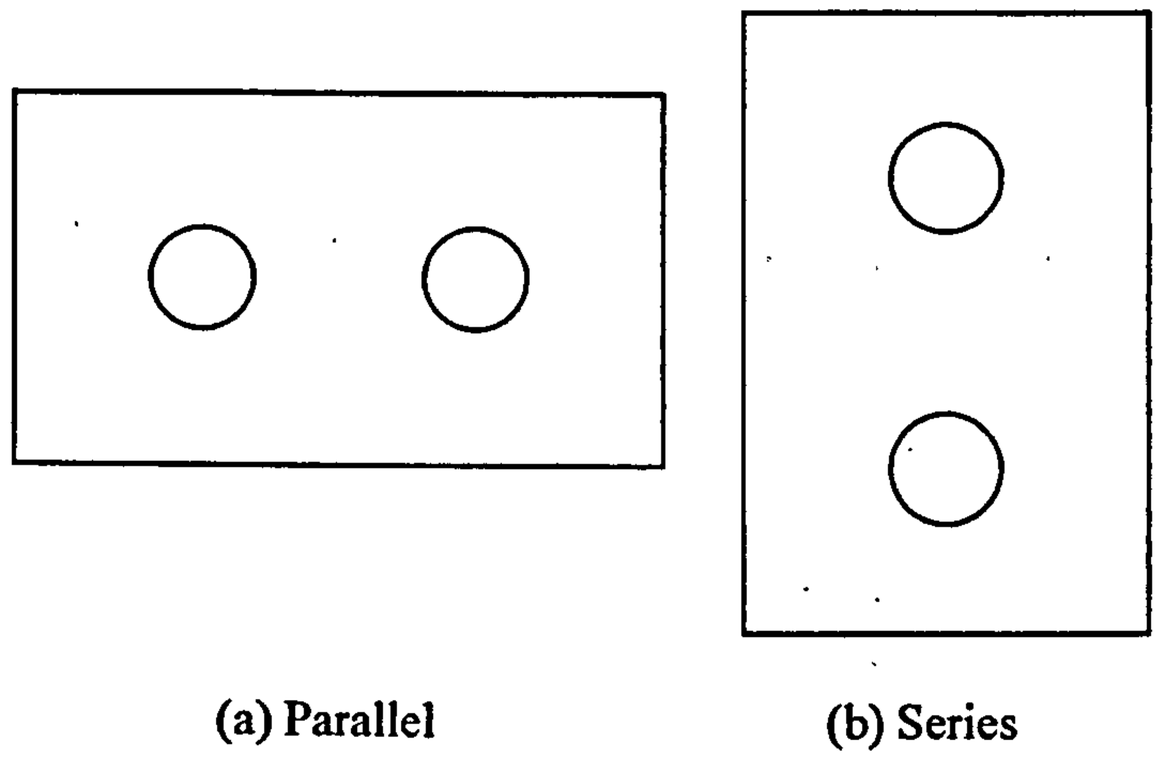

Figure 1.9. Description of multi-fastener joint arrangements.

Parallel arrangements have approximately 10% lower stress concentration at the net-tension plane, but increased bearing stress, and increased overall stress. Series arrangements demonstrate some discrepancy between FE and analytical results due to non-uniform load distributions and fastener load interaction due to bypass stresses. This means the linear assumption that an open hole solution can be added to a filled hole solution to provide the overall result is erroneous for multi-fastener joints, especially for pitches of less than 2.5d.

Madenci and Ireli. [27] analytically determine contact stresses for single, series, and perpendicular multi-row joints for finite dimension CFRP plates, using the modified mapping collocation technique along with the assumption of plane-stress analysis. Decreasing edge distance causes an increase in all stresses, agreeing with other work performed [28], [50]. Stresses are found to be material dependent as in work by Lin [50].

The design of composite laminates containing pin-loaded holes, again in single, series and parallel specimens, is examined by Chang et al [28]. The results show failure load increases with edge distance, differing from the results of reference [31]. When comparing the single, two-pin series and two-pin parallel specimens, the specimens with pins acting in parallel have the highest failure loads, while the single pin specimens have the lowest values. However, these values are only slightly below those of the series specimens, in agreement with reference [25]. When specimens containing multiple parallel fasteners in one and two rows are compared, there is only a slight difference in failure load between the two, and at lower pin diameters, the two row specimens have lower failure load than the single row specimens as per the results of references [24] and [30].

1.3.2.1.3 Two Dimensional (2D) FE

Blackie and Chutima [29] also study stress distribution in multi-fastener composite joints. Analytical models using pins are compared with FE models containing gap elements, which account for friction. Different two-row stagger patterns for multi-fastener joints are examined. The results show a non-uniform distribution of load transfer across multi-fastener joints, which imply that results for a single pin joint cannot simply be extrapolated to a multi-pin arrangement. The presence of friction significantly reduces axial contact stress, suggesting that it influences load distribution and should be considered. Pin rigidity also affects load distribution when the coefficient of friction is greater than 0.2. Recommendations include increasing the pitch distance from 3d to 4d to improve joint performance in double row joints, which differs from the results of reference [25], however, the fastener pattern also differs. In single row joints, increasing pitch distance actually increases radial stress, indicating significant differences between single versus multi-row joints.

Eriksson [30] uses 2D FE analysis to examine contact stresses in a single row joint. All stresses are found to be clearly dependent on laminate properties and lay-up. Lay-ups with a high number of 0° plies are closest to having a cosine radial contact distribution, while those with a high number of ±45° plies display the greatest deviation from the cosine curve. Increasing clearance decreases the

angle of radial stress, while increasing friction decreases the magnitude of maximum radial stress. Tangential and shear stresses are also reduced by increasing friction, but the angle of maximum tangential stresses increases with increased friction, which is intuitive based on the associated increase in contact area. Bolt elasticity has little effect, which is in agreement with Hyer et al. [56]. However, for coefficients greater than 0.2, Blackie and Chutima [29], indicate that pin elasticity has an effect on joint strength. Full contact models appear to be a better match with experimental data than do radial displacement boundary condition models, agreeing with the results from Chen [39].

Chang et al. [31] examine failure of pin loaded composite laminates, where the first step focuses on stress distribution using FE analysis, related to this current work. Single pin, two-pin series, and two-pin parallel specimens, similar to those in Figure 1.9, are examined using 2D analysis, while acknowledging that the potential error associated with neglecting through-thickness lay-up properties could lead to errors of 10-20% in strength prediction [32], [33], [34], [35], [36]. The assumption of a cosine distribution for contact stress, has been determined to be erroneous for certain lay-ups [30], [39], [57], [61]. For single fastener specimens, increasing width to diameter results in increased bearing strength agreed with references [24]-[26]. The ratio of edge distance to diameter has a lesser effect. Holes loaded in parallel show less variation with changing width to diameter and edge to diameter distances. Those loaded in series tend to behave similarly to single fastener specimens. In all cases, the strengths are dependent on lay-up.

1.3.2.1.4 Three Dimensional (3D) FE

In a 3D FE analysis, Airbus UK© [37] studies the effects of compressive and tensile loading of torque-tightened fasteners on a double lap, three fastener joint with Ti alloy laps and CFRP skin. The study uses a lay-up with 0° dominance and neglects friction, as well as uses a cosine contact distribution assumption. Results display high bypass at the first hole in a row of three, and a load distribution of 37% at hole 1, 29% at hole 2, and 34% at hole 3. This suggests that in multi-fastener joints, the load distribution is not intuitive due to complex bearing-bypass stress interactions, thereby justifying the need for further investigation using FE or other numerical solutions for contact analysis, and the need for experimental validation. In the study, torque level is reduced 3% over the course of the analysis, probably due to bolt bending and Poisson ratio effects. In a second study, preliminary thermal load calculations are performed using simple formulae and a spreadsheet method [38], which produce conservative results based on limited experimental comparison. Friction is neglected and two rows of fasteners are modelled, such that the second row of fasteners acts as the

constraint for thermal expansion of the joint materials. This time aluminium laps are used in place of titanium, and a quasi-isotropic lay-up is selected for the CFRP skin. The minimum pitch for 6.35mm bolts with 4mm thick aluminium laps and 10mm thick CFRP skin is 3d, which is in agreement with reference [25]. This pitch distance produces non-catastrophic bearing failure of the joint, rather than total tensile failure.

Chen et al. [39] use FE with a new transformation method derived from 3D contact kinematical conditions to perform a 3D contact stress analysis of a composite joint. A double lap joint design is used to study glass-fibre (GFRP) and carbon-fibre reinforced plastics (CFRP) with quasi-isotropic lay-ups. Allowing variation in contact area and sliding friction at contact surfaces, accounts for non-linearity associated with contact. Increasing friction decreases axial strain, while increasing clearance increases axial strain, thereby decreasing load capacity, implying that clearance should be modelled and that contact conditions are very important, as found in the work by Blackie and Chutima [29]. This work establishes that the cosine contact distribution assumption is not adequate for quasi-isotropic lay-ups, that lay-up changes tolerable stress, that bolt elasticity is not a consideration in immediate stress concentration, but does play a role in total joint stiffness, and that clamping pressure prevents delamination, thus improving joint strength. Comparing these results to previously determined experimental results [40] accuracy is verified.

Shokrieh and Lessard [41] examine the effects of material non-linearity using 3D FE for pin-loaded composites. The results of the examination reveal that transverse and interlaminar stresses are affected by non-linearity, but radial stress does not deviate significantly from the results of a linear elastic model. Hassan et al. [42] also use 3D FE to model single and multi-fastener double lap joints. Contact modelling is used in conjunction with layered shell elements and 3D gap elements to simulate clearance. The ultimate load capacity on the joint is not directly proportional to the number of fasteners used, which concurs with Hart-Smith's results [25]. Load distribution is not equal when using more than two rows of fasteners in series. Also, the magnitude of the net-tensile stress decreases rapidly at pitch distances of more than 1xdiameter, which implies that wider joints are not necessarily more efficient, results that differ from references [25] and [29].

Naik and Crews Jr. [43] look at stress analysis for clearance fit multi-fastener joints. The analysis models a single fastener, subject to bearing and bypass loading, with a rigid frictionless bolt and a quasi-isotropic laminate. Radial nodal displacement is used for the contact conditions, while the

entire analysis assumes linear elasticity. These assumptions may reduce the accuracy of the results. Dano et al. [57] and Camanho and Matthews [59], [60] suggest full contact modelling using master-slave analysis is more accurate than radial displacement. Shokrieh and Lessard [41] also conclude that linear elastic analysis is less accurate for radial stresses under contact conditions. The contact angle and peak stresses are strongly dependent on the bearing-bypass ratio. Increasing the bypass load results in increased contact angle for tensile loading. The peak tangential stress increases proportionally to an increase in bypass stress. Radial stress is not as sensitive to changes in the bearing-bypass ratio.

1.3.2.2 Single Fastener

Discussion of the single fastener work is once again broken down into experimental, analytical, 2D FE, and 3D FE.

1.3.2.2.1 Experimental

Single fastener joints have been studied in greater depth that multi-fastener joints. They provide a good basis for understanding more complex joints. However, these studies of single fastener joints do not account for bearing-bypass interaction, which plays a major role in load distribution of multi-fastener joints. Previous work does provide a good means for understanding other influences on joints, and supplements the few studies on multi-fastener regions. Bearing failure in metal/composite/metal double lap joints has been studied experimentally and analytically [44], [45] by Wang and Hung, respectively, and the results show that bearing damage can, in fact, be catastrophic in the absence of clamp-up force. The relationship between improved bearing strength and increased clamp-up pressure is almost linear at higher torques (>5Nm). A non-linear 2D FE model using a rigid washer and bolt design shows good agreement with experimental results.

Tsai and Morton [46] are more concerned with failure analysis of pin-loaded specimens, but their experimental results generate some interesting generalisations for stress analysis. Moiré interferometry is fed into 2D FE to analyse stresses around the contact surfaces. Friction causes a change in the sign of in-plane shear stresses, particularly under compressive loading, but the more important discovery is that this behaviour does not match that of isotropic materials, a fact not previously identified in purely analytical studies. This implies that the assumption of simple Coulomb friction may result in error due to local friction effects being dependent on fibre

orientations. Many numerical packages do not allow for in-depth friction analysis in combination with contact conditions. Chen and Lee. [47], based on their 3D numerical and experimental analyses for a single fastener, suggest that contact distribution is influenced more by lay-up than by friction.

Crews and Naik [48] look at open and closed holes in single fastener joints, both experimentally and using FE analysis. The model is a single fastener quasi-isotropic joint. Their studies show that bearing stresses cannot be accurately estimated by superposition of separate stress analysis on individual bearing and bypass loading, making analytical solutions difficult. Tangential stresses, on the other hand, can be estimated in this manner.

Yan et al. [49] perform an experimental study on the clamping effects on the tensile strength of composite plates with a single bolt-filled hole. Both 100% bypass, equivalent to an open hole, and 100% bearing loads, equivalent to a single filled hole, are examined. Clamping force can improve joint strength regardless of ply orientation, agreeing with references [25], [63], and [64]. Increasing washer size increases joint strength, agreeing with reference [25], up to an approximate washer diameter three times that of the fastener diameter, after which no improvement is noted. Washer sizes of less than 2d have a negative effect on joint strength. Friction has little effect on joint strength, in contradiction to the findings of references [29], [30], [39], [46], [51], [63], and [70].

1.3.2.2.2 Analytical

Lin and Lin [50] perform stress and strength analyses of orthotropic composite plates containing pins using the direct boundary element method. According to their findings, an edge distance of 2d is the minimum required to allow for the safer joint design failing in bearing, which agrees with the results of references [25] and [26]. As this ratio decreases, an increase in the stress concentration factor is observed with a corresponding decrease in joint strength. The study reaffirms that joint strength is dependent on laminate properties and lay-up as per the results of references [25], [39], [46], [56], [63], and [65].

1.3.2.2.3 Two Dimensional (2D) FE

Webber et al. [51] use FE to study strain distribution around fasteners subject to biaxial in-plane loading. A non-linear 2D FE ignoring interlaminar strains, but accounting for friction using interface elements is explored. Washers even out load distributions uniaxially, thereby increasing far field

allowable strain. Washers do not even out shear strain distribution, however. Friction plays an important part in strain determination, which is in agreement with Blackie and Chutima [29].

Chang et al.[52] study the strength of mechanically fastened joints using 2D FE. The cosine contact distribution assumption used has been shown to be an erroneous assumption in other work [30], [39], [57], [61]. According to other work [53], [61], [62], the stress distribution inside a body is relatively insensitive to assumed load distributions. Chang et al. confirms the results of reference [54], where stacking sequence has a 10-20% effect on strength and most certainly plays a role in load distribution; however, in agreement with reference [55], they also show that lay-up is less important when washer constraints are present. This implies that distribution varies significantly at different torque values. Increasing width to diameter ratios increases failure load. Using their analyses, Chang et al. determine that some lay-ups are more affected by edge distance. Increasing edge to diameter ratios in 90° lay-ups causes increased failure load.

The effects of a variety of variables on pin-loaded orthotropic plates are examined by Hyer et al. [56] using FE analysis. In a double lap joint study, for a perfect fit, frictionless case, elasticity has negligible effect on stress distribution and magnitude, which is in agreement with reference [29]; however, the exact result is dependent on lay-up. As the pin flattens, the bearing stress decreases due to increased contact region. When clearance is involved, pin elasticity is deemed to be more important. Increasing clearance causes decreased contact region and increased bearing stress, thereby reducing the load capacity by up to 12% for a quasi-isotropic lay-up. Clearance shifts the location and direction of maximum tensile stresses. The effect of friction is also examined and again results demonstrate that friction reduces bearing stress by increasing the contact angle, as per references [29] and [51]. However, it also increases tangential stress concentration factors, particularly in 0°-dominant lay-ups where the tangential stress actually changes from tensile to compressive. Due to this increased stress concentration, a decreased load capacity and a shift in location of peak stresses are observed. The effects of friction and clearance are greater than those of pin elasticity, reiterating the importance of their inclusion in modelling.

Dano et al. [57] investigate stress and failure mechanisms in single fastener joints using 2D FE, accounting for complex non-linear contact analysis through the use of a strict master-slave concept. Validating the results of previous experimental data [58], they show that the master-slave contact model is more accurate than either cosine distribution or fastener radial displacement boundary

condition, two of the more common contact assumptions. Camanho and Matthews [59], [60] also use the master-slave contact for 2D failure predictions, finding it an accurate representation of contact stresses. This illustrates that even in 2D analyses, full contact modelling is more accurate.

Waszczak and Cruse [61] study strength predictions and failure modes for anisotropic bolt bearing specimens. A single fastener expressly orthotropic bolt-bearing specimen is simulated using 2D FE analysis. An initial cosine contact distribution assumption is compared with two other distributions using different contact conditions. The contact is assumed to be frictionless. Significant variation from the original cosine distribution is observed and results in significant alterations of the calculated stress fields for the specimens considered, which concurs with the results of references [30], [39], and [57].

De Jong [62] studies stresses around pin-loaded holes in elastically orthotropic and isotropic plates. This work provides several general conclusions. Radial stress distribution depends solidly on the material properties of the plate and clearance, unlike the results in reference [70]. The resulting stress distributions in the isotropic and orthotropic plates are similar, depending on material properties and the width of the plate, and comparable to the results of references [24], [25], and [31]. The maximum tangential stress concentration does not always occur in the minimum net area, which makes it necessary to study more positions in orthotropic specimens than isotropic specimens. Orthotropic materials may fail with much lower stress at the edge of the hole. Therefore, an accurate representation of the stress distribution is essential.

1.3.2.2.4 Three Dimensional (3D) FE

Marshall et al. [63] use 3D FE on 0/90 lay-ups to examine pin and bolt loading. The investigation is primarily concerned with interlaminar effects, but the conclusions are valuable at a macroscopic level: increasing clamp-up increases strength, as in reference [24], increasing washer stiffness improves clamp-up distribution, as per reference [51], and increasing friction decreases bearing stress, agreeing with references [29], [30], and [56]. The bearing strength of a $90/0_s$ lay-up is better than that of a $0/90_s$ lay-up, reaffirming the importance of lay-up to overall performance.

A determination of bolt flexibility and its effects on joint strength is established by Postupka et al [64]. They compared experimental data and 3D FE analyses for single and double shear joints. Increased bearing strength is associated with increased torque, as per references [24] and [64], but as

the ratio of thickness to fastener diameter increases, torque has a lesser effect. In thicker specimens, bolts with smaller diameters are subject to bending, leading to increased stress concentrations. The stress concentrations cause local failure at lower overall joint stresses, reducing the strength of the joint as a whole. In other words, bearing strength decreases with increased clamp-up length, which, in turn, is proportional to the thickness of the joint. The uncertainty associated with determining the effects of bolt flexibility is greater than 20% when comparing FE and experimental results, differing from references [29] and [56]. This hints at the difficulty related to modelling more complex 3D effects.

Matthews et al. [65] study stress distribution around a single fastener joint, using 3D FE. The results show that the stress distribution depends on the type of fastener - pin or bolt. This demonstrates the necessity of modelling actual conditions, rather than simplifying the experiment by assuming pin fastening in place of the actual fastener. Stress concentration factors for bearing, net-tension and shear values are introduced.

Ireman produces some key works in the area of bolted joints [66], [67], [68], [69], [70]. Generally this work studies single-fastener single lap joints between CFRP and aluminium. FE and analytical models, using boundary collocation points, are compared [66]. The results indicate that contact stress distribution is strongly lay-up dependent. High 0° lay-ups result in nearly perfect cosine distribution, 90° lay-ups display a wider contact region and lower peak stresses, and lay-ups with more ±45° plies have peak stresses occurring at 45° from the bearing plane, reacting differently from conventional peak stresses at the bearing and net-tensile planes for radial and tangential stresses, respectively, agreeing with references [30], [39], [57], and [60]. Ireman's studies reiterate that an accurate load distribution is essential to the understanding of multi-fastener joints. Through-thickness effects, such as bolt and plate bending, call for 3D analysis to obtain an accurate representation of such load distributions. A 3D stress analysis uses the master-slave contact definition to study protruded head and countersunk fasteners [69]. A false thermal expansion induces an initial clamp-up. This model provides good agreement to the experimental test results [68], providing confidence in the 3D FE technique. The study indicates the importance of ensuring the coefficient of friction used in the model is representative of the torque level induced, which agrees with references [29], [30], [39], [46], [51], and [63] where the importance of friction is also emphasised. Finally, a parametric study ranks the influence of several factors on the strength of a single lap, one-bolt joint [70]. FE simulates the experiments, designed on a reduced two-level

factorial technique [71]. Thickness and friction have the greatest influence. Increasing joint thickness decreases failure stress for a given bolt size, while increasing friction increases failure stress. Clamp-up, fastener type - protruded head or countersunk, and the presence of lateral support to prevent bending of the single lap joint have lesser effects. Increasing clamp-up causes increased failure stress agreeing with references [24], [63], [64], and [75], countersunk fasteners decrease failure stress, and using lateral support increases failure stress. Fastener diameter, lay-up, and clearance have very little influence, which contradicts references [56] and [62]. The small effects of lay-up are somewhat surprising given that a number of other studies [25], [39], [46], [50], [56], [63], [65], [75] find it to be very important. Increasing fastener diameter slightly increases failure stress as in reference [64], using more highly 0° dominant lay-ups as opposed to quasi-isotropic decreases failure stress, and increasing clearance also reduces failure stresses. It must be recognised that all results are dependent on the failure model used.

1.3.3 Combined Thermal - Mechanical Load Conditions

Very limited work exists on the subject of combined thermal and mechanical loading in mechanically fastened joints, and studies with the inclusion of dissimilar materials in these joint regions are even more limited. The work that exists emphasises the importance of these considerations, and indicates the uniqueness of the current problem. Parvatareddy et al. [72] studies CFRP in aircraft thermal environments, in temperatures up to 423K. Although the bulk of their work concentrates on interlaminar investigation, which is beyond the scope of the current work, some of their findings relate to macrostructure behaviour. At higher temperatures CFRP can exhibit up to 40% loss in bending strength, 60% loss in ultimate strain, and approximately 20% increase in modulus. These dramatic changes in properties are obviously material as well as lay-up dependent; however, they indicate further consequences of the unique aircraft thermal environment.

Motavalli et al. [73] study a bonded aluminium/CFRP box beam at low temperatures, and compare 2D analytical models with 3D FE and experimental strain gauge results, with good agreement. In essence, this work is another example of the importance of understanding thermal mismatch in constrained structures.

Scarponi et al. [74] investigate the importance of temperature and lateral pressure on quasi-isotropic pin-loaded joints using 2D FE and experimental data. The results indicate that increases in temperature decrease the slope of the load-displacement curve as well as the failure load. Torque

improves the linearity of the load-displacement curve, and temperature has a significant influence on clamp-up pressure, due to associated expansion. This work shows that temperature has consequential effects on overall joint behaviour, which can influence mechanical loads and associated stress and strain distributions.

Eriksson [75] use 2D plane stress analysis to examine moisture and temperature effects on the bearing strength of bolted composite joints. At room temperature with no moisture, increasing the number of 0° plies improves bearing strength, while changing the number of ±45° plies has no significant effect. A slight increase in strength is observed with an increase in fastener diameter. At higher temperature with moisture, increasing the number of ±45° plies improves bearing strength, whereas 0° plies has little effect. In all cases, increasing clamp-up improves bearing strength, which agrees with references [63] and [64], the lay-up influences the stress distribution as in references [25], [39], [46], [50], [56], [63], and [65], and non-linear behaviour near the hole moves to approximate linear behaviour 1d from the hole edge.

Peterson et al. [76] examine thermo-mechanical design characteristics, with particular application to aircraft structures. 3D FE is used to study CFRP structures under intense sun irradiation to provide steady state and transient temperature distributions in a wingbox. Although the conditions are somewhat different, the results are similar to previous results [10]. Peterson examines buckling effects as the mechanical loads, and demonstrates that thermal loading causes a number of stress concerns.

Kim and Whitney [77] investigate the effect of temperature and moisture on pin bearing strength in composites. At high temperature (400K) - wet conditions, the bearing strengths of all three experimental lay-ups are 40% less in strength than at room temperature - dry conditions. Test results identified no superposition relationship between temperature and moisture on strength degradation. Individually, however, temperature and moisture have negative effects.

The effect of elevated temperature on pin-bearing strength is also examined by Chen and Lee [78], comparing FE analysis and temperature dependent material properties to experimental tests. Results show that for graphite/epoxy laminates there is little effect on bearing strength with temperatures to approximately 500K. These results differ from those of references [74] and [77]. The lay-up itself

has the greatest effect on bearing strength agreeing with results from references [25], [31], [39], [46], [50], [56], [63], [65], [66], and [75].

1.4 General Design Considerations

Given the limited work on thermal and mechanical behaviour [72]-[78], particularly in a hybrid joint region, this work is an important new step to gaining an understanding of the effects of unique aircraft environment on mechanically fastened joint behaviour. Based on existing heat transfer work [10], [11], [21], 2D FE models in Chapter 2 with various simplified wingbox conditions provide a basis for the study of associated mechanical effects of such thermal loading.

Following the global heat transfer study of Chapter 2, two analytical models are designed in Chapter 3, further to previous works [1], [15], [16], and use results from reference [6] to include the complex boundary conditions of convection and radiation at both external surfaces of a slab of finite dimension. Integral transforms and separation of variables are used for the solutions.

Upon gaining insight into the thermal environment, a sequential stress analysis in Chapter 4 verifies the area of concern for associated mechanical loading using the global wingbox model. Having identified the double lap joint between the aluminium laps and CFRP skin as the area for further investigation, an experimental specimen is designed, which is also described in Chapter 4. The specimen contains two parallel rows of three fasteners in series, and considering the results of references [24], [37], [63], [64], and [70], where the impact of clamp-up on strain distribution is demonstrated to be important, two different torque levels are examined. Tensile testing is chosen for the mechanical load, since it is generally considered more critical to aircraft joints [25]. The exact joint design follows specifications by Airbus UK©. However, according to suggested design guidelines in references [24], [25], [26], [29], and [37], the bolt pitch is approximately 3d. The lay-up is 0° dominant, and is not varied, since variation can cause significant alteration in strain distribution [25], [31], [39], [46], [50], [56], [63], [65], [66], [75]. The goal of the current study is to examine strain distribution for a specific lay-up to be used in the outer wingbox design. A 3D FE model, described in Chapter 4, containing full master-slave contact, because of its greater accuracy, based on references [30], [43], and [57]-[60], is designed to validate and supplement the experimental results. 3D is chosen over 2D, since through-thickness effects are important in contact analysis [31], [67], particularly for thermal loads [74]. Friction is included [29], [30], [39], [46],

[51], [56], [63], [69], [70], as is bolt elasticity [29], [39], [56]. Analyses are limited to strain distributions within the elastic region of the joint, as opposed to complete failure, due to the size of the specimen, which prevents the manufacture of a large number of samples and makes failure loading experimentally difficult. The aim is to gain an understanding of load distribution prior to further joint investigations. The details of these combined thermal-mechanical tests are given in Chapters 5 and 6. This combined thermal and mechanical study is a novel investigation with regard to temperature and strain distributions in multi-fastener hybrid wingbox joints.

1.5 Thesis Structure

Chapter 2 consists of the formulation of the global wingbox 2D model, and the heat transfer analyses for full, half-full, and empty fuel tank cases. Chapter 3 includes the analytical study of a single CFRP skin layer subject to convection and radiation boundary conditions at both surfaces using the integral transform technique. Chapter 3 then furthers the analytical study by using separation of variables to solve for the temperature distribution in the aluminium/CFRP/aluminium joint region for combined boundary conditions. Chapter 4 explains the sequential thermal-stress analysis on the global wingbox, discusses the design of the experimental specimen and associated 3D FE model, and describes a mesh refinement study for this model. Chapter 5 and Chapter 6 contain the experimental results, with FE model comparisons for the finger-tight torque (1Nm) and full torque (35Nm) tests, respectively. Chapter 7 provides the conclusions of the current work and Chapter 8 discusses the scope for future work in related fields.

Chapter 2 Global Heat Transfer Model

The first portion of this work is aimed at attaining an appreciation for the temperature environment of the simplified wingbox structure described in Chapter 1 under conditions simulating an aircraft resting on a tarmac over the course of a hot, dry day. Once this environment is realised, more detailed heat transfer analyses, then stress studies will follow. Section 2.1 describes the wingbox structure examined. Section 2.2 discusses the thermal loading conditions on the structure, which is further broken down into 2.2.1 for the general conditions, 2.2.2 covering the conditions external to the wingbox, and finally 2.2.3 containing a description of the conditions used internally within the structure. Section 2.3 describes the FE models developed for the analyses. Section 2.4 covers the results and is broken down into 2.4.1 containing the temperature profiles from the FE models, 2.4.2 which discusses more specifically the influence of each of the methods of heat transfer: conduction, convection, and radiation at various positions in the wingbox structure, 2.4.3 compares the 2D spanwise and chordwise results, and 2.4.4 shows the results of including titanium pins in the joint of the model on the overall temperatures. Finally, Section 2.5 summarises and compares all results.

2.1 Description of Wingbox Structure

This work is centred on a CFRP/Aluminium double shear joint region in a simplified wingbox structure. Because this work is novel, the structure was simplified from a typical aerofoil shape, which is curved, to a box structure made up of straight edges. This eliminated the uncertainty associated with curvature effects, while improving the ease of modelling of a three dimensional structure. Typical wing geometry, provided by Airbus UK©, was used to approximate the wingbox dimensions. Figure 2.1 is a 3D diagram of the wingbox structure used to create the heat transfer models.

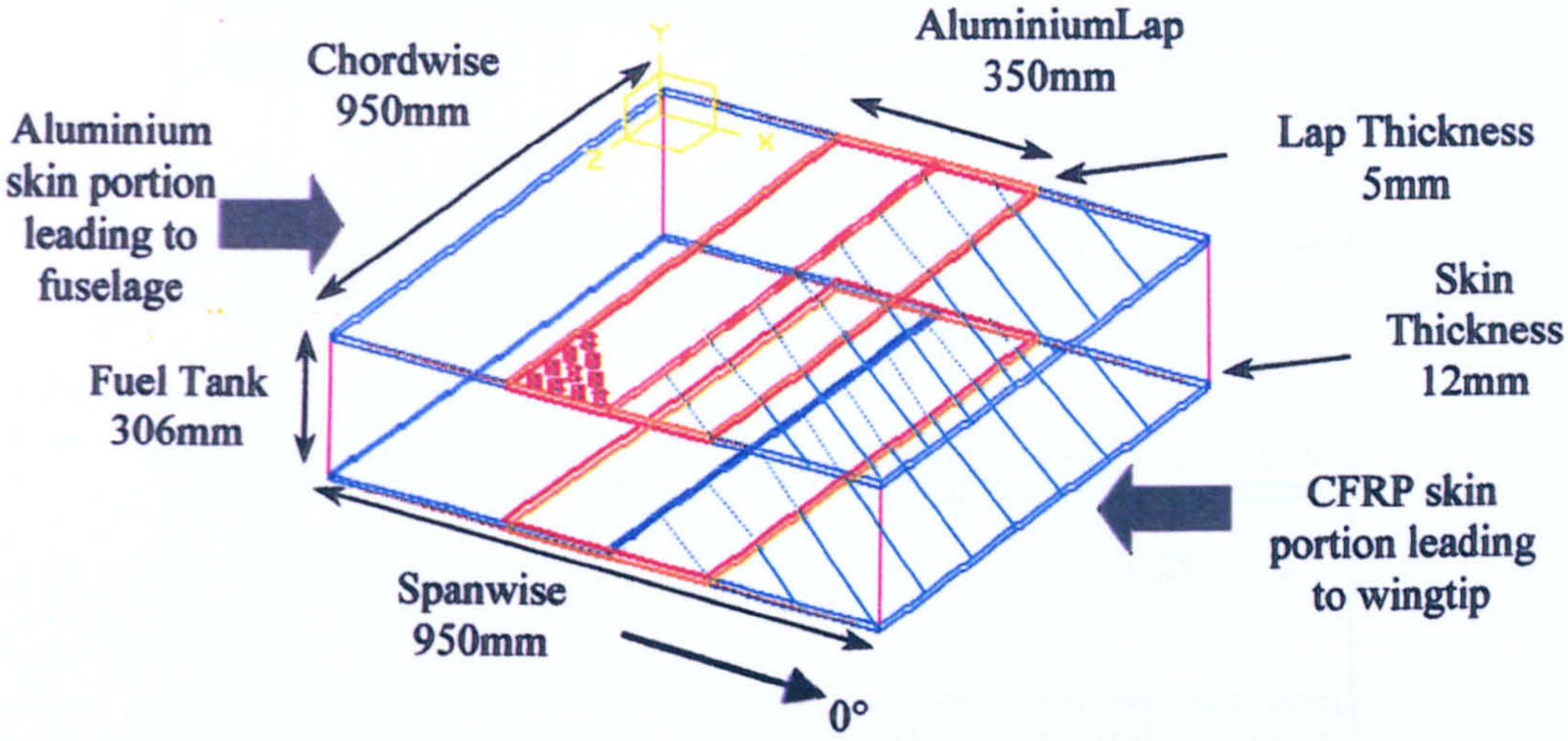

Figure 2.1. Global wingbox structure with approximate pin placement.

This structure is broken down to represent the unique thermal environment of an aircraft wing resting on a tarmac over the course of a very hot (290-370K), dry, twelve-hour day in both spanwise and chordwise directions. The wingbox is made up of both aluminium and CFRP. As described in Chapter 1, this represents an aluminium inner wingbox joined to an outer CFRP wingbox. The aluminium portion would be connected to the fuselage, while the CFRP portion would proceed to the wingtip. The key area in this work is the joint region itself. The joint is made up of two aluminium laps with titanium fasteners to create a double shear joint. The lap plates within the joint are not tapered and the skin thickness in this region is not altered from its thickness away from the joint region. At this region, three differing materials interact: aluminium, CFRP, and titanium. This interaction becomes an area of concern thermally due to the difference in thermal conductivities, which will influence the thermal loading, as well as mechanically due to the thermal expansion coefficients and associated constraints of a fastened double shear joint. Using such a structure to study both thermal and mechanical impacts is, to the best of the author's knowledge, unique to this work.

Finite element (FE) analysis, using ABAQUS, is chosen as the method of solution for the wingbox structure. As a first approximation, the wingbox was studied in two dimensions; spanwise and chordwise, respectively. Figure 2.2 shows the two-dimensional geometry.

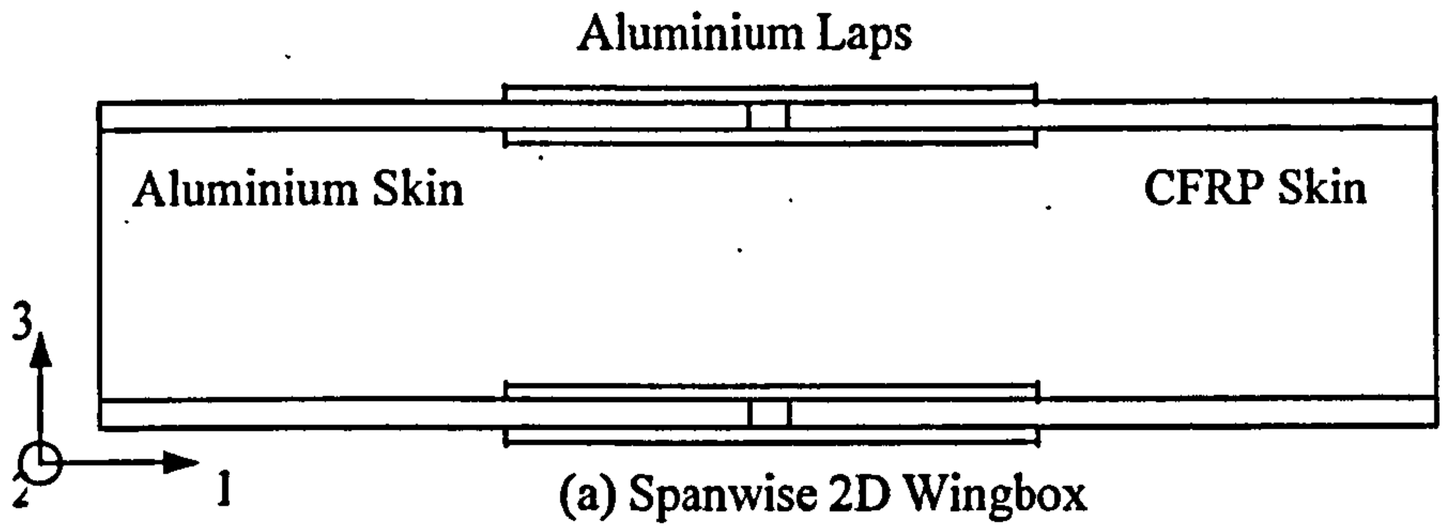

Figure 2.2. Spanwise and Chordwise 2D Wingbox Geometry.

A detailed description of the FE models used is included in Section 2.3. First, the analyses are performed without the use of any fasteners to study the heat transfer behaviour through the aluminium and CFRP alone. Following this, titanium fasteners are added for comparison. As the relative geometry of the pins was small in comparison to the entire wingbox structure, the fasteners are approximated using pins with simple 1d spacing. A more detailed study of protruded head fasteners with predefined spacing is left for later analyses associated with the mechanical structural loading, which is included in later chapters.

The skins are aluminium and CFRP. The CFRP is assumed to be homogeneously orthotropic, with 50% 0°, 40% ±45°, and 10% 90° properties, or simply stated, 50/40/10 properties, which was provided by Airbus UK© based on previous stress analyses. The properties of pure titanium are applied to the pins. The fuel properties and the CFRP properties are drawn from a previous report [10], where they were determined experimentally. All other material properties (ε, k, c_p, ρ) for the desired temperatures are obtained from the CRC Handbook [79]. The material properties used in the various analyses are located in Table 2.1. All properties between the given bounding temperatures are determined by linear interpolation.

Table 2.1. Thermal Material Properties.

Material	Emissivity ε	Conductivity k (W/mK)				Specific Heat c_p (J/kgK)		Density ρ (kg/m^3)	
		270K		500K		270K	500K	270K	500K
		1*	3*	1	3				
CFRP	0.8	8.38	0.81	11.99	1.37	848	1485	1550	1550
Aluminium	0.69	164.0	164.0	164.0	164.0	883	883	2787	2787
Titanium	0.48	21.6	21.6	21.6	21.6	528	528	528	528
Air**	-	0.024	0.024	0.037	0.037	1011	1011	1.25	1.25
Fuel	-	0.149	0.149	0.126	0.126	2100	2900	780	700

* 1= lengthwise (chord or span) direction, 3= through-thickness direction

** All values for air properties are given at 273K and 473K rather than 270K and 500K, respectively.

2.2 Thermal Loading Conditions

2.2.1 General Development of Conditions

The thermal boundary conditions are meant to represent a realistic, worst-case scenario for the wing of an aircraft out in the open on a tarmac. The given weather conditions are those of a very hot, dry, twelve-hour day. The effects of conduction, convection, and radiation on external skin surfaces and within the tank are studied.

Given the combination of loading conditions as described in Chapter 1, Figure 1.5, some assumptions are required in order to fully define the problem. For the general boundary conditions in the heat transfer analyses, it is assumed that all exterior surfaces of the wingbox were exposed to air, with the top surface being exposed directly to the sun, while the bottom surface received heat energy from the ground. It is assumed that the laps and skins are perfectly flat with perfect contact at all interfaces. No individual surfaces are defined in the FE mesh to form contact conditions, rather the mesh is designed with element continuity between all adjoining surfaces. It is recognised that the internal conditions of the tank will have a significant impact on the overall heat transfer analyses. As such, the wingbox is tested at conditions approximating fuel tanks as empty, full, and half-full, in order to determine the effects of fuel level in the thermal analyses.

As a base for all heat transfer analyses, sink temperatures, T_∞, must be defined. These temperatures are used in convection and radiation methods of heat transfer to determine the influence of the

surroundings on the surface of the object being studied. The involvement of these temperatures were shown in Chapter 1 equations (1-3) and (1-4). Figure 2.3 illustrates the various sink temperatures for the analyses.

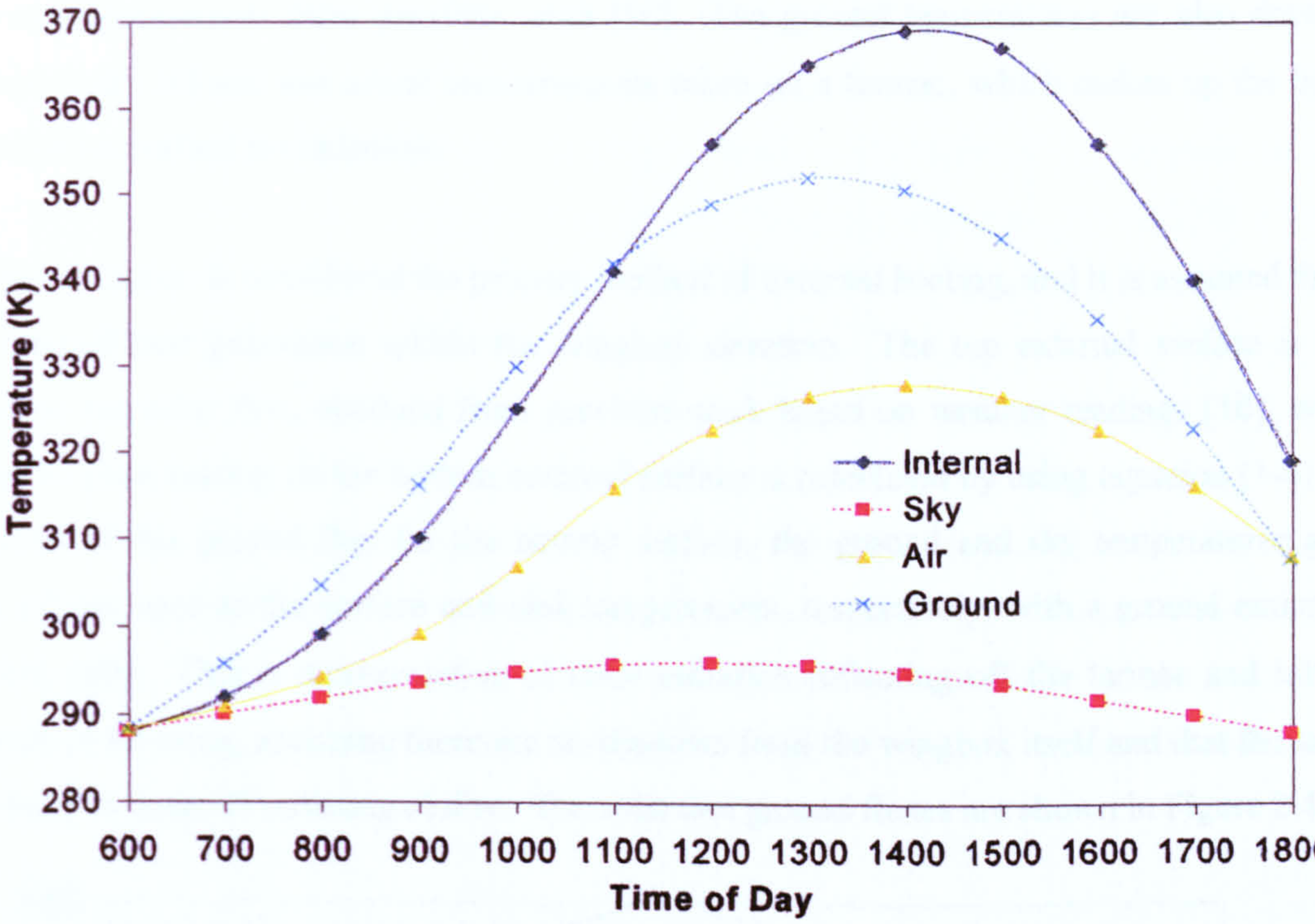

Figure 2.3. Internal and external sink temperatures.

The internal and external air temperatures are used in convection analyses, whereas the sky and ground temperatures are used in radiation analyses. The internal temperature is the mid-tank temperature found by performing heat transfer analyses with conduction as the only mechanism of heat transfer, whereas all other temperatures are based on experimental results of previous work [10]. The size of the wingbox allows the upper and lower surfaces to be treated as separate thermal environments, based on preliminary comparative results and previous work [5], [12], [80]. Conduction is the most inefficient method of heat transfer through fluids, compared to convection and radiation, and therefore it provides the hottest or worst-case sink temperatures at the mid-tank point. The internal environment is divided into two separate convection problems, which is discussed in detail later in this chapter. The air temperature is based on experimental results and on optimum conditions for a very hot, dry day [10]. This air is assumed to surround the entire wingbox. Therefore, this sink temperature is used for external convection at both surfaces. The sky temperature is representative of the upper bounding condition for the top surface of the wingbox for

radiation. Radiation involves heat energy radiating from one object to another in its path. This path implies that radiation operates within a bounded region. Because the sky is assumed to be cloudless, this boundary for the upper wingbox surface is the atmosphere. These temperatures represent changes in the atmospheric or "sky" temperatures over the course of a twelve-hour period, and are based on measurements from previous work [10]. The ground temperatures are also drawn from previous work [10] and use actual measurements taken on a tarmac, which makes up the boundary for the bottom surface for radiation.

Solar flux radiation is considered the primary method of external heating, and it is assumed that there is no internal heat generation within the wingbox structure. The top external surface is directly exposed to the solar flux, obtained from previous work based on weather readings [10], while the flux due to solar heating on the bottom external surface is calculated by using equation (1-4). In the calculation of the ground flux for the bottom surface, the ground and sky temperatures given in Figure 2.3 are used as the surface and sink temperatures, respectively, with a ground emissivity of 0.67 [10], [69]. This is representative of solar radiation reflecting off the tarmac and hitting the underside of the wing, assuming there are no shadows from the wingbox itself and that the tarmac is a grey body in terms of radiating ability. The solar and ground fluxes are shown in Figure 2.4.

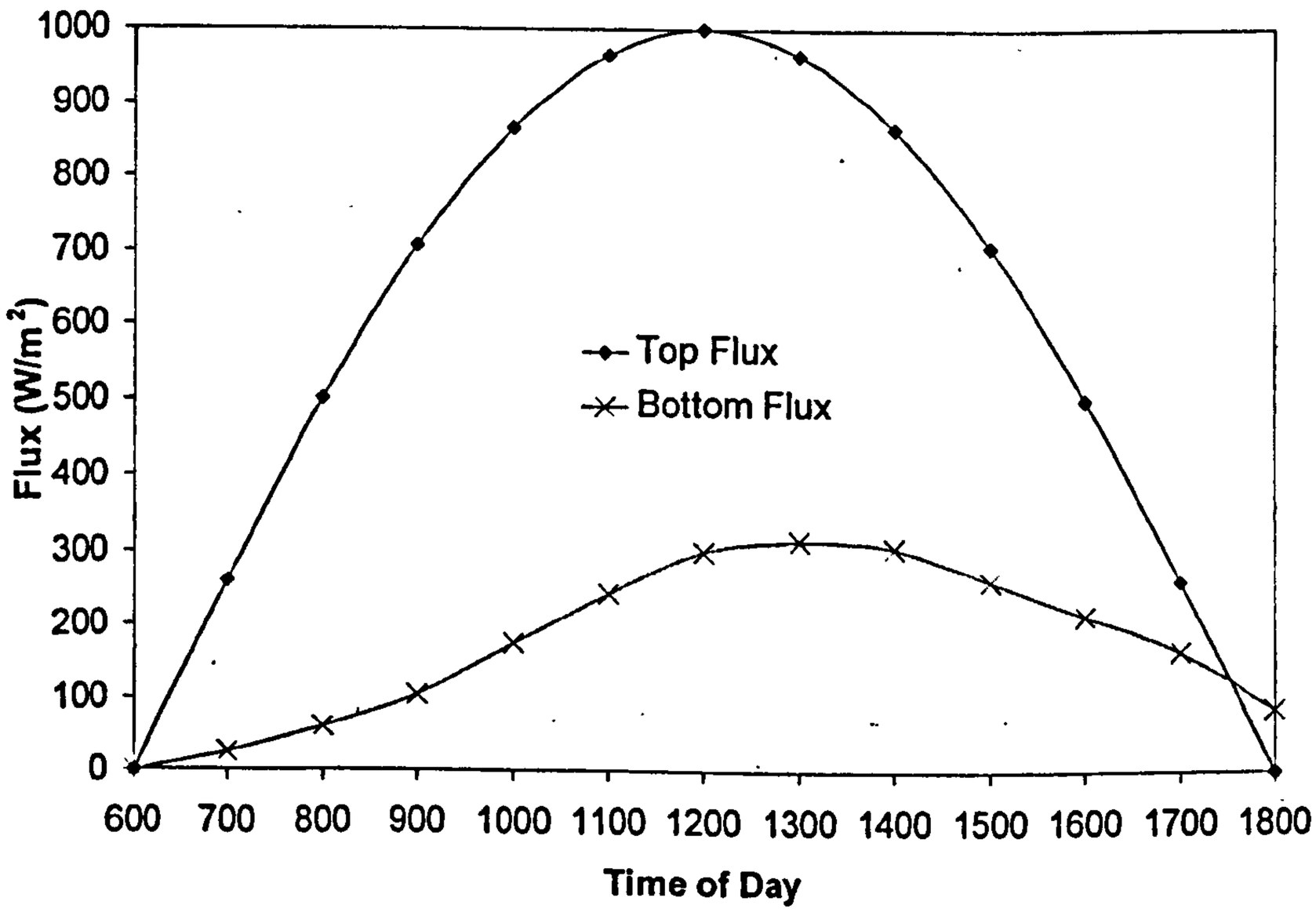

Figure 2.4. Solar (Top) and Ground (Bottom) fluxes.

2.2.2 External Conditions

Externally on the wingbox, some boundary condition assumptions are made. A condition of no wind, with natural convection on the external skin surfaces is assumed as this is the worst-case condition, since no cooling can be induced by forced convection over the wingbox surface. The skin itself is assumed to be unpainted CFRP or aluminium, with the emissivities as given in Table 2.1. It is assumed that the lateral bounding surfaces, or four sides of the wingbox, behave like CFRP spars, for a spanwise analysis, or ribs, for the chordwise analyses. As such the elements of these surfaces were given the material properties of CFRP. These bounding surfaces were assumed to act as insulated ribs or spars to create a worst-case scenario.

The skin is assumed to have perfect thermal contact at the laps and titanium pins, which was achieved by modelling the entire wingbox as one part in the FE analyses. The CFRP is treated as a homogeneous orthotropic material whose properties are assumed to be constant in the 1 and 2 directions, representing the in-plane and transverse directions, respectively. The CFRP through-thickness (3-direction) properties are considered the same for both spanwise and chordwise directions.

2.2.3 Internal Conditions

Within the tank, individual studies are made on each of the three methods of heat transfer: conduction, convection, and radiation. Conduction analysis in ABAQUS [81] is straightforward, using equation (1-2), and requiring no additional definition. Radiation and convection within the tank are more complicated and are explained in further detail.

2.2.3.1 Internal Radiation

Radiation within a cavity or enclosure requires additional equations. However, this is facilitated through ABAQUS, using the predefined capability of *RADIATION and associated commands [81]. In ABAQUS, radiation within an enclosure is treated similarly to external radiation. The incoming flux is partially absorbed and partially reflected. The only additional calculation, in this case compared to external radiation, is based on the fact that the absorbed radiation can be re-emitted to other surfaces. Thus, the incoming radiation at a given surface is made up of radiation re-emitted

and reflected from other surfaces, as outlined in Figure 2.5. Radiation reflected and emitted from surface 2 combines to form the incoming radiation at surface 3. This incoming energy is then partially absorbed and reflected, as well as surface 3 emitting its own radiation. The percentages of radiation absorbed and reflected are a function of a given material's emissivity.

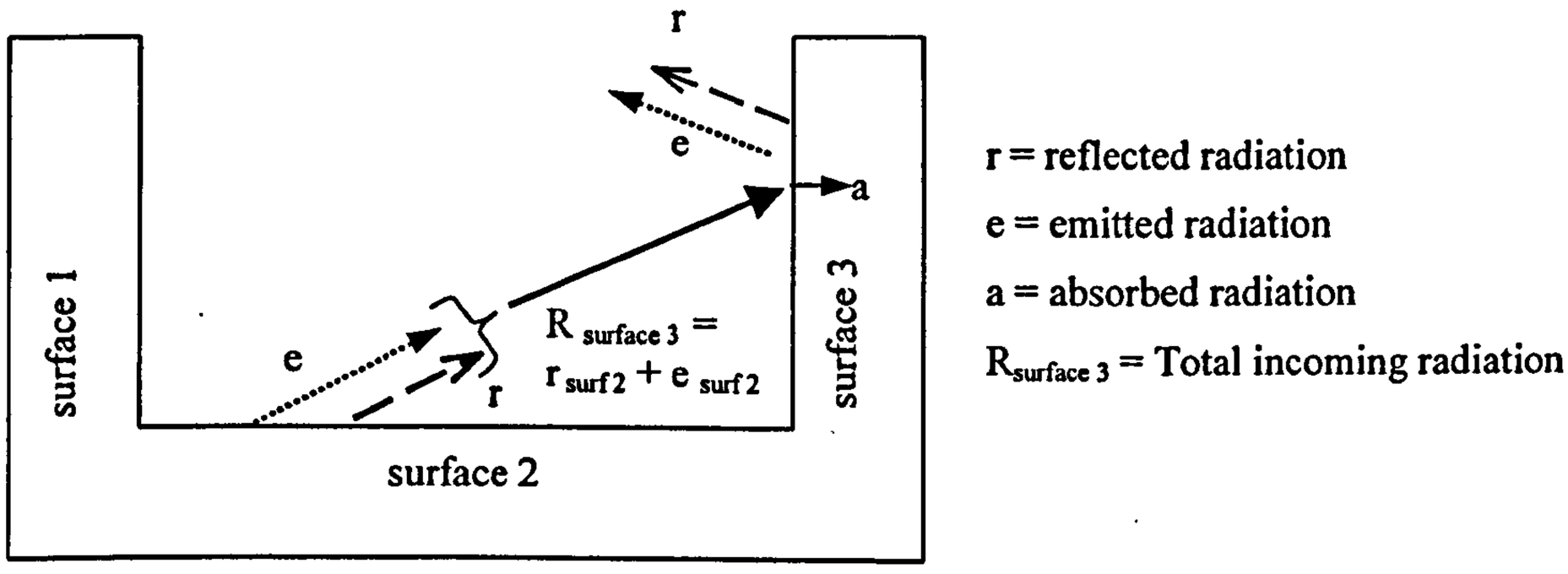

Figure 2.5. Radiation within a partially enclosed cavity.

ABAQUS calculates the effects of radiation within such an enclosure using equations containing shape factors. In effect, view or shape factors account for the path of energy that leaves one surface of the enclosure and reaches every other surface within the enclosure. It is a relation of the portion of any one surface that can be 'seen' by any other surface. Since the surfaces are assumed to be grey, any reflection diffuses[2] according to the material emissivity. This reflection of radiation from one surface to another leads to the formation of a radiation network. Within the current FE model, the internal solid surfaces are used to define the cavity for the radiation analyses. For the view-factor calculations, the internal aluminium lap plates in the spanwise direction are assumed not to intrude into the cavity in such a manner as to have a significant effect on each face's ability to 'see' each other. They are ignored in the cavity network in order to simplify the problem and reduce computing time. Figure 2.6 defines the surfaces used in the cavity for the current spanwise 2D wingbox model.

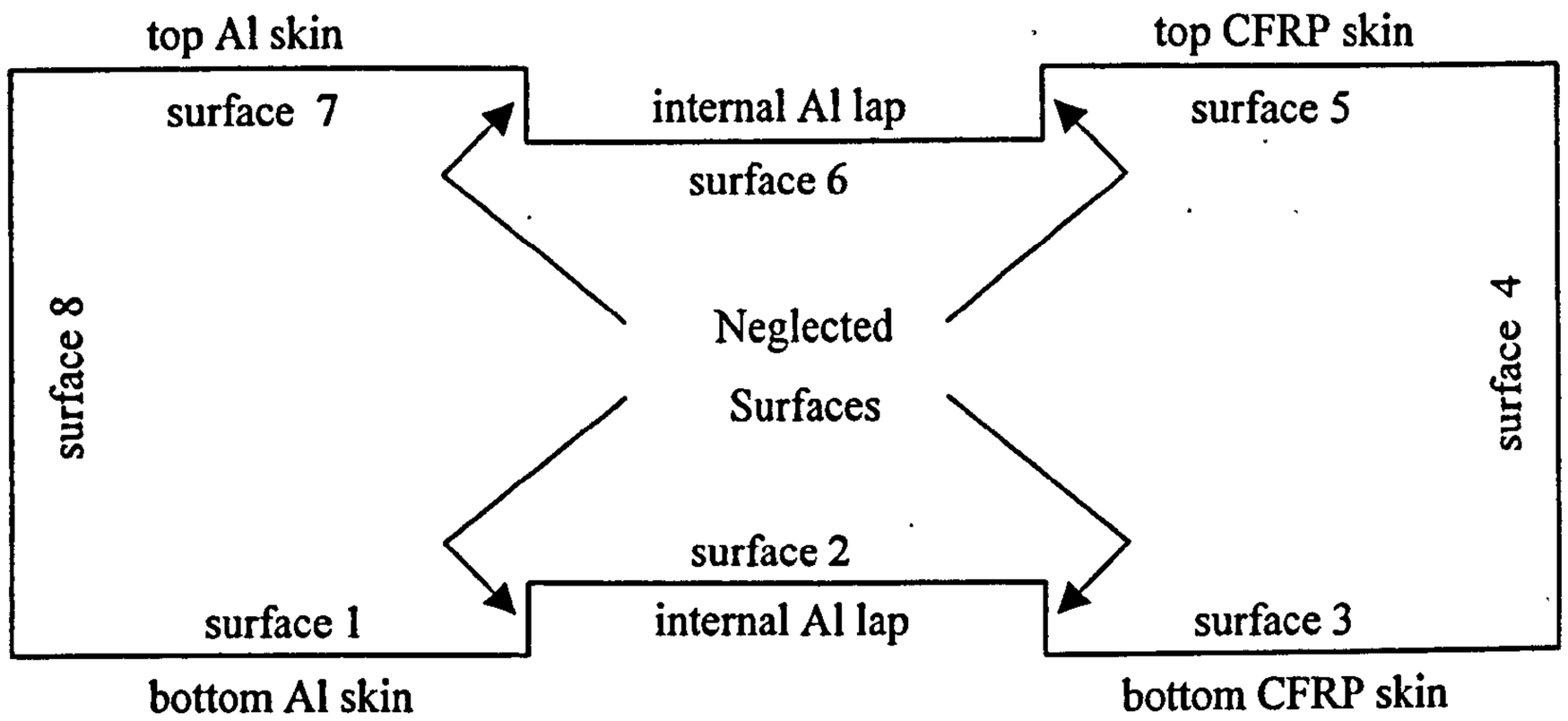

Figure 2.6. Internal spanwise cavity for internal radiation view-factor calculations.

2.2.3.2 Internal Convection

ABAQUS' capability to model convection within an enclosure or cavity is limited to forced convection. Therefore an alternative approach, similar to that used for external convection conditions, is used to account for natural convection within the tank.

Since the wingbox is considered to be part of an aircraft resting on a tarmac, it is assumed that there is no fuel-flow into or out of the wing fuel tank (i.e. the internal box structure). Therefore, the only type of convection within the tank is natural convection. ABAQUS does not have a pre-defined method for solving for the effects of natural convection within an enclosure. From preliminary conduction-only models, discussed in Section 2.4, it became evident that this factor should be included in this study, since under the given thermal loading conditions the box can become hotter on the bottom surface than on the top. This leads to a less dense material lying beneath a material of higher density, which in turn causes natural convection currents. As a detailed Computational Fluid Dynamics (CFD) approach is deemed beyond the scope of the current work, and because the actual influence of the natural convection within the cavity is undetermined, it was decided that the effects of natural convection within the tank should be approximated using the same approach as external natural convection. This allowed the use of ABAQUS' pre-defined convection equations while providing an initial estimate of the impact of natural convection within the tank.

Internally, the relatively large distance between the top and bottom tank walls allows the skins to be treated as infinite plates within separate thermal environments. The justification for this assumption comes from comparing conditions and results of previous studies of convection within air- and water-filled enclosures of finite dimensions [5], [82], [83]. In other words, the top and bottom surfaces are considered as separate thermal environments, with the sink temperature taken as the mid-tank temperature, at designated times, from the results of the conduction-only analysis. This is representative of the worst-case scenario because of the inefficiency of using conduction as the only method of heat transfer through a fluid, which results in increased temperatures at the mid-plane. Dividing the wingbox into two thermal environments allows each environment to be treated the same as if it was external natural convection. Figure 2.7 displays an example of the top surface convection environments. The bottom surface environment is identical.

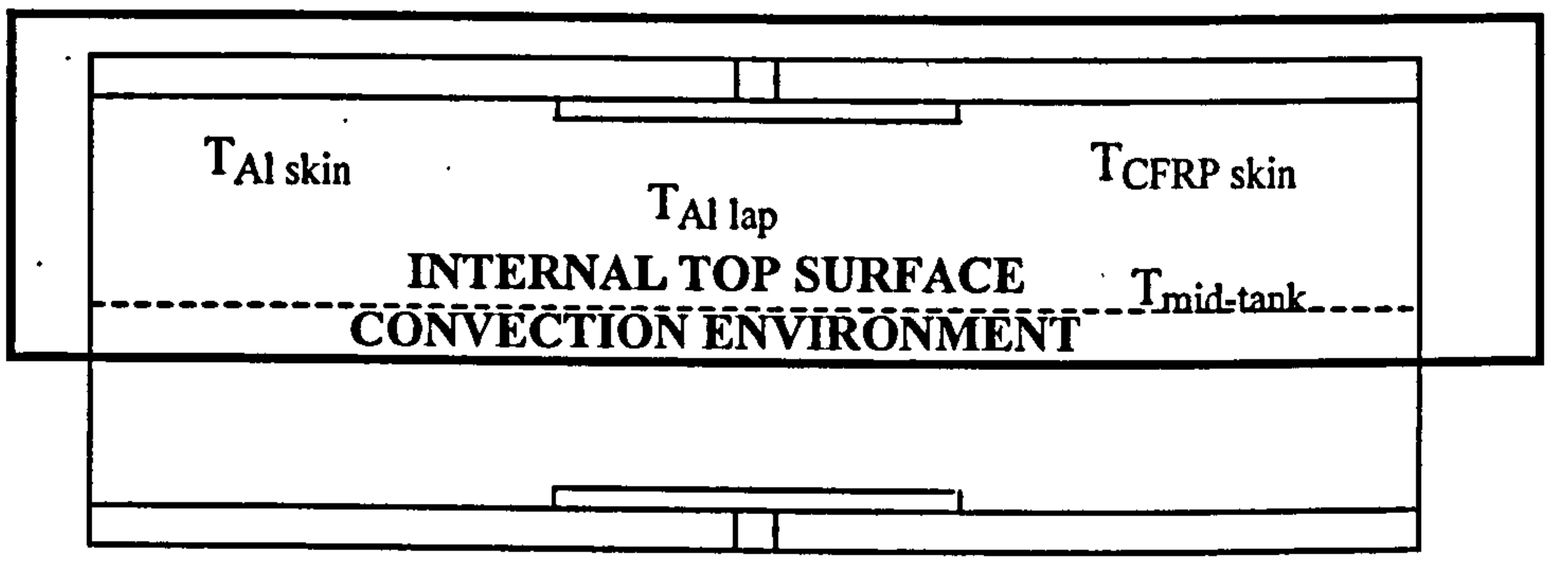

Figure 2.7. Example of internal top surface convection environment.

In order to model natural convection at any position, the convection heat transfer coefficient for each given surface must be calculated. The principal influencer of the heat transfer coefficient of a particular surface is the orientation of the surface itself. The discussion of convection heat transfer coefficients herein uses horizontal plates facing up or down as the orientations, corresponding to the upper and lower skin surfaces of the given wingbox structure. Convection at the vertical edges is not considered, since the horizontal temperature gradient is the primary concern in the present analyses, and due to the relative size of the top and bottom surfaces compared to the side walls. The effects of these side walls are believed to be secondary, assuming insulation at the vertical edges. It is understood that under this boundary condition some convection currents may occur, but given that the sources of incoming heat flux are in a horizontal direction, and in reference to work done by Vliet [84], the horizontal convection has the greatest impact on the overall temperature. As well, the

primary region of interest is the joint, which is at an additional distance from the side walls, further negating the edge impact on the natural convection currents.

There is no mathematical prediction method, to date, that has been established for the determination of the convection heat transfer coefficient. The only methods that exist for determining these coefficients are either experimentation, which is specific to a given case, or the use of trend analysis of previous experimental data with similar conditions to predict the current coefficient, which is the more common method. Due to the different experimental conditions used in each particular case, and with the addition of experimental error itself, the margin of error associated with using any particular trend analysis formula to find the heat transfer coefficient for new modelling conditions can be substantial. These potential sources of error are well recognized, and a margin of error to 20%, depending on the approximations made for the given problem, has been suggested as a safe estimate when using the convection heat transfer coefficient equations [2].

The first step then, is to determine the orientation of the surface exposed to natural convection conditions. In the current work, the fact that the wingbox provides horizontal plate conditions is a help, as these are the most commonly used and therefore have the most associated previous work, which improves confidence in the method. Figure 2.8 shows the definitions for orientations of a heated plate face up and a heated plate face down. The heated plate face down is equivalent to the top internal surface of the wingbox where the solar flux has heated the wing skin (plate) and the air beneath the plate inside the tank is cold. Therefore, the heat energy travels from hot to cold, increasing the temperature inside the wingbox tank due to natural convection. Similarly, the heated plate face up is equivalent to the lower wingbox surface exposed to ground flux.

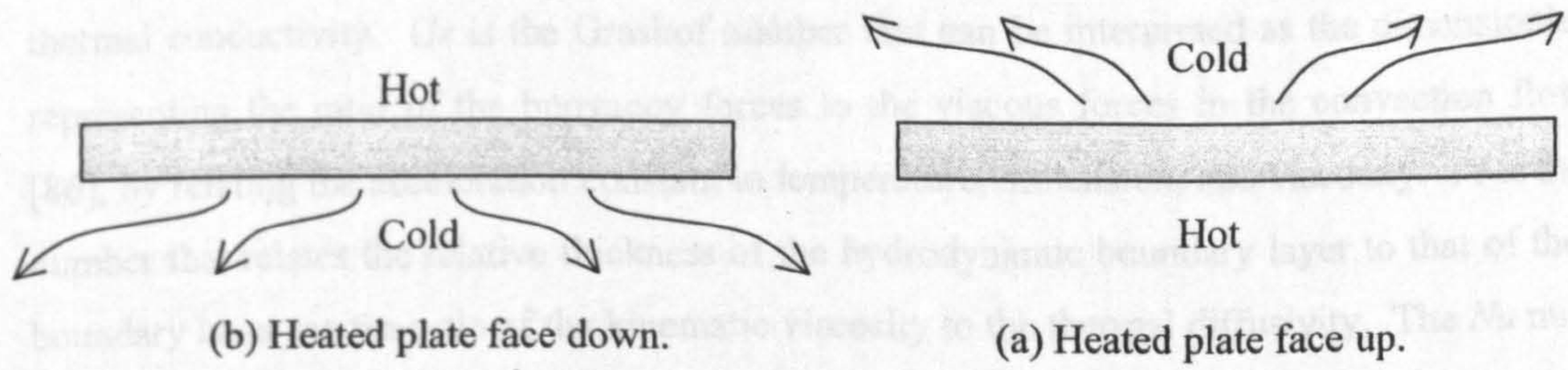

(b) Heated plate face down. (a) Heated plate face up.

Figure 2.8. Convection orientation descriptions.

Upon determining the orientation of the upper and lower wingbox surfaces in terms of convection coefficients, the next step is to correlate these orientations with given equations from previous work

to determine the best estimate for the heat transfer coefficients. The assumptions required are as follows: based on convection heat transfer work studying edge effects [5], the top and bottom skins are treated as infinite plates, because of their considerable length to thickness ratio, the convection properties of fuel are assumed to be similar to those of water, and the internal dimensions of the tank are approximated by the distances shown in Figure 2.1.

The most commonly used equations, based on trend analyses, for the calculation of heat transfer coefficients are based on isothermal conditions. Fujii and Imura [85] have determined three equations for upward and downward facing heated plates, based on experiments with water as the convection fluid. These equations have also been accepted for use with air as the convection fluid, based on the correlation of independent experiments as summarised in Holman [2]. Equations (2-1) and (2-2) can be used to find the convection heat transfer coefficient for the upper surface of a heated plate (heated plate face up) for $2 \times 10^4 < GrPr < 8 \times 10^6$ and $8 \times 10^6 < GrPr < 10^{11}$, respectively. Equation (2-3) can be used for the lower surface of heated plates (heated plate face down) for $10^5 < GrPr < 10^{11}$.

$$Nu = 0.54(Gr\,\mathrm{Pr})^{1/4} \tag{2-1}$$

$$Nu = 0.15(Gr\,\mathrm{Pr})^{1/3} \tag{2-2}$$

$$Nu = 0.27(Gr\,\mathrm{Pr})^{1/4} \tag{2-3}$$

Nu is the Nusselt number that contains the ratio of the convection heat transfer coefficient to the thermal conductivity. *Gr* is the Grashof number that can be interpreted as the dimensionless group representing the ratio of the buoyancy forces to the viscous forces in the convection flow system [86], by relating the acceleration constant to temperature, dimension, and viscosity. Pr is the Prandtl number that relates the relative thickness of the hydrodynamic boundary layer to that of the thermal boundary layer via the ratio of the kinematic viscosity to the thermal diffusivity. The *Nu* number, *Gr* number, and Pr number can be represented by:

$$Nu = \frac{hL'}{k} \tag{2-4}$$

$$Gr = \frac{g\beta(T_s - T_\infty)L^3}{\nu^2} \tag{2-5}$$

$$\Pr = \frac{\nu}{\alpha} = \frac{c_p \mu}{k} \tag{2-6}$$

All of the thermal material properties involved in equations (2-4) to (2-6) are taken at the material film temperature, or T_f. Here, g is the gravitational constant, β is the inverse of the film temperature, ν is the kinematic viscosity, and α is the thermal diffusivity. T_f is given by equation (2-7) for ideal gases such as air, but must be determined experimentally for liquids, which has been performed by numerous authors for water. The film temperature is given as:

$$T_f = \frac{T_s + T_\infty}{2} \tag{2-7}$$

In the present case, equation (2-3) is used for the upper internal surface of the wingbox, while equation (2-2) is used for the lower surface. Singh et al. [80] suggest slightly different equations, based on independent trend analyses, for the calculation of the convection heat transfer coefficient for a downward facing heated plate under isothermal experimental conditions for specimens of differing geometry:

$$Nu = 0.716(Gr\,\Pr)^{1/5} \tag{2-8}$$

$$Nu = 0.50(Gr\,\Pr)^{1/5} \tag{2-9}$$

Equation (2-8) provides good correlation for square plates, and equation (2-9) for infinite strips. Given the dimensions of the current wingbox, its behaviour is anticipated to be somewhere between the two. The top internal surface coefficient was calculated again using an average of equations (2-8) and (2-9). Singh et al. [80] studied geometric effects in more detail whereas Fujii and Imura [85] concentrated on different experimental conditions for what was considered an infinite strip. Besides isothermal conditions, Fujii and Imura [85] also performed experiments under constant flux conditions with air as the fluid, resulting in:

$$Nu = 0.16(Gr\,\mathrm{Pr})^{1/3} \tag{2-10}$$

$$Nu = 0.13(Gr\,\mathrm{Pr})^{1/3} \tag{2-11}$$

$$Nu = 0.58(Gr\,\mathrm{Pr})^{1/5} \tag{2-12}$$

Equation (2-10) can be used for heated surfaces facing upward or cooled surfaces facing down for $Gr\mathrm{Pr}<2\times10^{8}$ and equation (2-11) for $2\times10^{8}<Gr\mathrm{Pr}<10^{11}$. For a heated surface facing downward or a cooled surface facing upward, equatin (2-12) can be used in the range $10^{6}<\mathrm{GrPr}<10^{11}$. Here, equation (2-12) was used to calculate the coefficient for the internal top surface and equation (2-11) for the internal bottom surface. Although the experiments performed by Fujii and Imura [85] used air as the convection medium, Holman [2] surmises that these equations can be used to approximate the convection coefficient for most fluids, including water, as long as the error of 20% is recognised. This is also the case for the previous equations (2-1) to (2-3) under isothermal conditions with water as the convection medium. In the case of constant flux, the thermal properties are evaluated at the environmental temperature, T_e:

$$T_e = T_s - 0.25(T_s - T_\infty) \tag{2-13}$$

It is interesting to note that for the case of a heated downward facing plate, equation (2-12) appears to be near the average of equations (2-8) and (2-9). Even though the experiments are performed under different conditions of isothermal and constant flux, the resulting equations are similar for the heated plate facing downward case, implying that a good approximation can be obtained for the upper, internal wingbox surface.

Vliet [84] developed a different equation for predicting the heat transfer coefficient for a heated plate face up using a modified Grashof number based on the heat flux arriving at a surface, rather than the temperature of the surface itself:

$$Nu = 0.23(Gr^{*}\,\mathrm{Pr})^{1/4} \tag{2-14}$$

Gr^* is the modified Grashof number,

$$Gr^* = \frac{g\beta q_w L^4}{kv^2} \tag{2-15}$$

Within this modified Grashof number, q_w is the flux at the surface (W/m^2). This method is valuable when the surface temperatures are unknown boundary conditions. Unfortunately, this work does not apply to downward facing plates, thus limiting this application. It is used for comparison for the bottom, internal wingbox surface calculations.

The convection heat transfer coefficients are calculated using the aforementioned equations with the following additional information. The characteristic length used in the calculation of the heat transfer coefficients is taken as the area over the perimeter using dimensions from Figure 2.1. The wall temperatures are determined by performing a heat transfer analysis of the wingbox model with conduction as the only method of heat transfer within the tank. The sink temperature for the external skins is taken as the air temperature over the course of the day from Figure 2.3. The internal sink temperatures are the mid-plane temperatures, as shown by the "Internal" curve of Figure 2.3. The properties of air are used for the empty tank case, whereas water properties are used in the full tank case. The half-full case is taken as a combination of the empty and full tank cases, with independent sink temperatures. As stated previously, each heat transfer coefficient is calculated using at least two different methods. When compared, the results are very similar.

As discussed previously, the error associated with the calculation of convection heat transfer coefficients is quite high, given that the equations are based on experimental correlation of data, whereas the experimental conditions are almost certainly to be different than those of the problem at hand. Furthermore, the equations make use of properties taken at an average temperature, based on surface temperatures that must be estimated from a conduction-only analysis. Therefore, the upper and lower bounds of the present heat transfer coefficient calculations are determined, using a 20% error approximation, as suggested by Holman [2]. In order to provide a worst-case scenario, the most conservative values are used in the analyses. Table 2.2 presents the heat transfer coefficients and sink temperatures used in the analyses.

Table 2.2. Convection Heat Transfer Coefficients and Sink Temperatures.

		h (W/m^2K)	T_∞ (K)
External Top Skin Surface		8	Air
External Bottom Skin Surface		3	Air
Internal Top Skin Surface	**Empty**	2*	Internal
	Full	220	290
	Half	2	290
Internal Bottom Skin Surface	**Empty**	4**	Internal
	Full	1300	290
	Half	1300	290

*For times 6am to 3pm, then set equal to zero for 4pm to 6pm.
**Equal to zero for times 6am to 3pm, then equal to the values in the table for 4pm to 6pm.

From Table 2.2, the smallest heat transfer coefficients appear when air is the convection fluid. The ability of air to transfer heat by convection is known to be significantly less than that of a liquid [2], so these results are not surprising. The fact that the external top surface coefficient is higher than the bottom surface coefficient is largely due to the difference in flux, since the top surface is exposed too much higher levels of heat energy, which leads to greater surface temperatures, influencing the *Gr* number. The reason that internal bottom coefficients are higher than their counterparts is due to the fact that these surfaces represent a heated surface face up, which through use of the previously developed equations, generally results in higher heat transfer coefficients than the heated surface face down. The exposure to heat flux and sink temperatures is nearly identical within the tank, thereby limiting the influence of these parameters unlike in the external case. The convection coefficients within the tank are only used on the higher temperature surface capable of creating buoyancy effects and natural convection currents. The surface with the lower temperature cannot cause buoyant forces and is, therefore, removed from the convection condition.

These heat transfer coefficients are a function of wall and surface temperatures, which are known to vary throughout the day, suggesting that the heat transfer coefficients will also vary. This assumption is examined, and twelve different heat transfer coefficients are used over the course of the twelve-hour day to represent this effect. The difference in results from this analysis and results from analyses that use a constant heat transfer coefficient throughout the day is negligible. Taking into account the error associated with the calculation of the heat transfer coefficients, and the minimal change in results, little improvement in accuracy is gained by varying the heat transfer coefficients. Thus, the convection coefficients are held constant for all analyses using the values seen in Table 2.2.

2.3 FE Models

In order to study the temperatures at different regions in the wingbox, two general FE models, designed using IDEAS, are presented in Figure 2.9. The meshes themselves are biased, so as to obtain detailed information in the skin and joint regions, with fewer elements from the centre of the tank. This design permits quicker run times (<5min CPU time on a Unix based machine with 5Gbytes hard disk space), while still providing adequate information. ABAQUS [81] is used as the FE solver, and the models are made up of 736 spanwise (a) and 800 chordwise (b), DC2D8 two-dimensional quadratic heat transfer elements. The coloured elements in Figure 2.9 show the elements whose material properties are changed to perform the various analyses. Through the examination of the results of both models, it is possible to gain an understanding of the temperature profiles at and away from the joint region, in both spanwise and chordwise directions. Note, only one element is used to model the through-thickness of the skins and laps.

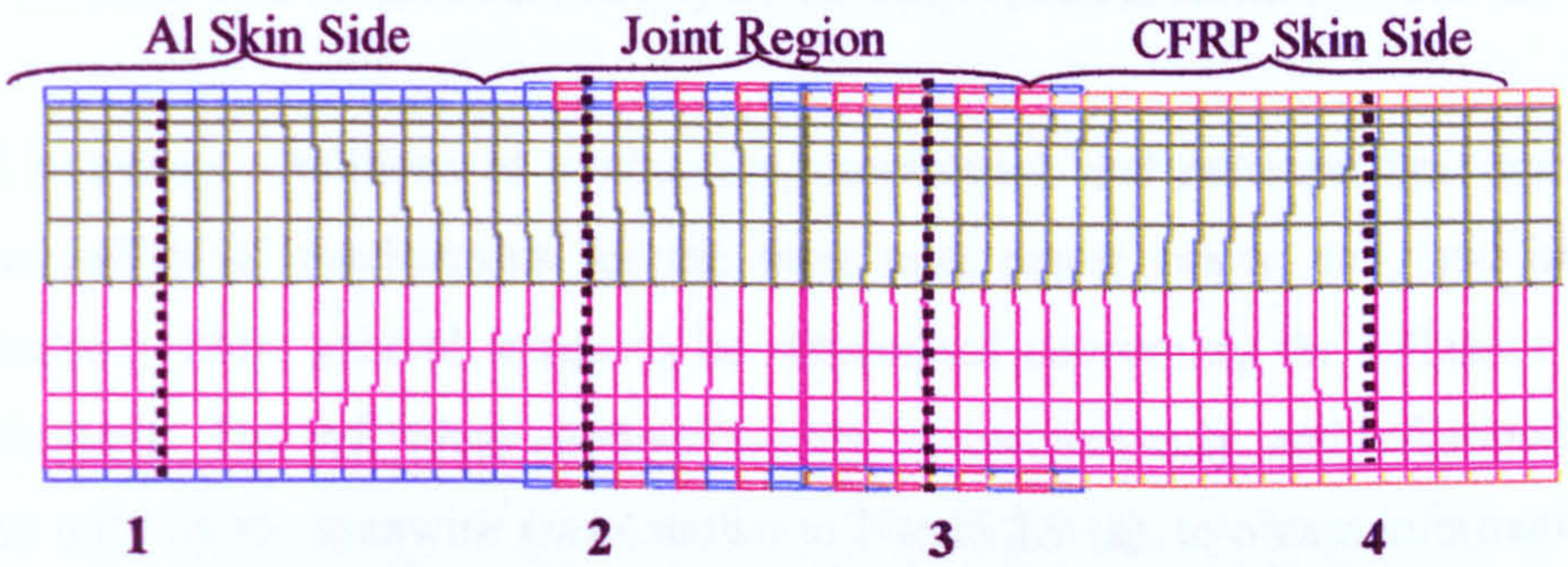

(a) Spanwise Model

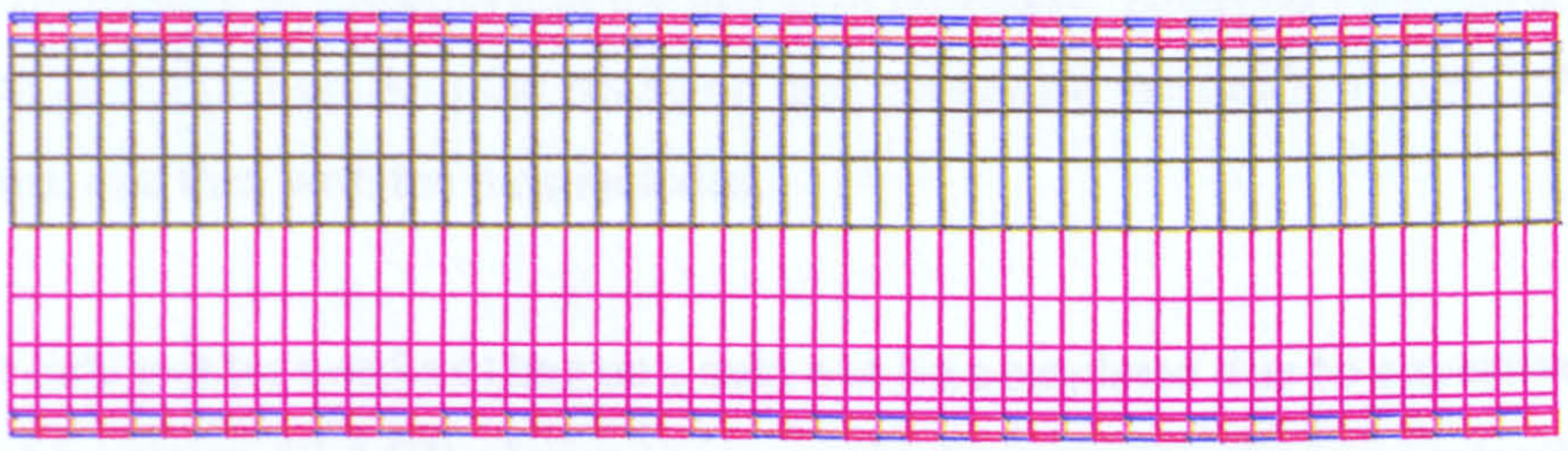

(b) Chordwise Model

Figure 2.9. FE heat transfer models.

In Figure 2.9(a), blue represents the aluminium elements, red the titanium pins, when, orange the CFRP elements, green the top half tank elements, and magenta the bottom half tank elements. In

Figure 2.9 (b), orange CFRP skin is shown, but aluminium properties are also used. The dashed lines in Figure 2.9 (a) represent the nodal temperatures. These temperatures are used to create the temperature profiles through the aluminium skin, aluminium skin side of the joint, CFRP skin side of the joint, and CFRP skin, from left to right, respectively. The skin is assumed to be unpainted CFRP or aluminium, which will have an impact on results as paints have different emissivities and are generally produced to improve reflected heat energy, thereby reducing overall skin temperatures.. The lateral bounding surfaces of the models are assumed to be similar to CFRP spars or ribs, depending on whether it is a spanwise or chordwise analysis, and the elements of these surfaces are given the material properties of CFRP. Resulting node temperatures are taken at positions **1, 2, 3,** and **4,** as indicated in Figure 2.9, for the spanwise model and at the centre for the chordwise model. Positions **1** and **4** are sufficiently far from the joint region to exhibit pure skin behaviour as well at a sufficient distance from the side walls to ensure no additional influence on the temperatures. Positions **2** and **3** are located sufficiently far from the joint edge to preclude edge effects and at the greatest possible distance from one another so as to represent the resulting temperatures of the two skin sides of the joint with the greatest stability in the temperature gradient between the two sides.

The internal boundary conditions of conduction, convection, and radiation heat transfer are first considered as individual mechanisms for the three tank cases: empty, full, and half-full. The individual analyses allow general trends to be determined concerning the influence of each heat transfer mechanism. The individual conduction-only, convection-only, and radiation-only analyses are performed only on the spanwise mesh shown in Figure 2.9 (a), to obtain information at all four aforementioned positions in a single run, so as to reduce the time spent on these analyses without sacrificing understanding of the effects at the different positions. Analyses combining the individual effects are then performed on both the spanwise and chordwise meshes in Figure 2.9, first without the titanium pins, and then with the pins included.

A 3D model could not be used as the run could not be completed due to excessive pre-memory requirements. An estimated 3.5 GB of memory is required to complete the pre-processing alone, with more than double that memory required for the actual run. This is currently too large a memory requirement due to computing limitations. This size requirement is attributed to the view-factor calculations for the cavity radiation portion of the analysis. Before the model can be defined in its entirety, the portion of each face that 'sees' every other face in the tank must be determined. This calculation is computationally expensive, even for relatively small cavities, since the radiation

diffuses and reflects in multiple directions from each face. If the cavity radiation is omitted in the model, the reduction in computational efforts might allow the run to be completed; however, the results would be a meaningless comparison to the 2D models. Based on the results of the spanwise and chordwise models, and their comparable results to previous work [10], [21], it is believed that the problem is well modelled by these 2D models, negating the need for an additional 3D comparison.

2.4 Results

2.4.1 Display of Temperature Profiles

In order to fully appreciate the wingbox thermal behaviour, the results of the FE analyses are displayed in different formats. The first display method uses ABAQUS CAE for post-processing of the analyses. This method displays the mesh at given time increments using different colours to represent the different temperatures throughout the wingbox. Figure 2.10 is an example of FE temperature profiles for a spanwise, empty tank analysis at three specific times over the course of the day.

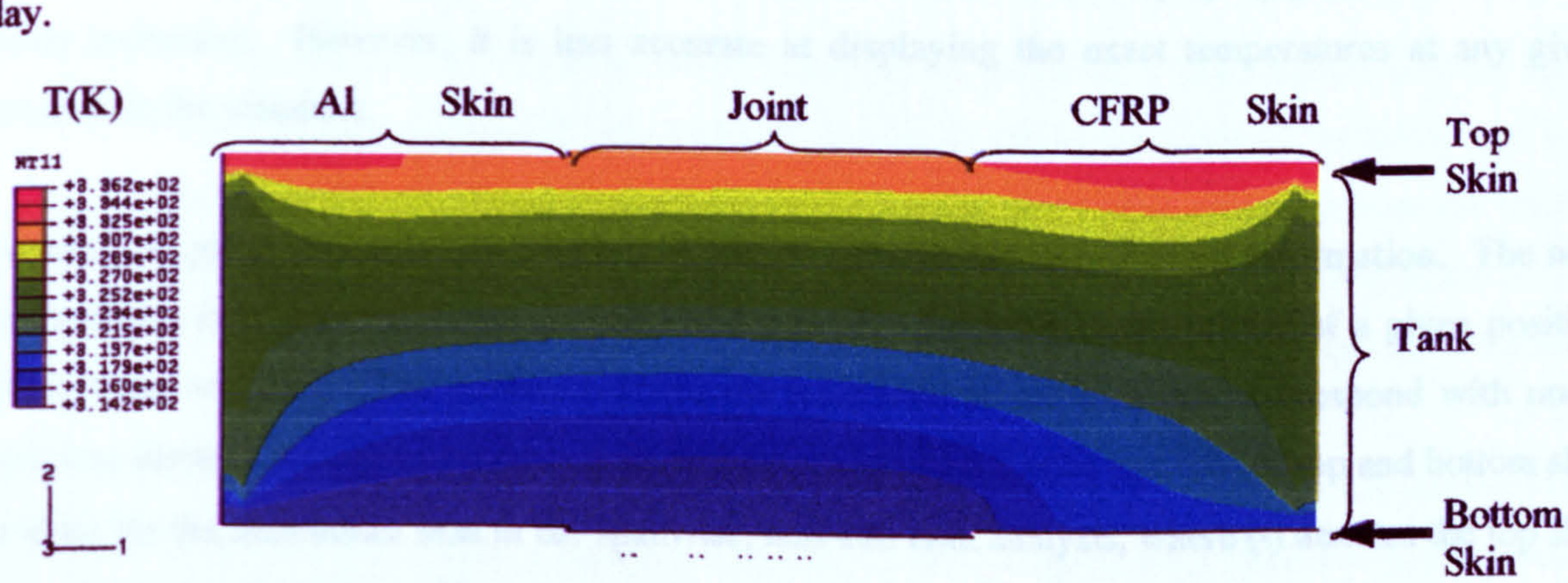

(a) 0900 (9am)

(b) 1400 (2pm)

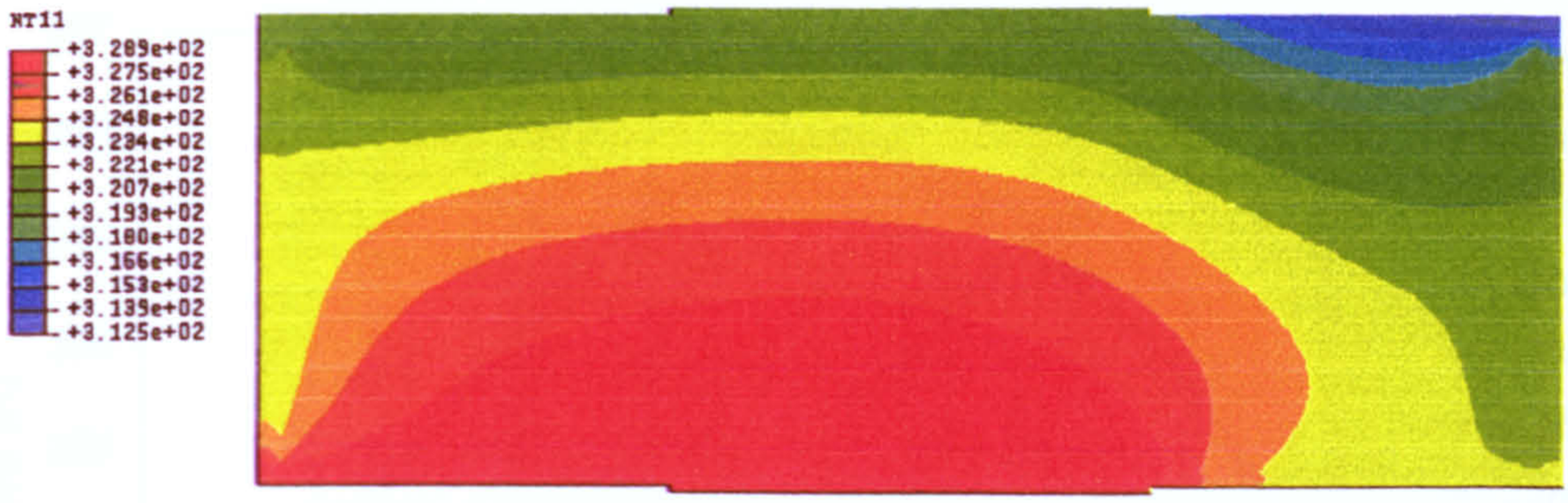

(c) 1800 (6pm)

Figure 2.10. Examples of FE temperature profiles for a spanwise empty tank analyses.

Figure 2.10 reveals that the top skins are hotter than the joint area at 0900 (9am) and 1400 (2pm). At 0900 the maximum temperatures are observed on the CFRP skin side of the joint, whereas at 1400 the maximum temperatures occur through the aluminium skin and the joint region. At 1800 (6pm), the bottom wingbox surface has become hotter than the top surface, the maximum temperatures occur on the aluminium skin side and the CFRP skin is the coolest area in the wingbox. These resulting temperatures are largely influenced by the different conductivities of the materials, as well as the other thermal material properties. This method is effective for displaying general trends at any given increment. However, it is less accurate at displaying the exact temperatures at any given position in the wingbox.

Accuracy at given points in the wingbox is gained through the use of nodal information. The next method uses data gathered from specified nodes to plot the temperature profile of a given position through the wingbox. The positions where the temperatures are measured correspond with nodal positions through the top and bottom skin surfaces. Figure 2.11 is an example of top and bottom skin profiles for the aluminium skin in the spanwise, half-full tank analysis, where (t) denotes the top skin and (b) denotes the bottom skin.

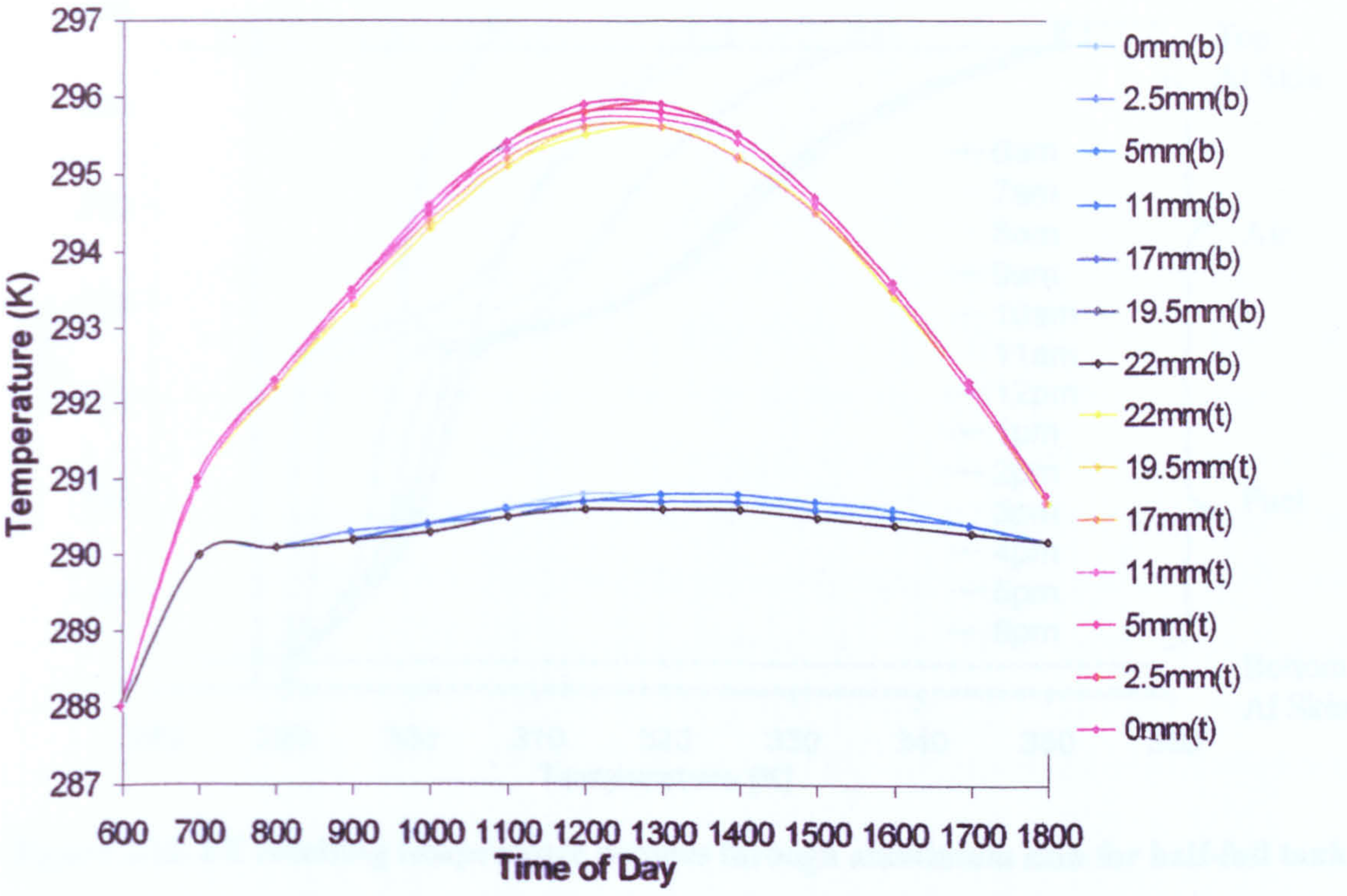

Figure 2.11. Aluminium skin through-thickness temperatures for a half-full tank case.

Using nodal temperatures at specified mesh positions to produce a temperature profile, as in Figure 2.11, shows that the hottest temperatures always occur at the external surfaces, and with slightly cooler temperatures at the internal skin surfaces. This trend is observed over all thermal loading conditions. This method is effective for studying the maximum temperature profiles for any given loading conditions, but is not as efficient at displaying the overall trends through the wingbox.

Finally, the temperature profiles at all time intervals, and at various nodal positions through the entire wingbox, are plotted such that a complete picture of the wingbox behaviour for given loading conditions over the course of the day, as specified by Airbus UK from Figure 2.3 and Figure 2.4, can be obtained via one plot. Figure 2.12 shows an example of a graphical temperature profile through the composite skin side of the joint for a full tank case.

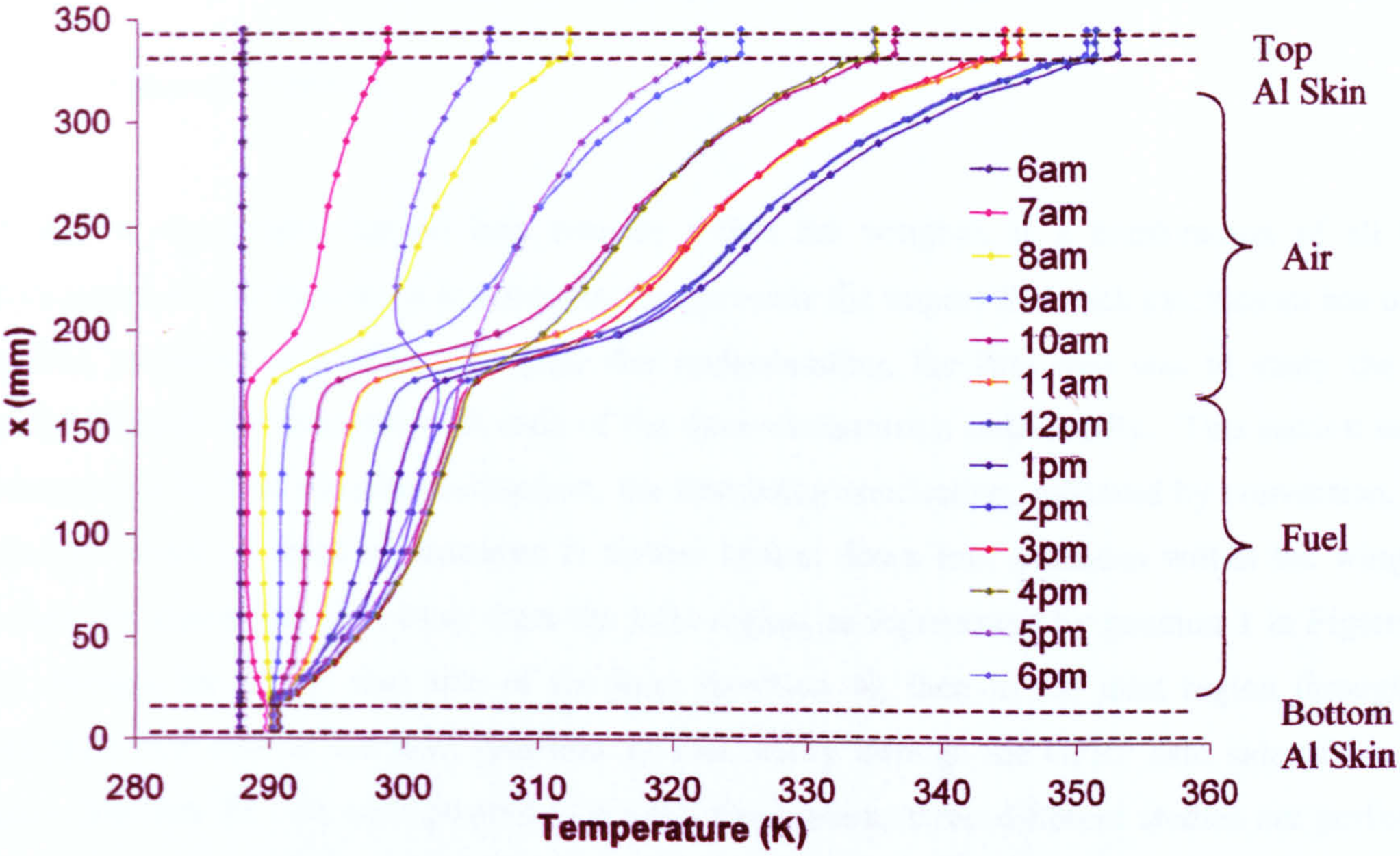

Figure 2.12. FE resulting temperature profiles through aluminium skin for half-full tank.

In Figure 2.12 the areas contained within the dashed lines represent the top and bottom skins, with the distance through the tank measured from the bottom surface toward the top surface. A profile through the tank is given every hour throughout the day, indicated by different coloured lines. The sudden change in the slope of the plots seen half way through the tank occurs at the mid-tank fuel level of the half-full case. The significantly cooler temperatures in the bottom half of the wingbox demonstrate a substantial cooling ability of the fuel when all methods of heat transfer are present. This analysis shows that the hottest temperature on the top skin occurred at 1300 (1pm), while there appears to be only slight deviation from the initial condition of 288K at 0600 (6am). From this figure it is also possible to note a slight reversal in slope at 1800 (6pm) when the external top surface is cooling due to the external drop in temperature at the end of the day, but there is still heat trapped within the tank keeping the temperature up near the mid-point. This method of graphical temperature profiling is the most efficient at displaying the overall trends over the course of the day, and providing a more detailed account of the temperature at various positions through the wingbox. However, for behavioural comparisons, the method demonstrated in Figure 2.11 is used as it provides the clearest results in the specific area of concern.

2.4.2 Conduction-Only, Convection-Only, Radiation-Only and Combined Analyses

2.4.2.1 General Overview

While it is recognised that all heat transfer within the wingbox is a combination of all three mechanisms of heat transfer, it is necessary to appreciate the impact that each mechanism has on the resulting temperature profiles. To gain this understanding, the first step was to study the heat transfer through the wingbox with each of the three mechanisms individually. This section is first broken down by heat transfer mechanism, the first being conduction, followed by convection, then radiation. Each of these mechanisms is further broken down into positions within the wingbox: through the aluminium skin away from the joint region, as represented by position 1 in Figure 2.9, then through the CFRP skin side of the joint (position 4), then in the joint region through the aluminium skin side of the joint (position 2), and finally through the CFRP skin side of the joint region (position 3). At each position, for each mechanism, three different studies are performed using the wingbox fuel tank positions: empty, full, and half-full.

The simplest analysis involves conduction as the only method of heat transfer through the tank. Not surprisingly, the highest temperatures are observed in the empty tank. This is explained by the poor conductivity of the air within the tank. Full tank results show only a marginal difference. When the effects of natural convection within the tank are studied, there is a reduction in the maximum temperature in the full tank case, as expected due to the large convection coefficient of the fuel. Radiation-only analysis has the greatest impact in the empty tank case. The difference between the surface and sink temperatures increases the effect of the fourth-order radiation effects. The final analyses combining all three heat transfer mechanisms result in reduction in the maximum temperatures observed.

2.4.2.2 Results Through Aluminium Skin Away From Joint Region

The first area of study through the aluminium skin away from the joint is represented by the left-most dashed lines (position 1) in Figure 2.9(a). Figure 2.13 to Figure 2.15 show the results for the empty, full, and half-full tank cases, respectively, where (t) and solid lines represent the top skin results and (b) with dashed lines represent the bottom skin results.

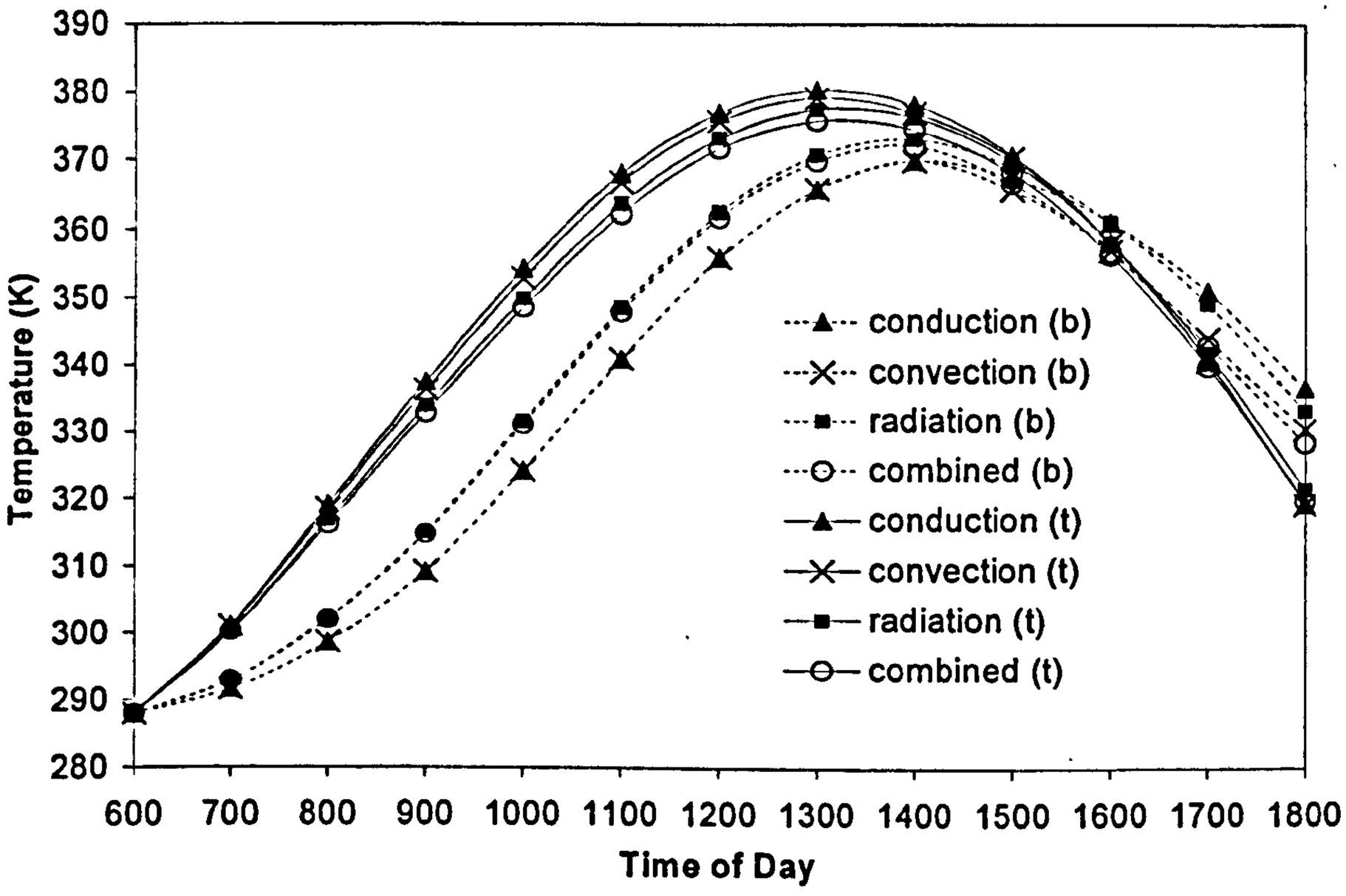

Figure 2.13. Analyses through aluminium skin away from the joint for an empty tank.

Figure 2.13 shows the empty tank case in this study. From the analysis, it is apparent that there is a time, at approximately 1530 (3:30pm), when the bottom skin becomes slightly hotter than the top skin. This reversal is due to the lag in the maximum ground flux, as presented in Figure 2.4. This lag results from the time required for the ground to absorb, reflect, and in particular re-emit the incoming solar flux. Until this reversal time, the conduction-only analysis produces the highest temperatures for the top skin, and the radiation-only analysis produces the highest temperatures for the bottom skin. This difference in dominant mechanisms is due to the fact that emission of radiation is a function of temperature gradient within the wingbox tank. When the top skin is at the higher temperature, the temperature gradient moves from the upper wingbox surface to the lower surface. The top surface emits radiant energy as a method of cooling. This leads to lower temperatures on the top surface in the radiation-only analysis compared to the conduction-only analysis. The bottom skin absorbs the incoming energy from the top skin because of its lower temperature. The only way the bottom surface can cool itself is to reflect a portion of the radiation back toward the top skin, by definition of a grey body. Because the bottom skin cannot actually emit radiation at this time due to the temperature gradient, it continues to absorb heat. This explains the higher temperatures in the radiation-only analysis compared to the conduction-only analysis for the bottom skin.

At a certain time in the day, in this case 1530 (3:30pm), the effects of conduction-only and radiation-only on the top and bottom skins reverse. This is explained by the reversal of the temperature gradient, which is caused by the fact that the upper external surface is exposed to a lower solar flux, while due to the lag, the ground flux continues to increase. After the reversal time, the hotter bottom surface has the ability to emit radiation, and therefore, cool itself, while the top surface is forced to absorb and reflect this incoming radiation. Figure 2.13 shows that the convection-only and conduction-only trends for both the top and bottom surfaces are very close at all times, suggesting that the cooling effects of internal convection are small. However, as demonstrated in the combined analysis, the convection effects should not be considered negligible. The resulting combined analyses produce temperature profiles that suggest the overall temperatures are an additive function of each of the mechanisms of heat transfer.

The influence of each separate mechanism is found by comparing the individual and combined analyses profiles. On both the top and bottom surfaces, radiation has the greatest influence in the overall temperature profiles before the reversal time. This influence is measured by using the conduction-only and the combined results as benchmarks. The other analyses (convection and radiation) are compared by the percent difference from the benchmark. For example, convection-only results show a 25% decrease in temperature when compared to the conduction-only analysis of the top skin at the hottest point at 1300 (1pm), assuming the combined analysis results in the 100% or maximum temperature decrease. Similarly, radiation at this time experiences a 75% decrease in temperature. Summing these two influences approximates the combined results.

On the top skin, radiation is the primary mechanism of heat transfer before the reversal time. This is due to the fact that the convection heat transfer coefficient is small, and behaves more like an insulator rather than a path for cooling. Furthermore, because the top surface is at a higher temperature than the bottom surface, there are minimal buoyancy forces, which cause convection currents. After the reversal time, the influence of the individual mechanisms is less obvious in all profiles. This implies that neither convection nor radiation is particularly effective at removing heat. This is evident as the combined analysis results are positioned near those of conduction-only. Convection has no influence since the heat transfer coefficient is set to zero at the temperature gradient reversal point for the top surface, as seen Table 2.2. The diminished role of radiation is explained by the change in the temperature gradient. Since the top surface is no longer emitting radiation, the effects of the small amounts of heat reflected by the diffused surface are negligible.

On the bottom skin, radiation is the only mechanism for heat transfer up to the reversal time, since the bottom convection coefficient is zero at this time due to the temperature gradient. Convection quickly takes the primary role in heat transfer after the reversal time, making up more than 80% of the combined analysis results. This increase of convection on the bottom skin comes into effect because of the larger heat transfer coefficient of the bottom skin as compared to the top skin, explained previously as a function of the surrounding sink temperature, and because the bottom surface does not emit radiation until after the reversal time. Because the reversal time is late in the day, there is not adequate time for the effects of the radiation to become dominant.

The full tank results in Figure 2.14, display very different temperatures than those of the empty tank. A reversal time is observed only in the conduction-only and radiation-only analyses. When convection is involved, the fuel's ability to remove excess heat from the skins prevents temperature build-up in the tank.

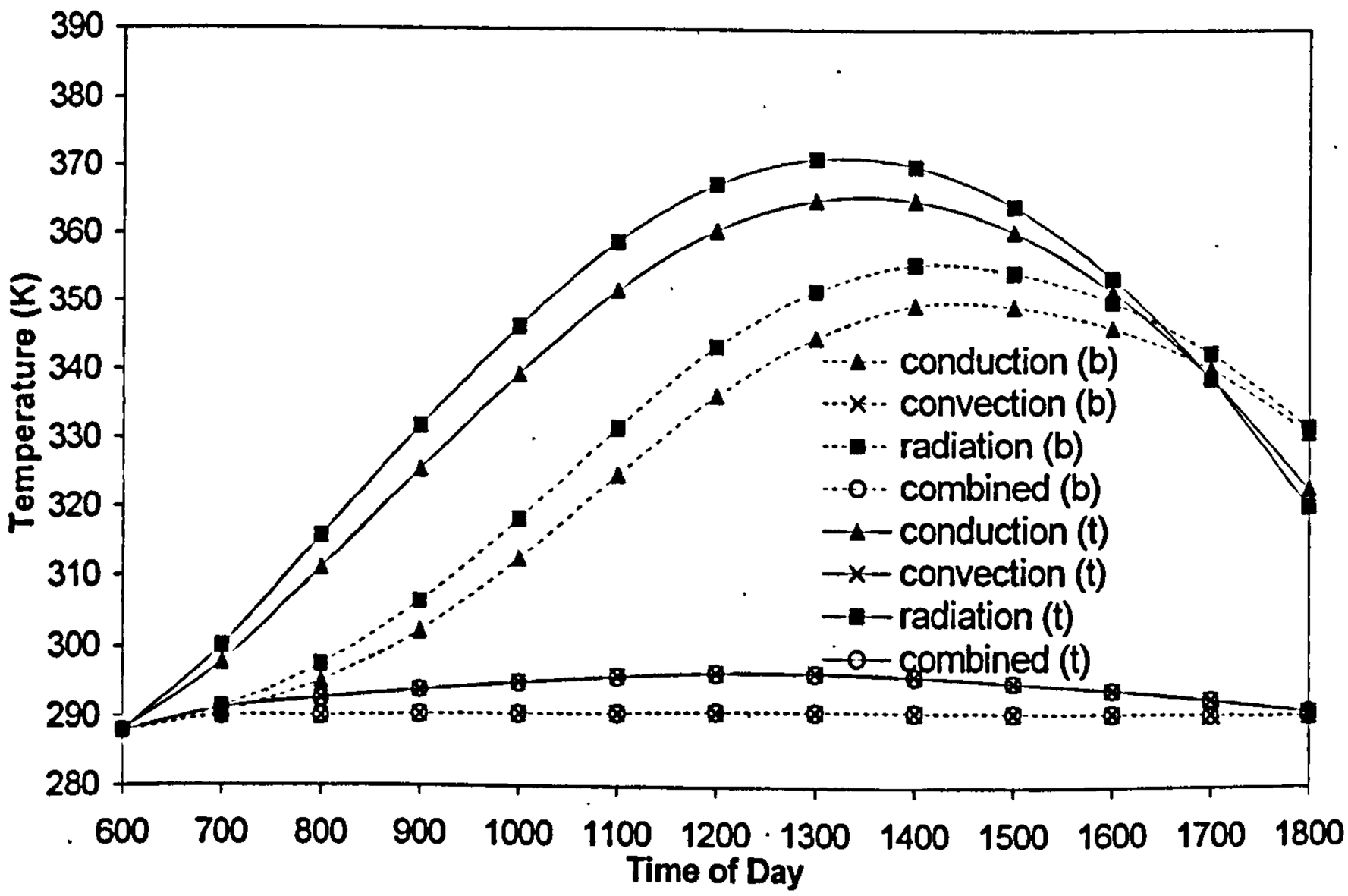

Figure 2.14. Analyses through aluminium skin away from the joint for a full tank.

In Figure 2.14, the conduction-only temperatures are considerably reduced (~ 20°) from those of the empty tank, because of fuel's higher conductivity, which is over an order of magnitude greater than that of air. The temperatures for both the top and bottom skins for radiation-only boundary conditions are above those of the conduction-only analysis. This behaviour change in the top skin results from lower conduction-only temperatures and radiation-only behaviour. It is important to note that ABAQUS does not consider attenuation of radiation in the cavity medium. In other words, the fact that the tank is now filled with fuel, as opposed to air, does not play a part in the radiation-only analysis. This implies that the trends of the radiation-only analyses for an empty and a full fuel tank are similar. The radiation-only results for the empty and full tank cases are not identical because the sink temperatures used in the radiation-only analyses are taken from the conduction-only analyses results. Due to the change in conduction-only temperatures of the full tank, the corresponding radiation analysis results are also altered. Overall, the radiation effects in the combined analysis are minimal, since radiation effects in a liquid are known to be small in comparison to those in a gas, explaining the difference between the empty tank and full tank cases.

For both the top and bottom surfaces, the combined convection-radiation temperatures and convection-only temperatures are virtually identical, proving the heavy influence of convection in a full tank. The influence of convection is so much greater than that of radiation that it dominates the heat transfer, eliminating the superposition effect observed in the empty tank case. This is to be expected given the large convection heat transfer coefficients associated with fuel, which differs from that of air by nearly three orders of magnitude, as seen in Table 2.2.

In Figure 2.15, the results for the half-full tank case are divided into two distinct patterns. The results of the top half of the tank resemble those found in the empty tank case, and the results of the bottom half are similar to results found in the full tank case.

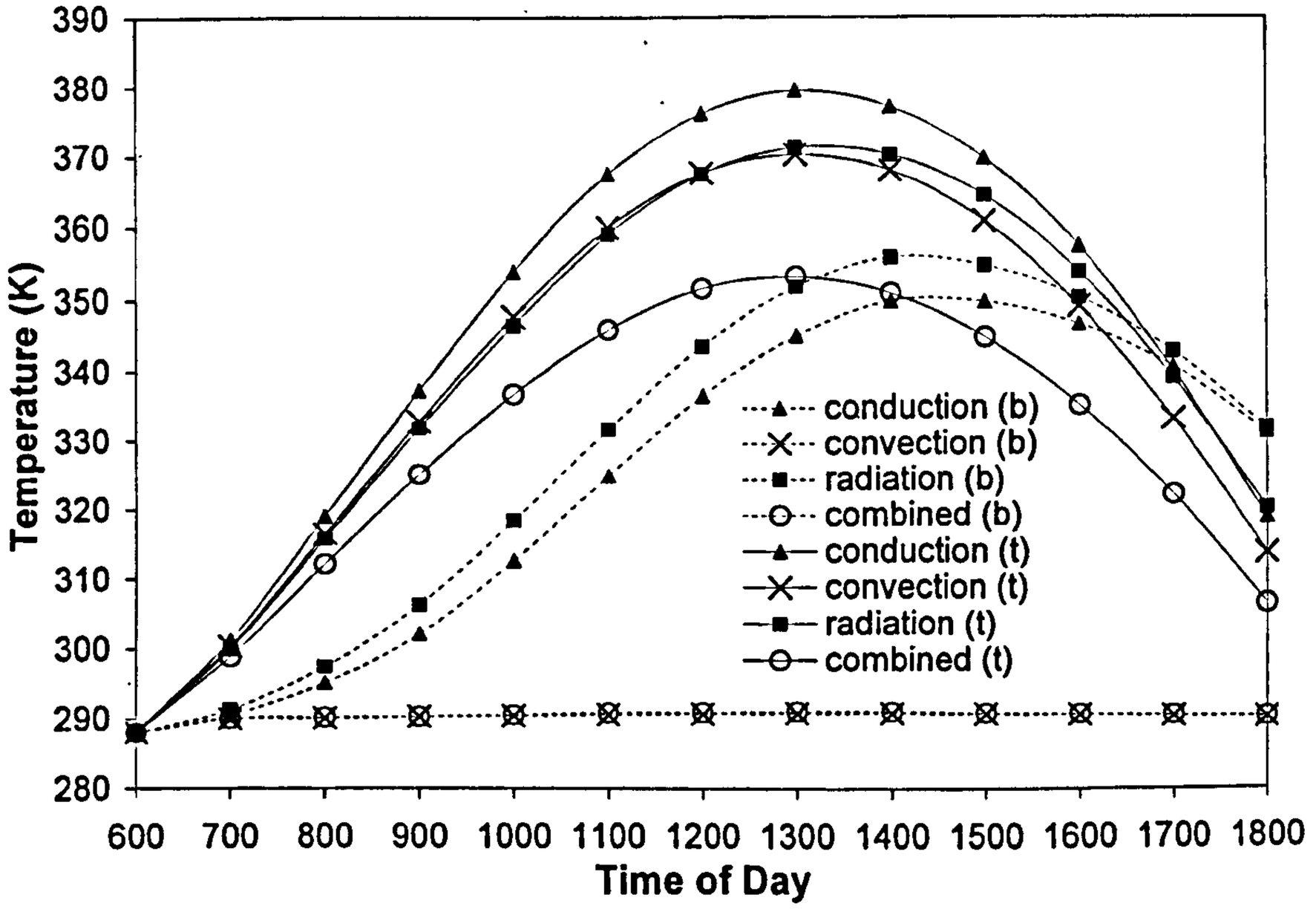

Figure 2.15. Analyses through the aluminium skin away from joint for a half-full tank.

From Figure 2.15, the only difference between the half-full tank and corresponding half of the empty and full tank behaviour is an improvement in the efficiency of the convection in the top half of the tank, which shows a reduction in maximum temperature of approximately 30° compared to the empty tank results, due to the benefit of having fuel in the bottom portion. Rather than having a minimal effect, convection provides more significant cooling capabilities, resulting in a drop in the temperatures for the combined convection-radiation analysis as compared to those of the empty tank case. As anticipated, the top skin is always significantly hotter than the bottom skin, because of its similarity in behaviour to the empty tank case.

2.4.2.3 Results Through CFRP Skin Away From Joint Region

The next section looks at the results for the heat transfer through the CFRP skin away from the joint, as represented by the right-most dashed lines (position 4) in Figure 2.9(a). The temperature results through the CFRP skin for the empty tank shown in Figure 2.16 reflect slightly lower temperatures than those through the aluminium skin, with a difference of approximately 2°. This is related to the difference in emissivity between the aluminium and the CFRP, as observed in Table 2.2. Because the surface temperature is proportional to the flux striking the surface divided by the emissivity, as

shown in (1-4), when the emissivity of the surface increases, the temperatures decrease. In the case of CFRP versus aluminium, the emissivity of CFRP is approximately 15% higher, causing lower radiation temperatures, which in turn leads to lower combined results.

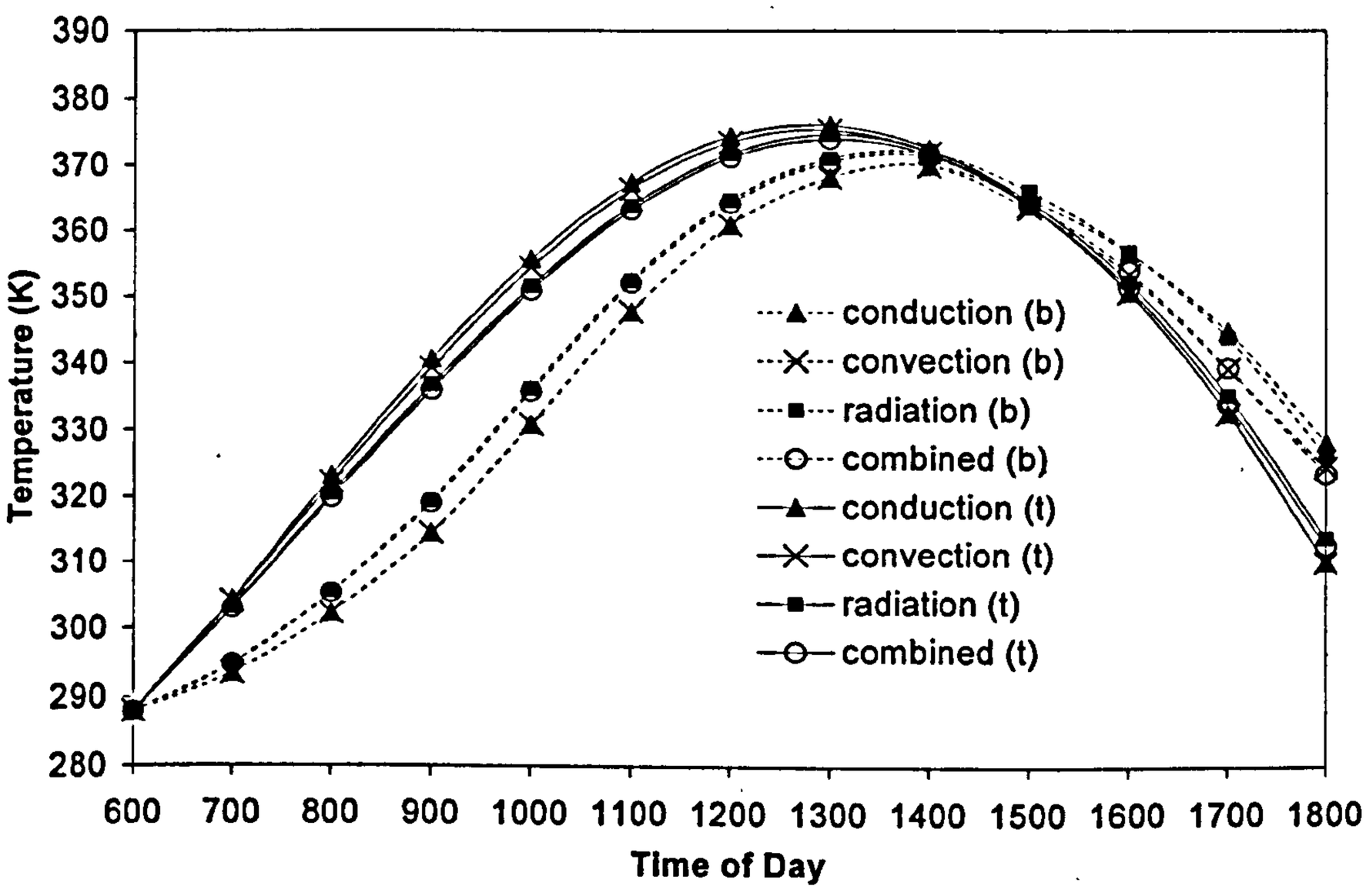

Figure 2.16. Analyses through the CFRP skin away from the joint for an empty tank.

Figure 2.16 illustrates that the reversal time through the CFRP skin comes earlier than through the aluminium skin side, at approximately 1400 (2pm). This can be explained by the CFRP's reduced ability to conduct heat through the skin. Less heat is conducted through the skin, as compared to the aluminium, allowing for a smaller amount of heat to build-up at the internal surface, where air acts as an insulator. Thus, when the ground flux increases, at approximately 1300 (1pm), the resulting increase in bottom skin temperatures is observed much sooner than in the aluminium skin behaviour.

The radiation-only boundary condition appears to have less influence through the CFRP skin. Again, this results from CFRP material properties as compared to those of the aluminium. The internal CFRP skin temperatures obtained from the conduction-only analysis are lower by approximately 5° due to lowered conductivity. Since these temperatures are used as the sink temperatures in the radiation analysis, the temperature difference used in the radiation calculation is smaller. Therefore, the fourth-order effects of radiation are less profound. Although the radiation-only results are lower

than those through the aluminium skin, radiation is still the principle mechanism affecting the temperatures in the combined analysis results.

The contribution of convection in the combined analysis is reduced, when compared with that of the aluminium skin, due to the lowered temperature gradient between the top and bottom surfaces. As shown in equation (1-3), the flux given by convection is a function of the difference between the surface and sink temperatures. Recall that the sink temperatures are approximated as the mid-tank temperatures, which are in turn influenced by the surrounding surfaces. It is evident that decreasing the difference between these two surface temperatures results in a lowered flux. This lowered flux dictates the role of convection in the combined analysis, and explains the smaller influence of convection in this particular case.

Figure 2.17 shows that the trends for the full tank case through the CFRP skin are very similar to those of the aluminium skin analyses; however the results show a greater maximum temperature in the combined analysis with an increase of approximately 14° due to the difference in material properties. The reversal time in the conduction-only and radiation-only analyses is approximately one hour earlier than that in the aluminium skin study. The poorer conductivity of CFRP is responsible for this situation, as it is in the empty tank case.

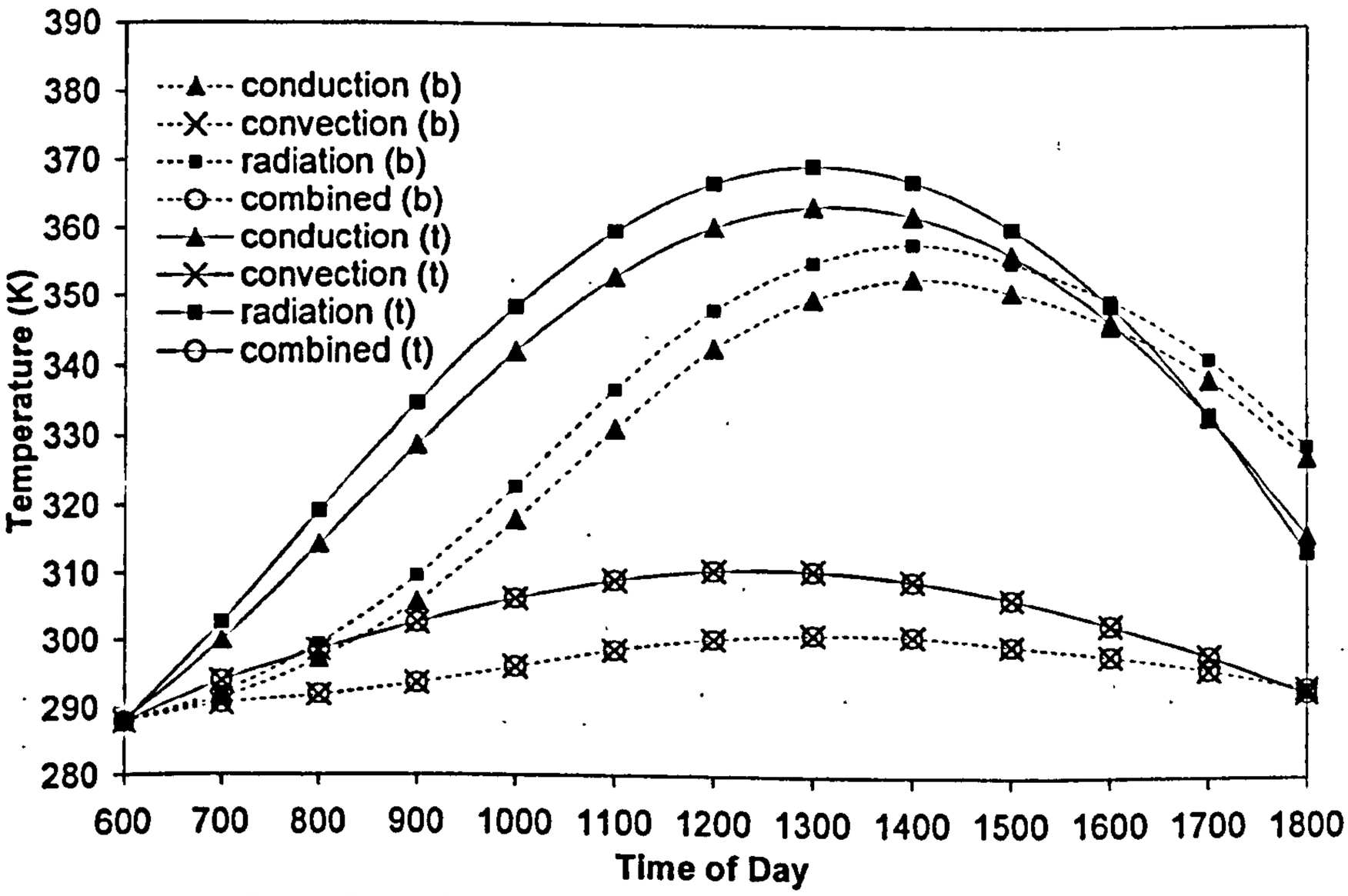

Figure 2.17. Analyses through the CFRP skin away from the joint for a full tank.

As seen in Figure 2.17, the results for the radiation boundary condition show little change from the empty tank case, and are similar to results in the aluminium skin. Because the material properties of the attenuating medium are ignored in the FE model, fuel and air behave the same. Only the surface temperatures obtained in the conduction-only analysis and the skin material itself can influence the temperature profiles. Less heat is built up in the CFRP skin in comparison to the aluminium skin, allowing for the increasing influence of the ground flux on the overall temperatures, thus resulting in an earlier reversal time.

Increases in the convection-only and combined analyses temperatures of over 10° in both cases, compared to those through the aluminium skin, are obvious. The CFRP skin is not as effective at conducting heat through to the fuel. This in turn results in the fuel being less capable to act as an efficient heat sink, causing an increase in the overall CFRP skin temperatures compared to those of the aluminium analyses.

The analyses trends through the CFRP skin for a half-full tank, shown in Figure 2.18, are similar to those of the aluminium skin analyses. However, both the top and bottom temperatures are higher, as expected given the results of the empty and full tank cases. Once again, this increase is due to the composites lesser ability to conduct heat into the tank, thereby, reducing the heat sink capabilities of the fuel, and increasing the temperatures.

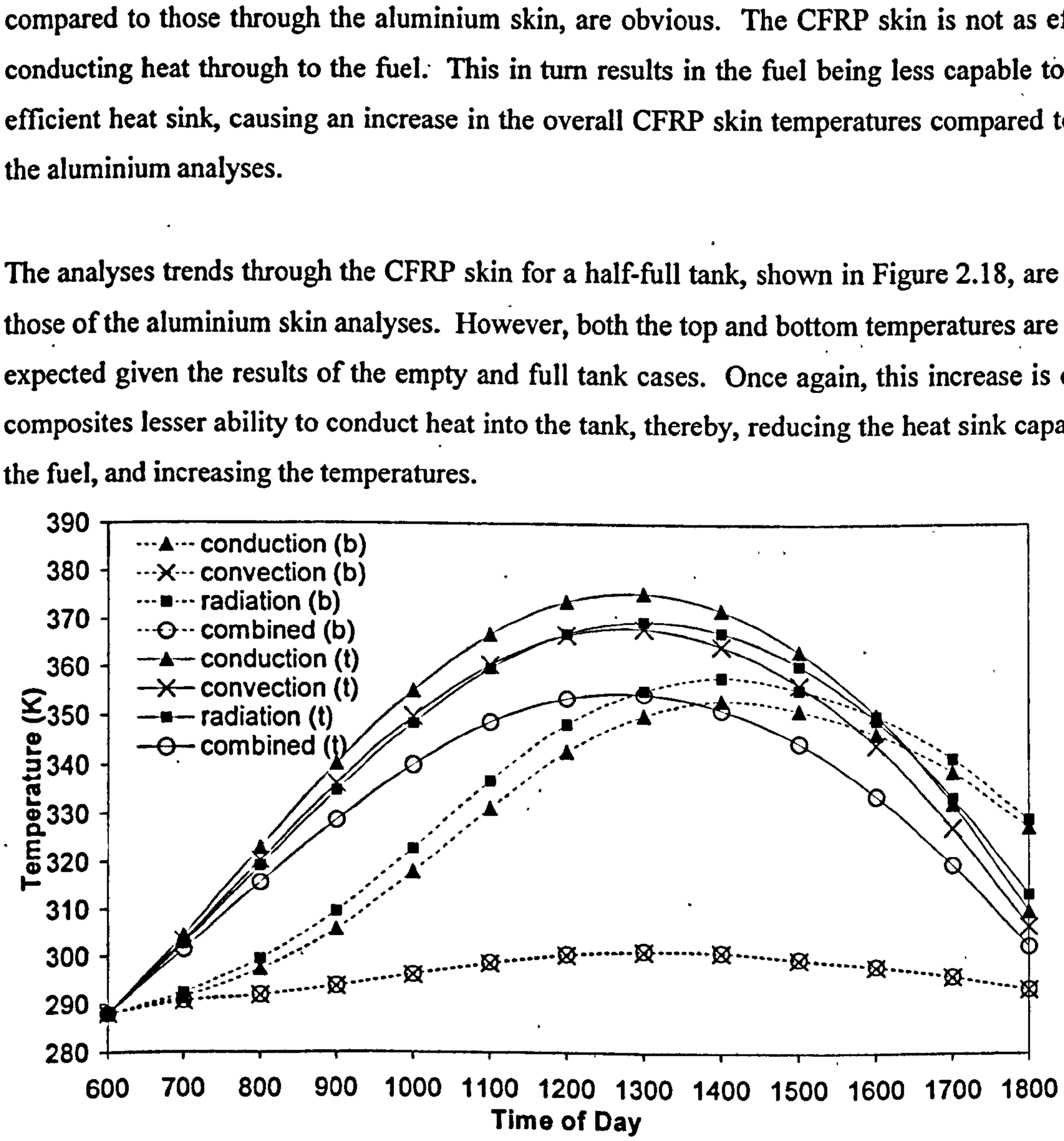

Figure 2.18. Analyses through the CFRP skin away from the joint for a half-full tank.

For the combined analyses, the maximum temperatures through both the aluminium and CFRP skins are found to occur at approximately 1300h (1pm) for the top skin surface and 1400h (2pm) for the bottom surface. This hour difference is due to the lag in the ground flux maximum compared to the solar flux maximum, as illustrated in Figure 2.4. Table 2.3 presents a summary of these maximum temperatures for the internal boundary conditions of conduction-only, convection-only, radiation-only, and combined analyses through the aluminium and CFRP skins away from the joint for empty, full, and half-full tank cases.

Table 2.3. Comparison of maximum day temperatures for top and bottom skin surfaces.

		Away From Joint					
		Al skin			CFRP skin		
		Empty	Full	Half	Empty	Full	Half
T_{max} Top (K)	Conduction	380	365	379	376	364	376
	Convection	379	296	370	376	311	368
	Radiation	373	371	371	375	370	370
	Combined	376	296	353	374	311	354
T_{max} Bottom (K)	Conduction	370	350	350	370	353	353
	Convection	370	291	291	370	301*	301*
	Radiation	373	356	356	372	358	358
	Combined	372	291	291	371	301	301*

*Maxima occurred at 1500 (3pm) rather than 1400 (2pm).

Table 2.3 shows that when the results of the individual heat transfer mechanisms are compared with the results of the combined analysis, radiation has a slightly greater effect than convection in the empty tank case for both the aluminium and CFRP skins. This is expected because, compared to fuel, air has a lower coefficient for convection heat transfer as well as conductivity leaving radiation as the influencing factor in the heat transfer. Gases are generally more affected by radiation than liquids [2], explaining the decrease in radiation influence with the presence of fuel. Convection is shown to contribute with and without the presence of fuel to the overall combined analyses results. To leave out this mechanism in any future models could lead to error. In the full tank case, the strong influence of convection is apparent. Again, this is expected because of the increased magnitude of the heat transfer coefficient associated with fuel, which in turn diminishes the influence of the other heat transfer mechanisms. Ignoring radiation in future models could be an option in the full tank case, but for completeness in this study, all three mechanisms are used in all three tank cases. The half-full tank case combines certain results from both the empty and full tank cases. The bottom half performs very much like the full tank case with a strong convection influence, whereas,

the temperatures in the empty top half are lower than the empty tank case because the presence of fuel in the bottom permits a greater convection cooling effect.

2.4.2.4 Results Through Aluminium Skin Side of Joint

The temperature profiles through the aluminium skin side of the joint are designated by position 2 in Figure 2.9 (a). Figure 2.19 shows the empty tank results.

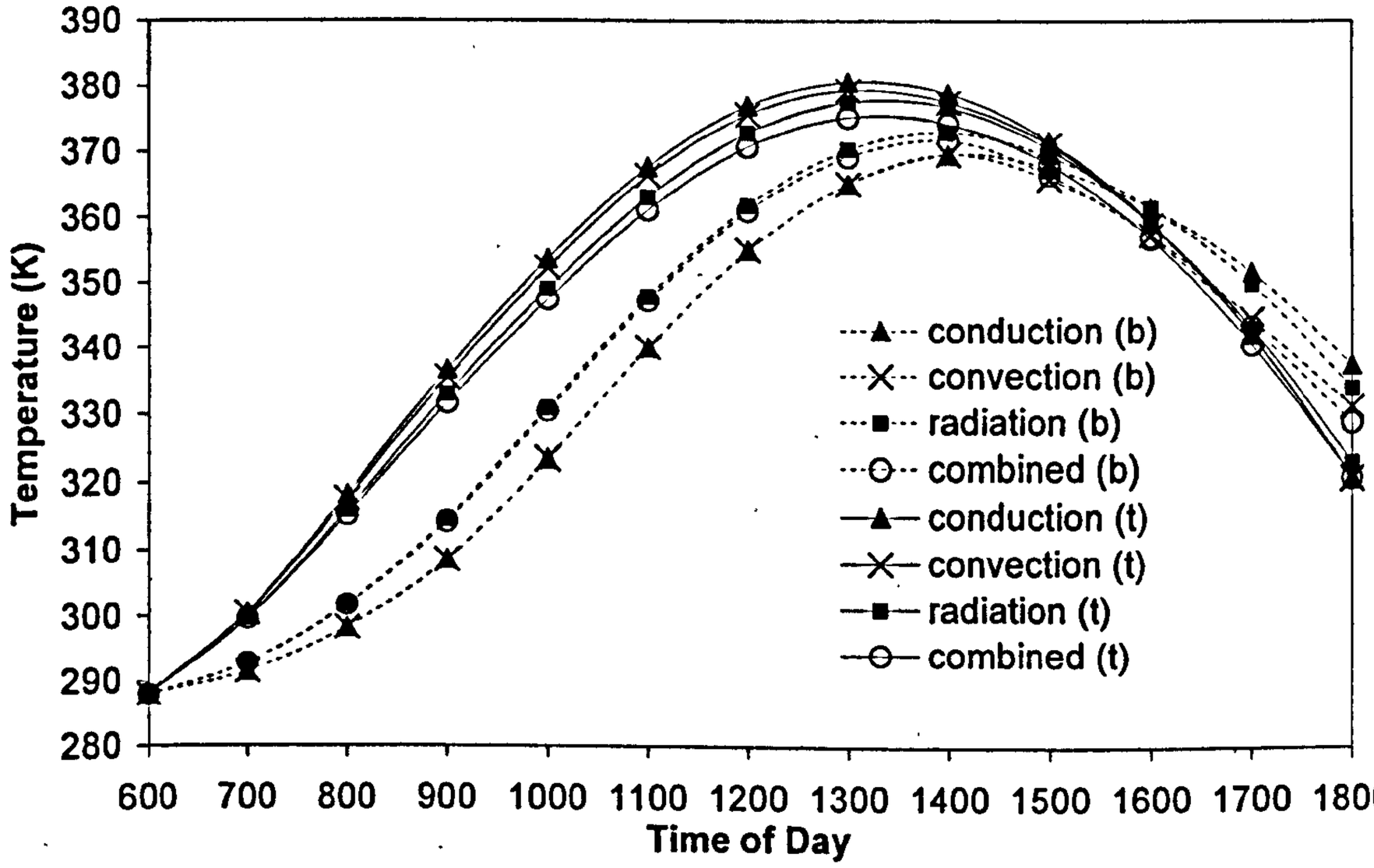

Figure 2.19. Analyses through the aluminium skin side of the joint for an empty tank.

The profiles through the aluminium skin side of the joint in Figure 2.19 are very similar to the aluminium skin profiles from Figure 2.13. In effect, the aluminium skin side of the joint behaves as a thicker aluminium skin.. The maximum temperatures on both the top and bottom skins are almost identical to those in the aluminium skin analysis. Although the skin thickness has increased, its length to thickness ratio remains relatively small. This means that the heat is conducted through the skin at approximately the same rate, causing the heat transfer mechanisms to behave in a similar manner and resulting in very similar temperatures.

Figure 2.20 shows the full tank results through the aluminium skin side of the joint. The profiles demonstrate almost identical trends to the aluminium skin away from the joint analyses, shown in Figure 2.14. The maximum temperatures for each mechanism on both the top and bottom skins are

equal to those for the aluminium skin analyses. The influence of the skin thickness is negligible in this case, because the fuel is so efficient at removing the heat that is conducted through to the tank.

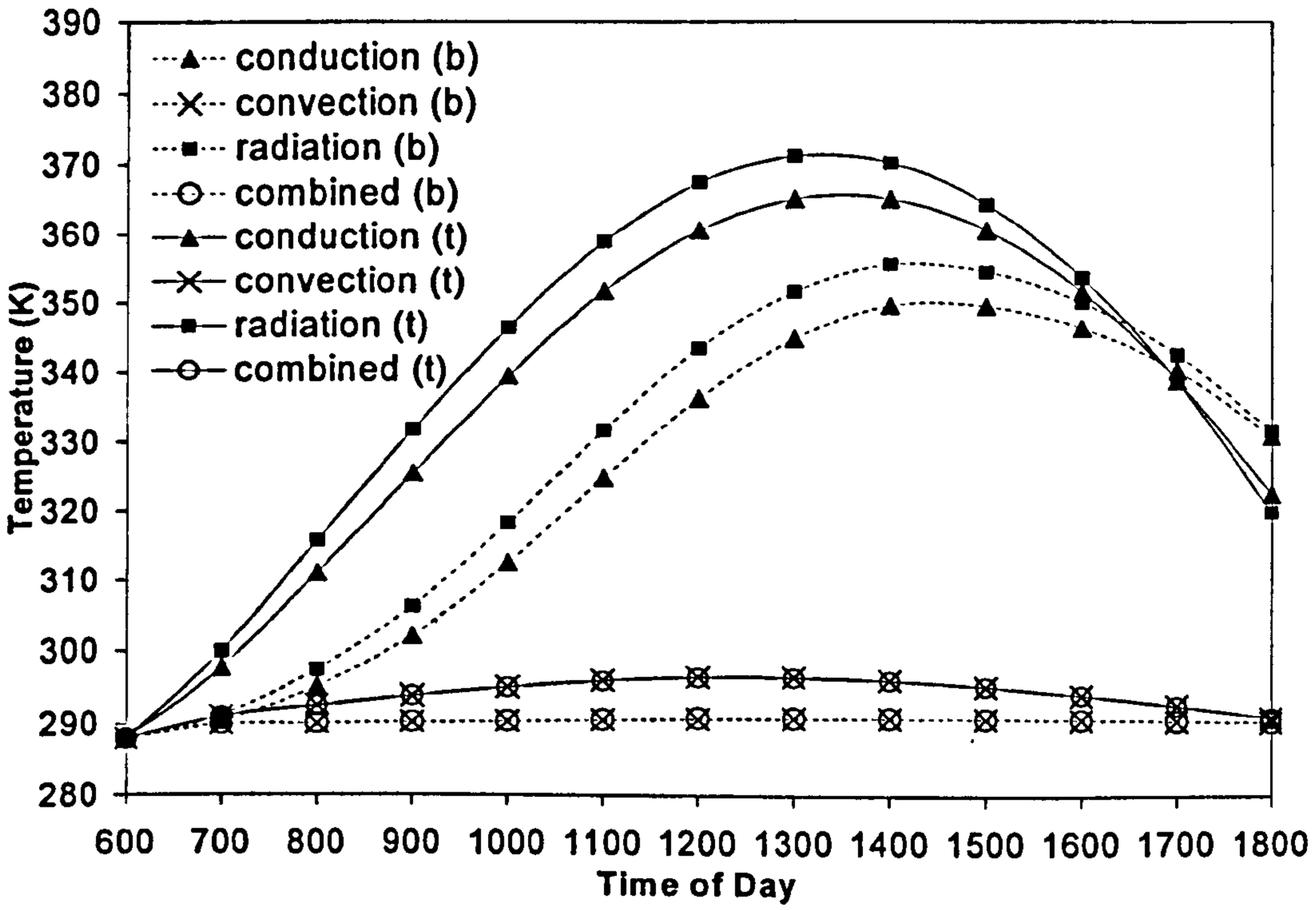

Figure 2.20. Analyses through the aluminium skin side of the joint for a full tank.

Figure 2.21 shows the results for the half-full tank case through the aluminium skin side of the joint. Again, a combination of the results of the empty and full tank analyses is observed. The resulting profiles and maximum temperatures are once again nearly identical to those for the aluminium skin analyses. This is as expected because the increase in skin thickness is small in relation to the overall plate size, resulting in approximately the same amount of heat traveling through the skins, and in turn, being removed from the internal surface by the individual mechanisms.

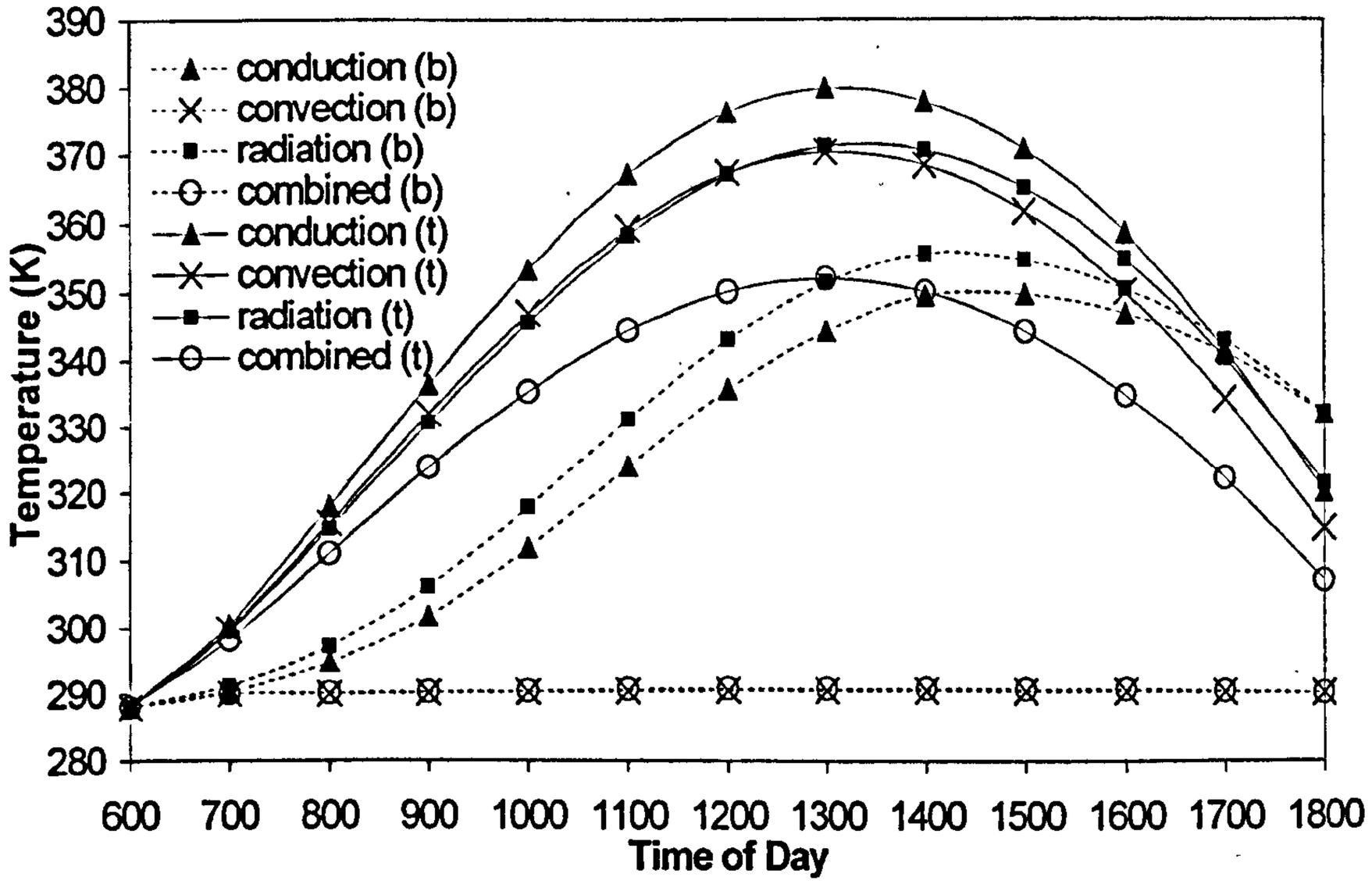

Figure 2.21. Analyses through the aluminium skin side of the joint for a half-full tank.

2.4.2.5 Results Through CFRP Skin Side of Joint

The temperature profiles through the CFRP skin side of the joint, position 3 in Figure 2.9(a), is the last area of study. Figure 2.22 to Figure 2.24 display the results for the empty, full, and half-full tank cases, respectively.

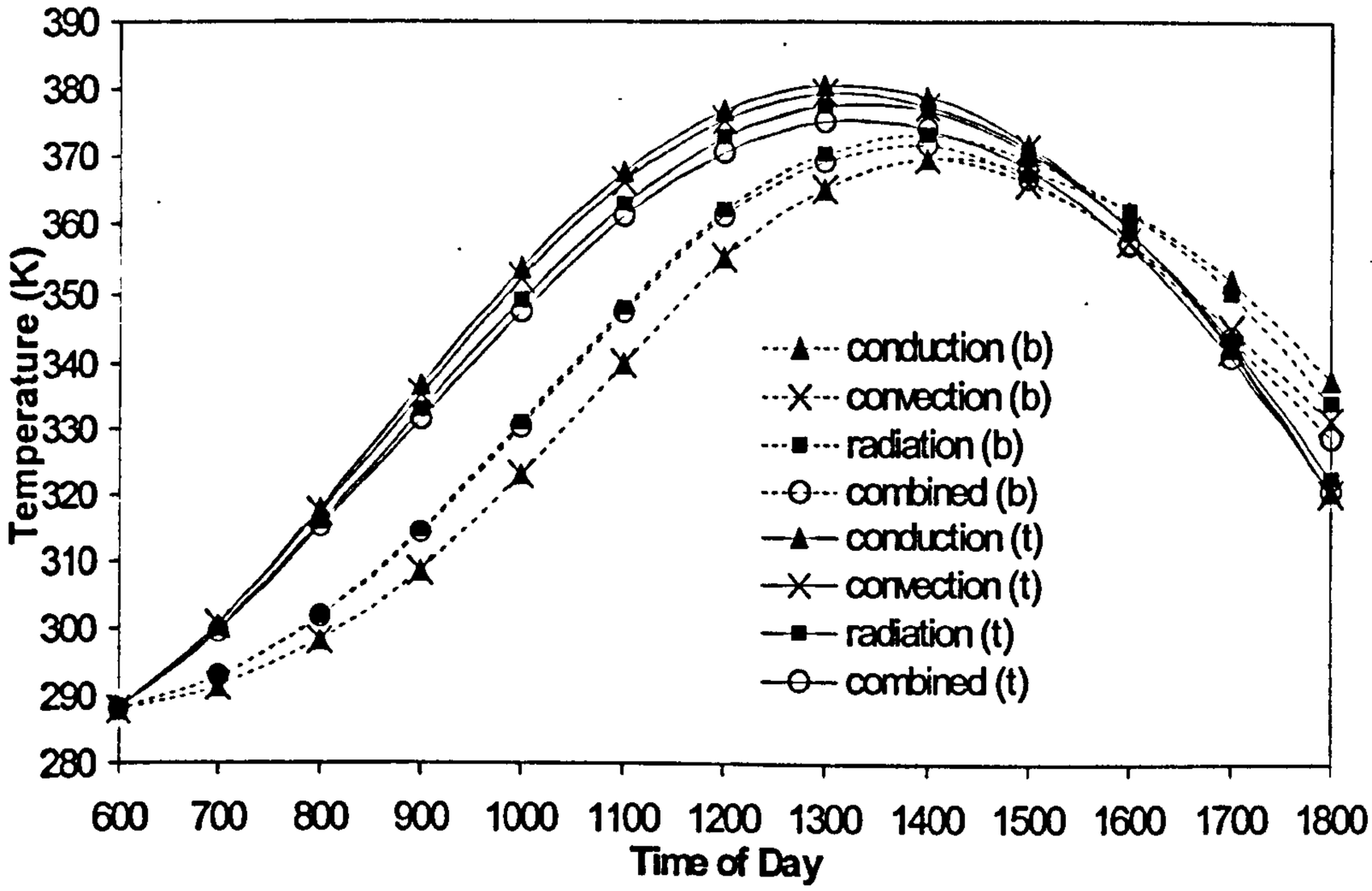

Figure 2.22. Analyses through the CFRP skin side of the joint for an empty tank.

Comparing Figure 2.16 and Figure 2.19 with Figure 2.22, it is evident that the trends through the CFRP skin side of the joint are nearly identical to those through the aluminium skin side of the joint, rather than those through the CFRP skin. This is a result of the aluminium laps dictating the flux that enters the joint area. The emissivity of the aluminium determines the influence of radiation, which has a large impact on the temperatures in the empty tank. The reversal time shifts from 1400 (2pm) as through the CFRP skin, to approximately 1530 (3:30pm), which is similar to the time in the aluminium analyses. This change is a result of the aluminium laps allowing heat to pass more quickly into the skin region. The maximum temperatures observed on the top surface are between one and four degrees higher than in the analyses through the CFRP skin alone, but less than one degree different than the aluminium skin results. The presence of the CFRP skin between the aluminium laps causes a slowing in the movement of heat to the internal surface, due to the lower conductivity. This, in turn, results in a slight accumulation of heat in the external aluminium lap. The maximum bottom surface temperatures are nearly identical to those in the CFRP skin analyses because the bottom flux is less. This leads to less heat build-up in the external lap, and therefore, no significant change in maximum temperatures from the CFRP skin analyses is observed. Because the air acts as an insulator at the internal surface, and the aluminium laps have a higher conductivity and lower emissivity, they, temperatures in combination with incoming heat fluxes, are the limiting factors dictating the surface.

The results shown in Figure 2.23 are for the full tank case through the CFRP skin side of the joint. These profiles bear a greater resemblance to those of the aluminium skin away from the joint and the aluminium skin side of the joint than they do to the CFRP skin away from the joint region behaviour.

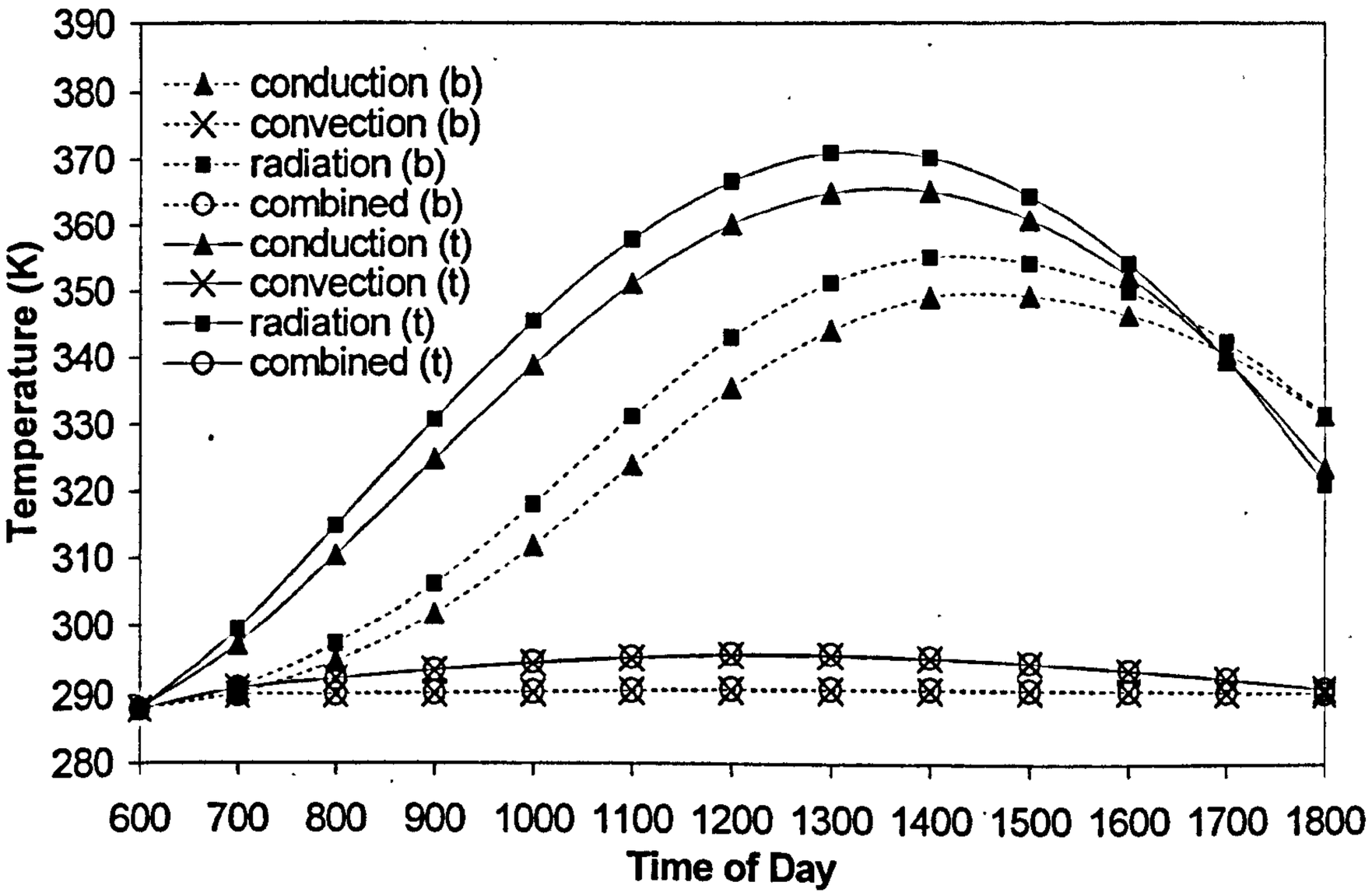

Figure 2.23. Analyses through the CFRP skin side of the joint for a full tank.

As shown in Figure 2.23, the top skin temperatures for the conduction-only and radiation-only analyses are increased by approximately two degrees as compared with the CFRP skin analyses. The reasons for this increase are the same as those of the empty tank analyses. The higher conductivity of the aluminium laps allows heat to be drawn in quickly, but this movement of heat is slowed when it reaches the CFRP skin, causing a build up in the external laps. Even though the conductivity of fuel is greater than the conductivity of air, it is still a relatively inefficient mechanism of heat transfer in this case. In the radiation analysis, the lower emissivity of the laps causes an increase in the surface temperatures and, therefore, the surfaces have a lesser ability to emit radiation as a method of cooling.

The bottom skin maximum temperatures for conduction-only and radiation-only analyses through the CFRP skin side of the joint are lowered by three degrees, compared to the analyses through the CFRP skin. Unlike the top surface, which is already at a maximum rate of heat transfer through the skin, and where adding the laps causes build-up, the bottom surface, which has a lower incoming

flux, is able to increase its heat transfer efficiency through the aluminium laps. On the bottom, the laps actually aid in the movement of heat through the skin, which results in cooling. The reduction in the conduction-only temperatures caused by the aluminium laps leads to a similar reduction in the radiation-only results because the difference between the surface temperature and sink temperature is decreased.

The half-tank case through the CFRP skin side of the joint results is shown in Figure 2.24. The results are again more similar to the aluminium skin side of the joint than through the CFRP skin alone.

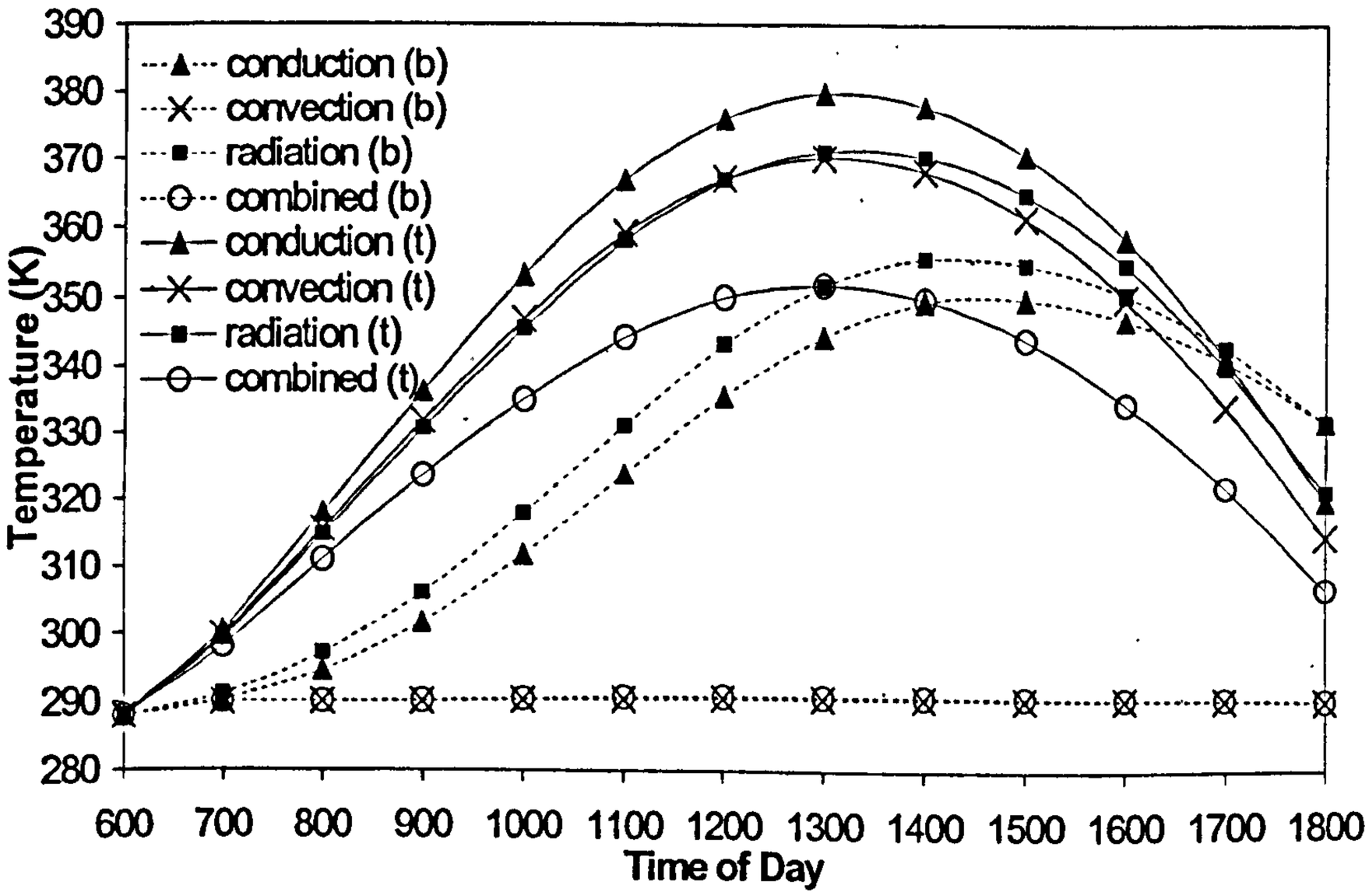

Figure 2.24. Analyses through the CFRP skin side of the joint for a half-full tank.

The conduction-only and radiation-only maximums are two to four degrees greater than those through the CFRP skin. Again this is due to an accumulation of heat in the external aluminium laps, because of an increase in conductivity, and a lowered surface temperature resulting from the lower surface emissivity of the laps compared to the CFRP skin. The maximum bottom surface temperatures are three to four degrees lower than the CFRP skin results, because of the aluminium laps' ability to increase heat movement through to the heat sink of fuel within the wingbox tank. The profiles are a combination of the empty tank and full tank results, with the top half corresponding to the empty tank results, and the bottom half corresponding to the full tank results. The convection-

only and combined results are nearer those of the aluminium analyses than the CFRP skin analyses. This demonstrates that the aluminium laps improve the wingbox ability to use the fuel as an efficient heat sink. The results for the analyses through the joint on both the aluminium and CFRP skin sides for the various heat transfer mechanisms and the three tank cases are summarised in Table 2.4.

Table 2.4. Comparison of maximum day temperatures for top and bottom joint surfaces.

		Through Joint					
		Al skin side			CFRP skin side		
		Empty	Full	Half	Empty	Full	Half
T_{max} top (K)	Conduction	381	365	380	381	366	380
	Convection	379	296	370	379	296	370
	Radiation	378	371	371	377	371	371
	Combined	375	296	352	375	296	352
T_{max} bottom (K)	Conduction	370	350	349	370	350**	350**
	Convection	370	291	291	370	291	291
	Radiation	373	356	355	373	356	356
	Combined	372	291	291	372	291	291

**Maxima occur at 1500 (3pm) rather than 1400 (2pm).

Table 2.4 shows that both sides of the joint, aluminium skin and CFRP skin, have nearly identical temperatures at the bottom, and only very slight differences at the top. These slight differences on the top are due to the larger solar flux, which promotes a greater accumulation of heat in the aluminium. In all cases, however, the behaviour of the CFRP skin side of the joint is more similar to the behaviour of the aluminium regions than to the CFRP skin behaviour. This is related to the different conductivity and emissivity properties of the aluminium and CFRP. The external aluminium laps have a lower emissivity than the CFRP skin. Because this emissivity is inversely proportional to surface temperature, the aluminium laps at the joint region result in increased temperatures in comparison to those of the CFRP skin. The increased conductivity of the aluminium draws more heat into the joint area, which then slows upon reaching the CFRP skin, resulting in a build up of heat in the external aluminium laps. Since the heat transfer coefficients are a function of the surface material properties, which in this case are all aluminium including the CFRP skin region of the joint, the convection values are also influenced by the presence of the aluminium laps. Thus, all mechanisms of heat transfer are influenced by the presence of the aluminium laps, regardless of the underlying skin material, in the joint region.

For the analyses both through and away from the joint, the hottest overall temperatures are found through the aluminium skin in the empty tank case. This is due to its smaller thickness, and to its strong ability to conduct the heat, which causes a build-up of heat at the internal surface where the air acts as an insulator, rather than a heat sink. The maximum temperatures of all the empty tank cases are similar in value, suggesting that the material in the tank, rather than the skin material or joint thickness, plays the most important role. The hottest overall temperatures for the full and half-full tank cases are found in the CFRP skin because of its inability to conduct the heat through quickly enough to make full use of the dissipating capabilities of fuel. Table 2.3 and Table 2.4 demonstrate that the maximum temperatures for the combined analyses are a function of both the convection and radiation results. The exclusion of either of these heat transfer mechanisms in future models could lead to unrealistic or inadequate representation of the heat transfer problem.

2.4.3 Spanwise and Chordwise Analyses

In order to examine the temperature effects in a 3D sense, the combined analyses are broken down into two directional components, spanwise and chordwise, for the FE analyses using the meshes shown in Figure 2.9. A study of the chordwise skin regions is also performed using the mesh described by Figure 2.9(b), with the aluminium laps removed. Using the results from the previous section to establish the requirement for the inclusion of internal natural convection and radiation heat transfer mechanisms in the models, combined boundary conditions are used in all three tank cases. The resulting heat transfer differences between spanwise and chordwise analyses are discussed below.

As anticipated, the results of the spanwise and chordwise analyses for any given condition are very similar. Table 2.5 summarizes the differences in the maximum temperatures attained in each of the four surface positions, as shown in Figure 2.9, for each of the three tank cases.

Table 2.5. Comparison of maximum top and bottom temperatures.

		Away from joint				Through joint			
		Spanwise Analysis		Chordwise Analysis		Spanwise Analysis		Chordwise Analysis	
		Al skin	CFRP skin	Al skin	CFRP skin	Al skin side	CFRP skin side	Al skin side	CFRP skin side
T_{max} Top (K)	Empty	376	374	3767	374	375	375	373	374
	Full	296	311	296	309	296	296	296	296
	Half	***353***	***354***	***351***	***350***	352	352	352	352
T_{max} Bottom (K)	Empty	372	371	373	371	372	372	370	370
	Full	291	301	291	300	291	291	291	291
	Half	291	301	291	301	291	291	291	291

Table 2.5 shows that all of the full tank spanwise and chordwise results are within one degree of each other. This small discrepancy can be attributed to discrepancies in the calculations caused by the slightly different geometries. Similarly, the bottom surfaces of the half-full analyses behave in the same manner as the corresponding full tank cases, and the results for spanwise and chordwise analyses differ by only a single degree, again due to numerical error.

The empty tank cases show differences of just over a degree. This increase in discrepancy is attributed to higher temperatures in comparison to the full tank results, causing the geometry-induced error to become more apparent. The only results that are actually different for the two sets of directional analyses are the top surface temperatures away from the joint in the half-full tank, shown in bold in Table 2.5.

In these analyses, through both the aluminium and CFRP skin, the spanwise temperatures are three to four degrees higher than the chordwise results. These discrepancies are a result of the influence of the joint region in the spanwise analyses. The chordwise analyses have constant properties over the wingbox width, and therefore, cannot be influenced by what is occurring at the joint. The effect of this influence in the spanwise analyses is only apparent on the top surface of the half-full tank case because it is the only case where the heat sink is present, and yet far enough from the top surface for an interaction to occur between the joint heat transfer and the heat transfer through the skins. In the empty tank, the air acts as an insulator, so heat is not effectively removed from either the skin or joint regions. In the full tank, the fuel is a big enough heat sink to draw the heat away from the joint region before any interaction can occur. In the half-full case there is a horizontal temperature gradient along the width of the spanwise analysis caused by the presence of the fuel in the lower half

of the tank, which results in interaction between the joint region and the skin regions away from the joint.

This can be better understood by examining the chordwise results through and away from the joint for the half-full case. It is evident that the temperatures through the joint are higher than the temperatures through the skin alone, because of the high conductivity of the aluminium and the insulating ability of the air at the internal surface, as discussed in the previous sections. In other words, the empty portion of the tank slows the heat transfer to the fuel, and as such traps the heat in the joint region. In the spanwise analysis, this heat trapped in the joint region makes use of the lower temperature area in the skin regions to help cool the joint region. This results in the skins having an increased temperature in the spanwise analysis when compared to the chordwise analysis, where no other gradient influences are present. Despite these small discrepancies, it is evident from Table 2.5, that the differences between the spanwise and chordwise results are small. This means that either 2D model is adequate at describing the heat transfer problem.

2.4.4 Effect of Titanium Pins

The study of titanium pins in the model is included to gain a better understanding of the temperature profiles for an aluminium double-lap joint fastened with titanium pins, as in the current case. It is necessary to recognize the impact of such fasteners on the overall heat transfer and temperature profiles in the wingbox. The material properties, as depicted in Figure 2.9 by the red elements, are changed to titanium, and the emissivity of titanium is included to determine the cavity radiation for the internal tank surfaces associated with the pins. The temperature profiles remain much the same and the effect of the pins is small. The FE temperature profiles show slight variations in the surface temperatures. An example is given in Figure 2.25 for the chordwise direction, full tank case in the joint region with aluminium skin. The empty and half-full cases do not show the same degree of variation across the surface of the FE profiles, but a change in the maximum temperatures is observed. Figure 2.26 represents an FE profile through a half-full tank case in the spanwise direction.

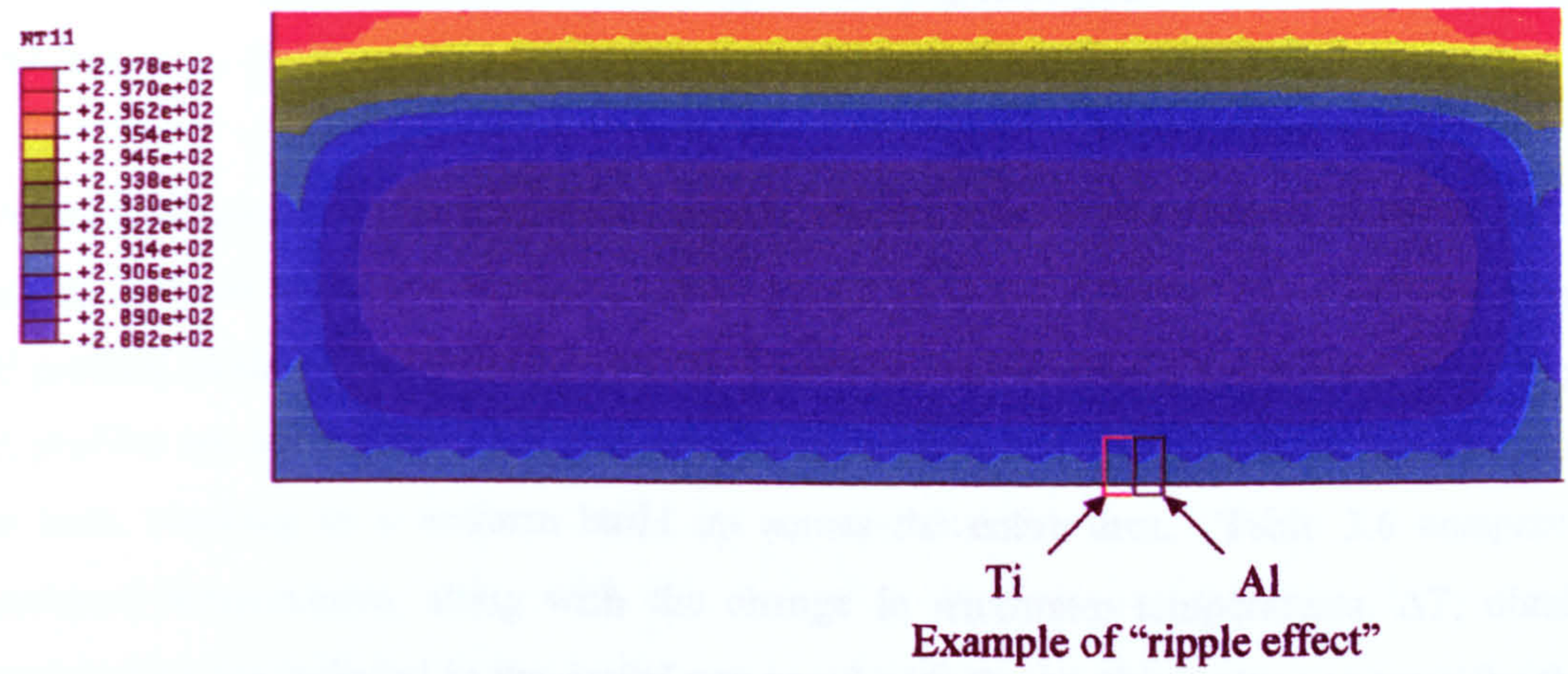

Figure 2.25. Effect of titanium pins through the aluminium skin side of the joint for a full tank at 1400 (2pm).

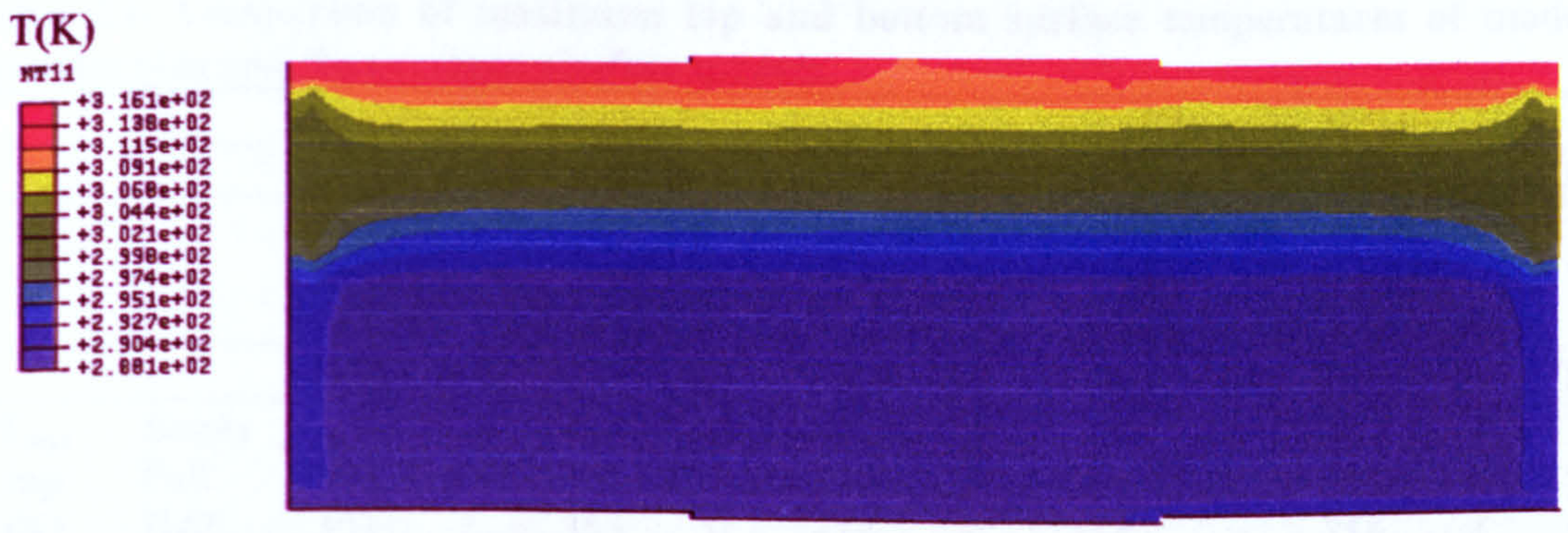

Figure 2.26. Effects of titanium pins in the spanwise model for a half-full tank at 0700 (7am).

From Figure 2.25, it appears that the aluminium skin builds up more heat than the titanium pins, as represented by the ripples in the FE temperature profiles. Although the titanium pins appear to alter the FE profiles in the full-tank cases, the overall effect on the maximum temperatures in these analyses is minimal. The maximum temperatures are generally altered by less than a degree. The ripples in the full tank temperature profiles are due to the fact that the emissivity of the aluminium is nearly 30% greater than that of titanium. By Kirchhoff's identity [87], emissivity is equal to absorptivity for non-transmitting solids. This implies that the inverse relationship of emissivity to surface temperature results in a greater influx of heat on the aluminium lap elements as compared to the titanium elements. This difference is made noticeable by the heat-dissipating effects of the fuel at the internal surfaces. The temperature difference is further increased by the difference between the conductivity of aluminium and titanium. The conductivity of aluminium is an order of magnitude

greater than that of the titanium, which means that at a given position through the thickness, the temperature change in the aluminium is significantly greater than that of the titanium for the same heat flux.

The titanium pins have the greatest impact on the maximum temperatures in the empty tank cases and top surfaces of the half-full cases, even though their individual effects are not as apparent in the FE profiles, as shown in Figure 2.26 by the more even distribution across the surfaces. Ripples in the FE profiles are not observed in these cases because the air at the internal surface does not dissipate the heat, resulting in a uniform build up across the entire area. Table 2.6 compares the new maximum temperatures, along with the change in maximum temperatures, ΔT, obtained when titanium pins are included in the model compared with the maximum temperatures for the previous pin-free models.

Table 2.6. Comparison of maximum top and bottom surface temperatures of models with titanium pins and the previous pin-free models.

		Away from Joint *				Through Joint							
		Spanwise Analysis				Spanwise Analysis				Chordwise Analysis			
		Al skin side		CFRP skin side		Al skin side		CFRP skin side		Al skin side		CFRP skin side	
		T(K)	ΔT	T(K)	ΔT	T(K)	ΔT	T(K)	ΔT	T(K)	ΔT	T(K)	ΔT
T_{max} top (K)	Empty	377	1	374	0	377	*2*	377	*2*	377	*4*	378	*4*
	Full	296	0	311	0	296	0	297	1	296	0	296	0
	Half	352	1	355	0	354	*2*	354	*2*	356	*4*	356	*5*
T_{max} bottom (K)	Empty	373	1	372	0	373	1	373	1	372	*3*	373	*3*
	Full	291	0	301	0	291	0	292	1	291	0	292	1
	Half	291	0	301	0	291	0	292	1	291	0	292	1

*Chordwise analysis is omitted from this table since the FE model contains no Ti material, and therefore no results are obtained for comparison.

Table 2.6 indicates that the titanium pins have the largest impact on the temperatures in the joint region, as expected. They also have a slight effect on the temperatures in the aluminium skin away from the joint for the empty and half-full tank cases. The increase in the empty tank temperatures is caused by the increase in temperature through the joint, because of a greater accumulation of heat due to the lower conductivity of titanium in comparison to aluminium, as was the case for the CFRP skin. The lower emissivity of the titanium compared to aluminium further increases maximum temperatures.

The decrease in temperatures observed through the aluminium skins in the half-full tank case suggests that, although the joint temperatures increase, the horizontal temperature gradient does not change proportionally. Although the titanium pins cause an increased build up of heat in the joint, this build up is more evenly distributed through the joint thickness due to slower conduction of heat in the pin areas. This is different than the more concentrated accumulation of heat at the internal surface in the pin-free case. This more even distribution causes a lower horizontal temperature gradient along the width, explaining the lower aluminium skin temperatures.

The fact that the empty tank temperatures increase, while the half-full tank temperatures decrease, is directly related to the efficiency of the heat sink within the tank. In both cases, the titanium reduces the concentration of heat at the internal surface, and lowers the horizontal temperature gradient. In the empty tank case, because air is poor at dissipating heat, an increase in maximum temperature is observed. In the half-full tank the fuel is more efficient at removing the heat from the internal skin surface. With an increase in the amount of heat at the internal surface created by the titanium pins, a decrease in temperature occurs caused by the efficiency of fuel at removing heat. These effects are not seen in the CFRP skin because the heat does not build-up at the internal surface in the same manner as in the aluminium skin. As shown previously, the CFRP skin is less affected by the lowered horizontal temperature gradient.

In the joint region itself, the titanium pins have the greatest impact when air is the material on the internal surface. Then the empty tank case temperatures and half-full case top temperatures are increased by approximately three degrees. The increase is again due to lower conductivity of titanium in comparison to aluminium. These increases do not have a large impact on the more global temperature profiles. It is interesting to note that the chordwise analyses through the joint produce an increase in ΔT that is approximately double that of the spanwise analyses. This emphasizes the cooling effects of the skins away from the joint in the spanwise analyses, as recognised in the previous pin-free analyses. Because the chordwise model cannot make use of such alternative heat paths, its temperatures are higher. The effects of pins on the full tank case and the bottom temperature of the half-full case are much less pronounced and not considered noteworthy given the uncertainties associated with numerical analyses and the convection heat transfer coefficients.

2.5 Global Heat Transfer Model Summary

The influence of each mechanism of heat transfer, conduction, convection, and radiation are studied individually in empty, full, and half-full fuel tank cases over the course of a very hot, dry, twelve-hour day. ABAQUS is used to perform spanwise and chordwise FE analyses of a wingbox structure. In every analysis, the maximum wingbox temperatures occur on the top skin, which is expected given the greater impact of solar flux in comparison to ground flux. In most of the analyses, the top surface is hotter than the bottom skin up until a reversal time, generally around 1500h (3pm), when the impact of the ground flux outweighs the solar flux and the bottom surface becomes hotter.

The simplest form of analysis involves conduction as the only method of heat transfer through the tank. Not surprisingly, the empty tank results have the highest temperatures. The poor conductivity of air causes the air to act as an insulator on the internal skin surfaces. The next type of analysis includes the effects of natural convection within the tank. This inclusion has an impact on the maximum temperature observed especially for the full tank case, due to the large convection heat transfer coefficients of fuel, which dramatically reduce the tank temperatures by providing a heat sink to remove incoming heat energy. The final analysis includes radiation-only within the tank. When compared with the conduction-only analysis, the greatest temperature changes are observed in the empty tank model. These results are explained by the fourth-order-effects of radiation. Because the empty tank has the largest difference between surface and sink temperatures, the fourth-order power of these temperatures increases this difference, which in turn increases the effects of radiation. These analyses with a single internal boundary condition are followed by an analysis using all heat transfer mechanisms or "combined" analysis. This analysis demonstrates that in order to obtain a realistic and accurate temperature prediction model, it is necessary to include the internal boundary conditions of natural convection and cavity radiation. The results are similar to those of the individual cases, with radiation having the greatest influence in the empty tank, the full tank behaving more like the convection-only case, and the half-full tank being a combination of the two.

In the empty tank case, the combined analyses shows a reduction in the maximum temperatures compared to individual analyses' results. Convection and radiation act by superposition to reduce the temperatures of the conduction-only values. Radiation is the major influence in these temperature profiles, especially before the reversal time, where it makes up approximately 75% of the combined analyses' profiles. Convection plays a significant role, particularly after the reversal time, when the

temperature gradient changes from top-down to bottom-up. The contribution of natural convection within the tank is significant. The reversal time occurs around 1530h (3:30pm) for all results of studies with aluminium material, as well as results through the joint on the CFRP skin side, but at approximately 1400h (2pm) for studies on the CFRP skin. This time delay in the aluminium studies is explained by aluminium's capability to build up a heat store, requiring a longer time to dissipate the heat from the top internal surface. Because the CFRP skin does not tend to build up heat in the same manner due to its lower conductivity, its top and bottom skin temperatures are more directly influenced by the external fluxes, thereby explaining the earlier reversal time.

The empty tank case suffers the highest maximum skin temperatures, up to approximately 377K or 104°C and 373K or 100°C on the top and bottom aluminium skins with no titanium pins, respectively. These high temperatures are due to the insulating characteristics of the air in the tank. The inclusion of titanium pins with 1d spacing elevates the empty tank temperatures by a few degrees. The maximum temperatures on the top and bottom surfaces of the CFRP skin side of the joint are approximately 378K or 105°C and 373K or 100°C, respectively. Only the top surface temperature changes significantly from that of the pin-free model, increasing nearly four degrees.

In the full tank case, the maximum temperatures observed on the top and bottom CFRP skins are approximately 311K or 38°C and 301K or 28°C, respectively, with the aluminium skin temperatures remaining near 288K or 15°C. The CFRP has less ability to conduct the heat energy through to the heat sink, thereby resulting in higher maximum temperatures. Convection is the primary mechanism of heat transfer, making up over 99% of the heat transfer of the combined temperature profiles. The influence of titanium pins is insignificant in the full tank temperature profiles because the fuel heat sink is large enough to dissipate any additional energy.

The maximum temperatures for the half-full case also occur through the CFRP skins, with a top skin temperature of approximately 355K or 82°C and a bottom skin temperature of approximately 301K or 28°C. Radiation plays a major role in the top half temperatures, while convection dominates the bottom half. The effects of the titanium pins are only evident on the top surface. Because the bottom surface behaves similarly to the full tank case, there is no significant influence of the titanium pins on the temperatures. However, the titanium pins increase the maximum temperatures on the CFRP skin side of the joint to 356K or 83°C, a difference of just over four degrees from the pin-free model.

The effects in spanwise and chordwise directions are also examined using two different models under combined boundary conditions. The only significant differences between the two are observed in the top surface skin temperatures of the half-full tank case. The spanwise analyses produces temperatures about four degrees higher in the half-full tank resulting from the horizontal heat gradient caused by the joint region. The heat moving through the joint uses up some of the limited heat sink available at the internal surface, decreasing the amount of heat removed from the skins. Table 2.7 and Table 2.8 summarize the results of all the combined convection-radiation analyses.

Table 2.7. Comparison of maximum top and bottom surface temperatures in the spanwise direction with and without titanium pins.

		Away from Joint				Through Joint			
		Al Skin		Comp Skin		Al Skin Side		Comp Skin Side	
		T (K) No Ti	T (K) Ti	T (K) No Ti	T (K) Ti	T (K) No Ti	T (K) Ti	T (K) No Ti	T (K) Ti
T_{max} top	Empty	376	377	374	374	375	377	375	377
	Full	296	296	311	311	296	296	296	297
	Half	353	352	354	355	352	354	352	354
T_{max} bottom	Empty	372	373	371	372	372	373	372	373
	Full	291	291	301	301	291	291	291	292
	Half	291	291	301	301	291	291	291	292

Table 2.8. Comparison of maximum top and bottom surface temperatures in the chordwise direction with and without titanium pins.

		Away from Joint				Through Joint			
		Al Skin		Comp Skin		Al Skin Side		Comp Skin Side	
		T (K) No Ti	T (K) Ti	T (K) No Ti	T (K) Ti	T (K) No Ti	T (K) Ti	T (K) No Ti	T (K) Ti
T_{max} top	Empty	377	-	374	-	373	377	374	378
	Full	296	-	309	-	296	296	296	296
	Half	351	-	350	-	352	356	352	356
T_{max} bottom	Empty	373	-	371	-	370	372	370	373
	Full	291	-	300	-	291	291	291	292
	Half	291	-	301	-	291	291	291	292

Based on good comparison with previous work [10] and Airbus UK© experimental results under similar conditions [21], the 2D models appear to adequately describe the heat transfer problem in both primary directions, providing an effective recognition of 3D real-life circumstances.

Chapter 3 Analytical Models

Although FE is common practice, analytical models are another popular method of solution for heat transfer methods. As well as improve confidence in the numerical results, analytical models offer additional physical insight into heat transfer problems. A number of analytical solution methods have been proposed for boundary conditions ranging from more simple constant temperature or flux conditions at the surface to the more complex convection and radiation conditions, as well as including combinations of such conditions. Each model is applicable to a given set of boundary conditions and plate geometry only, making the analytical analysis more cumbersome than FE. In the current case, analytical modelling is performed using two methods of solution to study the heat transfer though the skin and joint regions using a single layer model and multiple layer model, as shown in Figure 3.1. These areas are chosen for more detailed study based on the results of the Global Heat Transfer Analyses of Chapter 2.

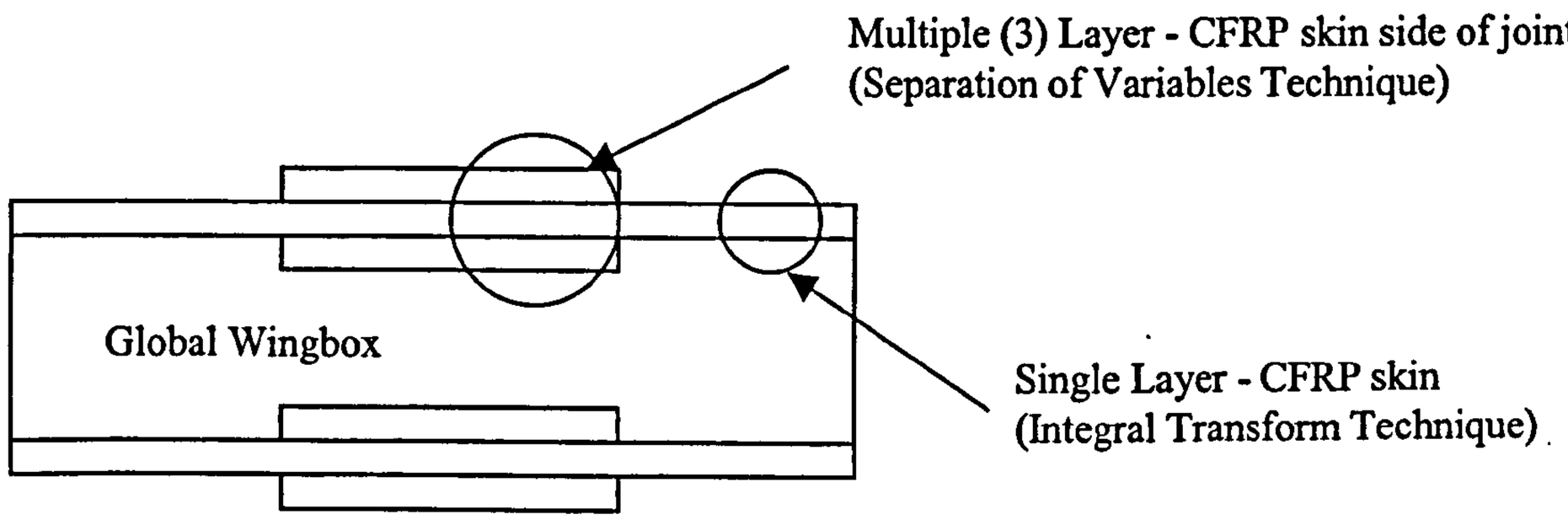

Figure 3.1. Areas of detailed analytical analysis.

The models are first developed for convection boundary conditions at both the external and internal surfaces, based on previous work [12]-[15]. Although these heat transfer conditions are well known, due to the complexity of modelling convection boundary conditions for finite geometry, little work containing fully developed models for such conditions is found in the open literature. The current work then builds on these convection conditions and further develops the models to study the effects of radiation at the boundaries as well. No work was found in the open literature containing models including the effects of radiation at the external surfaces. Finally, a novel approach allows for the study of combined convection and radiation boundary conditions.

Section 3.1 discusses the single layer model through the CFRP skin using the integral transform solution method, which is developed from the separation of variables method, and is broken down into 3.1.1 containing convection boundary conditions, 3.1.2 containing radiation boundary conditions, and 3.1.3 containing combined convection and radiation conditions. Section 3.2 moves on to the multiple layer model for the joint region with CFRP skin. The multiple layer model requires the use of separation of variables technique. The development of the equations for the separation of variables technique, with complex boundary conditions and finite geometry, is shown in 3.2.1. This method is then put to use with the multiple layer model itself in 3.2.2. Section 3.2.2 is broken down into convection (3.2.2.1), radiation (3.2.2.2), and combined (3.2.2.3) conditions. Finally, Section 3.3 discusses the analytical model conclusions.

3.1 Single Layer Model

The simplest geometry, a single layer, allows for the use of the integral transform method of solution, which Ozisik [1] describes as the most elegant solution technique for heat transfer problems. This was deemed as the best starting point for analytical solution as it offers an introduction to heat transfer modelling, is more efficient than separation of variables for a single layer. Separation of variables serves as the basis for the integral transform solution method. Appendix 3A describes the basic formulation of the separation of variables technique, while Appendix 3B continues with the integral transform method. Appendix 3C contains further details on Green's Theorem used in the development of the integral transform method. This work commences with convection conditions, then further develops the boundary conditions to account for radiation, and finally combines convection and radiation.

3.1.1 Convection Boundary Conditions

Convection boundary conditions are the most complex conditions in the open literature for plates of finite boundaries. This forms the starting point for analytical modelling of the wingbox geometry. Integral transforms are used to obtain steady-state and transient solutions for temperature through the skin. The general problem for the single layer model under convection boundary conditions is illustrated in Figure 3.2.

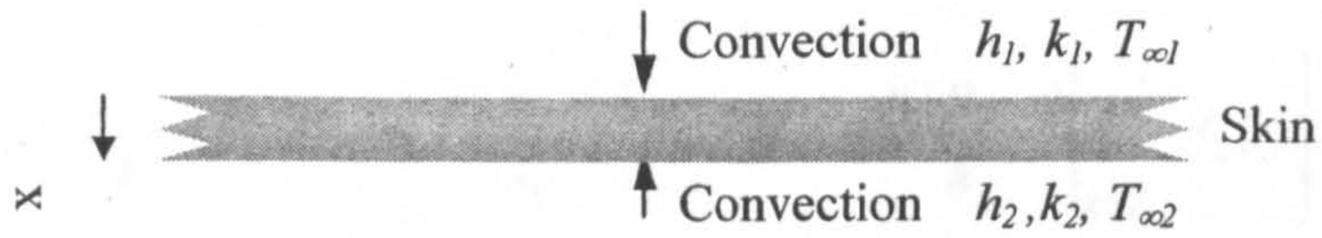

Figure 3.2. Single layer heat transfer problem.

The Fourier Heat Transfer Equation is used to describe the above problem, such that:

$$\frac{\partial^2 T(x,t)}{\partial x^2} + \frac{g(x,t)}{k} = \frac{1}{\alpha}\frac{\partial T(x,t)}{\partial t} \quad \text{in } 0 \le x \le L, t > 0 \tag{3-1}$$

Here x is through-thickness dimension, t is time, g is internal heat production, k is conductivity, and α is thermal diffusivity. The boundary and initial conditions for the above problem are:

$$-k_1(t)\frac{dT}{dx} + h_1(t)T = h_1(t)T_{\infty 1}(t) \qquad \text{at } x=0 \tag{3-2}$$

$$k_2(t)\frac{dT}{dx} + h_2(t)T = h_2(t)T_{\infty 2}(t) \qquad \text{at } x=L \tag{3-3}$$

$$T = T_i \qquad \text{at } 0 \le x \le L, t = 0 \tag{3-4}$$

The skin is considered a homogeneous material, making k_1 and k_2 equal. The convection heat transfer coefficients at the external surfaces, the sink temperatures, and the conductivity are kept as constant values throughout the analysis. Because the skin is relatively thin (12mm), and the aforementioned variables constant, a steady-state condition is rapidly achieved. Therefore, analysis times of 30s, 300s (5min), and 3600s (1hr) are used to study transient heat transfer through the CFRP skin. From Appendix 3B, the general solution for heat transfer through a single layer using the integral transform technique is:

$$T(x,t) = \sum_{m=1}^{\infty} e^{-\alpha\beta_m^2 t} K(\beta_m, x)\left[\overline{F}(\beta_m) + \int_{t'=0}^{t} e^{\alpha\beta_m^2 t'} A(\beta_m, t')dt'\right] \tag{3-5}$$

Within this solution:

$$A(\beta_m,t)=\frac{\alpha}{k}\bar{g}(\beta_m,t)+\alpha\left[\left.\frac{K(\beta_m,x)}{k_1}\right|_{x=0}\cdot f_1(t)+\left.\frac{K(\beta_m,x)}{k_2}\right|_{x=L}\cdot f_2(t)\right] \tag{3-6}$$

$$\bar{T}(\beta_m,0)=\int_{x'=0}^{L}K(\beta_m,x')F(x')\equiv\bar{F}(\beta_m) \tag{3-7}$$

From Ozisik[1], for the conditions described by equations (3-2) to (3-4), the kernel, $K(\beta_m,x)$, is given by:

$$K(\beta_m,x)=\sqrt{2}\frac{\beta_m\cos(\beta_m x)+H_1\sin(\beta_m x)}{\left[\left(\beta_m^2+H_1^2\right)\left(L+\frac{H_2}{\left(\beta_m^2+H_2^2\right)}\right)+H_1\right]^{1/2}} \tag{3-8}$$

The solution of the eigenvalues, β_m, are the positive roots of the transcendental equation:

$$\tan(\beta_m L)=\frac{\beta_m(H_1+H_2)}{\beta_m{}^2-H_1H_2} \tag{3-9}$$

Here, H represents the ratio of the heat transfer coefficient, h, to the conductivity, k, of a surface. In the present analysis, the Newton-Raphson method is used to simultaneously solve the tangent (left-side) and hyperbolic (right-side) parts of equation (3-9). The eigenvalues, β_m, can be derived from the intersection points of the cotangent and hyperbolic curves as described by the boundary conditions, an example of which is depicted in Figure 3.3. The inverse of equation (3-9) is used, since the cotangent curves are simpler to plot. The new variables $\xi_m=\beta_m L$ and $B\equiv {}^{hL}/_{k}=HL$, where B is also known as the Biot number, are defined to simplify the problem.

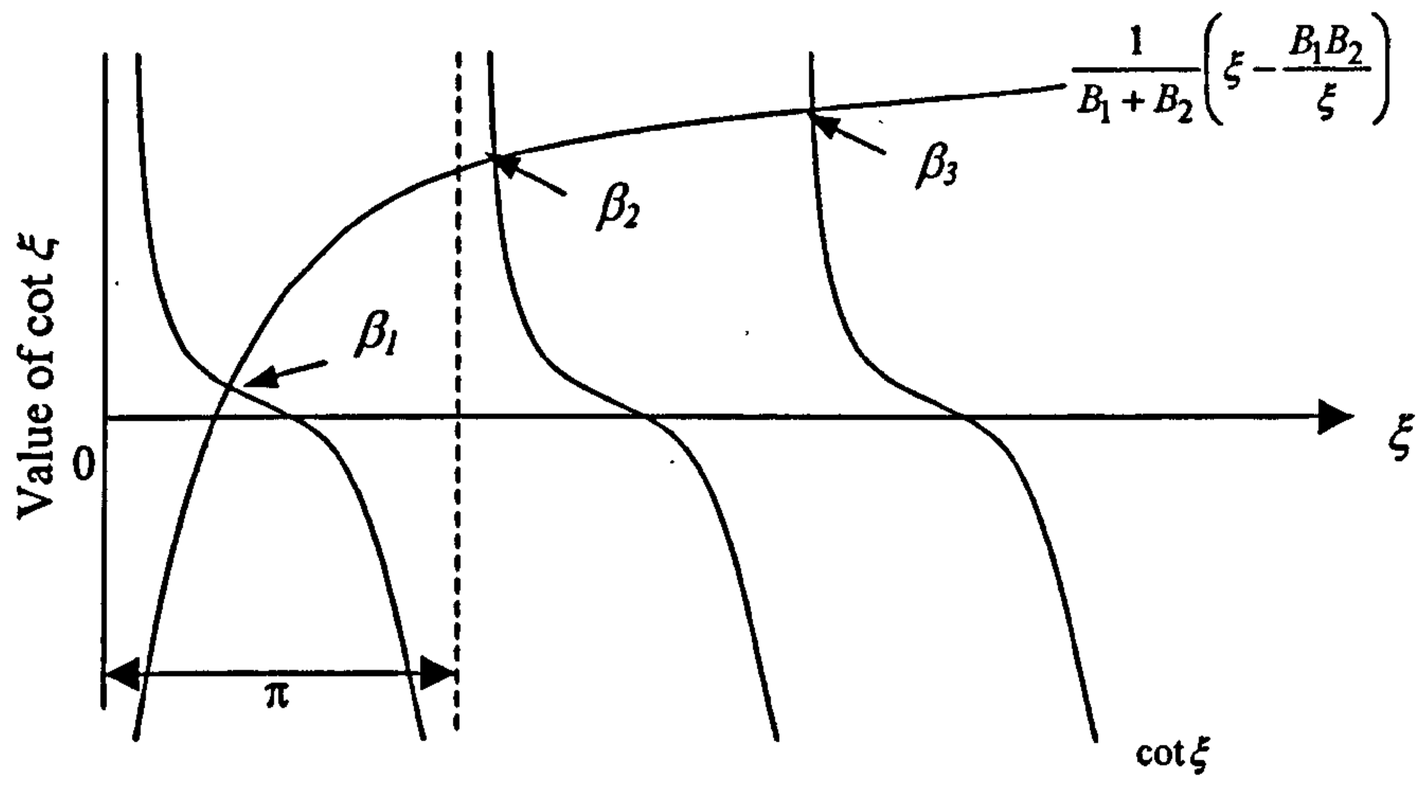

Figure 3.3. Geometrical determination for roots of the transcendental equation (3-9).

Under third-order boundary conditions of convection to the environment on both top and bottom of the skin, and with the assumptions stated above, the analytical equation developed to describe the temperature profile through the skin is as follows:

$$T(x,t)=\sum_{m=1}^{\infty}\frac{2(\beta_m\cos(\beta_m x)+H_1\sin(\beta_m x))}{\left[\left(\beta_m^2+H_1^2\right)\left(L+\frac{H_2}{\left(\beta_m^2+H_2^2\right)}\right)+H_1\right]}\cdot\left\{\begin{array}{l}T_i e^{-\alpha\beta_m^2 t}\cdot\left(\sin(\beta_m L)-\frac{H_1}{\beta_m}\cos(\beta_m L)+\frac{H_1}{\beta_m}\right)+\\ \left(1-e^{-\alpha\beta_m^2 t}\right)\left(\frac{H_1T_{\infty 1}}{\beta_m}+\frac{H_2T_{\infty 2}}{\beta_m^2}\left[\beta_m\cos(\beta_m x)+H_1\sin(\beta_m x)\right]\right)\end{array}\right\} \tag{3-10}$$

In order to validate the model, FE results of identical geometry and material properties and midplane temperature estimations, are obtained using the Heisler chart [2]. Heisler charts are experimentally based trendlines for specific boundary conditions. Heisler performed a number of experiments with different plate dimensions and boundary conditions. The results are then interpolated to form diagrams for a complete set of conditions. In the current case, the chart for a thin plate with infinite width and convection conditions at both plate surfaces is used for comparison with the analytical results. The limiting conditions of the Heisler chart are that for convection to occur at both plate surfaces, the boundary conditions on the external and internal surfaces must be identical. In other

words, h_1 and h_2 are equal, as are $T_{\infty 1}$ and $T_{\infty 2}$. ABAQUS is used to perform the FE analysis. The 2D FE model consists of three DC2D8 heat transfer elements through the thickness, and ten elements along the width, to prevent edge effects. These are the same two-dimensional quadratic heat transfer elements used in the previous chapter. All measurements are made at the centre of the plate. The properties used in the various analyses are shown in Table 3.1.

Table 3.1. Heat transfer properties.

	k (W/mK)	h_1 (W/m^{2}K)	h_2 (W/m^{2}K)	T_o (K)	$T_{\infty 1}$ (K)	$T_{\infty 2}$ (K)	$T_{\infty 1r}$ (K)	$T_{\infty 2r}$ (K)
Condition 1	0.81	5	5	288	328	328	-	-
Condition 2	0.81	8	2	288	328	369	-	-
Condition 3	0.81	8	2	288	*T_{air}	**$T_{internal}$	-	-
Condition 4	0.81	5.52	5.52	288	-	-	296	369
Condition 5	0.81	12.71	6.71	288	328	369	312	312

* $T_{air} = at^4 + bt^3 + ct^2 + dt + e$; a fourth order polynomial used to represent plot in Figure 2.2, where a-e are constants.

** $T_{internal} = at^4 + bt^3 + ct^2 + dt + e$; a fourth order polynomial used to represent plot in Figure 2.2, where a-e are constants.

Notes:

Condition 1= Identical convection conditions at both surfaces to compare to Heisler Charts
Condition 2= Convection Conditions
Condition 3= Transient Convection Conditions
Condition 4= Radiation Conditions
Condition 5= Combined Convection-Radiation Conditions

Although the Heisler charts are quite straight forward, and their use is well established, they are rather limited in applicability. Simple Heisler charts can only be used to estimate the mid-plane temperature at a given time in the analysis. This generally results in a lower degree of accuracy because the user must interpolate from the charts. Furthermore, the use of Heisler charts is restricted to a specific class of boundary conditions. Whilst the Heisler chart is limited to identical boundary conditions on both sides of the finite plate, the current analytical model has the capability to include different boundary conditions at each edge. FE models are also a popular method of conducting heat transfer analysis, and it is generally accepted that the results of such analysis can be used for design purposes. The developed analytical model serves to verify the results from FE models, while providing an alternative method of obtaining temperature profiles through a solid, under convection boundary condition.

A comparison of the three methods for convection boundary conditions at both surfaces, as described by equation (3-10), are shown in Figure 3.4. Appendix 3D shows a Fortran program produced for

analytical solution with more complex boundary conditions, but which is similar in form to that used in the current case.

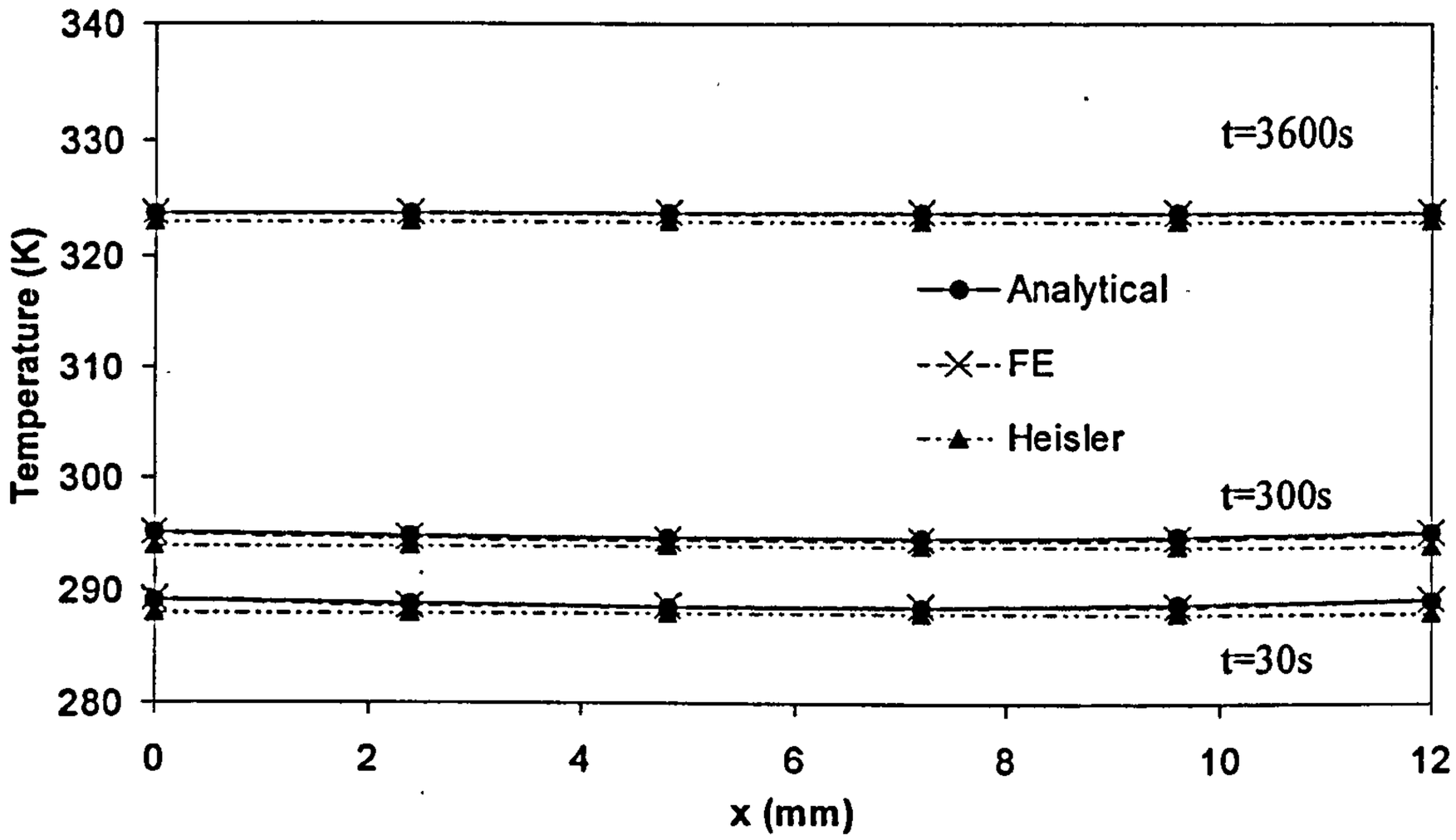

Figure 3.4. Comparison of Analytical, FE, and Heisler chart temperature prediction through the CFRP skin for convection boundary conditions at both surfaces.

It is evident from Figure 3.4 that all three models compare favourably. The analytical and FE models are almost identical, while the Heisler chart method under predicts slightly the temperature each time, due to the error associated with the user interpolation of the charts.

The two main sources of error associated with the analytical model are the series truncation and the calculation of the β_m values. An infinite series, in theory, provides exact temperature values, while a shorter, truncated series provides an approximation of the temperature. Obviously, the trade off is accuracy for computing time. Fortunately, the evaluation of equation (3-10) is straightforward. Therefore, the effect of the number of terms in the series can be studied. Table 3.2 shows a comparison of the results calculated using m terms in the series with those found by FE analysis at a given time.

Table 3.2. Error associated with truncation of the series after *m* terms.

	FE T(K)	m=5 T(K)	m=50 T(K)	m=100 T(K)	m=500 T(K)	M=1000 T(K)	m=10000 T(K)
t=30s	289.2	288.25	289.12	289.17	289.21	289.22	289.22
t=300s	295.2	294.28	295.25	295.20	295.24	295.25	295.25
t=3600s	323.8	322.88	323.75	323.80	323.84	323.84	323.84

From Table 3.2, it appears that terms in excess of m=1000 do not contribute to the accuracy of the analytical results. The values for m=100 appear to be the closest match to the FE values, suggesting that the FE analysis may also contain error due to truncation. Given these results, the analytical method has the potential for a higher degree of accuracy if the series contains an appropriate number of terms. Thus, for future analytical models, m=1000 is used. The computing times associated with this number of series terms is approximately five minutes on a Unix-based 5GPa machine, which is approximately 50% longer than the FE analyses.

The second source of error, the calculation of the β_m values, has a major impact on the accuracy of the results. Due to the ill conditioning of the transcendental equation (3-8), it is necessary to solve the β_m values using double precision accuracy. Because of the sensitivity of the equation, the approximation of a series for the calculation of the terms containing cosine or sine by the numerical solver results in error. Perfect convergence of the solutions cannot be reached, regardless of the number of terms used in the series. However, the margin of error is minute, and is not expected to be significantly greater than the numerical error associated with FE analysis.

Having gained confidence in the analytical model's capabilities, different values for the coefficients are implemented at each surface. This capability surpasses the limitations of the Heisler charts. Therefore, the only method for comparison is FE analysis. The heat transfer coefficients and sink temperatures are different at each surface, similar to the wingbox heat transfer coefficients. These values are still held independent of time. Heat transfer coefficients of h_1=8W/m^{2}K and h_2=2W/m^{2}K and sink temperatures of $T_{\infty 1}$=328K and $T_{\infty 2}$=369K are used on the top and bottom surfaces, representing sky and internal temperature from Condition 2 of Table 3.1, respectively. Figure 3.5 shows a comparison with FE results.

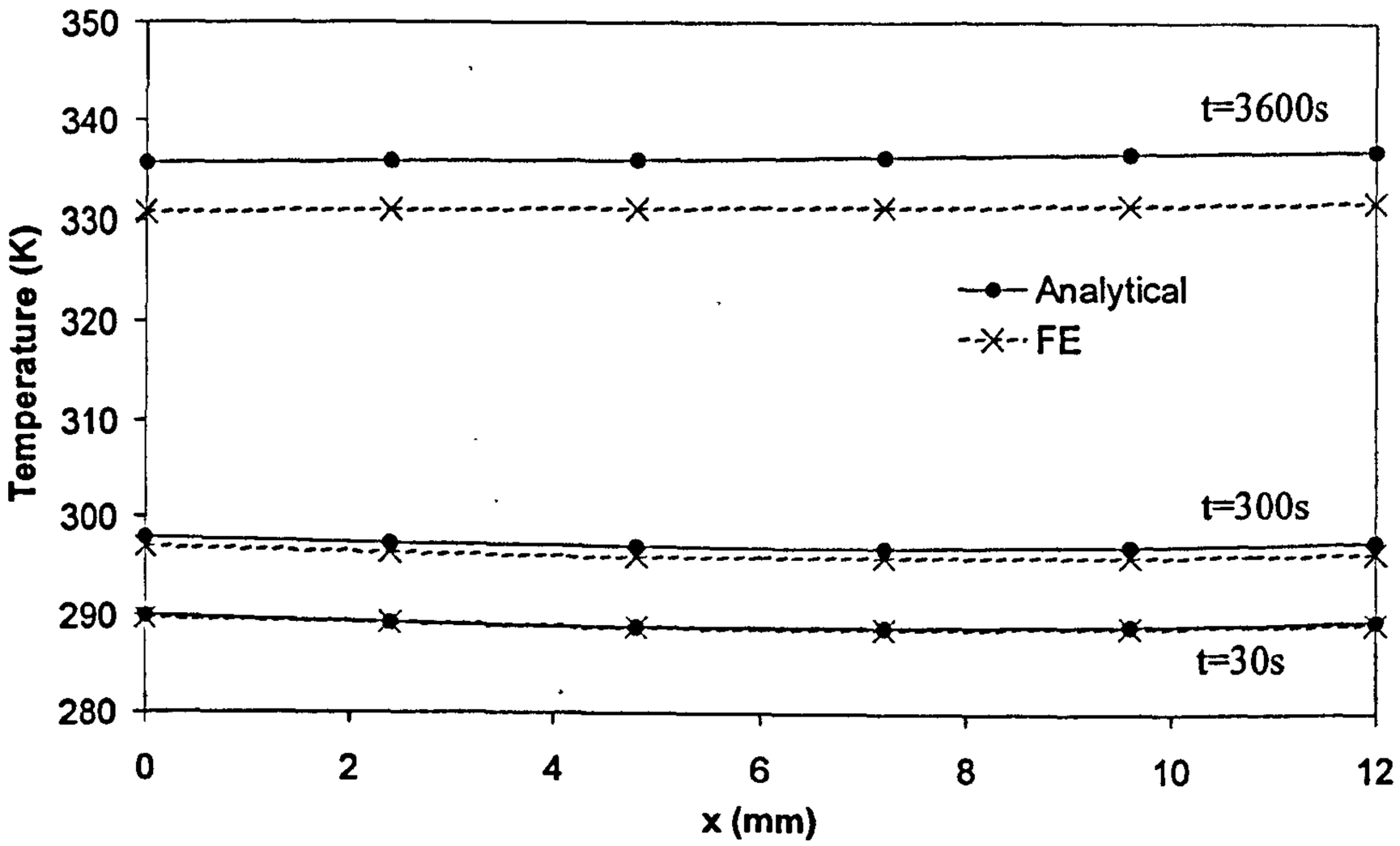

Figure 3.5. Comparison of analytical and FE temperature prediction through the skin for convection boundary conditions at both surfaces.

The differences between the analytical results and the FE results are more profound than in the previous case. The discrepancy appears to grow as the time increases, to a maximum difference of approximately five degrees at steady state (time=3600s). This mounting difference in values is due to the ill conditioning of the transcendental equation used to obtain the eigenvalues, β_m. The effects of this ill conditioning are magnified in the exponential nature of the function $\left(1-e^{-\alpha\beta_m^2 t}\right)$ with increased time.

The effects of this ill conditioning are less evident when the sink temperatures are the same on both surfaces because the hyperbolic form of the transcendental equation can be reduced to the form, $\frac{1}{2}\left(\frac{\xi}{B}-\frac{B}{\xi}\right)$. This reduction improves the mathematical stability of the solution of the transcendental equation, resulting in less variation in the equation for small changes in the eigenvalues. The greater the difference between the sink temperatures and heat transfer coefficients at the external surfaces, the greater the effect of the ill conditioning. The increased ill conditioning results in an increase in the number of required significant figures in order to reach an acceptable level of convergence. Even with double precision, truncation errors occur in the eigenvalues under these conditions. This leads

to the analytical results being higher than the FE results, and an increase in time increases the discrepancy to a maximum, in this case, of approximately five degrees, at steady state.

Although the difference in results is greater under these boundary conditions, a maximum value is reached. Even at this worst-case scenario, the discrepancy is still within 5%, and given the uncertainty associated with the heat transfer coefficients used, as well as the error involved in the FE analysis, this certainly falls within an acceptable range. The fact that this model over-predicts the temperatures should not be considered inaccurate, particularly where 'worst case scenarios' are the desired conditions of study.

In order to make the analysis more similar to the actual conditions experienced by the wingbox, the next step involves the variation of $T_{\infty 1}$ and $T_{\infty 2}$ with time. The convection heat transfer coefficients are held constant with respect to time because, as proven in the global wingbox FE analyses of Chapter 2, variation of these parameters with time has negligible effect on the temperature profiles. The adapted version of equation (3-10) accommodates varying sink temperatures over the course of the day and is given by:

$$T(x,t)=\sum_{m=1}^{\infty}\left\{\begin{array}{l} T_i e^{-\alpha\beta_m^2 t}\cdot\left(\sin(\beta_m L)-\dfrac{H_1}{\beta_m}\cos(\beta_m L)+\dfrac{H_1}{\beta_m}\right)+ \\ \left(H_1\displaystyle\int_0^t T_{\infty 1}(t)e^{\alpha\beta_m^2 t}dt+H_2\left[\beta_m\cos(\beta_m x)+H_1\sin(\beta_m x)\right]\int_0^t T_{\infty 2}(t)e^{\alpha\beta_m^2 t}dt\right)\end{array}\right\} \quad (3\text{-}11)$$

$$\cdot\frac{2\left(\beta_m\cos(\beta_m x)+H_1\sin(\beta_m x)\right)}{\left[\left(\beta_m^2+H_1^2\right)\left(L+\dfrac{H_2}{\left(\beta_m^2+H_2^2\right)}\right)+H_1\right]}$$

The external sink temperature, $T_{\infty 1}(t)$, is assumed to be the air temperature, and is profiled in Figure 2.2. The internal sink temperature, $T_{\infty 2}(t)$, is taken as the internal temperature, also from Figure 2.2. Both sink temperatures are represented to an accuracy of 0.001 (R^2>0.99) with fourth-order polynomials. This approximation allows the integrals in equation (3-11) to be written in the form,

$$\int_0^t t^n e^{\alpha\beta_m^2 t}\,dt \tag{3-12}$$

where n represents the degree of the polynomial. The solution of equation (3-12), then becomes relatively straight-forward, although, somewhat tedious, as shown by:

$$\int_0^t t^n e^{\alpha\beta_m^2 t}\,dt = \frac{e^{\alpha\beta_m^2 t}}{\alpha\beta_m^2}\left(t^n - \frac{nt^{n-1}}{\alpha\beta_m^2} + \frac{n(n-1)t^{n-2}}{(\alpha\beta_m^2)^2} - \ldots \frac{(-1)^n n!}{(\alpha\beta_m^2)^n}\right) \tag{3-13}$$

In Figure 3.6, the temperatures for the top and bottom CFRP skin surfaces for an empty tank case, Condition 3 in Table 3.1, calculated with equation (3-11) are compared with FE results, where (t) represents the top surface, and (b) the bottom surface.

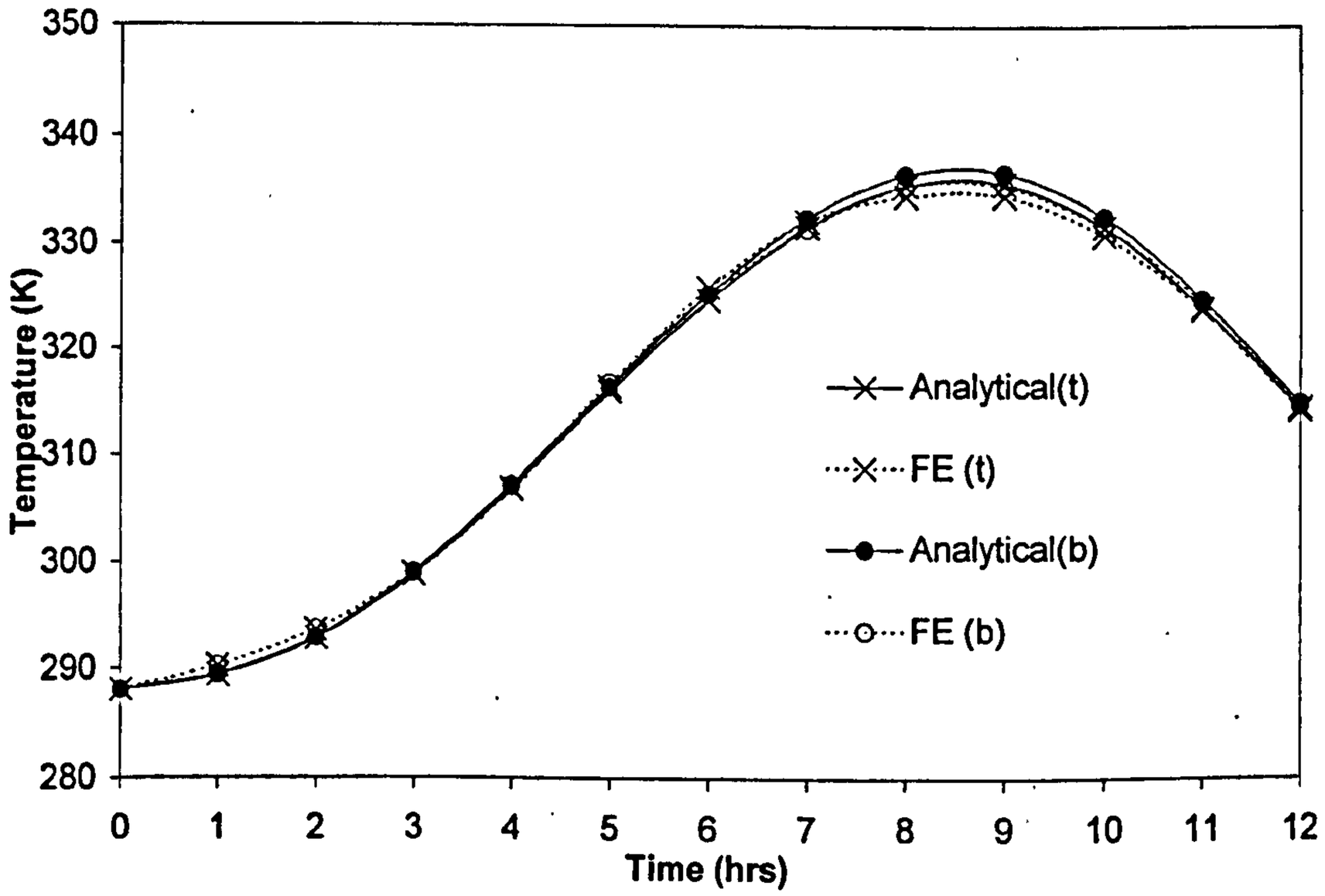

Figure 3.6. Comparison of Analytical and FE top (t) and bottom (b) skin surface temperatures for convection boundary conditions with transient sink temperatures.

The similarity between the FE and analytical results is apparent. It is also evident that there is little variation in temperature through the CFRP skin at any time. Maximum variation between the results occurs at maximum temperature. The analytical model over-predicts the maximum day temperatures

by about one degree, while at other times throughout the day, the differences between the two models are reduced to decimal places.

The errors involved in the FE results are standard errors found in any numerical analysis. The discrepancies associated with the analytical model are caused by two approximations. The first is the representation of the sink temperatures by a polynomial rather than the use of the exact temperatures, as in the FE analysis. The second error is again related to the calculation of the β_m values and the resulting series approximation for cosine and sine terms. The discrepancies seen in this graph for the analytical analysis are not believed to be a function of series truncation because, as mentioned previously, the inaccuracy of the values for series greater than 1000 terms is negligible.

3.1.2 Radiation Boundary Conditions

A new approach is adopted in order to include the effects of radiation boundary conditions. The previous analytical model given by equation (3-11) for convection boundary conditions is adjusted to include new approximations for radiation conditions. The fourth-order effects of radiation are linearised, and a transformed heat transfer coefficient is developed.

Zerkle and Sunderland [18] have summarised work done on transient radiation temperature prediction via analytical analyses. An equation given by Chapman [88] is proposed in order to obtain an approximate solution, if the heat flux at the slab surface is almost linear. In the case of radiation, it is suggested that when the ratio of the initial temperature to the sink temperature is greater than approximately 0.75, the treatment of radiation as a linear flux is valid. In other words, the radiation equation (1-4) becomes identical to the convection equation (1-3), but with the heat transfer coefficient defined according to the radiation conditions, such that equation (1-4) becomes,

$$q = h_R\left(T - T_\infty\right) \tag{3-14}$$

where h_R is the new radiation heat transfer coefficient. Jakob [89] also discusses the validity of this approximation and concludes that under the conditions specified above, this is an accurate representation of radiation conditions. Jaeger [90] suggests a quadratic approach be used. Jaeger's work, however, is limited to the behaviour of black bodies radiating to a medium at absolute zero, which makes a quadratic solution viable. Because the current wingbox is radiating to grey bodies at

both surfaces, a quadratic approach is not an accurate representation of the current problem. Therefore, linear conditions are assumed, based on the work by Zerkle and Sunderland [18], as well as Jakob [89].

First, the equation for a radiation-only boundary condition as given by equation (1-4) is modified to suit the form:

$$q = \sigma\varepsilon T_\infty\left(1-\left(\frac{T}{T_\infty}\right)^4\right) = \sigma\varepsilon T_\infty\left(1-\left(1-\frac{T}{T_\infty}-1\right)^4\right) \tag{3-15}$$

By letting $X=1-T/T_\infty$, equation (3-15) can be rewritten as:

$$q = \sigma\varepsilon T_\infty^4\left(1-\left(X-1\right)^4\right) \tag{3-16}$$

The full expansion of the term $(X-1)^4$ is given by:

$$\left(X^4-4X^3+6X^2-4X+1\right) \tag{3-17}$$

Studying the influence of each term in equation (3-17), shows that the first order term, $4X$, provides over 95% of the solution, for the conditions of $T_i/T_\infty > 0.75$ or, for the current case when $X = (1-T_i/T_\infty)$ such that $X<0.25$, is met. In the current problem, the maximum value for X is 0.22; thereby further justifying the assumption of approximately linear behaviour. Furthermore, the influence of the first term is found to grow as $X \Rightarrow 0$, improving the accuracy of approximating equation (3-17) using a single term. The equation for a radiation only boundary condition can then be rewritten as:

$$q = \sigma\varepsilon T_\infty^4\left(4X\right) = 4\sigma\varepsilon T_\infty^4 - 4\sigma\varepsilon T_\infty^3 T \tag{3-18}$$

Equation (3-18) can then be rewritten in the same form as for convection-only boundary conditions, such that the form of the radiation boundary condition, based on the aforementioned assumptions, is given by:

$$-k\frac{dT}{dx}+h_R T = h_R T_\infty \tag{3-19}$$

By comparing equations (3-18) and (3-19), the radiation heat transfer coefficient, h_R, can be defined as:

$$h_R = 4\sigma\varepsilon T_\infty^3 \tag{3-20}$$

Using the new radiation heat transfer coefficient as stated in equation (3-20) and the equation (3-10) developed for temperature profiling through skin, temperature distributions are calculated with heat transfer coefficients and sink temperatures independent of time, represented by Condition 4 in Table 3.1. These temperature distributions and the temperature distributions through the CFRP skin found using FE analyses are compared in Figure 3.7.

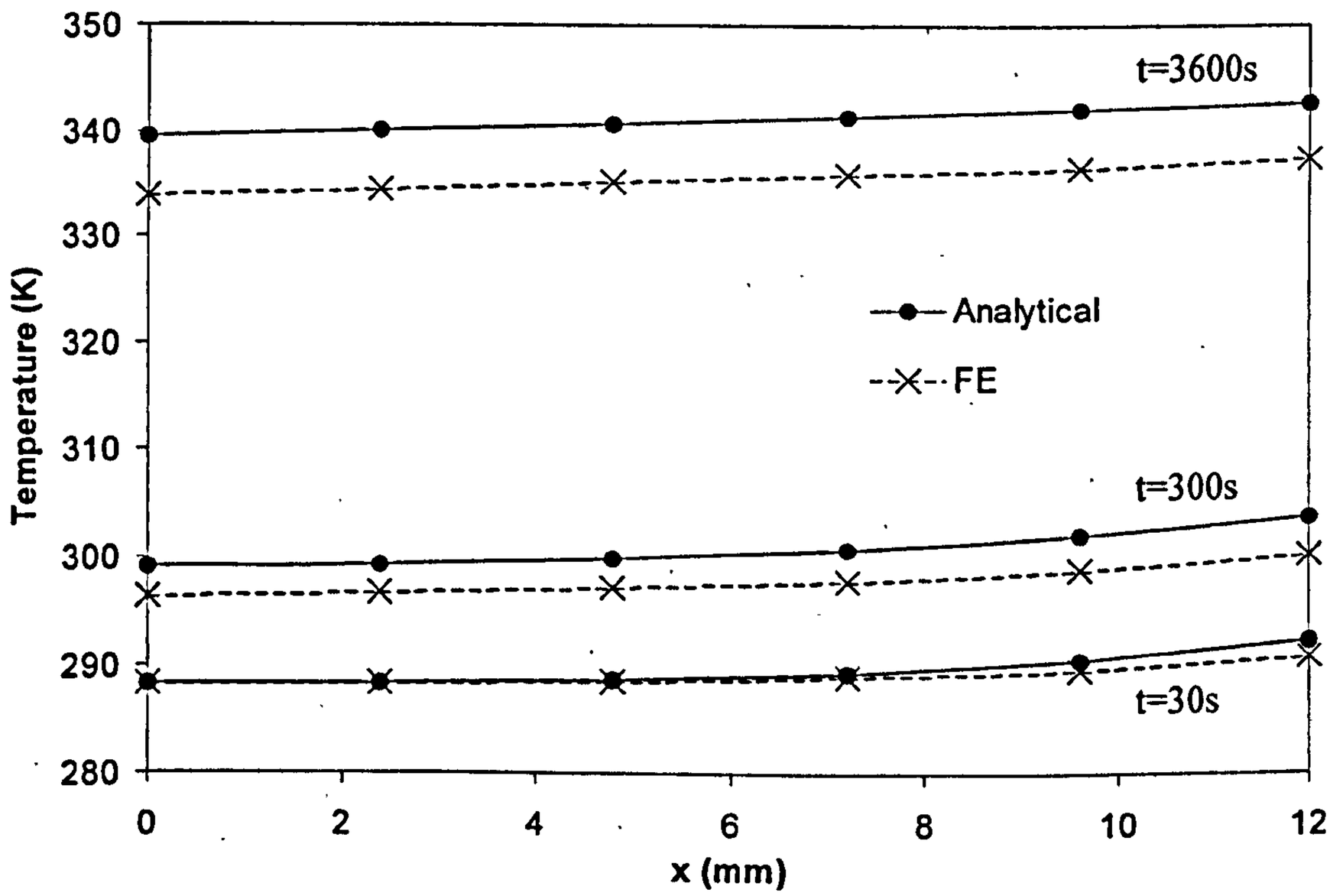

Figure 3.7. Temperatures for radiation boundary conditions with constant sink temperatures.

The results in Figure 3.7, show that the discrepancies between the analytical and FE results over longer timeframes are slightly larger than those in the convection analysis, to a maximum of approximately six degrees at steady-state. This is due to the increased influence of the second term

$\left(1-e^{-\alpha\beta_m^2 t}\right)$ ... in equation (3-10) over time. Because this term is more heavily affected by the heat transfer coefficients than the first term, the error associated in assuming that radiation conditions can be approximated linearly, becomes greater as time and the influence of this term increase.

The errors associated with ill conditioning of the transcendental equation, as seen in the analytical model for convection boundary conditions, still exist. By comparing Figure 3.4 with Figure 3.7, the error associated with linearising radiation becomes obvious. Because of this assumption, the analytical results for temperature are always higher than are those of the FE due to the error associated with the approximation of equation (3-17) using a single order term. It is for this reason that Jaeger [90] suggests using a quadratic, rather than linear, approximation.

However, from Figure 3.7, it is evident that the assumptions of linear radiation boundary conditions in the analytical model deliver accurate results to within 5% of the FE model. With this strong agreement, and because the slight improvement in accuracy achieved by modelling quadratic radiation effects does not justify the additional complexity and difficulties associated with this modelling, the linear analytical model is deemed accurate for establishing radiation boundary conditions.

The use of this model with radiation boundary conditions is, however, limited to sink temperatures that are independent of time. Because the radiation heat transfer coefficient is a function of the sink temperature, every term must remain within the integral of equation (3-11), unlike convection-only boundary conditions, where the heat transfer coefficients are external to the integral. When creating a radiation heat transfer coefficient, all terms containing that heat transfer coefficient must be integrated with respect to time. Due to the multiplication of these terms with the exponential function, this integration becomes extremely cumbersome. Further errors are also introduced by approximating the heat transfer coefficients, as well as the sink temperatures, with polynomials. The result is a more difficult and less accurate estimation, which does not fit with the goal of creating simple and effective analytical models.

3.1.3 Combined Convection-Radiation Boundary Conditions

In reality, the conditions at a solid surface are generally a combination of convection and radiation. Therefore, to make the analytical model as useful as possible with respect to realistic conditions, a case of combined convection and radiation boundary conditions at each surface is examined. By combining equations (1-3) and (1-4), the general heat transfer equation for combined convection-radiation boundary conditions can be written as:

$$q = h_C\left(T - T_{\infty C}\right) + \sigma\varepsilon\left(T^4 - T_{\infty R}^4\right) \tag{3-21}$$

Here, h_C refers to the convection heat transfer coefficient, and the sink temperatures are now in terms of convection, $T_{\infty C}$, and radiation, $T_{\infty R}$, respectively. For the reasons stated in the radiation section, this analysis is limited to sink temperatures that are independent of time. The general boundary condition for equation (3-21) is:

$$-k\frac{dT}{dx} + \left(h_C + h_R\right)T = h_C T_{\infty C} + h_R T_{\infty R}. \tag{3-22}$$

The value of h_R is again found by using equation (3-20). In order to use the analytical model, equation (3-22) must be rewritten to fit the general form given by equation (3-2). Thus, a combined heat transfer coefficient can be defined as:

$$h = h_C + h_R \tag{3-23}$$

The difficulty then, is combining the sink temperatures. Based on comparative analyses, the most accurate representation of a combined sink temperature is the average of both the convection and radiation values. Using a combined heat transfer coefficient, equation (3-10) is used to perform analyses with combined convection and radiation boundary conditions, represented by Condition 5 in Table 3.1. Figure 3.8 shows a comparison of the analytical model with the FE model for combined conditions.

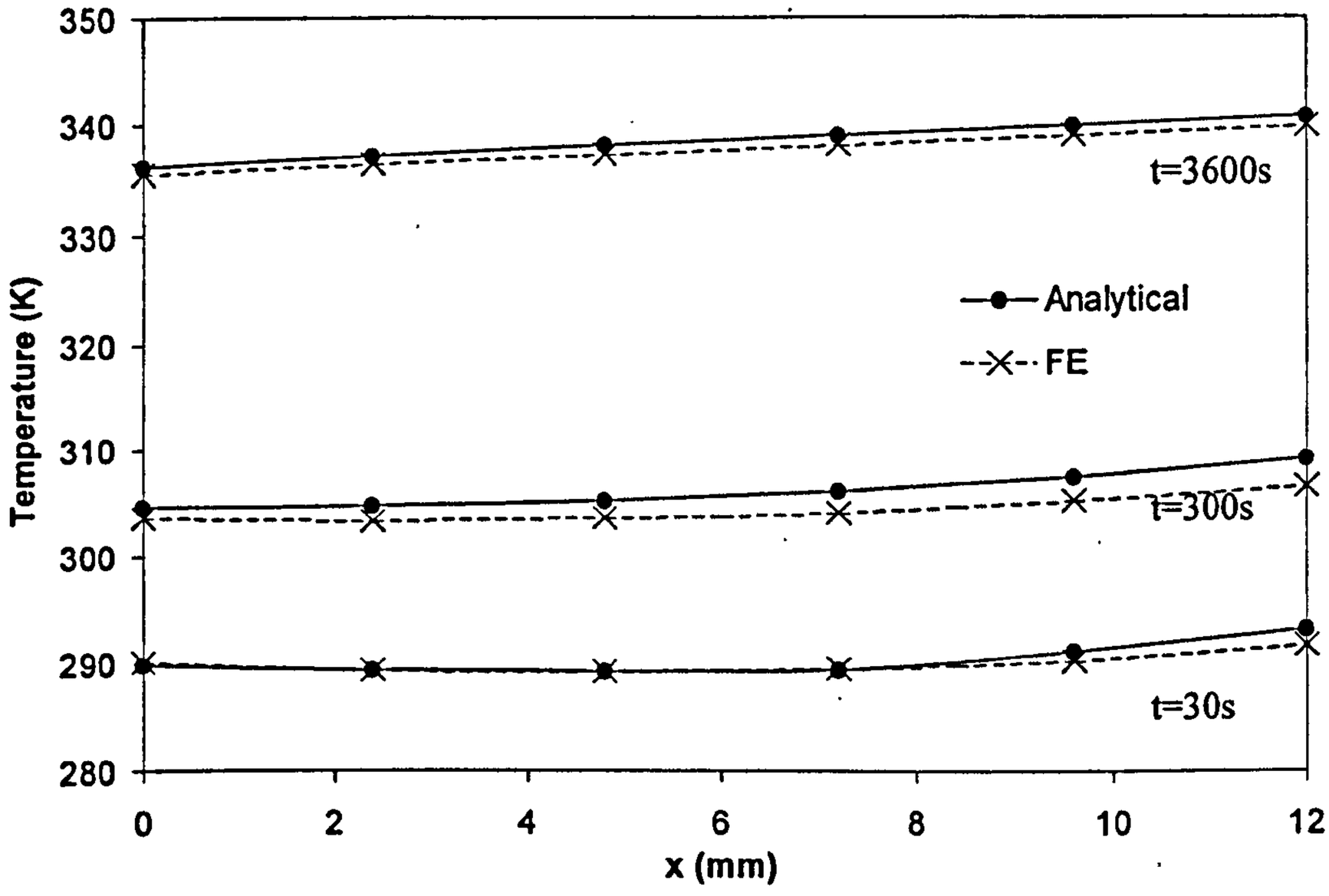

Figure 3.8. Comparison of Analytical and FE temperature prediction through the skin for combined convection-radiation boundary conditions at both surfaces

From Figure 3.8, it is evident that the model for combined boundary conditions is relatively accurate. The results of the combined analysis show closer agreement with the FE over that of convection-only and radiation-only boundary conditions. This improvement results from assuming average sink temperatures. With this assumption, the sink temperatures used on the surfaces are lower in comparison to the convection-only analysis. Because the form of the analytical model is based on convection boundary conditions, this is equivalent to performing convection analysis with lower temperature. The FE sink temperatures, however, are not changed. Thus, as the influence of the second term in the analytical model grows over a longer period of time, the results remain closer because of this 'perceived' lowering of the sink temperature in the analytical analysis.

3.2 Three-Layer Model

3.2.1 Development of Equations

A three-layer model designed using a modified separation of variables technique, can apply an analytical solution in a primary area of interest, the joint region. Antonopoulos and Tzivanidis [16] have developed the models suggested by Ozisik [1] further, to include convection boundary conditions at both external surfaces. Figure 3.9 gives an example of multiple layers with convection conditions at both outer surfaces.

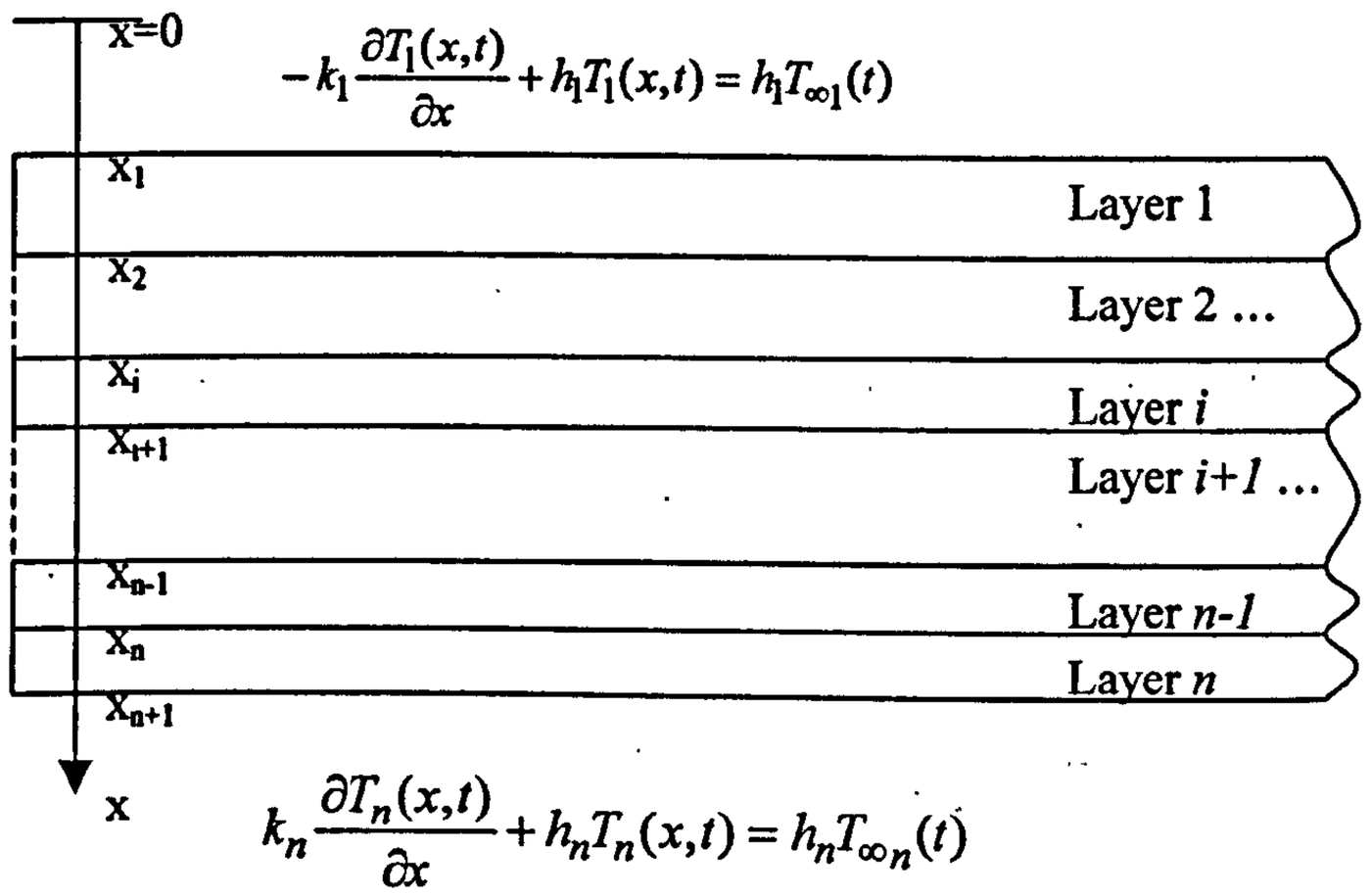

Figure 3.9. Composite region consisting of *n* parallel layers.

Again, certain assumptions are necessary in order to simplify the modelling. It is assumed there is perfect thermal contact between layers. Each layer in the region is assumed to have temperatures, conductivity, and thermal diffusivity dependent only on the material of that particular layer, and the material properties are assumed to be independent of time. The heat transfer equation for each layer, assuming no heat generation and one-dimensional heat transfer, can be written in the form:

$$\alpha_i\frac{\partial^2 T_i(x,t)}{\partial x^2}=\frac{\partial T_i(x,t)}{\partial t} \qquad t>0 \qquad x_i\le x\le x_{i+1} \qquad i=1,2,3,\ldots,n-1 \quad (3\text{-}24)$$

Note that in this case, the thermal diffusivity, α, is left with the spatial component, unlike the general form of separation of variables as described by equation (3A-7). The boundary conditions for the

external surfaces are identical to those for a single layer model. Additional boundary conditions are needed to describe behaviour at the interior interfaces. Conditions of continuous temperature at the interface and continuous flux are used. The entire set of boundary conditions required to fully define this problem are

$$-k_1\frac{\partial T_1(x,t)}{\partial x}+h_1T_1(x,t)=h_1T_{\infty 1}(t) \qquad x=x_1 \qquad (3\text{-}25)$$

$$T_i(x,t)=T_{i+1}(x,t) \qquad x=x_{i+1} \qquad i=1,2,3,\ldots,n\text{-}1 \qquad (3\text{-}26)$$

$$k_i\frac{\partial T_i(x,t)}{\partial x}=k_{i+1}\frac{\partial T_{i+1}(x,t)}{\partial x} \qquad x=x_{i+1} \qquad i=1,2,3,\ldots,n\text{-}1 \qquad (3\text{-}27)$$

$$k_n\frac{\partial T_n(x,t)}{\partial x}+h_nT_n(x,t)=h_nT_{\infty n}(t) \qquad x=x_n \qquad (3\text{-}28)$$

The initial conditions can also be given in terms of layers, where:

$$T_i(x,0)=F_i(x) \qquad x_i\le x\le x_{i+1} \qquad i=1,2,3,\ldots,n\text{-}1 \qquad (3\text{-}29)$$

Because this is a complex nonhomogeneous problem containing two convection conditions, Antonopoulos and Tzivanidis [16] suggest a method of homogenising the problem by introducing a new variable, $\theta(x,t)$. While the technique of introducing a new dependent variable is common in solving more complex separation of variables problems, two convection boundary conditions have yet to be addressed in literature [1], [2], [16]. The normalised equation for the heat transfer problem given by equation (3-24) is:

$$\theta_i(x,t)=T_i(x,t)-q_i(x,t) \qquad x_i\le x\le x_{i+1} \qquad i=1,2,3,\ldots,n\text{-}1 \qquad (3\text{-}30)$$

The variable q is formulated by using the desired form of homogenised boundary conditions and working backward to define the necessary variable, in order to achieve the end result. Here q is defined for any layer, $i=1..n$, as:

$$q_1(x,t) = \frac{(x_2 - x)^2 h_1 T_{\infty 1}(t)}{(x_2 - x_1)(h_1 x_2 - h_1 x_1 + 2k_1)} \tag{3-31}$$

$$q_i(x,t) = 0 \qquad i=2,3,...,n-1 \tag{3-32}$$

$$q_n(x,t) = \frac{(x - x_n)^2 h_n T_{\infty n}(t)}{(x_{n+1} - x_n)(h_n x_{n+1} - h_n x_n + 2k_n)} \tag{3-33}$$

Using these normalised equations, the problem and boundary conditions can be rewritten in homogeneous form:

$$\alpha_i \frac{\partial^2 \theta_i(x,t)}{\partial x^2} + \alpha_i \frac{\partial^2 q_i(x,t)}{\partial x^2} = \frac{\partial \theta_i(x,t)}{dt} + \frac{\partial q_i(x,t)}{dt} \quad t>0 \quad x_i \le x \le x_{i+1} \quad i=1,2,3,...,n-1 \tag{3-34}$$

$$-k_1 \frac{\partial \theta_1(x_1,t)}{\partial x} + h_1 \theta_1(x_1,t) = 0 \tag{3-35}$$

$$\theta_i(x_{i+1},t) = \theta_{i+1}(x_{i+1},t) \qquad i=1,2,3,...,n-1 \tag{3-36}$$

$$k_i \frac{\partial \theta_i(x_{i+1},t)}{\partial x} = k_{i+1} \frac{\partial \theta_{i+1}(x_{i+1},t)}{\partial x} \qquad i=1,2,3,...,n-1 \tag{3-37}$$

$$k_n \frac{\partial \theta_n(x_{n+1},t)}{\partial x} + h_n \theta_n(x_{n+1},t) = 0 \tag{3-38}$$

$$\theta_i(x,0) = F_i(0) - q_i(x,0) \equiv f_i(0) \quad x_i \le x \le x_{i+1} \quad i=1,2,3,...,n-1 \tag{3-39}$$

An example of how the convection conditions are transformed is given in Appendix 3E. According to separation of variables technique, the solution can be expressed in the form:

$$\theta_i(x,t) = \sum_{m=1}^{\infty} X_{im}(x) \cdot \Gamma_m(t) \qquad x_i \leq x \leq x_{i+1} \qquad i=1,2,3,\ldots,n-1 \quad (3\text{-}40)$$

The calculation of the spatial and time terms is more complex than in an ordinary separation of variables problem, since this problem contains complex boundary conditions and a homogenised temperature variable.

The eigenvalue problem for the spatial variable, $X(x)$, is much the same as equation (3A-10). However, this time the thermal diffusivity, α, is included in the equation. The second order partial derivative is left in the general form using the Laplacian operator [92]:

$$\alpha_i \nabla^2 X_{im}(x) + \beta_m{}^2 X_{im}(x) = 0 \quad x_i \leq x \leq x_{i+1} \quad i=1,2,3,\ldots,n-1 \qquad (3\text{-}41)$$

The corresponding boundary conditions are the same for the outside layers as for the one-layer problem, and new conditions for the internal interfaces are defined as:

$$-k_1 \frac{\partial X_{1m}(x_1)}{\partial x} + h_1 X_{1m}(x_1) = 0 \qquad (3\text{-}42)$$

$$X_{im}(x_{i+1}) = X_{i+1,m}(x_{i+1}) \qquad x_i \leq x \leq x_{i+1} \quad i=1,2,3,\ldots,n-1 \quad (3\text{-}43)$$

$$k_i \frac{\partial X_{im}(x_{i+1})}{\partial x} = k_{i+1} \frac{\partial X_{i+1,m}(x_{i+1})}{\partial x} \quad x_i \leq x \leq x_{i+1} \qquad i=1,2,3,\ldots,n-1 \quad (3\text{-}44)$$

$$k_n \frac{\partial X_{nm}(x_{n+1})}{\partial x} + h_n X_{nm}(x_{n+1}) = 0 \qquad (3\text{-}45)$$

Equation (3-41) is a homogeneous linear equation of the second order, which means that the solution must be defined by the superposition principle [91]. This requires that the solution have the form of a linear combination of two, twice differentiable functions, $\phi(x)$ and $\psi(x)$, multiplied by two arbitrary constants, C and D, such that $X_{im}(x) = C_{im}\phi_{im}(x) + D_{im}\psi_{im}(x)$. Again, this problem is in the form of the Helmholtz equation and, for Cartesian co-ordinate systems, has a trigonometric solution, as stated

in the introduction to the separation of variables method. The only change is the inclusion of thermal diffusivity into the eigenvalue problem. The modified solution is given by:

$$X_{im}(x) = C_{im}\cos\left(\frac{\beta_m x}{\sqrt{\alpha_i}}\right) + D_{im}\sin\left(\frac{\beta_m x}{\sqrt{\alpha_i}}\right) \tag{3-46}$$

The boundary conditions must by used in order to determine C_{im} and D_{im}. By substituting the general form of equation (3-46) into the conditions equations (3-42) to (3-45), *2n* equations are obtained for the solution of the arbitrary constants for *n* layers:

$$[h_1\phi_{1m}(x_1) - k_1\phi'_{1m}(x_1)]C_{1m} + [h_1\psi_{1m}(x_1) - k_1\psi'_{1m}(x_1)]D_{1m} = 0 \tag{3-47}$$

$$\phi_{im}(x_{i+1})C_{im} + \psi_{im}(x_{i+1})D_{im} - \phi_{i+1,m}(x_{i+1})C_{i+1,m} - \psi_{i+1,m}(x_{i+1})D_{i+1,m} = 0$$

$$i=1,2,3,\ldots,n\text{-}1 \tag{3-48}$$

$$k_i\phi'_{im}(x_{i+1})C_{im} + k_i\psi'_{im}(x_{i+1})D_{im} - k_{i+1}\phi'_{i+1,m}(x_{i+1})C_{i+1,m} - k_{i+1}\psi'_{i+1,m}(x_{i+1})D_{i+1,m} = 0$$

$$i=1,2,3,\ldots,n\text{-}1 \tag{3-49}$$

$$[h_n\phi_{nm}(x_{n+1}) - k_n\phi'_{nm}(x_{n+1})]C_{nm} + [h_n\psi_{nm}(x_{n+1}) - k_n\psi'_{nm}(x_{n+1})]D_{nm} = 0 \tag{3-50}$$

Here $\phi'(x)$ and $\psi'(x)$ denote the derivatives with respect to x. These equations can be written in matrix form. For a three-layer problem like the joint region, a six by six matrix is created. The matrix coefficients for a three-layer slab with the above boundary conditions are given in Appendix 3F. These coefficients are then multiplied by the $[C_{1m}, D_{1m}, C_{2m}, D_{2m}, C_{3m}, D_{3m}]$ vector to form the complete set of equations as given by equations (3-47) to (3-50). According to Craemer's Theorem [91], this homogeneous set of equations can only have nontrivial solutions if the determinant is zero. This means that by setting the determinant of the matrix to zero and collecting the positive roots, the eigenvalues, β_m, can be found. These *2n* eigenvalues can then be used to determine D_{1m}, C_{im},...D_{nm}, where C_{1m} is determined arbitrarily, and has a value of say, one. This means that all other constants can be written in terms of C_{1m}. For a three-layer problem then, there are six equations and five unknowns, since C_{1m} is arbitrarily determined. For six equations, row reduction is performed on the first five equations to rewrite every other coefficient in terms of the

known C_{1m}. The sixth equation is then used as a check. The Fortran program example in Appendix 3H gives the appropriate equations for each constant, C_{1m} to D_{3m}, using the matrix terms *a(1,1)* to *a(6,6)*, as given by the subroutine MATRIX, formally written in Appendix 3F.

In order to solve for the time component, $T(t)$, expressions for the $q(x,t)$ variables as well as for the initial condition, $f(x)$, are required. From equation (3-34), it can be seen that expressions for $\partial q_i(x,t)/\partial t$ and $\alpha_i \partial^2 q_i(x,t)/\partial x^2$ are needed. Since the Fourier series can be used to represent any continuous function, these expressions can be rewritten in series form [91]. The resulting series must contain the appropriate space and time variables. The unknown Fourier constants are given as, V_m*, I_m* and f_m*, and the required expressions are given by [16]:

$$\frac{\partial q_i(x,t)}{\partial t} = \sum_{m=1}^{\infty} V_m{}^*(t) X_{im}(x) \qquad i=1,2,3,\ldots,n \tag{3-51}$$

$$\alpha_i \frac{\partial^2 q_i(x,t)}{\partial x^2} = \sum_{m=1}^{\infty} I_m{}^*(t) X_{im}(x) \qquad i=1,2,3,\ldots,n \tag{3-52}$$

$$f_i(x) = \sum_{m=1}^{\infty} f_m{}^* X_{im}(x) \qquad i=1,2,3,\ldots,n \tag{3-53}$$

Orthogonality is used to determine the values of these Fourier constants. First, both sides are multiplied by $\alpha_i/k_i[X_{ip}(x)]$, then integrated over an individual layer. The ratio of thermal diffusivity to conductivity is used, since it is equal to the discontinuous weighting function given by Tittle and Robinson [92] in a similar type of analysis. For example, equation (3-51), when taken over all layers *i=1,2,3,...,n*, becomes:

$$\sum_{i=1}^{n} \frac{k_i}{\alpha_i} \int_{x_i}^{x_{i+1}} \frac{\partial q_i(x,t)}{\partial t} X_{ip}(x)dx = \sum_{i=1}^{n} \left[\sum_{m=1}^{\infty} V_n{}^* \frac{k_i}{\alpha_i} \int_{x_i}^{x_{i+1}} X_{im}(x) X_{ip}(x)dx \right] \tag{3-54}$$

Due to orthogonality, as shown in equation (3A-15), the only time that the right hand side can have values other than zero is when $p = m$. This allows equation (3-54) to be rewritten as:

$$\sum_{i=1}^{n}\frac{k_i}{\alpha_i}\int_{x_i}^{x_{i+1}}\frac{\partial q_i(x,t)}{\partial t}X_{ip}(x)dx = V_n * \sum_{i=1}^{n}\frac{k_i}{\alpha_i}\int_{x_i}^{x_{i+1}}X_{im}^2(x)dx \tag{3-55}$$

V_n* can then be defined as:

$$V_n*(t) = \frac{\sum_{i=1}^{n}\frac{k_i}{\alpha_i}\int_{x_i}^{x_{i+1}}\frac{\partial q_i(x,t)}{\partial t}X_{im}(x)dx}{N_m} \tag{3-56}$$

Similarly, I_n* and f_n* are given by:

$$I_n*(t) = \frac{\sum_{i=1}^{n}\frac{k_i}{\alpha_i}\int_{x_i}^{x_{i+1}}\alpha_i\frac{\partial^2 q_i(x,t)}{\partial x^2}X_{im}(x)dx}{N_m} \tag{3-57}$$

$$f_n* = \frac{\sum_{i=1}^{n}\frac{k_i}{\alpha_i}\int_{x_i}^{x_{i+1}}f_i(x)X_{im}(x)dx}{N_m} \tag{3-58}$$

Similar to the *Norm* defined in Appendix 3A, N_m, is defined as:

$$N_m = \sum_{i=1}^{n}\frac{k_i}{\alpha_i}\int_{x_i}^{x_{i+1}}X_{im}^2(x)dx \tag{3-59}$$

The heat transfer equation (3-34) is rewritten using equations (3-57), (3-58), and (3-59), such that,

$$\sum_{m=1}^{\infty}\left[\alpha_i\Gamma_m(t)\frac{\partial^2 X_{im}(x)}{\partial x^2} + I_m*(t)X_{im}(x)\right] = \sum_{m=1}^{\infty}\left[\frac{\partial\Gamma_m(t)}{dt}X_{im}(x) + V_m*(t)X_{im}(x)\right] \tag{3-60}$$

From equation (3-41), it is seen that $\alpha_i \nabla^2 X_{im}(x) = -\beta_m{}^2 X_{im}(x)$. This implies that equation (3-60) can also be written in a form containing the eigenvalues, β_m:

$$\sum_{m=1}^{\infty}\left[\frac{\partial \Gamma_m(t)}{dt} X_{im}(x) - \Gamma_m(t)\beta_m^2 X_{im}(x) - I_m{}^*(t) X_{im}(x) + V_m{}^*(t) X_{im}(x)\right] = 0 \qquad (3\text{-}61)$$

Because $X_{im}(x)$ is common in all terms it, as well as the summation, can be removed by dividing into zero. The remaining equation contains only the $\Gamma_m(t)$ term, thus allowing a solution for the time variant portion:

$$\frac{\partial \Gamma_m(t)}{dt} + \Gamma_m(t)\beta_m^2 = I_m{}^*(t) - V_m{}^*(t) \qquad (3\text{-}62)$$

Using the initial condition, a relationship for $\Gamma_m(0)$ can be formulated according to similarity:

$$\theta_i(x,0) \equiv f_i(x) = \sum_{m=1}^{\infty} X_{im}(x)\Gamma_m(0) = \sum_{m=1}^{\infty} X_{im}(x) f_m{}^* \Rightarrow \Gamma(0) = f_m{}^* \qquad (3\text{-}63)$$

The problem then becomes a simple nonhomogeneous linear differential equation like that described in Appendix 3G, which has the solution:

$$\Gamma_m(t) = e^{-\alpha\beta_m^2 t}\left[\int_{t'=0}^{t} e^{\alpha\beta_m^2 t'}\left[I_m{}^*(t) - V_m{}^*(t)\right]dt' + f_m{}^*\right] \qquad (3\text{-}64)$$

Because $I_m{}^*$ and $V_m{}^*$ exist only at the external boundaries, this solution is only valid at $i = 1$ and $i = n$. $I_m{}^*$ and $V_m{}^*$ are zero at the internal surfaces because $q(x,t)$ is zero at these interfaces. Equation (3-62) simplifies to:

$$\frac{\partial \Gamma_m(t)}{dt} + \Gamma_m(t)\beta_m^2 = 0 \qquad i=2,3,\ldots n-1 \qquad (3\text{-}65)$$

The internal surfaces can, therefore, be considered part of a homogeneous problem with respect to time, with a solution given by:

$$\Gamma_m(t) = e^{-\alpha\beta_m^2 t} f_m * \tag{3-66}$$

The problem of the time variable is now addressed and the eigenvalue problem of the space variable has been previously determined. The general form of the separation of variables technique equation (3-40) is then used to formulate the final expressions for $\theta(x,t)$:

$$\theta_i(x,t) = \sum_{m=1}^{\infty} X_{im}(x) e^{-\alpha\beta_m^2 t} \left[\int_{t'=0}^{t} e^{\alpha\beta_m^2 t'} [I_m * (t) - V_m * (t)] dt' + f_m * \right] \quad i=1 \text{ and } i=n \tag{3-67}$$

$$\theta_i(x,t) = \sum_{m=1}^{\infty} X_{im}(x) e^{-\alpha\beta_m^2 t} f_m * \qquad i=2,3...n-1 \tag{3-68}$$

The temperature at any specified position and time, $T_i(x,t)$ can then be found using equations (3-67) and (3-68) in combination with (3-30).

3.2.2 Multiple Layer Model

3.2.2.1 Convection Boundary Conditions

A three-layer model of the joint region illustrates the usefulness of this procedure. Figure 3.10 shows the geometry. The material properties for the aluminium laps and CFRP skin are the same as those given in Table 2.1.

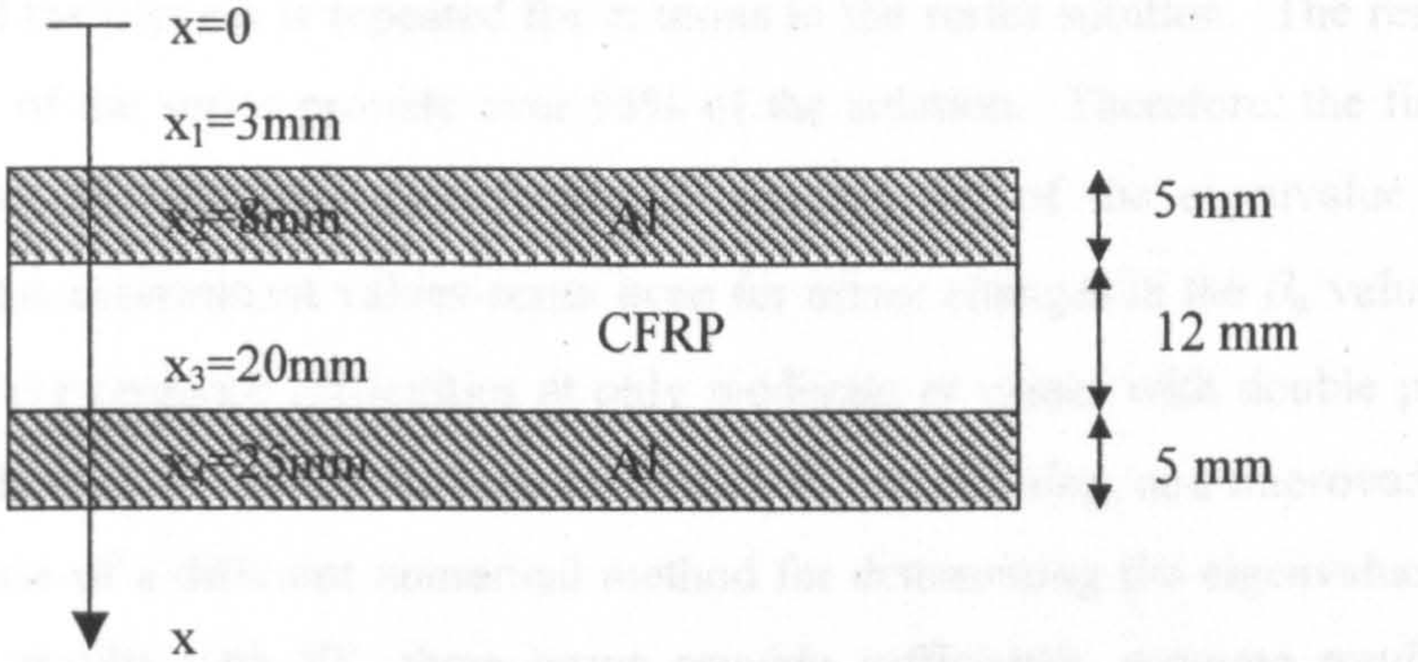

Figure 3.10. Three-layer model of joint region through CFRP skin side.

A specifically developed Fortran program calculates the temperatures. An example of the program is provided in Appendix 3H. A crude predictor-corrector method is used to determine the appropriate eigenvalues, β_m. Because only positive roots are required, two arbitrary β values, $\beta 1$ and $\beta 2$, close to zero are chosen. The difference between these values is kept to a minimum so that the two values of the determinant for these eigenvalues bound the $Det = 0$ value of β_m, as demonstrated Figure 3.11.

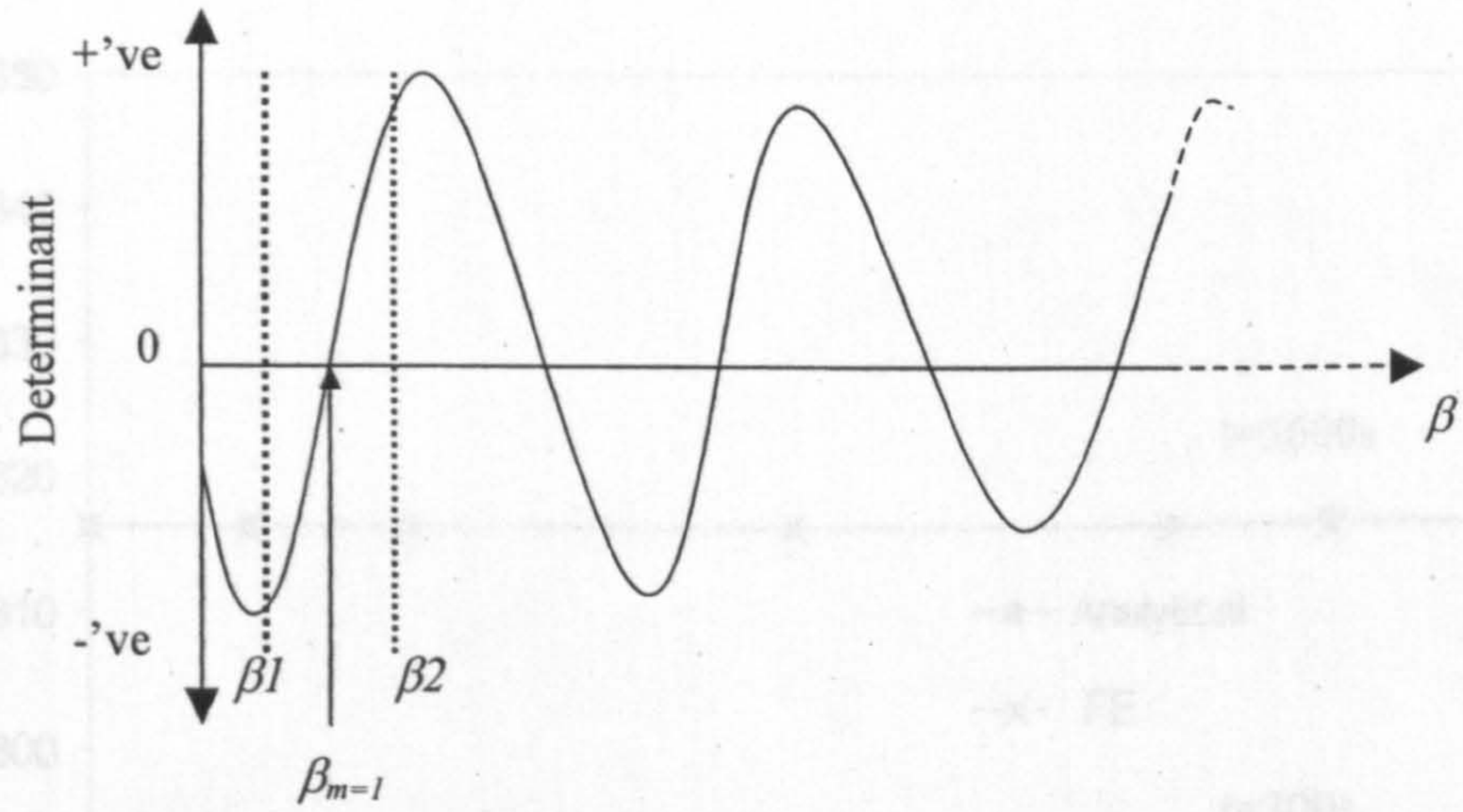

Figure 3.11. Graphical description of determination of β_m values.

Once the first eigenvalue is established, the corresponding matrix values of the boundary condition matrix, as given in Appendix 3F, are calculated. Through the manipulation of these matrix terms, the Fourier constants $C_{1,m=1}$ to $D_{3,m=1}$ are determined. This implies that $X_{i,m=1}$ is also known. The coefficients for the space variable are then, fully described. The eigenfunctions, $X_{i,m=1}$ are then used to determined the coefficients f_m*, V_m*, and I_m*. Thus, all the components of the expression of $\theta_i(x,t)$

are known, and the process is repeated for m terms in the series solution. The results show that the first two terms of the series provide over 95% of the solution.. Therefore, the first three terms are used to estimate to solution. Due to the ill conditioning of the eigenvalue equations, severe oscillations in the determinant values occur even for minor changes in the β_m values at higher terms. This results in convergence difficulties at only moderate m values with double precision accuracy. Scaling methods exist to reduce the effects of such ill conditioning, and improved efficiency can be gained by the use of a different numerical method for determining the eigenvalue. However, when comparing the results with FE, three terms provide sufficiently accurate results without further modelling implications. Using the series solution, the final temperatures at a specified position, for a given time, are then found.

Convection conditions with constant sink temperatures are examined, applying the same conditions as used in the single layer model. Heat transfer coefficients of $8W/m^2K$ and $2W/m^2K$ are used for the top and bottom surfaces, respectively. Sink temperatures of 328K and 369K, equivalent to Condition 2 in Table 3.1, are used on the respective surfaces. Figure 3.12 shows a comparison of the results to FE analysis.

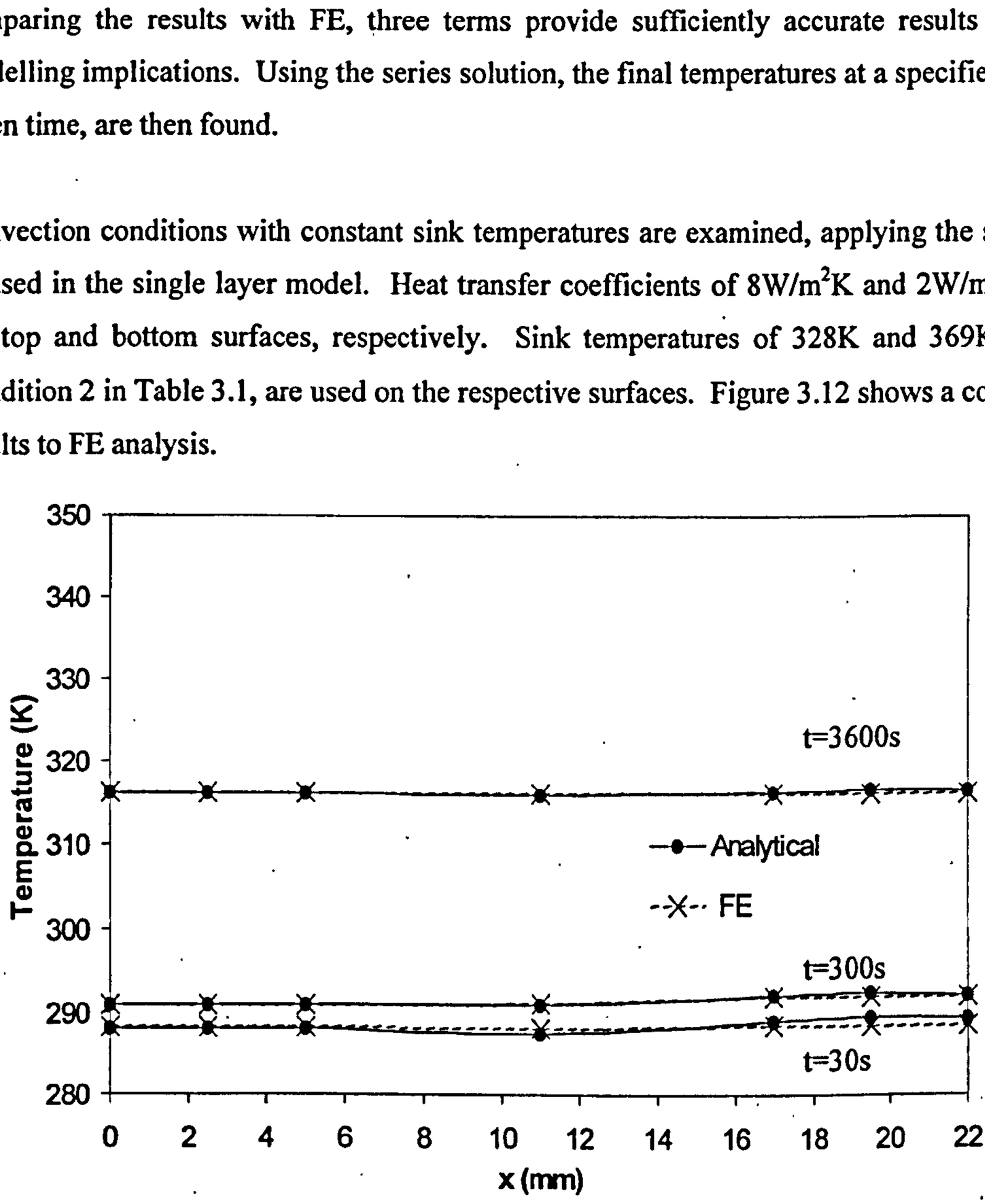

Figure 3.12. Temperatures for convection boundary conditions with constant sink temperatures.

The agreement between FE and analytical is greater than 99% at any given time. This is an improvement of approximately 4% over the single layer model. Even with longer times, agreement remains excellent. This implies that using the determinant of a matrix approach, as adopted in the three-layer model, reduces the ill conditioning involved in the determination of the eigenvalues, when compared with using the roots of a transcendental equation in the single layer model. The improved mathematical stability of the model reduces the influence of truncation in the eigenvalue determination.

Transient convection conditions are also examined. The same heat transfer coefficients used in the semi-transient analysis are applied. The ambient or sink temperatures are the same as those used in the single layer model, described as Condition 3 in Table 3.1, and are represented by a fourth-order polynomial in the Fortran program. Temperatures at three different positions, x=3mm, x=14mm, and x=25mm, are established and then compared to FE results in Figure 3.12 to Figure 3.15. It should be noted that x=3mm corresponds to x=0 for the top surface, but due to the form of the equations, it becomes necessary to chose the surface distance equal to an arbitrary value, in this case, x=3mm.

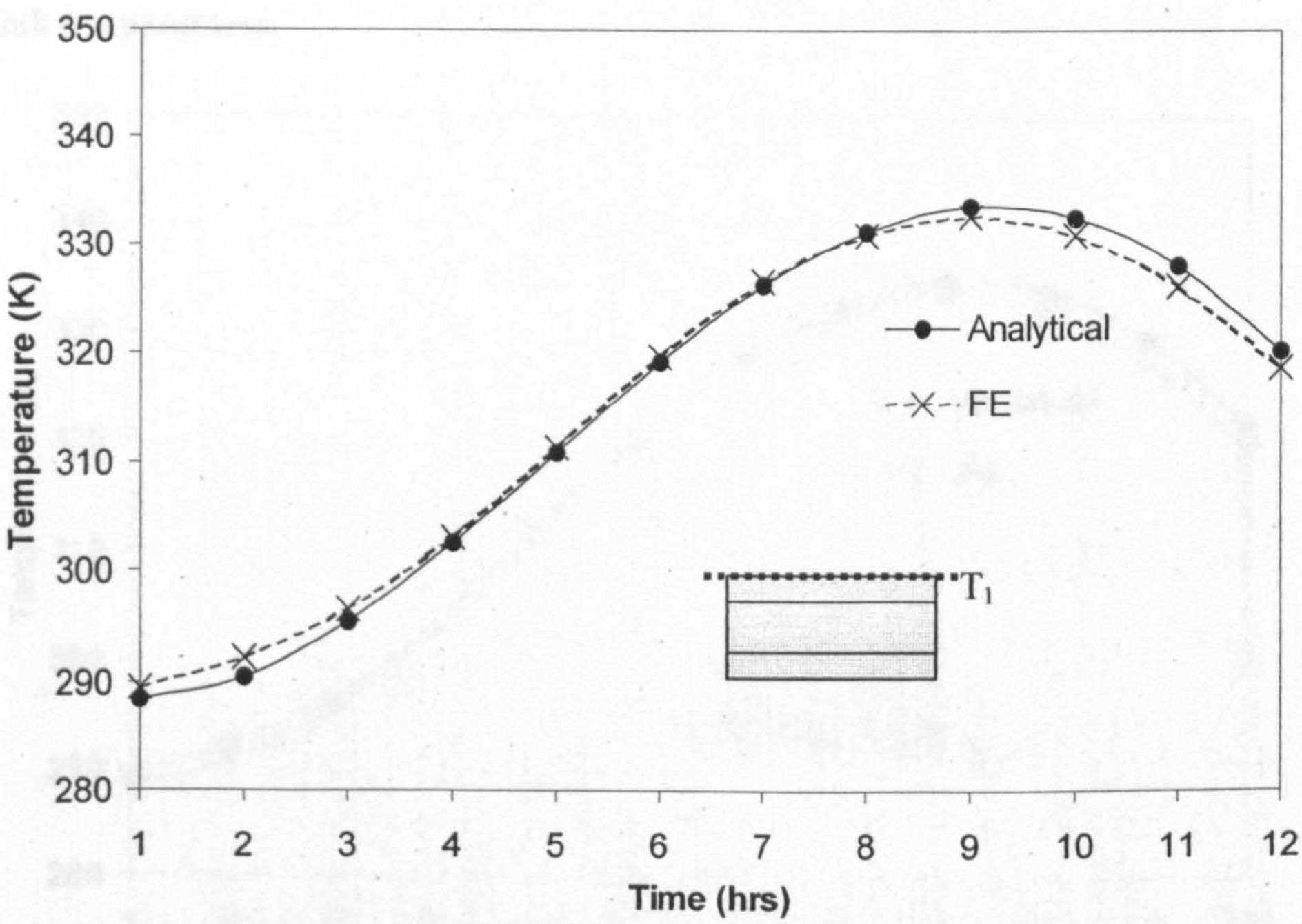

Figure 3.13. Temperature at top surface (x=3mm) for convection conditions with transient sink temperatures.

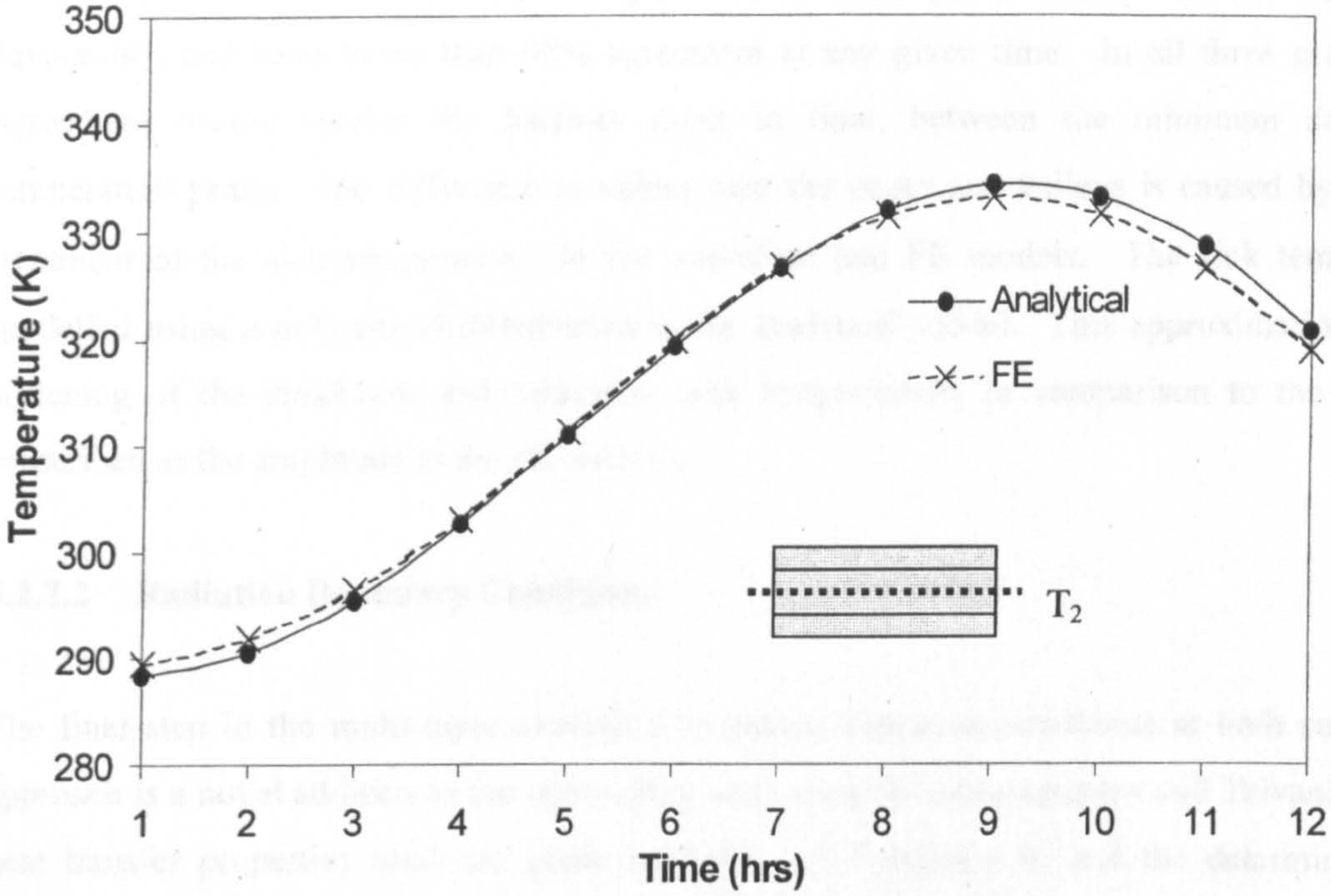

Figure 3.14. Temperature at mid-surface (x=14mm) for convection conditions with transient sink temperatures.

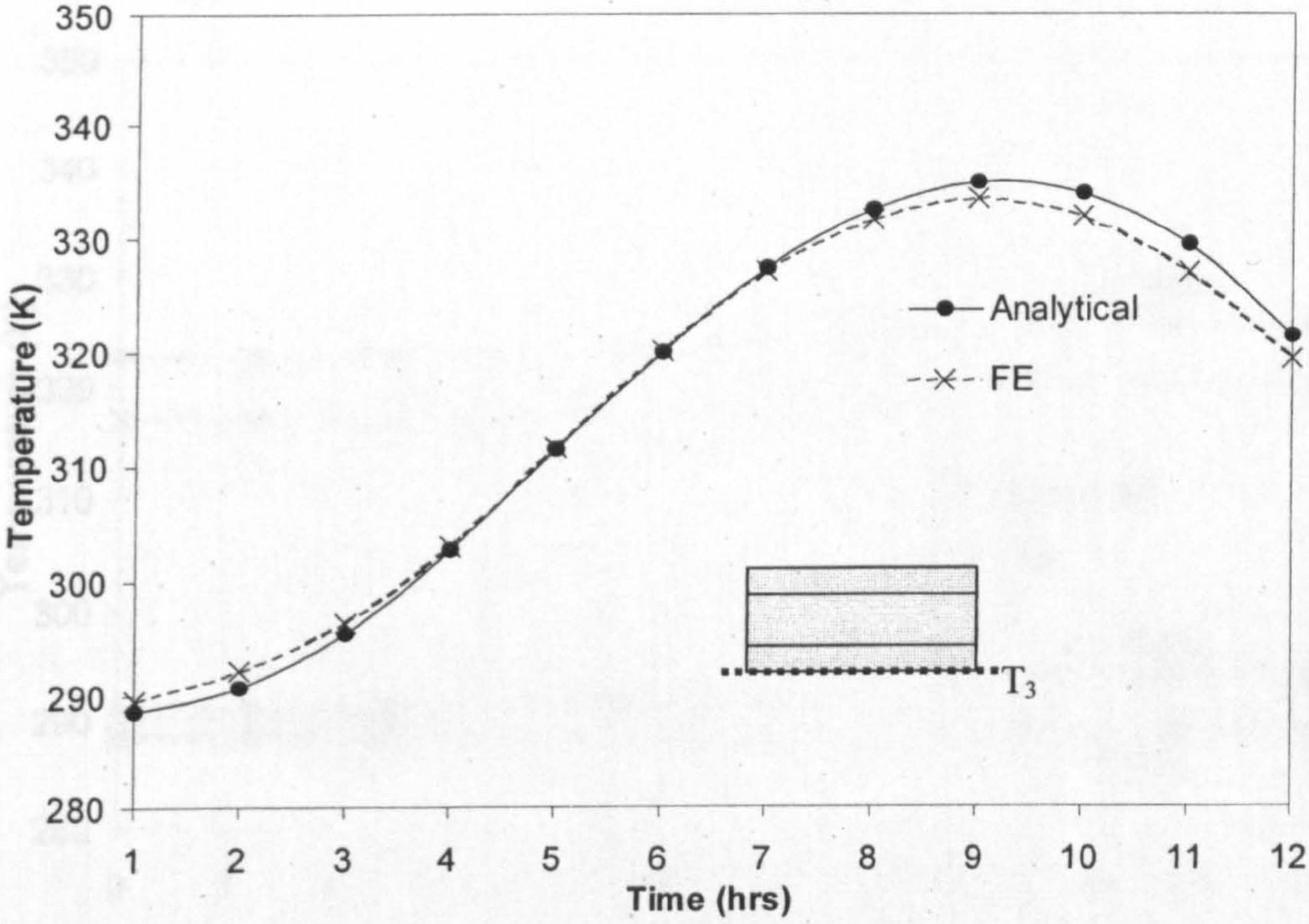

Figure 3.15. Temperature at bottom surface (x=25mm) for convection conditions with transient sink temperatures.

It becomes evident from the above figures that the analytical model and FE results compare favourably, and have better than 98% agreement at any given time. In all three graphs, the best agreement occurs nearest the halfway point in time, between the minimum and maximum temperature peaks. The difference in values near the peaks and valleys is caused by the different treatment of the sink temperatures in the analytical and FE models. The sink temperatures are modelled using a polynomial distribution in the analytical model. This approximation results in a softening of the maximum and minimum sink temperatures, in comparison to the exact values prescribed as the amplitude in the FE analysis.

3.2.2.2 Radiation Boundary Conditions

The final step in the multi-layer analysis is applying radiation conditions at both surfaces. This approach is a novel addition to the convection work done by Antonopoulos and Tzivanidis [16]. The heat transfer properties used are given in Table 3.1 Condition 4, and the determination of the radiation heat transfer coefficient uses the same method developed for the single layer model. Trends similar to those observed in the single layer integral transform analysis are observed and are shown in Figure 3.16.

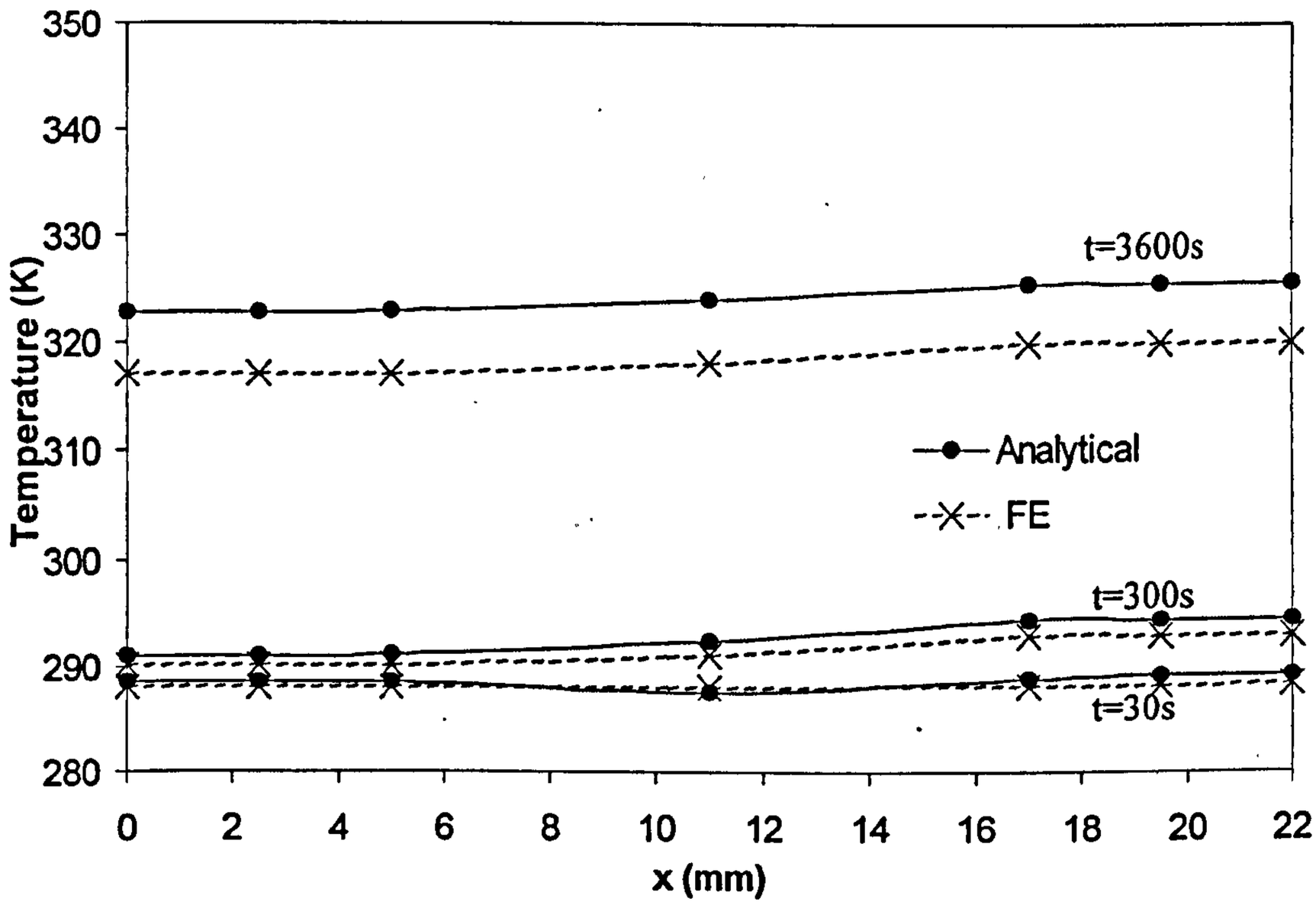

Figure 3.16. Temperatures for radiation boundary conditions with constant sink temperatures.

The analytical model over predicts the temperatures, to a maximum of almost seven degrees at steady state. Since the convection-only analysis demonstrated that the ill conditioning effects were minimal in the current model, the difference then is mainly due to the approximated linearity of the radiation itself. As time increases, the influence of the terms containing the approximated heat transfer coefficient increases, and the error associated with this linearised approximation becomes more evident. It is evident from Figure 3.16 that the overall temperature trends predicted by the analytical model are consistent with those of the FE. The relative error of the analytical method is less than 3%.

3.2.2.3 Combined Convection-Radiation Boundary Conditions

Combined convection-radiation boundary conditions are also examined with the three-layer model. The conditions are identical to those used in the single-layer analyses represented by Condition 5 in Table 3.1, and the results are shown in Figure 3.17.

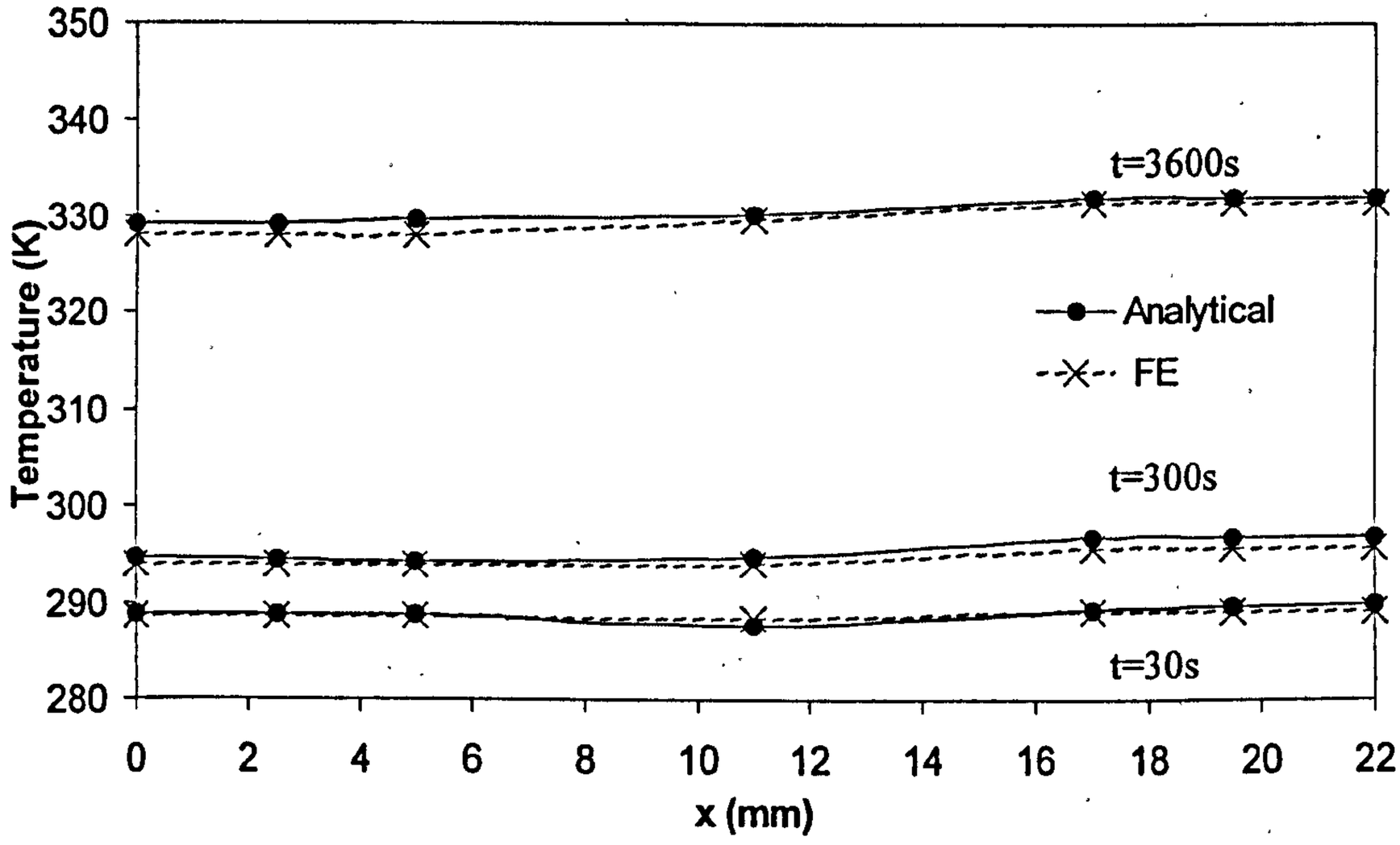

Figure 3.17. Temperatures for combined convection-radiation boundary conditions with constant sink temperatures.

The agreement between the FE and analytical is excellent, less than 1% difference. This improvement over the radiation-only conditions is again due to the perceived lowering of the sink temperatures in the analytical analysis, recalling that the average of the convection and radiation sink temperatures is used, as in the single-layer model.

3.3 Analytical Model Conclusions

The developed analytical models serve to improve confidence in the FE models, while providing an accurate, closed-form method of heat transfer analysis under specific conditions. The results of the FE and analytical temperature prediction modelling are also shown in [93]. Table 3.3 summarises the maximum temperature differences in the single layer and three-layer analytical models and the FE models respectively for cases of convection, radiation, and combined convection-radiation boundary conditions with sink temperatures independent of time.

Table 3.3. Comparison of analytical and FE results for convection-only, radiation-only and combined convection-radiation boundary conditions at various analysis times.

	ΔT								
	Convection			Radiation			Combined		
SINGLE LAYER	30s	300s	3600s	30s	300s	3600s	30s	300s	3600s
Top Surface	0.2	0.9	4.8	0.9	2.6	5.6	0.3	1.2	0.6
Bottom Surface	0.3	1.3	5.4	1.4	3.5	5.4	1.4	2.5	0.9
THREE LAYER									
Top Surface	0.2	0.1	0.0	0.6	0.8	5.8	0.3	0.9	1.0
Bottom Surface	0.8	0.2	0.2	0.8	1.4	5.6	0.8	1.5	0.5

From Table 3.3, it can be seen that the biggest difference in results occurs in the radiation-only analyses. This is expected due to the error incurred by assuming the radiation boundary conditions can be approximated by a linear equation. As the influence of the term containing the approximated heat transfer coefficients increases with time, so does the error associated with the approximated linearity of the radiation. This error reaches a maximum of 3-4% at steady state. There are differences in the analytical and FE results in the convection-only analysis for the single-layer model as well. This error comes from the ill conditioning of the transcendental equation needed to determine the eigenvalues. Despite the use of double precision, truncation errors still occur. The increased influence of the $\left(1-e^{-\alpha\beta_m^2 t}\right)$ term magnifies the effects of these truncation errors. Even with these errors, agreement is better than 98% between analytical and FE. The combined convection-radiation boundary conditions display improvement over the individual analyses in the single-layer model. This improvement results from using an average sink temperature in the analytical analyses. The FE analyses use individual radiation and convection sink temperatures. The average sink temperature is lower than that used in the convection-only analysis. This effectively allows the analytical analysis to be performed with a lowered sink temperature. Even though the

analytical model over predicts the temperatures, this 'perceived' lowering of the sink temperature permits the overshoot to be in the same range as the FE results.

The combined analysis results of the three-layer model displays strong agreement, consistent with the individual analyses. The effects of ill conditioning are not observed in the three-layer model, but are the primary source of error in the single-layer model. This suggests that using the determinant of a matrix, in place of the roots of a transcendental equation, to solve for the eigenvalues improves stability and decreases the potential ill conditioning effects.

Series truncation error is negligible in the single-layer model. Table 3.2 shows that 1000 terms are sufficient. Only three terms are used in the three-layer model because of the rapid increase in the ill conditioning of the determinant values with increases in time. Still the error associated with this truncation is less than 2%.

Results of transient convection boundary conditions are within 98% of the FE results, at any given time, for both the single-layer and three-layer models. The largest discrepancies are in the regions of the maximum and minimum temperatures in the analytical modelling, due to the approximation of the sink temperatures with polynomials. Transient analyses are extremely difficult for the radiation-only and combined conditions, because of the form of the approximated radiation heat transfer coefficient. This heat transfer coefficient contains the sink temperatures, and is thus required in all of the integral equations. This results in very cumbersome and difficult integral relations, which negates the benefit of creating a simple analytical model. The added time and complexity associated with this modelling is not deemed to be efficient. The analytical model, however, does provide an accurate closed-form option for the conditions mentioned above.

Chapter 4 Sequential Thermal Stress Analysis

Having analysed the temperatures within the wingbox environment, the next task is gaining an understanding of the effects of this environment on the structure. These temperature-induced strains are referred to as thermal strains. This chapter covers the development of the FE models and experimental specimen designed to gain an understanding of the thermal stresses in a 3D strain field at the CFRP/Al double shear joint with multiple columns of three rows of titanium fasteners. Section 4.1 covers the background introduction to thermal strains and initial analytical estimations for the current geometry. Section 4.2 discusses the use of the global wingbox FE model from Chapter 2 to determine the primary area of thermal strain concentrations. Section 4.3 then goes on to develop a three dimensional FE model to be used to study the area of concern in greater detail, discussing initial design concerns in 4.3.1 and a mesh refinement study in 4.3.2. The experimental specimen design is covered in Section 4.4, which is further divided into 4.4.1 Design Concerns, 4.4.2 Non-Destructive Testing, and 4.4.3 Strain Gauge Placement.

4.1 Introduction to Thermal Strains

Thermal strain is related to the thermal expansion coefficients (α) of a given material. Thermal strain occurs when materials with differing coefficients of expansion are constrained in some way. If a structure remains unconstrained, in other words, it is allowed to expand or contract freely with any change in temperature, no thermal strain is induced. Although mechanical or fatigue loads can cause stress, such strains are not attributed to thermal mismatch. In the case under study, the constraint involves the bolted joint where dissimilar materials (CFRP and aluminium with differing α) cause some degree of thermal strain. This thermal strain, either alone, or in combination with mechanical loads, has the potential to cause damage to the joint. Understanding the degree of influence of these strains on overall joint behaviour is essential.

Consider a simplified joint with a single fastener. Figure 4.1(a) represents such a joint with two aluminium laps and a CFRP skin. Assuming that the fastener is identical on both top and bottom, symmetry allows the aluminium laps to be represented as a single lap with a thickness equivalent to the two individual laps. Figure 4.1(b) shows this scenario where the top and bottom aluminium laps

in Figure 4.1(a) are combined to form a single top lap with a thickness equivalent to the combined thickness of the single laps. The CFRP remains the same.

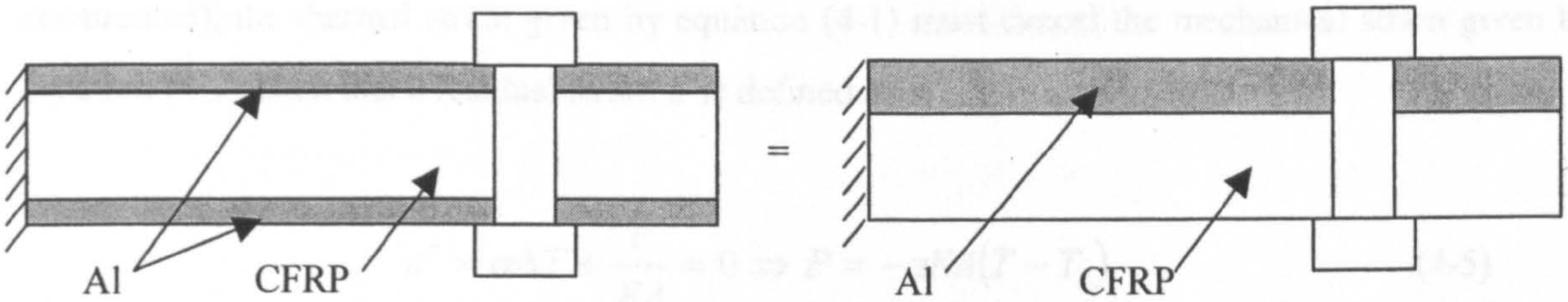

(a) Initial Geometry (b) Equivalent Geometry

Figure 4.1. Example of joint with dissimilar materials.

To develop the one dimensional (1D) fundamental equations associated with thermal strains, let aluminium be material 1, and denote all aluminium material properties with subscript $_1$. Similarly let CFRP be material 2. Assume there is no friction between the plates and the fastener, that there is a perfect fit between the fastener and the plates, and that the fastener is infinitely stiff, implying no load variation due to bending stresses. Although these assumptions neglect 3D effects and the simplifications are not entirely realistic of actual conditions, they overestimate the resulting strains, allowing a safe first approximation of the effects of thermal loading on a particular joint structure. If the fastener is removed and the plates allowed to freely expand, the strains due to a temperature change ΔT are written as [2], [3], [7]:

$$\varepsilon_1^t = \alpha_1 \Delta T \tag{4-1}$$

$$\varepsilon_2^t = \alpha_2 \Delta T \tag{4-2}$$

Here ^{t} indicates thermal strain. The strain of the aluminium and CFRP plates under mechanical loading is defined as [2]:

$$\varepsilon_1^m = \frac{P_1}{E_1 A_1} \tag{4-3}$$

$$\varepsilon_2^m = \frac{P_2}{E_2 A_2} \tag{4-4}$$

Here ^{m} indicates mechanical strain. If a plate cannot change in length, (i.e. it is completely constrained), the thermal strain given by equation (4-1) must cancel the mechanical strain given by equation (4-3), such that a residual strain ε^r is defined as:

$$\varepsilon^r = \alpha\Delta T + \frac{P}{EA} = 0 \Rightarrow P = -\alpha EA\left(T - T_o\right) \tag{4-5}$$

However, in the current problem, the plates are not completely constrained. Rather, each plate is constrained by the expansion of the opposing plate, which implies that the residual strain in the joint is described:

$$\varepsilon^r = \varepsilon_1^t + \varepsilon_1^m = \varepsilon_2^t + \varepsilon_2^m \tag{4-6}$$

Because the constraint between the two plates is through the fastener, load P_1 must equal to $-P_2$, where P_1 indicates the load in the aluminium and P_2 the load in the CFRP. Thus, from equation (4-3) and equation (4-4), along with $P_1 = -P_2$:

$$\frac{\varepsilon_1^m}{\varepsilon_2^m} = \frac{-E_2A_2}{E_1A_1} \tag{4-7}$$

Using equations (4-1), (4-2), (4-6), and (4-7), an expression for ε_1^m can be made in terms of thermally induced strains:

$$\varepsilon_1^m = \frac{\left(\alpha_2 - \alpha_1\right)\Delta T}{\left(1 + {E_1A_1}/{E_2A_2}\right)} \tag{4-8}$$

From equation (4-3), the associated load on the joint is then:

$$P_1 = \frac{\left(\alpha_2 - \alpha_1\right)E_1A_1\Delta T}{\left(1 + {E_1A_1}/{E_2A_2}\right)} = -P_2 \tag{4-9}$$

This load equation can then be used to calculate bearing, net-tension, and shear stresses. In the current analyses, the prime emphasis is on bearing and net-tension, as joints generally fail due to one of these mechanisms by standard design practice, as discussed in Chapter 1. The general bearing and net-tension stress equations are given by:

$$\sigma_b = \frac{P}{d \cdot t} \tag{4-10}$$

$$\sigma_{nt} = \frac{P}{t(w - nd)} \tag{4-11}$$

As more fasteners are added to the joint, a portion of the load shifts to the other fasteners [94]; however, these calculations can be used to estimate 2D joint loading caused by thermal variation. It is important to note that area defines the different strains, where $A=dt$ for bearing stresses and $A=(w-d)t$ for net-tension stresses.

As seen in Chapter 1, factors such as friction, clearance, and torque also have an impact on joint performance. In order to examine the effect of these factors, a more detailed analysis than the simplified 1D method discussed above must be performed. The distribution of load for three or more fasteners is indeterminate, since there is not an equal load share between all fasteners in the joint [25], [94]. This load distribution is dependent on a number of variables such as joint and fastener dimensions, fastener spacing, load application, friction, and fastener fit, as previously discussed. Due to this difficulty, a numerical model is used for analysis of the current joint.

Since temperatures are known, based on the results in Chapter 2, a study of the impact of these temperatures with respect to thermal stresses can be undertaken. A global analysis of the wingbox structure, followed by a detailed joint analysis, is performed. This work is pioneering since little work [95] has been performed on mechanically fastened joints at elevated temperatures, especially in the area of multi-fastener joint strength under these conditions.

4.2 Sequentially Coupled Thermal Stress Analysis Using Global Wingbox FE Model

The first step to analysing thermal strain is determining the effect of temperature loads, established during the wingbox temperature analysis (Chapter 2), on the stresses in the global structure. ABAQUS allows a sequentially coupled thermal stress analysis to be performed. During the heat transfer analysis, a temperature profile at each of the nodes is created and saved. These individual temperature profiles are then read into the stress analysis at the corresponding step times. In order to study through-thickness effects, solid rather than shell elements are required. In the current case, 2D quadratic solid plane strain elements (CPE8) are used to model the spanwise and chordwise geometries. These elements are utilized because the wingbox is sufficiently thick in both spanwise and chordwise directions to justify the assumption of no strain into the plane. The geometry remains the same in both analyses, but elements used in the heat transfer analysis can be removed from the coupled stress analysis if they are not structurally required.

The thermal material properties are the same as in the heat transfer analysis, Table 2.1, and the additional strength properties are shown in Table 4.1.

Table 4.1. Material Properties.

Material	Young's Modulus E x 10^{-3}(MPa)	Coefficient of Thermal Expansion α x 10^{6} (mm/K)	Poisson Ratio ν
CFRP 1*	75.2	0.86	0.2
CFRP 2	9.6	28	0.39
CFRP 3	36.2	5.0	0.02
Aluminium	71.7	23	0.3
Titanium	103.0	9	0.29

*1=in-plane, 2=through-thickness, 3=transverse

The CFRP properties come from a lay-up pre-selected by Airbus containing 46% 0°, 42% ±45°, and 12% 90° fibres. This lay-up is given nominally: $(\pm 45,90,0_3)(\pm 45,90,0_2)(\pm 45,0_2)(\pm 45,90,0_2)(\pm 45,0_2)]_s$. Insulated boundary conditions are used on both left and right sides. These boundary conditions form the worst-case scenario. Since no heat is transferred laterally to other parts of the wing, there is less of a cooling effect. In the sequential

stress analysis, an additional boundary condition of symmetry on the bottom wingbox surface is introduced in order to hold the model vertically in space, as displayed in Figure 4.2. Elements used in the heat transfer analyses to represent the cooling fluid, air or fuel, are removed for the stress analysis, leaving only the solid materials aluminium, CFRP, and titanium, for analysis.

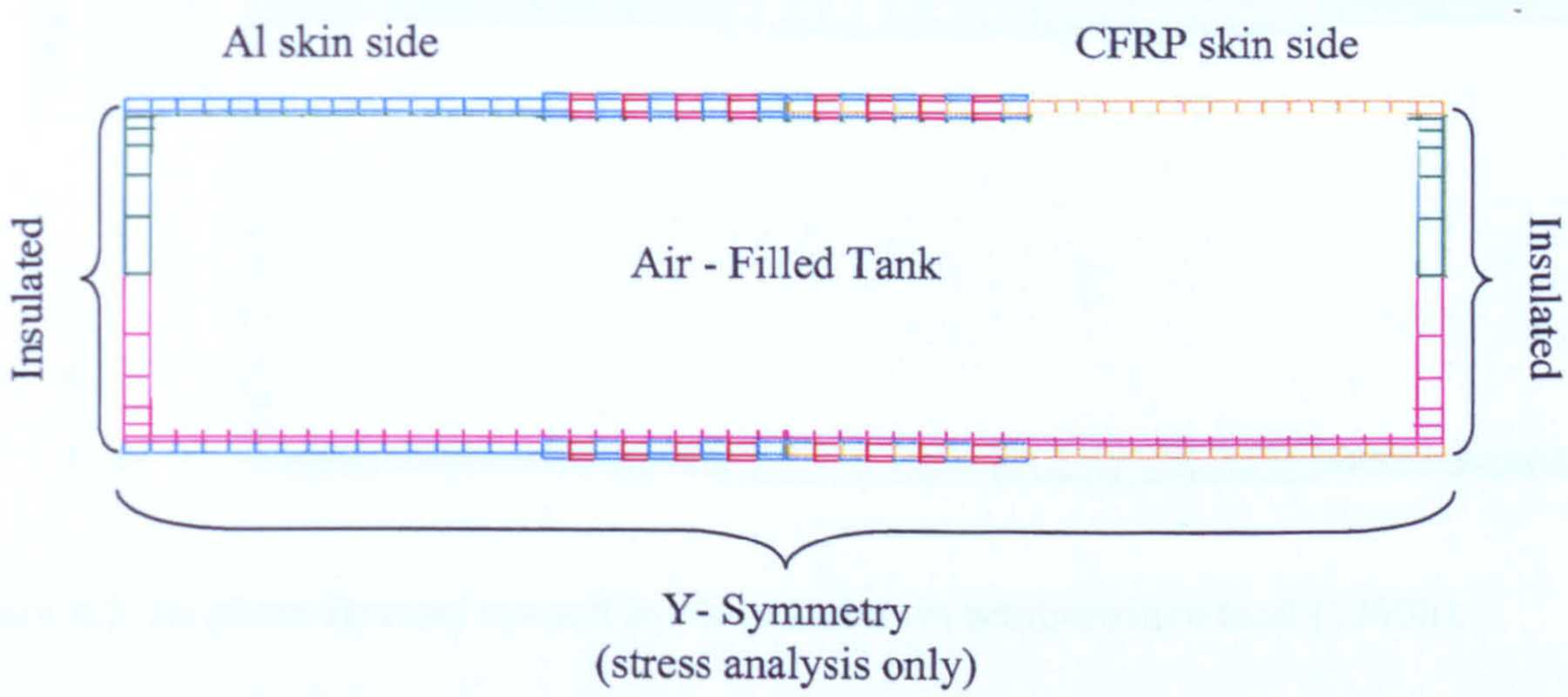

Figure 4.2. Boundary conditions for sequentially coupled thermal-stress analysis.

In this 2D global model, the fasteners are modelled as pins by changing the material property of every second element in the joint region. The one-to-one spacing is not representative of the actual joint region, but allows for a preliminary investigation of global heat transfer effects. It is important to note that each element is connected to every other element; that is, the model is one component including laps, skin, and fasteners. The clearance that exists between the fasteners and the laps, as well as between the skin and the laps, is assumed to be sufficiently small so no change in the temperature results from heat transfer across these gaps. Results from a simple model using gap radiation, whereby the resulting temperatures differ by less than one percent from the solid element analysis validate this assumption. It is anticipated that contact plays a role in stress distribution, especially due to the importance of friction (Chapter 1); however, this investigation is left for the more detailed strain analyses.

Figure 4.3 outlines the results of the sequentially coupled stress analysis for the spanwise model at the highest temperatures, which from the thermal analysis occurs at approximately 1300h (1pm) for the air-filled tank. The air-filled tank provides the worst-case scenario, resulting in the highest temperatures, and is chosen for further analysis. The highest temperatures provide the greatest

temperature difference, inducing the most significant thermal stress. These stresses are shown in the in-plane (y) direction.

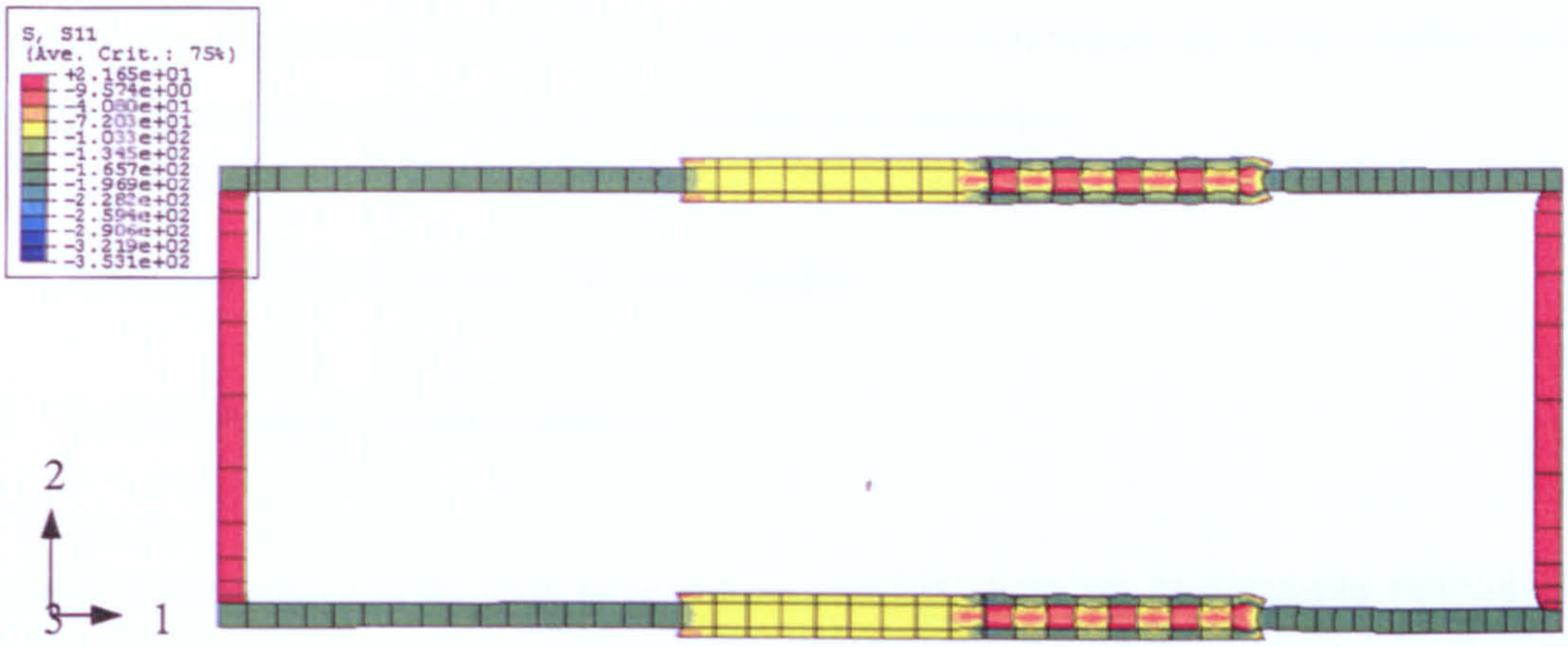

Figure 4.3. In-plane stresses caused by the maximum temperature load (1300h).

From Figure 4.3, it is evident that the highest stresses occur in the aluminium laps on the CFRP skin side of the joint region. This is as expected, given this area represents the greatest dissimilarity of material and corresponding coefficients of expansion. These peak stresses match well with those calculated using equations (4-9) and (4-10). A comparison of the FE and simplified analytical 2D results are shown in Table 4.2. Note all values are based on results between pins.

Table 4.2. Comparison of analytical and FE bearing stresses in the CFRP skin side of the 2D wingbox joint.

	Analytical Stress (MPa)	FE Stress (MPa)
CFRP skin	24	22
Al lap	-58	-103

Based on the above observations, this joint region of the wingbox requires further investigation in order to accurately characterize potential stress and strain concentrations in the vicinity of the fasteners and to gain a better understanding of the impact of thermal loading on such mechanically fastened joints. Even when the aircraft is resting on the tarmac, there is a combination of thermal and mechanical stresses on the wingbox at any given time. The mechanical stress results from the weight of the wing itself, which causes bending in the spanwise direction of the wingbox. Additional bending may be induced by temperature differences between the top and bottom skins. Bending in

turn, results in corresponding tensile loads on the top wingbox surface and compressive loads on the bottom wingbox surface. Since the top surface is of primary interest for thermal conditions, a tensile mechanical load on this surface is examined. This leads to a better understanding of the combined loading effects. To achieve this objective, the design of a detailed model of the double lap joint on the CFRP skin side of the top wingbox surface becomes necessary.

4.3 Detailed CFRP Joint FE 3D Model

4.3.1 Initial Design Considerations

The material mismatch and the high temperatures resulting from the heat transfer analysis make the area of the double lap joint on the CFRP skin side of the top wingbox surface the target of further investigation. A more accurate representation of such a joint is used to examine geometric effects and thermal mismatch in this area, which lends itself to combined thermal-mechanical load analyses. Airbus UK© [96], [97] provides a preliminary joint design with approximate geometry as shown in Appendix 4A. A pitch of 3d is used. The fastener dimensions are given in Table 4.3 and the nut dimensions in Table 4.4.

Table 4.3. Fastener dimensions.

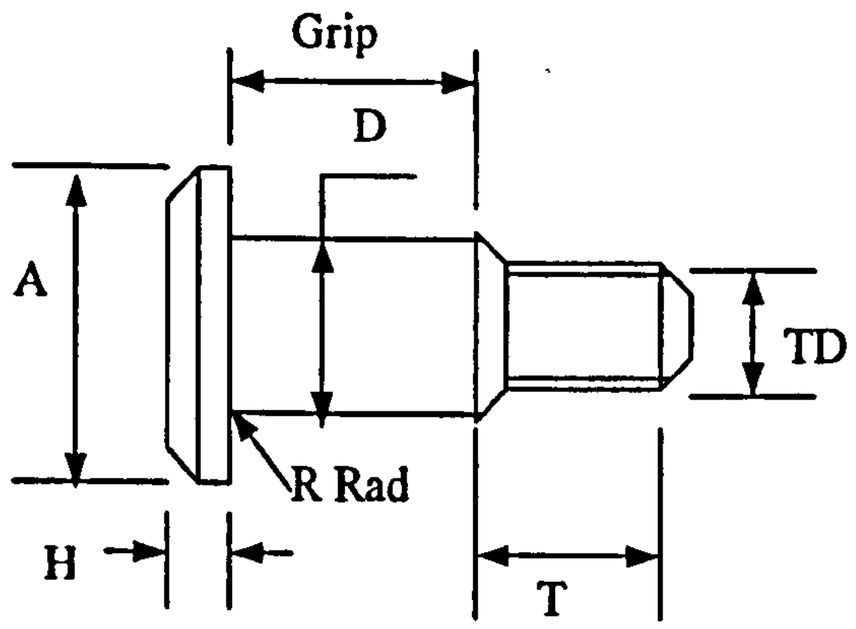

Thread UNJF – 3A (inches)	T	D	A	TD	H	R Rad
0.5000-20	13.34	12.687	19.56	12.522	4.77	0.76
		12.662	18.21	12.395	4.52	0.51

*All dimensions are in millimetres unless otherwise stated.

Table 4.4. Self-locking nut with captive washer dimensions.

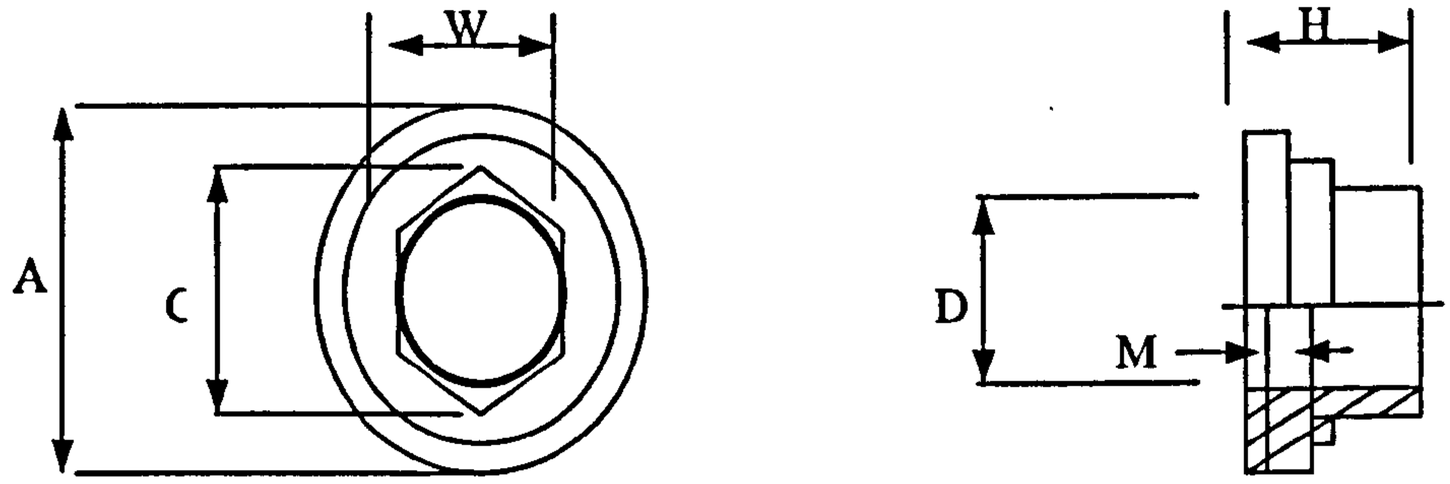

Thread Size UNJF - 3B (inches)	A Max	C Min	D Min	H Max	M Min	W Max	W Min
0.5000-20	21.84	16.18	13.74	11.05	1.83	14.38	14.02

*All dimensions in millimetres unless otherwise stated.

In order to include the effects of contact between the plates and the fasteners, which are shown to have a significant influence on stress distributions (Chapter 1), 3D models using solid brick and wedge elements (C3D8 and C3D6, respectively) are designed. The laps, skin, and fasteners are modelled as individual meshes; they contain no coincident nodes. This means that the only method of load transfer between the individual parts is through their contact surfaces. This allows for a more accurate representation of actual wingbox loading conditions. Note that because the washers used are captive within the nut, the nut, washer, and fastener are modelled as a single unit. Figure 4.4 shows an example of the contact surfaces for the fastener and joint.

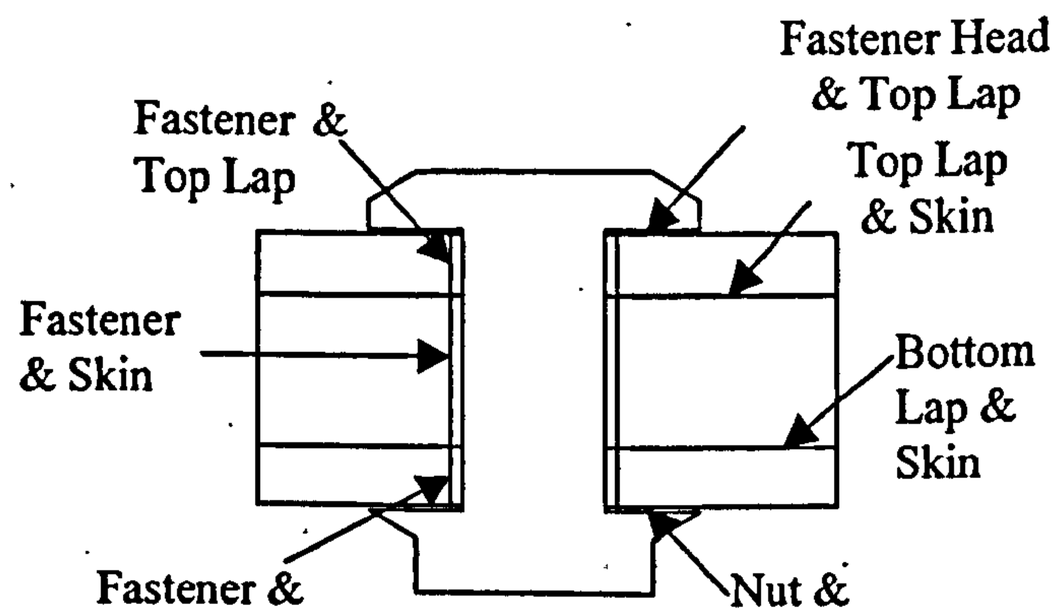

Figure 4.4. Contact surfaces.

Contact analyses are complex, and the accuracy of the results depends on how well the potential contacts are modelled. ABAQUS offers several potential contact analyses. The one most appropriate for the current problem is contact between two deformable bodies with minimal sliding. There are three steps in defining contact interaction: creating the surfaces, specifying which surfaces interact, and defining the governing behaviours at the surfaces, an example of which is friction. The user defines which surfaces interact in terms of contact pairs. For each node on the first surface (slave), ABAQUS attempts to find the closest point on the second surface (master), where the master surface normal passes through the node on the slave surface as depicted in Figure 4.5. The interaction is then discretized between the point on the master surface and the slave node.

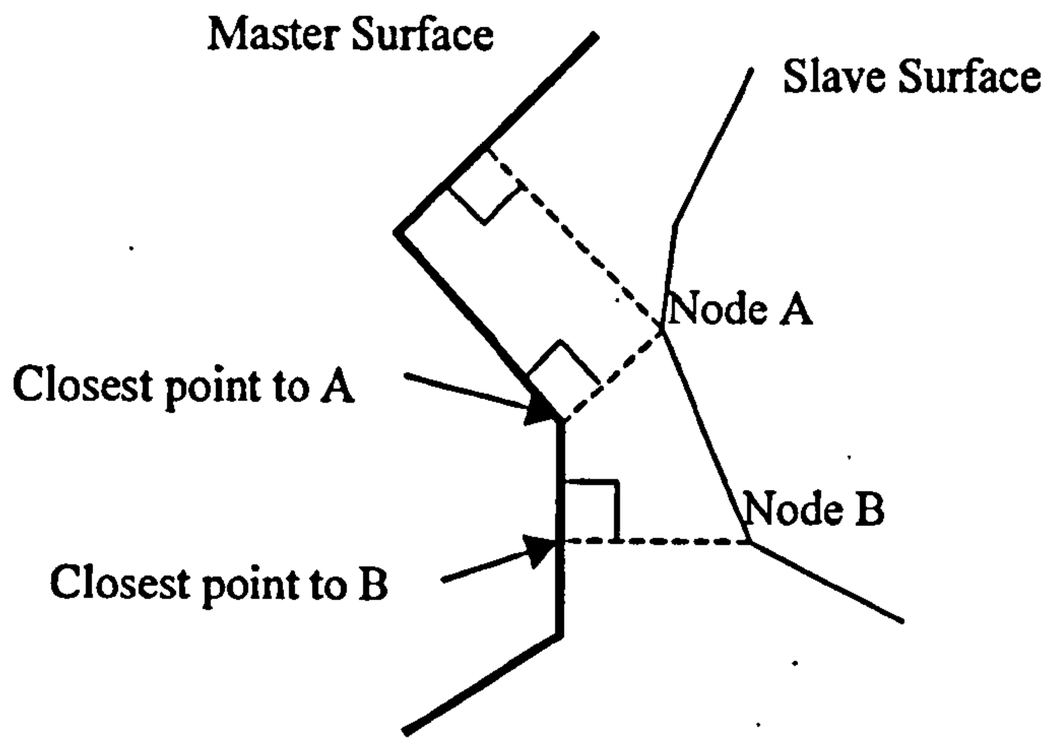

Figure 4.5. Master-slave contact description.

Using a strict "master-slave" algorithm, the slave nodes are constrained so as not to penetrate into the master surface; however, the nodes of the master surface can penetrate into the slave surface. The contact direction is always normal to the master surface.

4.3.2 Mesh Refinement Study

To determine the appropriate mesh required to achieve accurate strain levels, especially around the vicinity of the holes, a mesh refinement study is performed. Three different mesh sizes are studied to find the level of mesh refinement required to achieve convergence. The coarsest mesh has six elements around 180° of the diameter of the hole, and three elements radiating out from the hole. Through the thickness, there are two elements in each lap and three elements through the CFRP skin, as seen in Figure 4.6(a). The boundary conditions for all analyses are also shown in Figure 4.6(a).

Symmetry exists along the front face to allow for half-modelling, while the back face is left to move freely. The left side of the aluminium laps are constrained using x-symmetry, while the loading, in the form of a displacement (0.5mm), is applied to all nodes on the right side of the CFRP skin. Identical boundary conditions apply to all cases. The second mesh uses sixteen elements around the hole and five elements radiating out from the hole. Through the thickness, there are three elements in each lap and six elements through the thickness of the CFRP skin, demonstrated in Figure 4.6(b). The finest mesh has thirty elements around the hole, six elements radiating outward, three through the thickness of each of the laps, and eight through the thickness of the CFRP skin, Figure 4.6(c). A simple tensile test, where a displacement of 0.5mm is applied, provides a comparison of stresses.

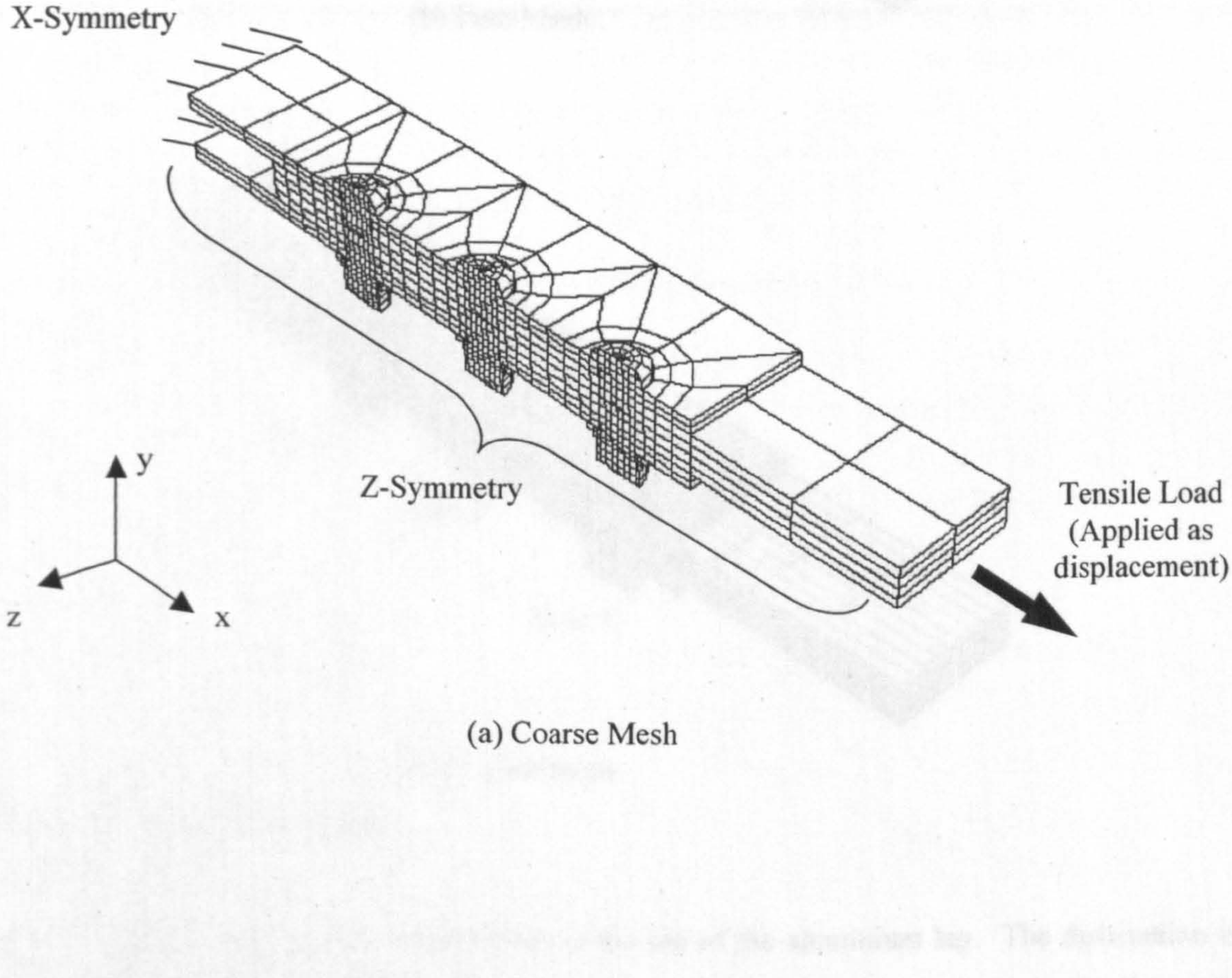

(a) Coarse Mesh

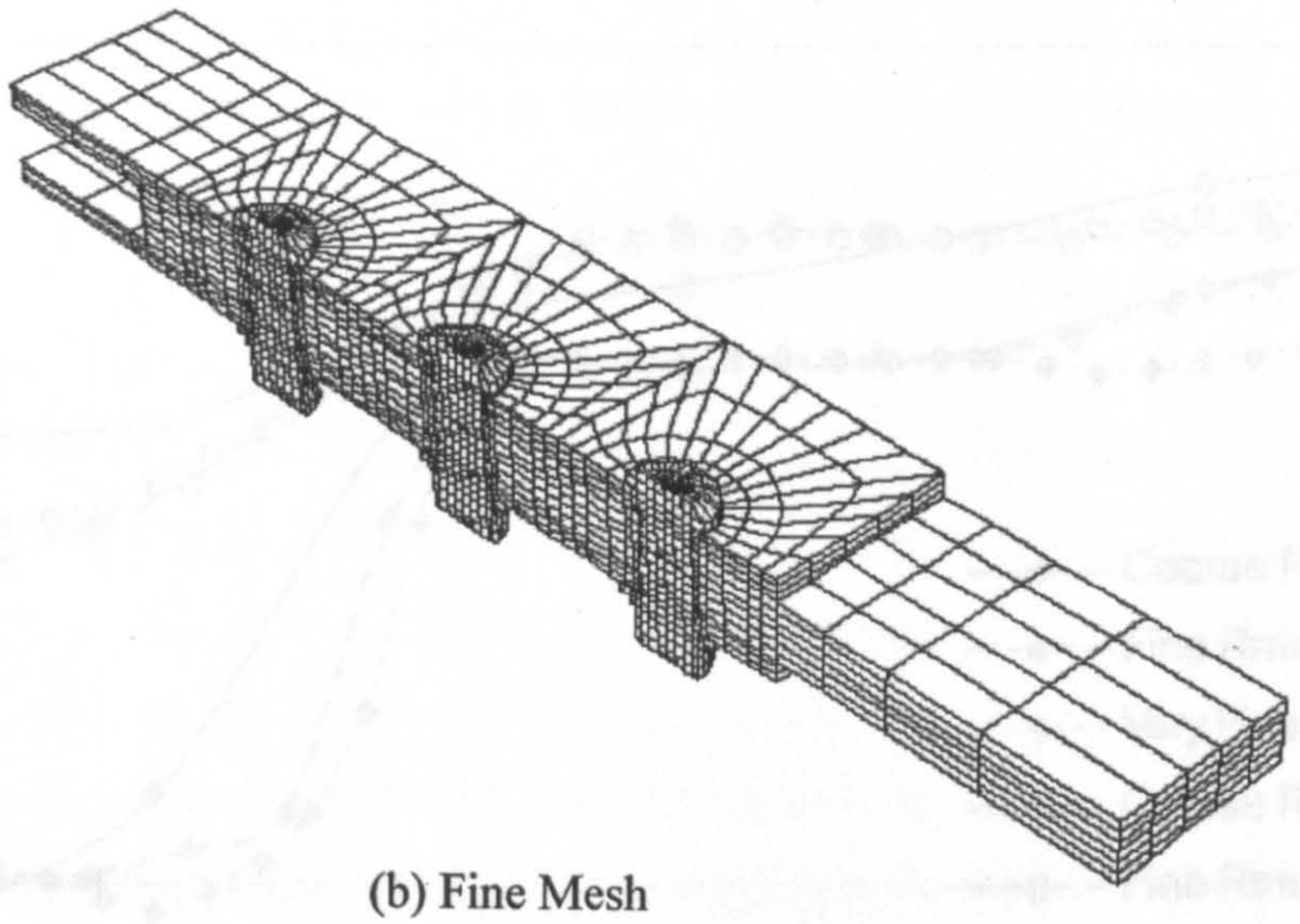

(b) Fine Mesh

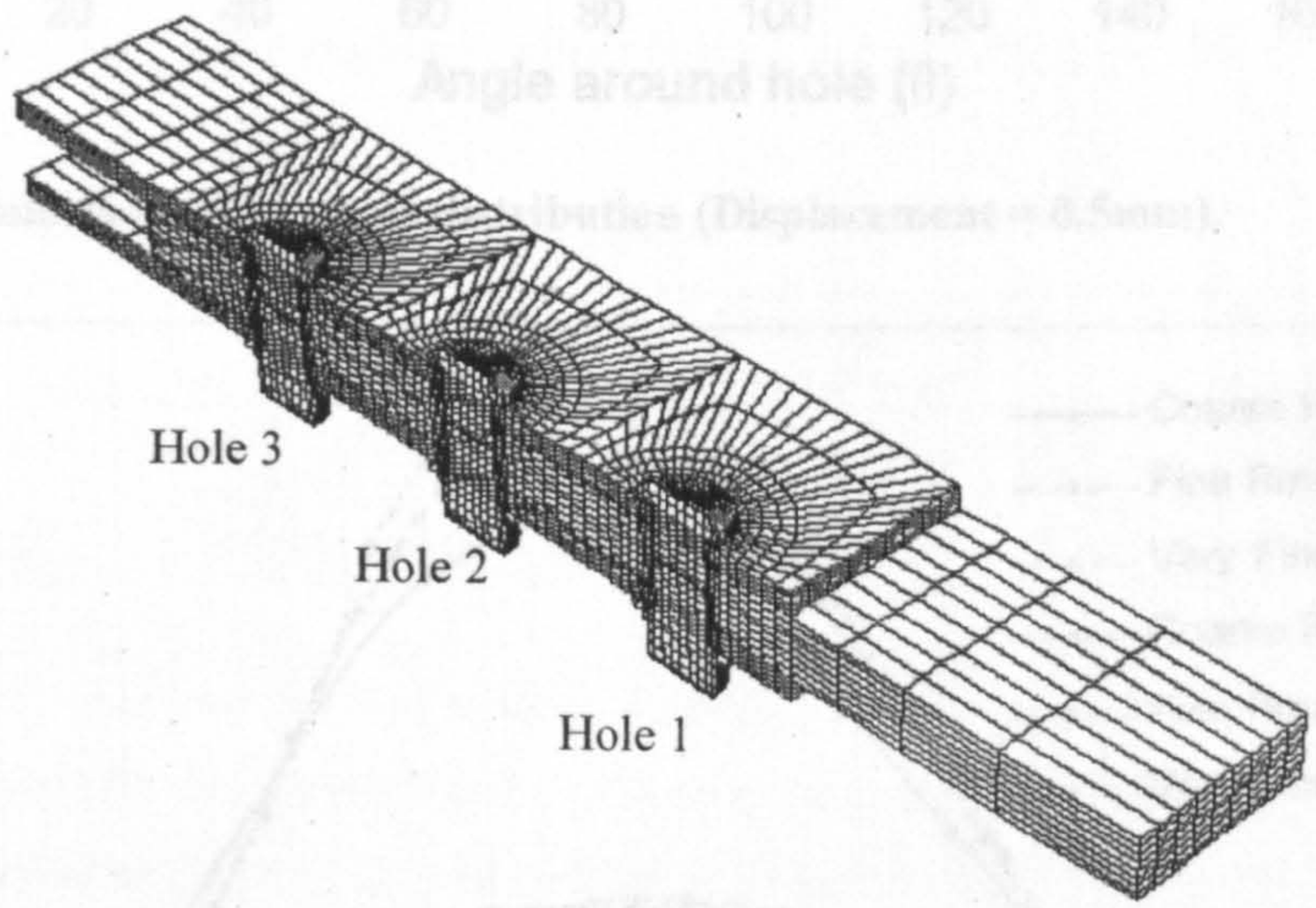

(c) Very Fine Mesh

Figure 4.6. FE mesh refinements.

Figure 4.7 details the radial stress distribution at the top of the aluminium lap. The distribution is shown around hole 1, where angle $\theta = 0°$ corresponds to the bearing plane. The stress distribution is normalized by taking σ_r/p_o, where $p_o = P/dt$. Figure 4.8 outlines the tangential stress distribution corresponding to the net-tension behaviour. The normalization in this case is $\sigma_t/[P/(w-d)t]$. For comparison, stresses are shown at two radii: R_{min}, directly at the hole edge, and R_{max}, 19mm from the edge of the hole.

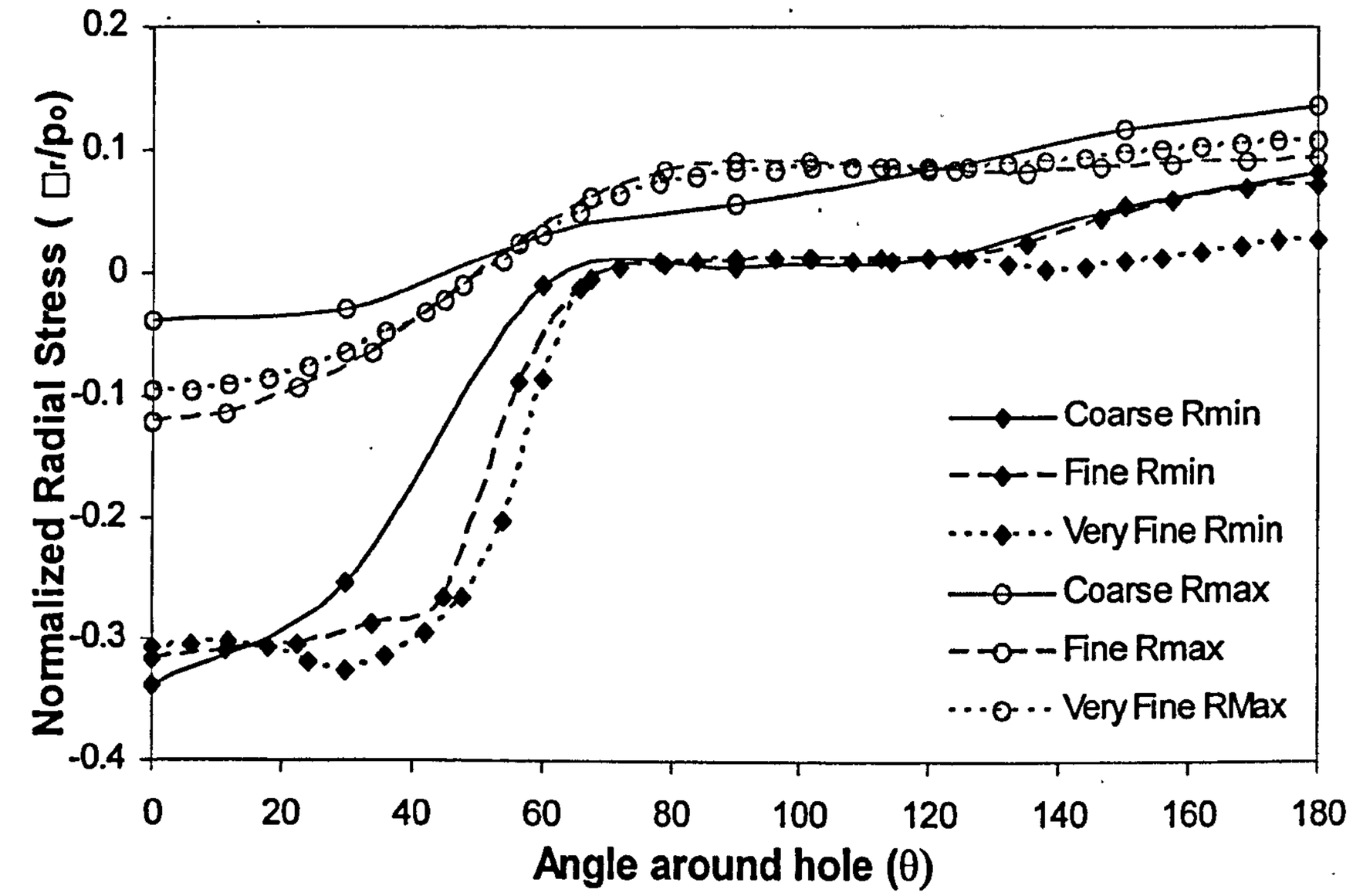

Figure 4.7. Normalized radial stress distribution (Displacement = 0.5mm).

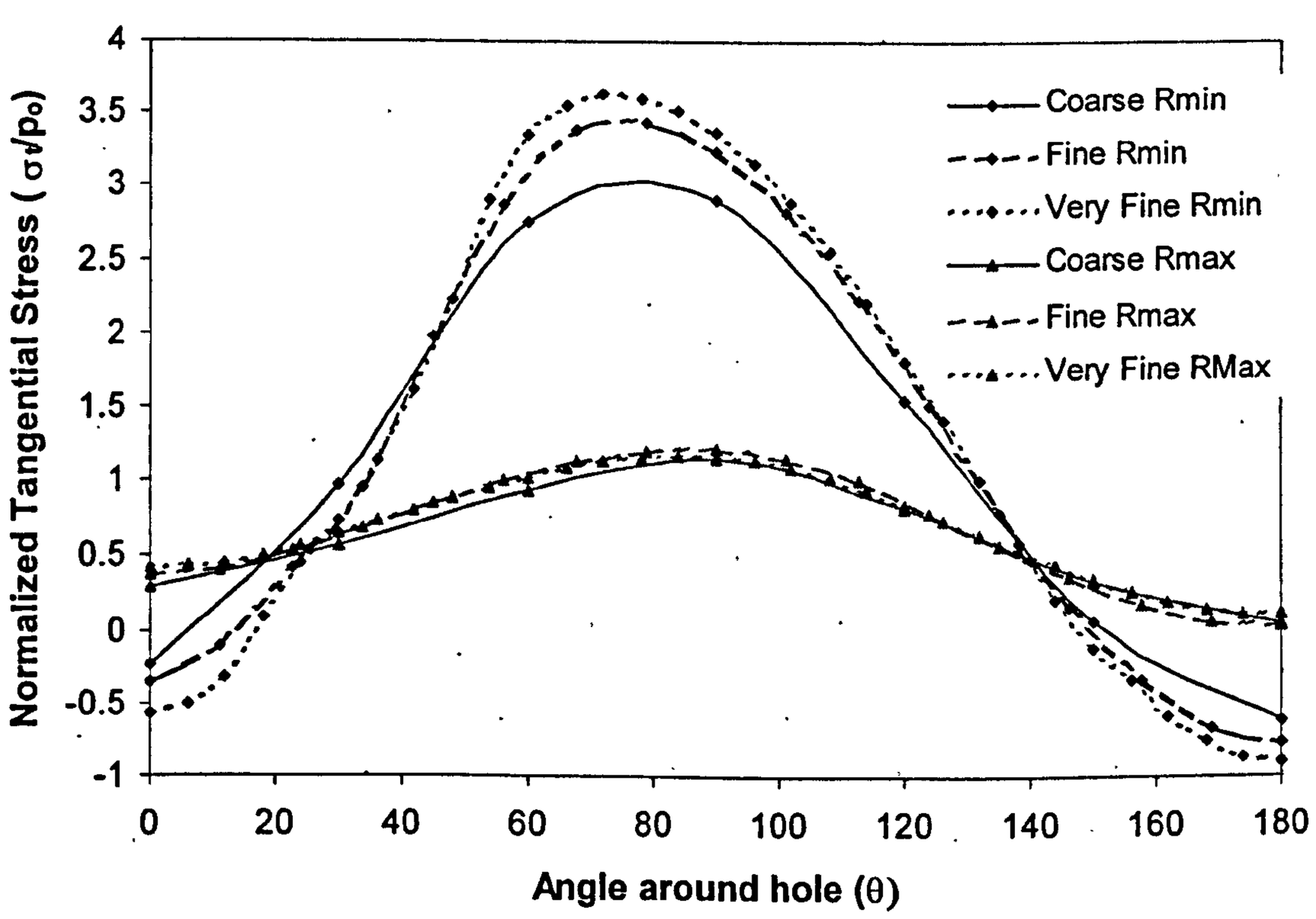

Figure 4.8. Normalized tangential stress distribution (Displacement = 0.5mm).

From Figure 4.7 it can be seen that the coarsest mesh shows the greatest discrepancy at $\theta = 50°$, where this mesh under-predicts the radial stress by as much as 37% compared to the finest mesh. The largest radial strains are shown to occur at 0° for the coarse mesh, but appear closer to 30°, suggesting these meshes better account for interaction between fasteners. This region is expected to have the maximum strains due to the contact relationships caused by the tensile load. From Figure 4.8, the greatest tangential stress by approximately 17% near $\theta = 75°$. The biggest difference occurs at the surface of the hole (R_{min}), as expected, given the of stress concentrations in the net-tension area due to tensile loading. All three meshes result in similar predictions at a radius of 19mm from the edge of the hole. The agreement between the fine and very fine meshes is good, with a maximum difference of 12% in terms of radial stress and less than 6% difference at the maximum tangential stress.

A comparison of the CPU times, memory, and disk space requirements for each of the three meshes is presented in Table 4.5. The computing system uses a Unix based system with 5 Gbytes disk space.

Table 4.5. Comparison of computing requirements.

Mesh Type	CPU Time (s)	Minimum Memory (Mbytes)	Minimum Disk Space (Mbytes)
Coarse Mesh	981.97 (16.36 min)	38.0	102.0
Fine Mesh	11116 (3.09 hrs)	254.85	901.97
Very Fine Mesh	80807 (22.45 hrs)	837.0	4150.0

The time and space required for the analysis increases dramatically as the number of elements increase. Disk space becomes prohibitive in the very fine mesh analysis. Furthermore, in more complex thermal-mechanical analyses, the disk space becomes insufficient to complete the analyses, thereby limiting the usefulness of the model. Given the closeness in accuracy of stress results between the fine mesh and very fine mesh, the most efficient and economical mesh design from a computing standpoint, as well as for numerical accuracy, is the fine mesh.

4.4 Experimental Design

4.4.1 Initial Specimen Design

In order to validate the results of the FE analyses, an experimental program is designed. The joint geometry, as given in Appendix 4A, is used as a reference to create a joint with two columns of three rows of fasteners. The lay-up outlined previously is used to form a 12mm thick CFRP skin, and 7075 Al, with the properties from Table 2.1, is used to form the two 5mm laps. Airbus UK provided the CFRP and the aluminium. Joints with protruding titanium fasteners, torque-tightened to two different levels, are investigated under thermal and mechanical stress conditions. The dimensions of the experimental specimen are given in Appendix 4B.

A Zwick Model 1466 Twin-column Servoelectric Universal Test Machine with a temperature control chamber performs tensile tests at room temperature (295K) and high temperature (373K). The high temperature is based on previous heat transfer analyses (Chapter 2). The temperature chamber contains an electrical heater to provide a constant heat source. However, it is not capable of heating at a given ramp speed. The CFRP is machined to the appropriate dimensions using a diamond saw, while the aluminium plates are prepared using conventional metal-working tools. Machining of the holes is a concern, due to possible delamination in the CFRP, which has the potential to lead to variation in the resulting strain distributions. Both Farrow et al. [98] and Persson et al. [99] demonstrate that the machining of holes in composite plates significantly affects strength at these holes. The effect of defects in holes is also shown to be a function of the material and lay-up by Pengra and Wood [100]. Delaminations introduced by the high axial forces at the tip of the drill reduce laminate strength. Farrow et al. [98] suggest using front and back plates to reduce entry and exit induced damage.

To reduce these delaminations and minimise damage, the aluminium laps are clamped to the CFRP plate and used as front and back drilling plates. This helps two-fold: it prevents push-through effects that generally cause delaminations, and it also serves to ensure the correct alignment of all three plates, which promotes a more even strain distribution. The holes are drilled using a standard metal drill bit, then reamed to achieve the desired dimensions as per Airbus UK© design specification [101]. The individual diameters of the holes, along with the corresponding fasteners, are measured. Table 4.6 gives these measurements. The same fasteners are used in the same holes for each test to

eliminate any dimensional discrepancies that might influence strain distribution. Holes 1 and 4 are at the top of the aluminium laps nearest the CFRP skin, while Holes 3 and 6 are at the bottom of the laps, as annotated in Figure 4.9.

Table 4.6. Hole and fastener diameters.

	Hole/Bolt 1	Hole/Bolt 2	Hole/Bolt 3	Hole/Bolt 4	Hole/Bolt 5	Hole/Bolt 6
Hole Laps	12.700	12.715	12.695	12.710	12.710	12.710
Hole Skin	12.700	12.715	12.695	12.710	12.710	12.710
Fastener	12.660	12.650	12.660	12.650	12.650	12.660
Clearance (Laps)	0.04	0.065	0.035	0.06	0.06	0.05
Clearance (Skin)	0.04	0.065	0.035	0.06	0.06	0.05

* All dimensions are in millimetres.

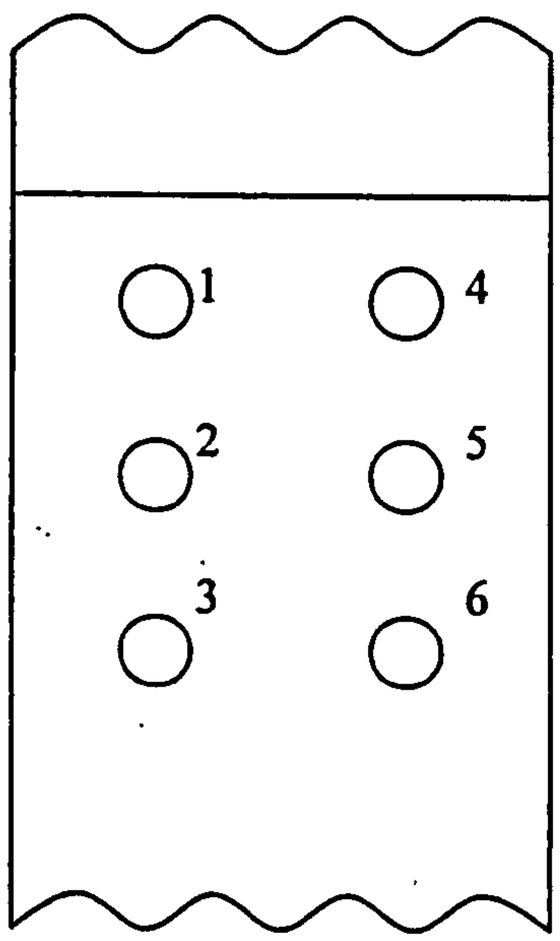

Figure 4.9. Experimental specimen hole numbering.

The hole tolerances are at the low end of those given in the Airbus Design Handbook[101], where it is suggested that the hole dimensions be within 12.713mm to 12.789mm. The fastener shanks fall slightly below the values of 12.662mm to 12.687mm, given in the Design Handbook. The values provided in the Airbus Design Handbook produce a minimum clearance of 0.026mm and a maximum clearance of 0.127mm. Table 4.5 demonstrates that the experimental values between

0.035mm and 0.065mm fall within the clearance boundaries, and are therefore, within acceptable tolerances.

4.4.2 Strain Gauge Placement

Temperatures are measured with high temperature rosette strain gauges, UFRA-2-23 [102], having the same coefficient of thermal expansion as aluminium ($\alpha = 23 \times 10^{-6}$) with a gauge length of 2mm. These gauges have a working temperature range of -60°C to 120°C. The CN (cyanoacrylate) adhesive has a temperature range of -30°C to 120°C. Rosette gauges permit the reading of tangential, radial, and shear strains in the vicinity of the fastening holes. However, the current joint is designed for bearing failure, net tension is catastrophic; therefore, experimental efforts concentrate on obtaining the resulting radial and tangential strains. Despite the fact that Figure 4.7 shows maximum radial strains at 30°, and Figure 4.8 indicates maximum tangential strains occur at approximately 75°, the size of the gauges limits the number that can be applied around each hole. In order to obtain a maximum number of results, while allowing for a direct comparison with FE nodal results, strain gauges were placed at angles of 0°, 45°, and 90°, with the measuring area of the strain gauge at a distance a = 6mm from the edge of the hole to allow sufficient space for the fastener head. In order to reduce edge effects on strain values, the gauges are positioned "inside" the joint, closer to the centreline, rather than near the outer edges. The resulting strains are expected to provide good characterisation of the strain patterns and magnitudes, as well as provide adequate validation of FE results.

Figure 4.10 shows the placement of gauges at holes 3 and 6 on the top surface of the upper aluminium lap. A second 0° gauge is placed on hole 6. This second 0° gauge provides confidence in the strain readings. Hole 3 also has gauges at 0° and 90° on the bottom face of the lower aluminium lap, as shown in Figure 4.10(b). These gauges check the degree of symmetry between the upper and lower aluminium laps. Since fasteners are used instead of pins, symmetry cannot be expected, but monitoring the variation in symmetry, especially at different torque levels, is a desired check. Holes 1 and 4, as well as 2 and 5, have identical gauge placements on the upper surface; however, none of these holes contain gauges on the lower aluminium lap.

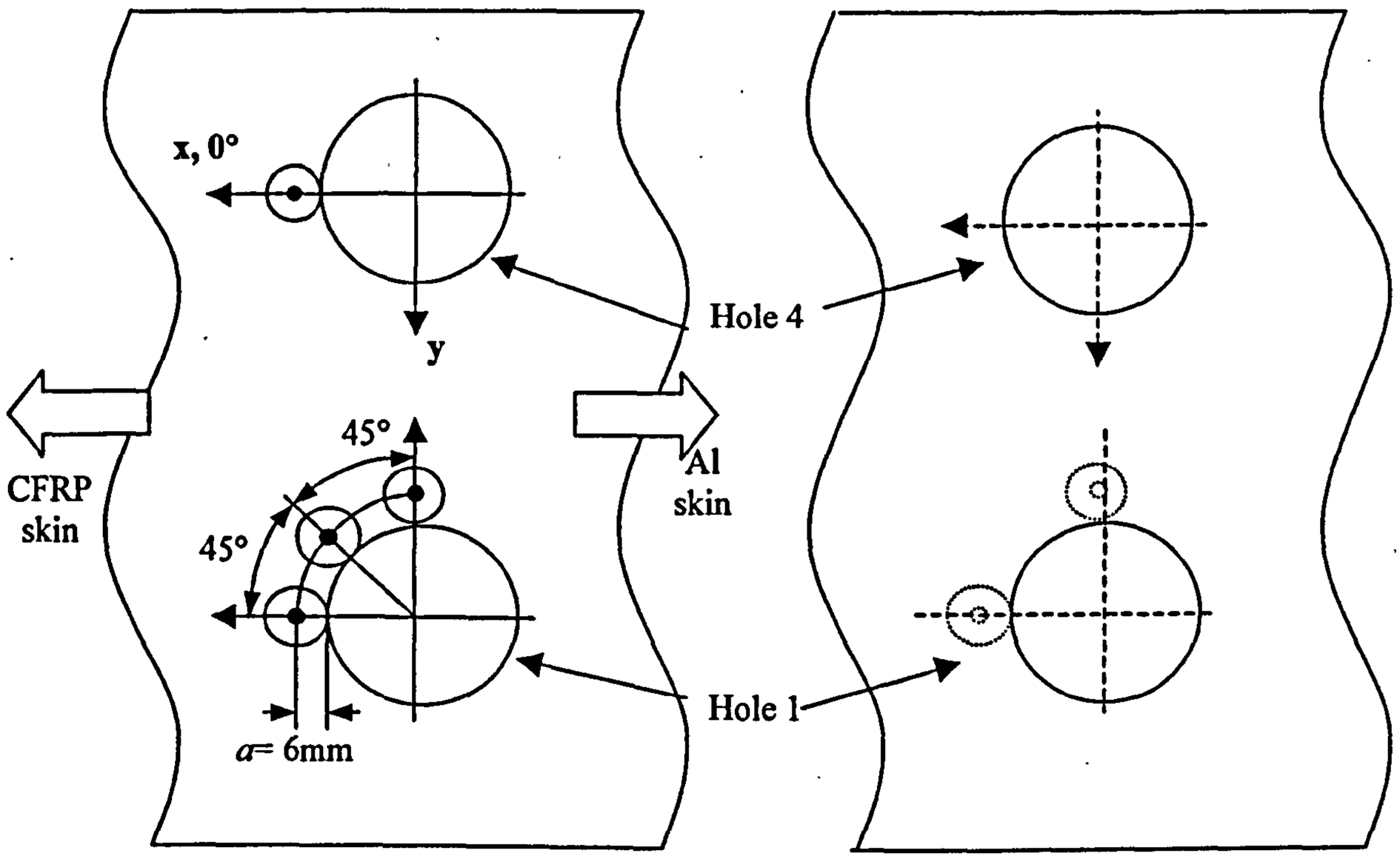

(a) Top face of upper aluminium lap

(b) Top face of lower aluminium lap

Figure 4.10. Strain gauge placement.

Once the gauges are positioned on the aluminium laps, the experimental joint structure can be assembled. The loading arrangement of the Zwick Model 1466 requires the specimen to be positioned vertically, suspended at the CFRP side, with loading applied to the aluminium lap side. Figure 4.12 shows the specimen inside the oven chamber attached to the Zwick Model 1466, while Figure 4.12 shows the specimens in detail, indicating hole numbers and gauge positions.

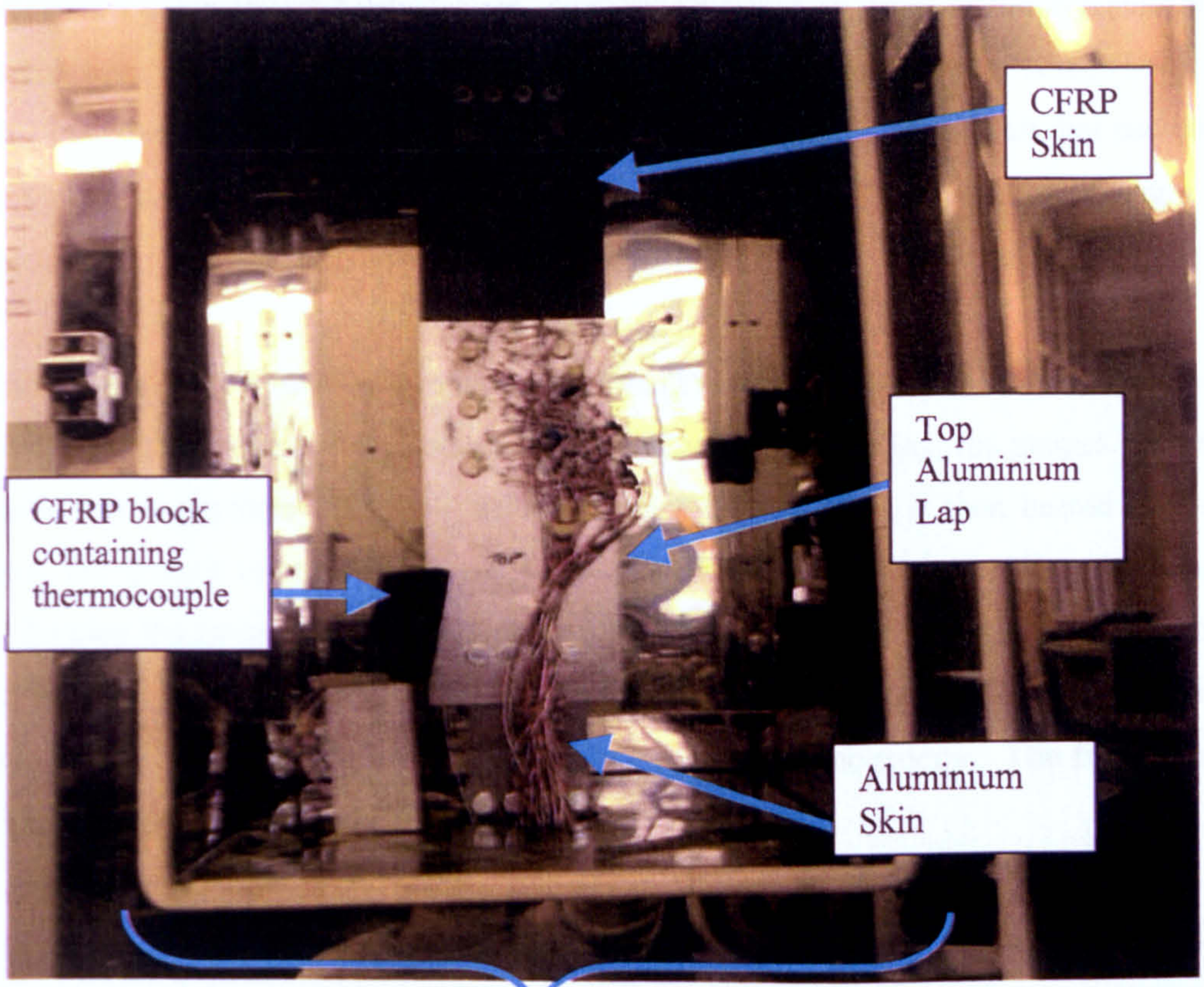

Figure 4.11. Picture of experimental set-up.

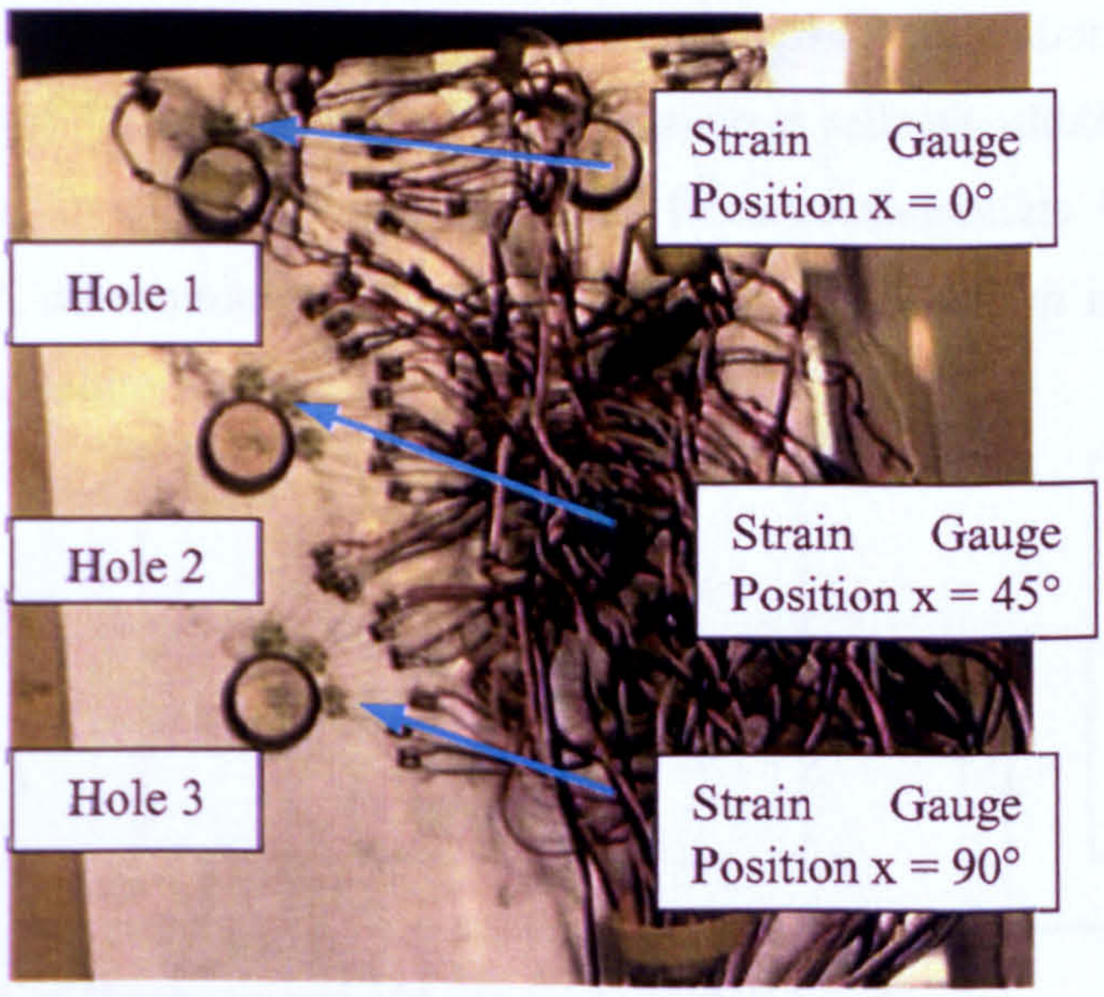

Figure 4.12. Picture of detailed specimen.

The data-collector contains eight strain gauge channels; therefore, in order to obtain results at each of the gauge positions, the experiments are run a number of times to obtain two readings at each of the 14 gauges. Based on similarity of results, two runs is deemed adequate. Recall that each of the 14 gauges actually contains three gauges (1 radial, 1 tangential, and 1 shear), each requiring a separate channel in the data recorder.

Tensile tests are run first at ambient room temperature (295K) then at 373K. Before each new gauge reading, the oven chamber returns to ambient temperature by air-cooling, the gauges are re-zeroed, and a tensile test is performed at room temperature. The specimen is then heated to the higher temperature, the gauges re-zeroed, and the specimen tensile tested while holding the temperature constant. Zeroing the gauges at room and again at high temperature, allows direct comparison of the tensile strains at both temperatures. Prior to any tensile testing, the specimen is held at the given temperature a minimum of 10 minutes to ensure temperature homogeneity. The full experimental procedure is outlined in detail in Appendix 4D.

In order to gain a temperature reading without influencing joint geometry, a thermocouple is placed in a hole drilled into a separate piece of CFRP. Reading this temperature, rather than the temperature of the oven chamber, determines joint saturation at a given temperature, and signals tensile testing commencement. Figure 4.13 illustrates the position of the thermocouple placement into the CFRP block, while Figure 4.12 shows the placement of this block within the experimental chamber. The block is positioned at the height of the test specimen to minimize variation due to thermal currents. Minimizing contact between the block and other components reduces additional heat transfer effects, and contributes to accurate temperature readings. Because aluminium has high conductivity in comparison to CFRP, determining temperature saturation in aluminium is not an issue; therefore, only a CFRP block is monitored.

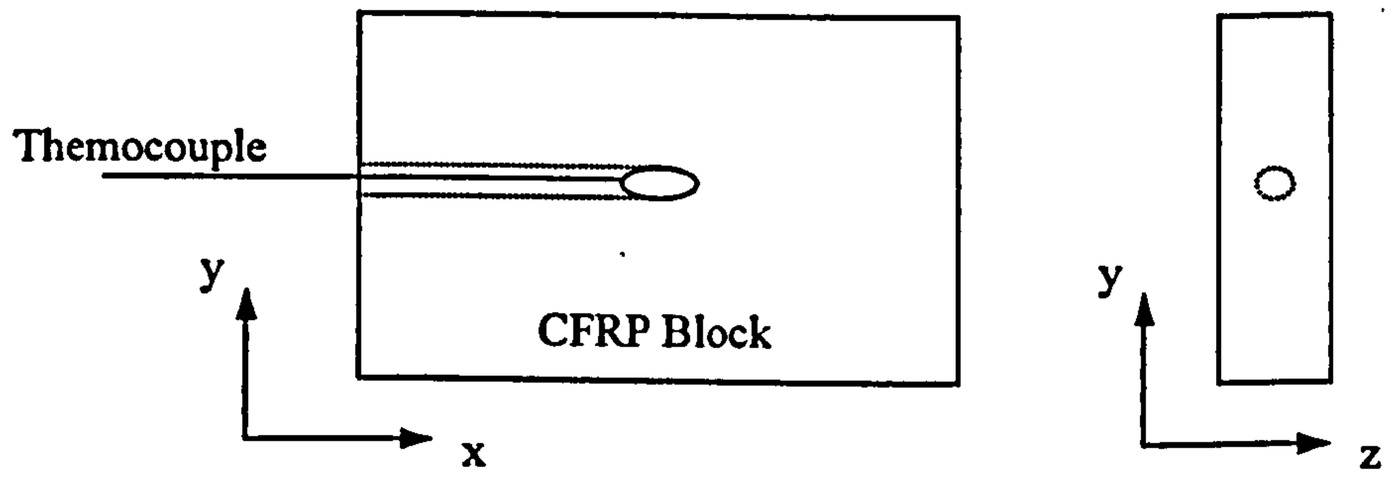

Figure 4.13. Position of thermocouple in separate CFRP block.

Based on this experimental procedure, and using the fine mesh as determined by the mesh refinement study, a method for studying the influence of thermal and mechanical loading on a multi-fastener joint specimen has been established.

Chapter 5 Experimental Results - Finger-Tight Torque (1Nm)

As outlined in Chapter 1, the torque level of a bolted joint plays a significant role in load distribution and overall strength of the joint. In the current work two torque-levels are examined: finger-tight (1Nm) and aircraft operationally torque-tight (35Nm)*. Firstly, the fasteners on the joint containing two columns of three fasteners each are tightened to 1Nm, equivalent to finger-tight. Tensile tests are then performed at 295K and 373K to compare temperature effects on joint strain. Strain gauge readings are taken at 0°, 45°, and 90°, and these values are compared with the FE results of the very fine mesh as detailed in Chapter 4. Figure 5.1 shows the gauge positioning and the direction of radial and tangential strains.

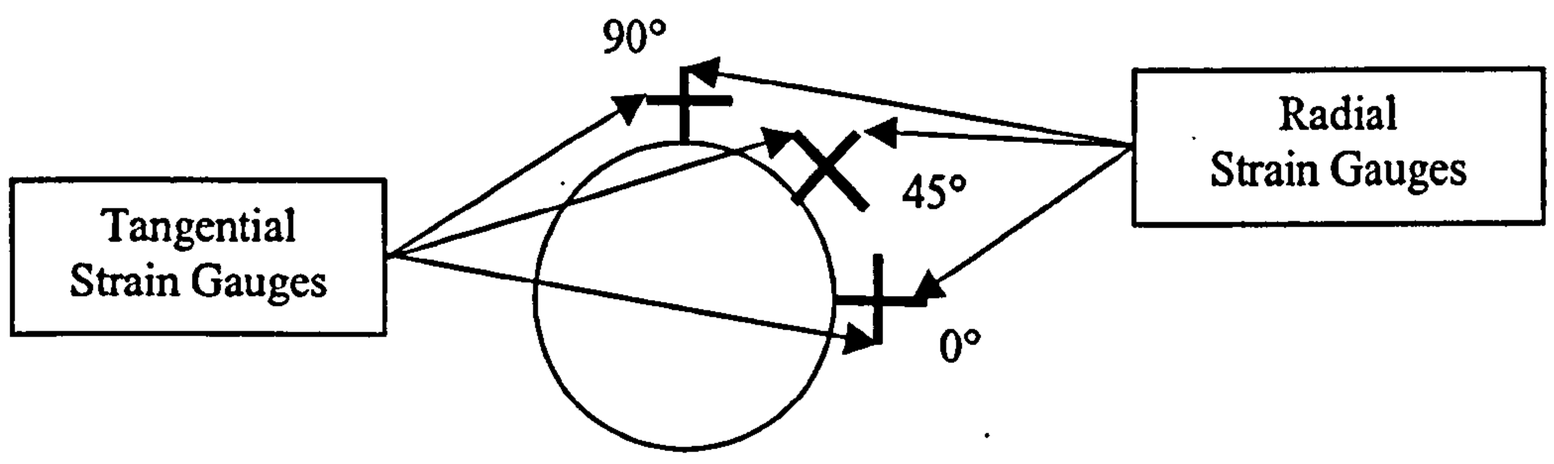

Figure 5.1. Diagram of radial and tangential gauge positioning.

Section 5.1 outlines load versus displacement results at 295K and 373K. Section 5.2 contains the radial strain results, and is divided into sections with 5.2.1, covering the 0° results, 5.2.2, the 45° results, and 5.2.3, the 90° results. Section 5.2.4 compares the through-thickness symmetry at 0° and 90°. Section 5.3 encompasses the tangential strains, with results at 0°, 45°, and 90° covered in 5.3.1, 5.3.2, and 5.3.3, respectively. Through-thickness symmetry is examined in 5.3.4. Section 5.4 summarizes the finger-tight results.

5.1 Load versus Displacement

The load versus displacement curve used in failure analysis is one of the most common output forms. Although, the current work does not progress to joint failure, this curve presents useful comparisons

---

* Based on work by Webber et al. [51] and Ireman [68] and [69].

of behaviour at 295K versus 373K, while confirming that the experimental loading remains within the elastic range of the joint at approximately 10% of aluminium bearing failure. Figure 5.2 illustrates the resulting load versus displacement curves, where #1 and #2 indicate the test run number. As the results are very similar, two test runs is deemed sufficient. The FE load versus displacement curves for the equivalent geometry are shown for comparison.

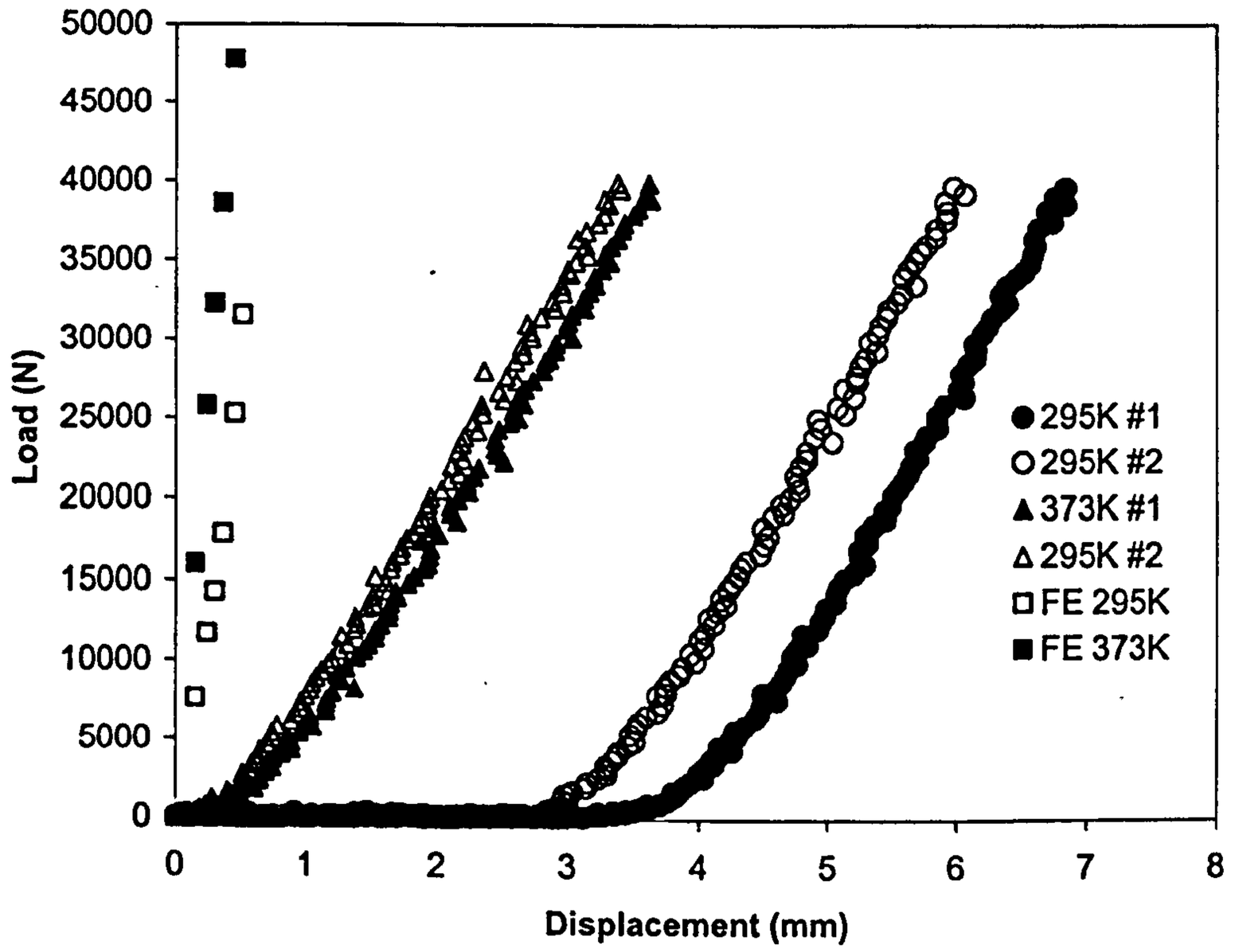

Figure 5.2. Load versus displacement curves at 295K and 373K.

One purpose of the load/displacement curves is to confirm that the experimental tests remain within the elastic range of the joint. This confirmation comes from the results in Figure 5.2, which establishes that all curves have a linear relationship.

It is interesting to note that there is more 'slack' in the specimen at room temperature, where the displacement of the testing machine reaches approximately 3mm before any significant loading is observed in the joint. This is anticipated due to the clearances associated with the connections within the joint itself, as well as between the specimen and the test machine. The specimen remains connected to the test machine during heating to 373K, resulting in some strains being induced within the joint. Prior to commencing tensile testing at 373K, these strains are reduced to zero by manually

unloading the test machine. Despite these thermal strains being accounted for, the above figure reveals that the clearances in the specimen decrease, causing almost immediate loading of the joint when displacement is imposed.

Figure 5.2 also confirms that an increase in temperature changes the slope of the load-displacement curves. The room temperature (295K) curves show excellent agreement in slope (13500 ± 200N/mm). The curves at 373K also demonstrate good agreement (12900 ± 300N/mm). These trends suggest that as temperature increases, the slope of load-displacement curve decreases. This behaviour agrees with limited previous work involving temperature variation in mechanically loaded joints [74]. In the previous work, the temperatures differ slightly from the current work (353K versus the current 373K); however, behavioural trends are almost identical for tensile loading, providing confidence in the current results.

The curvature depicted at lower loads indicates that approximately one third of the experimental test range is in a "low load" region. At low experimental loads, it is common for certain factors to contribute to uncertainty of results in this region, which are not generally present at higher loads. Factors such as surface roughness and bolt tolerances tend to skew results at lower loads until the load has been fully "introduced" and these secondary factors are overcome by the anticipated joint behaviours. Introduction of the load itself and the take-up within the joint at these lower loads also play a role in the results in this region. It is, therefore, expected that there will be some discrepancy in results at these lower loads. In the present study, the upper load limit is dictated by the equipment available. It is recognized that this is a limitation in the experimental results, and in general, the discussion herein will concentrate on higher load level results.

The FE results indicate loading commences much sooner in the model than in the experimental specimen. The FE model has boundary conditions that permit immediate load onset, whereas the experimental specimen has several bolted connections, and associated tolerances, as well as the other effects mentioned above at low-load levels to contend with, resulting in more displacement for a similar load. The fact that FE load onset occurs earlier may cause some discrepancy in results, however, as the joint loads achieved and the overall joint stresses are similar, this is not considered a significant issue.

5.2 Radial Strain Results

As illustrated in Figure 5.1, the strains are examined both radially and tangentially. The radial direction, perpendicular to the hole edge, is considered first since it is particularly relevant to understanding bearing behaviour of a joint. Bearing behaviour is an important component of joint design since bearing failure causes detectable material damage at the bearing plane prior to complete failure of the joint. Because of this feature, most joints, including the current design, are intended to fail by this mechanism.

5.2.1 Radial Results at 0°

The strain gauges at 0° are particularly noteworthy because they are positioned directly at the bearing plane. In order to compare the results from these strain gauges with the FE analysis, the resulting loads are converted to joint stress for a particular load condition, thereby removing association with specific geometries and allowing direct comparison. The joint stress is calculated:

$$\sigma_{joint} = \frac{P_{total}}{w_{joint} t_{joint}} \tag{5-1}$$

where P_{total} is the load induced by displacing the joint. Results are presented as an average of the two test run results, with bars indicating the individual test values.

Figure 5.3 shows the results for the tensile test at 295K, with Table 5.1 outlining the maximum strains at each hole. The FE results are given for the nodes at r2, a distance of 5.1375mm (0.2in) from the hole edge, and at r3, a distance of 7.1375mm (0.28in) from the hole edge. The experimental strain gauges are placed 6mm from the hole edge to allow adequate space for the fastener head and the gauge surface. The FE results are designed to bound the experimental strains. Appendix 5A contains an example FE program used to obtain the results.

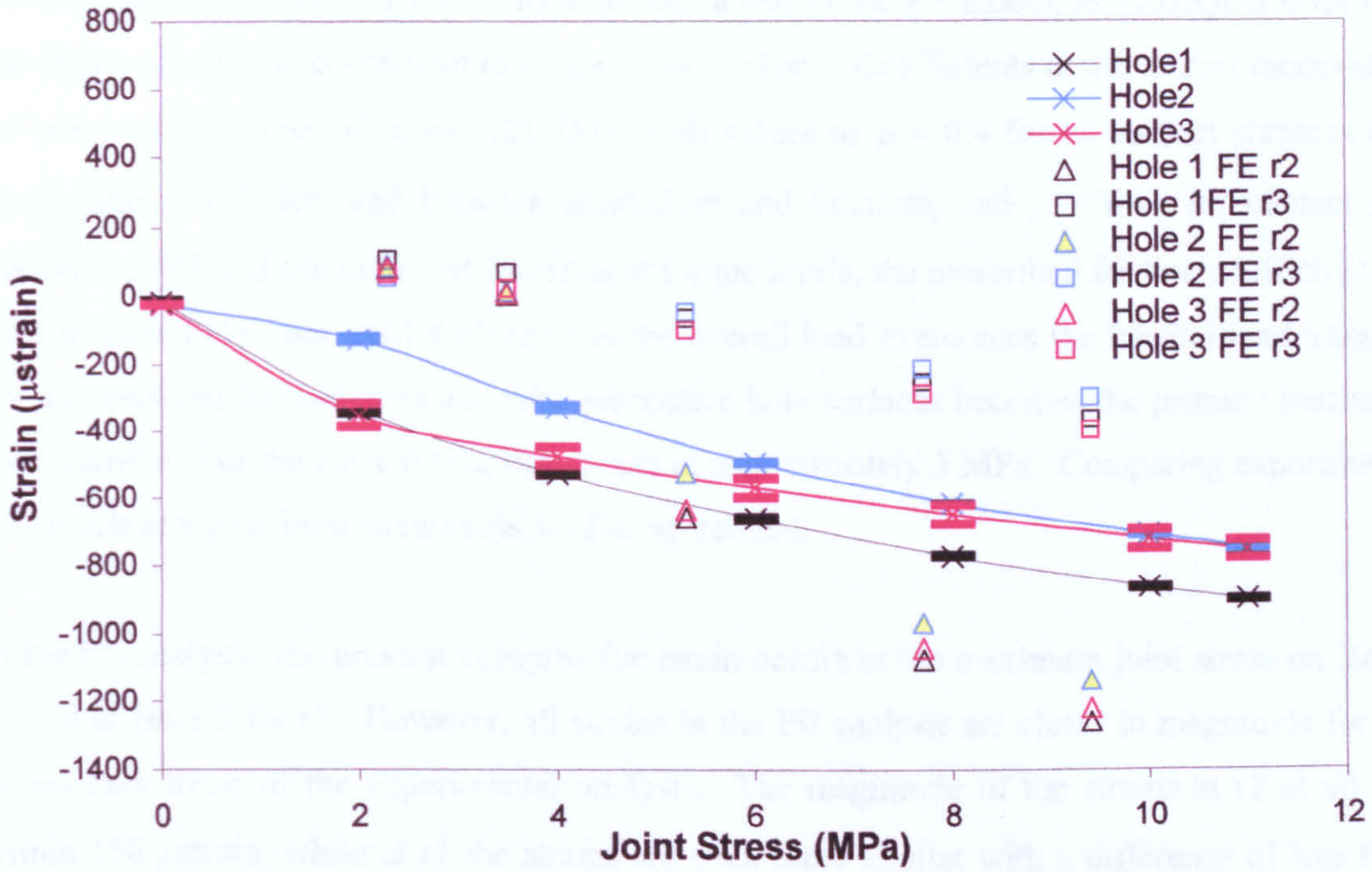

Figure 5.3. Joint stress versus radial strain at 0° (295K).

Table 5.1. Comparison of radial maximum strains at 0° (295K) at peak joint stresses.

	Hole 1 (μstrain)	Load Share	Hole 2 (μstrain)	Load Share	Hole 3 (μstrain)	Load Share
Experimental	**-900** ± 1	37%	-750 ± 6	31%	-756 ± 1	32%
FE r2	**-1260**	35%	-1136	31%	-1219	34%
FE r3	-367	34%	-301	29%	**-400**	37%

From Figure 5.3, it is apparent that at 0°, the radial compressive strain is significant. This is expected, given that this is the bearing plane. In Table 5.1, all maximum strains occur at the highest joint stress. The experimental results show Hole 1 as having the highest strain, with the strains at Hole 2 and Hole 3 similar in magnitude at the final joint stress. But the strains at Hole 3 are generally higher than those at Hole 2 throughout the analysis. This suggests that the largest percentage of load transfer occurs at the first fastener, with Hole 3 taking a large percentage of the load for the majority of joint stresses, and Hole 2 being less reactive. The FE results in Table 5.1 portray similar patterns with the outer holes performing the larger portion of load transfer.

Figure 5.3 verifies FE strains at approximately zero until a joint stress of 5 MPa, when compressive strains begin to appear. This discrepancy between FE and experimental likely results from the

assumption of a constant dynamic friction coefficient in the FE model, as ABAQUS does not have the ability to vary the coefficient throughout the analysis. Coefficients in the current model are based on previous experimental work [2], [51], with values of $\mu = 0.4$ for all contact surfaces between aluminium and CFRP, and between aluminium and titanium, and $\mu = 0.15$ for contact surfaces between CFRP and titanium. At finger-tight torque levels, the prescribed friction coefficients dictate load transfer behaviour until such time as the overall load overcomes the friction load transfer, and contact between the fasteners and their respective hole surfaces becomes the primary mechanism of load transfer. For the current test, this occurs at approximately 5 MPa. Comparing experimental and FE results at higher joint stresses shows fair agreement.

In the FE analysis, the greatest compressive strain occurs at the maximum joint stress on Hole 1 for r2, but at Hole 3 for r3. However, all strains in the FE analysis are closer in magnitude for a given radius than those of the experimental analysis. The magnitude of the strains at r2 at all holes is within 150 μstrain, while at r3 the strains are even more similar with a difference of less than 100 μstrain. The difference between Holes 1 and 3 at r3 is approximately 40 μstrain, which is similar to the r2 behaviour. The difference between Hole 2 and Hole 1 is 60 μstrain, which is 30 μstrain less than at the inner radius r2. The indication is that the largest percentage of the load is taken by the outer holes (1 and 3), while the middle hole (2) takes a smaller, but still significant portion of the load. This is in general agreement with the experimental results where Hole 1 takes the greatest portion, followed by Hole 3, then Hole 2. The FE results provide confidence in the experimental data, in that they bound the results.

Examining the slopes of the curves in Figure 5.3, it becomes apparent that the slope for the r3 curve is very similar to that of the experimental results, especially in the region after 5MPa, indicating good agreement between experimental and FE r3. Hole 1 and Hole 3 are close in maximum strains, but in the FE, Hole 3 results are more compressive than those of Hole 1. This finding differs from the results of the experimental run. However, at the inner radius of the FE, r2, Hole 1 demonstrates maximum strains, followed by Hole 3, then Hole 2. These results echo those of the experimental analysis. In the FE analysis at r2, the slopes after 5MPa are significantly greater than those at r3. This indicates that the strains nearer to the hole edge increase more rapidly with increased joint load, as expected, since stress concentrations in the immediate vicinity of the hole are known to be higher, as discussed previously in Chapter 1.

The errors associated with using FE to approximate the experimental run stem from a number of assumptions. First, the FE is only a one-quarter model of the experimental specimen. This means that boundary conditions must simulate the remainder of the specimen. In the current case, the nodes at the back of the model are constrained by the CFRP skin behaviour, through the use of a constraint equation at this back face of the FE model. This condition is selected because the CFRP has a lower Poisson's ratio and expansion coefficient than the aluminium. Forcing the aluminium to move in conjunction with the CFRP skin creates a worst-case scenario. Furthermore, the thickness and overall stiffness of the CFRP makes it the dominant material in terms of movement across the joint. This assumption, although relatively accurate when comparing the results in Figure 5.3, is not an exact replication of the experimental conditions where the movement of the material between the columns of fasteners is influenced by both the CFRP and aluminium.

Another source of discrepancy is the condition of symmetry applied across the front face of the FE model, equivalent to mirroring the conditions at the mid-plane of the fastener column such that an infinite number of columns are present. In the experimental specimen, there is only one mirrored half present at the other side of this mid-plane, rather than an infinite number. Experimentally, slight slippage around the holes can occur, relieving some of the associated strains due to the presence of the free-edge. In the FE model, the free-edge does not exist. These effects are secondary compared to the primary movement of load through the fasteners themselves. Furthermore, the primary concern in the present study is the strain concentrations in the vicinity of the hole, such that the edge effects are not considered part of the pertinent investigation at this time. This fact, coupled with the knowledge that any strain relief at the hole due to the presence of these free edges in the experimental specimen is a secondary concern to the primary route of load transfer, justifies the use of the symmetry boundary condition at the front face of the FE model.

The final boundary condition in the FE model is the condition of symmetry at the left-edge of the aluminium laps, used to approximate the transfer to the aluminium skin side of the joint. In the experimental specimen, the load is fully transferred to the aluminium skin. This is believed to cause little difference between the FE and experimental results, since all load has been transferred to the aluminium laps by this point, thereby allowing a full investigation of the behaviour of the fasteners at the CFRP skin side of the joint.

The final consideration for error within the FE analysis lies in the fact that FE is a numerical process dependent on mesh design and refinement. The mesh refinement study of Chapter 4 indicates good but not perfect agreement between the fine and very fine meshes. The fine mesh tends to overestimate certain results, meaning that the values produced for these tests may be slightly different than values produced with a higher mesh density. Increased accuracy is a trade-off for computing time and modelling simplicity. Given the high degree of agreement between the experimental results and the FE results shown in Figure 5.3, the fine mesh is deemed acceptable demonstrating limited numerical error.

The experimental analysis also has potential for error. Sources of error associated with the experimental data include: specimen misalignment, gauge position error, and torque level inaccuracy. Specimen misalignment can result if the geometric position of the hole when the part is manufactured does not quite follow drawing specifications. In this case, misalignment associated with the hole placement in the skin and the laps is not a factor, since drilling is performed through all three components at the same time. Load cell and test machine misalignment is a possibility, however, given the size of the specimen and the low load operating range, this is not likely a significant factor.

There is also potential for error with the positioning of the strain gauges on the aluminium lap. A gauge positioned not exactly at 0° or perfectly perpendicular to the hole edge can alter strain results.

Finally, torque level can cause discrepancies between experimental and FE results. In the FE model, the torque is applied as a compressive force in the through-thickness direction by shortening the corresponding fastener elements in order to induce load. This creates a 'perfect' clamp-up level. Experimentally, clamp-up is achieved using a torque wrench. The torque wrench indicates the level of clamp-up by measuring the degree of resistance to applied force. The wrench is not able to account for other factors, in particular friction, which can influence this degree of resistance. As an example, if the fastener is perfect fit (i.e. it is interacting with the hole walls), and the joint material is rough resulting in a particularly high coefficient of friction, the torque wrench can indicate that the desired level of clamp-up has been attained, whereas in actual fact, only a portion of the actual clamp-up load has been applied. As this test is performed at a low torque level, this margin of error is expected to be small, which appears to be the case, since there is strong agreement between FE and experimental results. Therefore, the sources of error with the greatest impact are the fact that the

experimental range is largely within a "low load" range and the possibility of error in the positioning of the strain gauges.

To confirm that the load is distributed evenly in the chordwise direction (across the width of the experimental plate), and to better understand potential experimental error, strain gauges are also placed at 0° on Holes 4 through 6, corresponding to Holes 1 through 3, respectively, as shown in Figure 5.4. The error bars for Holes 1 to 3 are examined in Figure 5.3.

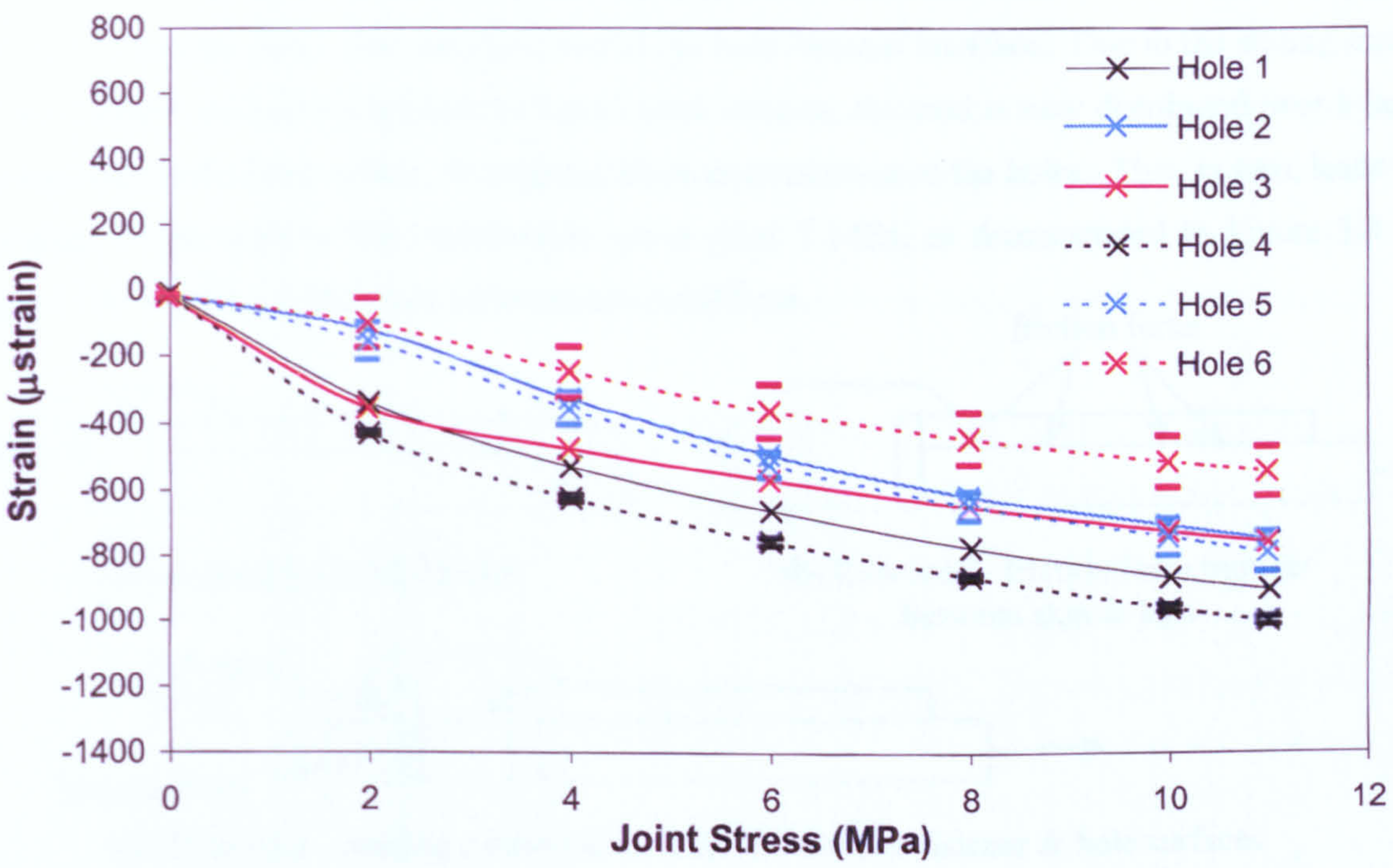

Figure 5.4. Comparison of radial strains at Holes 1 to 3 with Holes 4 to 6 (0° and 295K).

From Figure 5.4, it is evident that Holes 1 and 4, and Holes 2 and 5 display good agreement in chordwise symmetry, as the results are very similar. The strains at Holes 4 and 5 are slightly less compressive than the strains at Holes 1 and 2, with a maximum difference of 99 μstrain at Hole 1 and 39 μstrain at Hole 2. Maximum differences in strain occur at maximum tensile load (11 MPa joint stress), which is expected given that as the load increases discrepancies are magnified.

The results at Holes 3 and 6 show greater discrepancy. In this comparison, Hole 3 strain results are greater than Hole 6 results. Furthermore, the maximum difference is 252 μstrain occurring at a joint stress of 2 MPa, while the difference at 11 MPa is 215 μstrain. The results of all six gauges show slightly non-linear slopes with a change occurring at 2 MPa joint stress but the results at Hole 3 are

much more pronounced. Since the experiments are carried out in the elastic range of the joint, as verified in Figure 5.2, this change in slope is not due to physical deformation. The likely cause of the slope change is a change in contact distribution. There are two distinct contact conditions that occur at different load levels. At low joint stress, the load is first transferred between the skin and laps via friction up to the point where the joint load surpasses the frictional force and sliding between the parts occurs. At this time, the hole material slides around the fastener, which in turn increases the contact surfaces. This leads to the second type of contact condition, where the load is no longer primarily transferred by friction or shear force between the CFRP skin and aluminium laps, but rather by a bearing force that transfers load at the hole fastener interface. Due to the sliding motion of the material around the fastener at higher joint stresses, the load is now distributed over a larger contact area at the hole surface, decreasing stress concentration at the holes. This, in turn, leads to a lowering in the slope of the stress-strain curve after 2 MPa, as demonstrated in Figure 5.3 and Figure 5.4. Figure 5.5 describes these contact conditions.

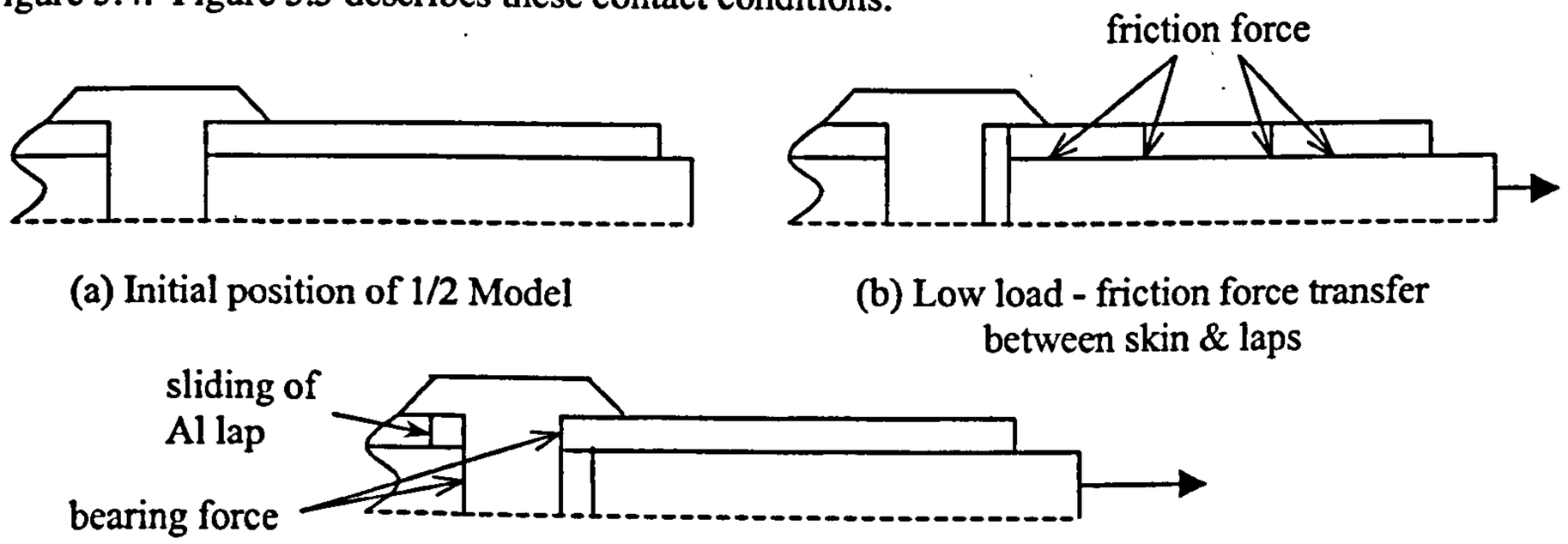

(a) Initial position of 1/2 Model

(b) Low load - friction force transfer between skin & laps

(c) High load - bearing contact force transfer between fastener & hole surfaces

Figure 5.5. Contact conditions.

It is also interesting to note from Figure 5.4 that the results from the second column of strain gauges (Holes 4 to 6) indicate that the load distribution among the fasteners decreases from Hole 4 to Hole 6, with maximum strains at increments of approximately 200 μstrain. This is a more even distribution than that indicated by the results from the first column of gauges where Hole 1 differs from Hole 2 and Hole 3 by 150 μstrain, and Holes 2 and 3 have nearly identical maximum strain. This difference in load distribution pattern suggests an error in experimental results. The FE analysis shows a more even distribution with the outer rows (Holes 1 and 3, corresponding to Holes 4 and 6) taking the largest portion of the total maximum strain (approximately 70% between the two fasteners) and the middle fastener carrying the remaining 30% at maximum joint stress. In the

experimental results, Hole 1 takes 37%, Hole 2, 31%, and Hole 3, 32%, while Hole 4 has 43%, Hole 5 has 34%, and Hole 6 carries the least with 23%. The behaviour at Holes 1 to 3 of the experimental results is more similar to the percentages of the maximum strain of the FE results in Table 5.1.

The discrepancy in the experimental results stems from the sources of error discussed earlier. However, at this point, the influence of individual sources of error can be examined further. The fact that the FE results compare well with the experimental data implies that the torque level is not a significant error. Furthermore, the experimental error associated with load cell or test machine misalignment is unlikely because of the good agreement in strains between the columns of fasteners, particularly at Holes 1 and 4 and Holes 2 and 5. The agreement of these results suggests that the error lies in the area of Hole 3. The fact that the slope change at 2 MPa for Hole 3 is more significant than that of the other holes further suggests a change in contact conditions around this region. This implies that a manufacturing error or gauge position error is the most likely cause.

To gain an appreciation of the effects of temperature elevation, and to further pursue the cause of errors, the same experiment is performed at 373K. Prior to heating, a calculation using (4-1) to (4-10) establishes the expected strain behaviour based solely on increased temperature with no additional mechanical loading. Table 5.2 compares the calculated analytical strain results with those of the experimental and FE tests for a temperature change to 373K. The analytical tool applies only to 2D plane stress estimation between simplified fasteners, Holes 2 and 3, and near the free edge, Hole 1, as described in Chapter 4.

Table 5.2. Comparison of analytical, experimental, and FE thermal strains at 0° ($\Delta T = 78°$).

	Hole 1 (μstrain)	Hole 2 (μstrain)	Hole 3 (μstrain)
Analytical	1800	920	920
Experimental	1840 ± 40	700 ± 45	870 ± 35
FE (r2)	1958	1155	1425
FE (r3)	1915	983	1196

Table 5.2 demonstrates good agreement between analytical, experimental, and FE results. The slight discrepancies are caused by errors associated with gauge placement in the experimental tests, and with the specimen remaining connected to the test machine. This connection is capable of inducing slightly different loading conditions. Also, the experimental measurements are taken only at one particular position on the strain gauge, whereas the analytical calculation assumes rigid fasteners and even distribution of strain through-thickness. Despite these errors, the agreement is sufficient to

confirm that the experimental conditions do not deviate significantly from the ideal conditions used in the analytical calculation.

The values of the FE results are higher than the analytical and experimental values for all holes. The effects of distance to hole edge are also evident, as all results at r2 are higher than those at r3. This deviation from the analytical predictions illustrates the complexity associated with comparing actual geometry to simplified ideal conditions. The differences between FE and experimental values arise from the fact that the FE model is free to expand in the loading direction during heating, whereas the experimental specimen has constraints imposed by its attachment to the test machine. When the experimental specimen is heated, the opposing force of the load cell attachments hinders expansion. These opposing forces result in lower values for the experimental results when compared with the FE data. The closeness in results at Hole 1 comes from its position in the joint nearer the aluminium lap free edge, where it is less influenced by constraints.

Once 373K is reached, the experimental and FE specimens are again subjected to mechanical tensile loading. The results of the tensile testing at 373K for Holes 1 to 3 are given in Figure 5.6. During heating, the gauge at Hole 1 released from the lap surface, rendering it incapable of producing results for the remainder of testing. Consequently, Hole 1 results do not appear in Figure 5.6 and Hole 4 results are used instead. Table 5.3 outlines the maximum strain comparison.

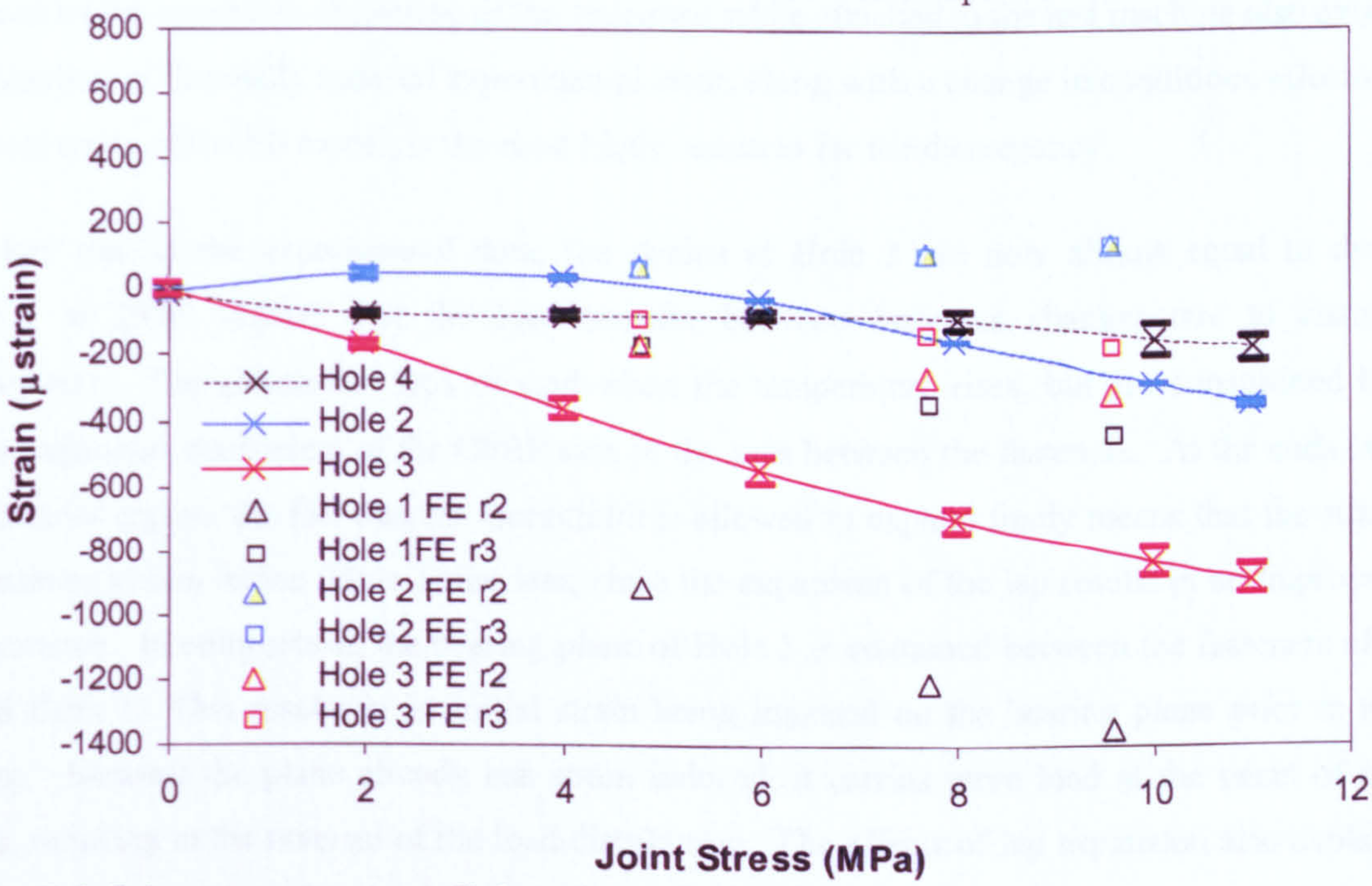

Figure 5.6. Joint stress versus radial strain at 0° (373K).

Table 5.3. Comparison of radial maximum strains at 0° (373K) at peak joint stresses.

	Hole 4 (μstrain)	Load Share	Hole 2 (μstrain)	Load Share	Hole 3 (μstrain)	Load Share
Experimental	-182± 35	13%	-356 ± 5	35%	-888 ± 42	62%
FE r2	**-1350**	75%	127	7%	-327	18%
FE r3	**-441**	59%	127	17%	-178	24%

Figure 5.6 provides evidence that behaviour at high temperature is much different from that at room temperature. Experimentally, Hole 3 now has the highest strains, while Hole 2 has a lower maximum strain, less than half of its value at 295K. Up to 5 MPa joint stress, Hole 2 strains are slightly tensile, after which they slowly become compressive. Hole 3 experiences approximately 130 μstrain more strain than at 295K. Since the gauge at Hole 1 became detached from the specimen during heating, results from Hole 4 are used in its place. The resulting strains at Hole 4 are low. The FE results predict a higher strain, similar in magnitude to the strains presently observed at Hole 3. This discrepancy results from errors in both FE and experimental analyses. In the FE analysis, the initial thermal strains are greater than the experimental values. These results are subtracted from the FE values for the tensile loading in order to effectively "zero" the strain prior to tensile testing. As a discrepancy exists in the thermal strains, a difference is also expected in the mechanically induced results. The experimental results are subject to possible temperature fluctuation in the chamber, and the errors associated with the 295K results. The possibility of load cell or specimen misalignment induced by the constraint of heating of the specimen while attached to the test machine also exists. A combination of thermally induced experimental error, along with a change in conditions affecting the representation of the FE model, is the most likely scenario for the discrepancy.

The fact that in the experimental data, the strains at Hole 3 are now almost equal to those at Hole 1 at 295K implies that the load transfer between fasteners changes due to change in temperature. The aluminium laps expand when the temperature rises, but are constrained by the lower expansion coefficient of the CFRP skin in the area between the fasteners. At the ends outside the fastener region, the fact that the aluminium is allowed to expand freely means that the strains at the bearing in this region (Hole 1) are less, since the expansion of the lap results in an improvement in clearance. In comparison, the bearing plane of Hole 3 is contained between the fasteners of Hole 2 and Hole 3. This results in an initial strain being imposed on the bearing plane prior to tensile testing. Because the plane already has strain induced, it carries more load at the onset of tensile stress, resulting in the reversal of the load distribution. The effects of lap expansion also explain the slightly tensile strain at Hole 2 initially.

Hole 2 changes in slope at 6 MPa and Hole 4 at 8 MPa, indicating changes in load distribution. The experimental results at Holes 2 and 4 up to this point show negligible strains. This verifies that behaviour at 373K differs significantly from that at 295K. The slopes of the FE results for Holes 1 and 3 display similarity to Hole 3 of the experimental results, but suggest that the results at Hole 1 (represented by Hole 4) may not be representative of expected joint behaviour. The decrease in strain of 718 μstrain at Hole 1 (4) from the maximum strain at 295K also suggests experimental error. The FE results, expected to be a slightly higher given the results at 295K, are more in line with expected behaviour. In any case, there are significant differences at 373K as compared to 295K. The load distribution changes to incorporate greater strains at Hole 3. The maximum strains are lower than the resulting values at 295K. The expansion of the aluminium laps relieves some of the induced tensile load. Symmetry between the bolt columns is shown in Figure 5.7. Due strain gauge malfunction, results from Hole 1 are not presented.

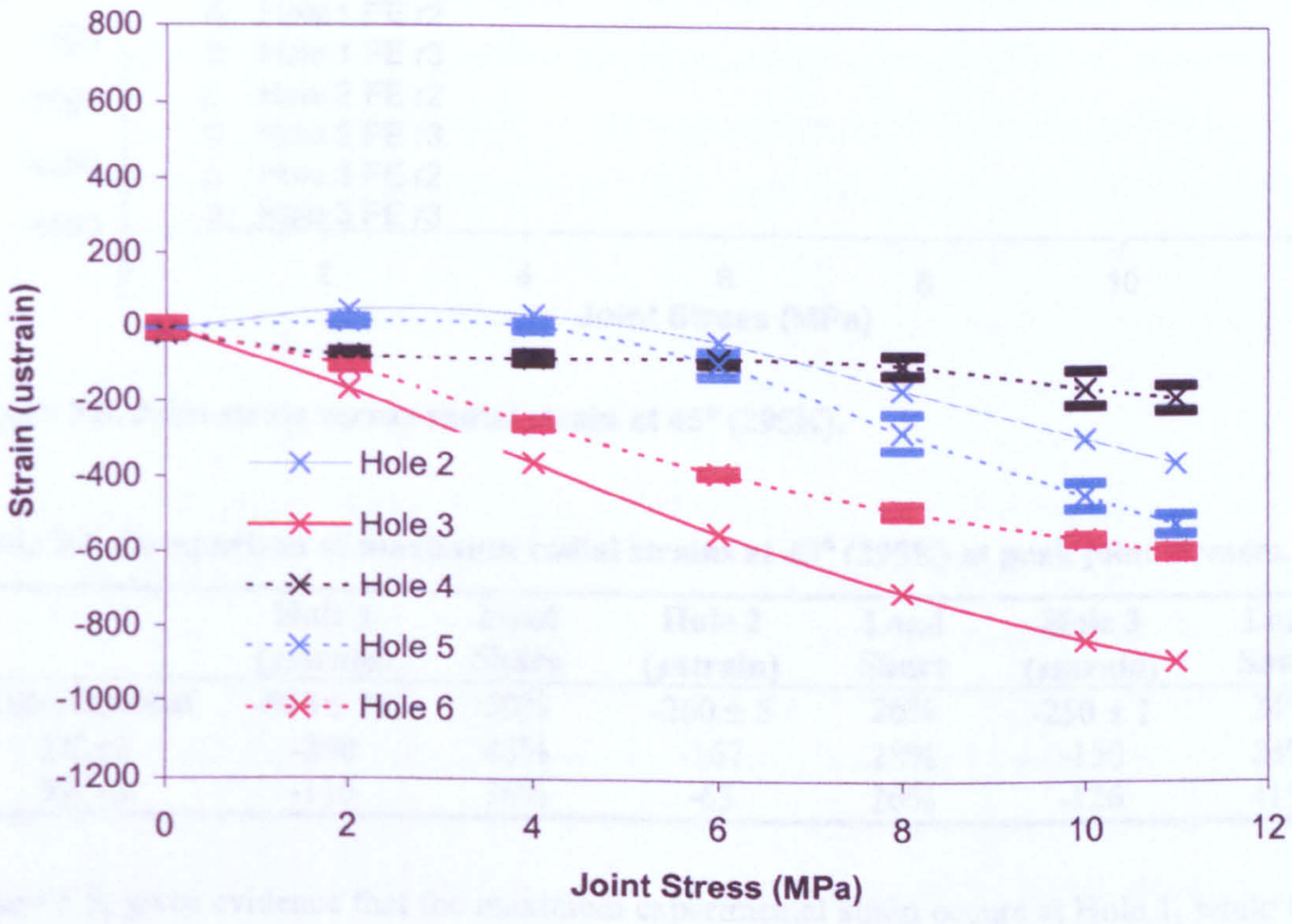

Figure 5.7. Comparison of radial strains at Holes 2 to 3 with Holes 4 to 6 (0° and 373K).

The results in Figure 5.7 are similar to those in Figure 5.4, where both columns of holes show similar strain values. Holes 2 and 5 have a maximum difference of 180 μstrain, and Holes 3 and 6 a maximum of 287 μstrain. The trends, however, are similar, suggesting good symmetry between columns and providing confidence in the results.

5.2.2 Radial Strains at 45°

Moving away from the bearing plane, the results from the gauge at 45° are examined. Figure 5.8 gives the radial strain results for tensile load at the 45° gauge at 295K, and Table 5.4 displays a comparison of maximum strains.

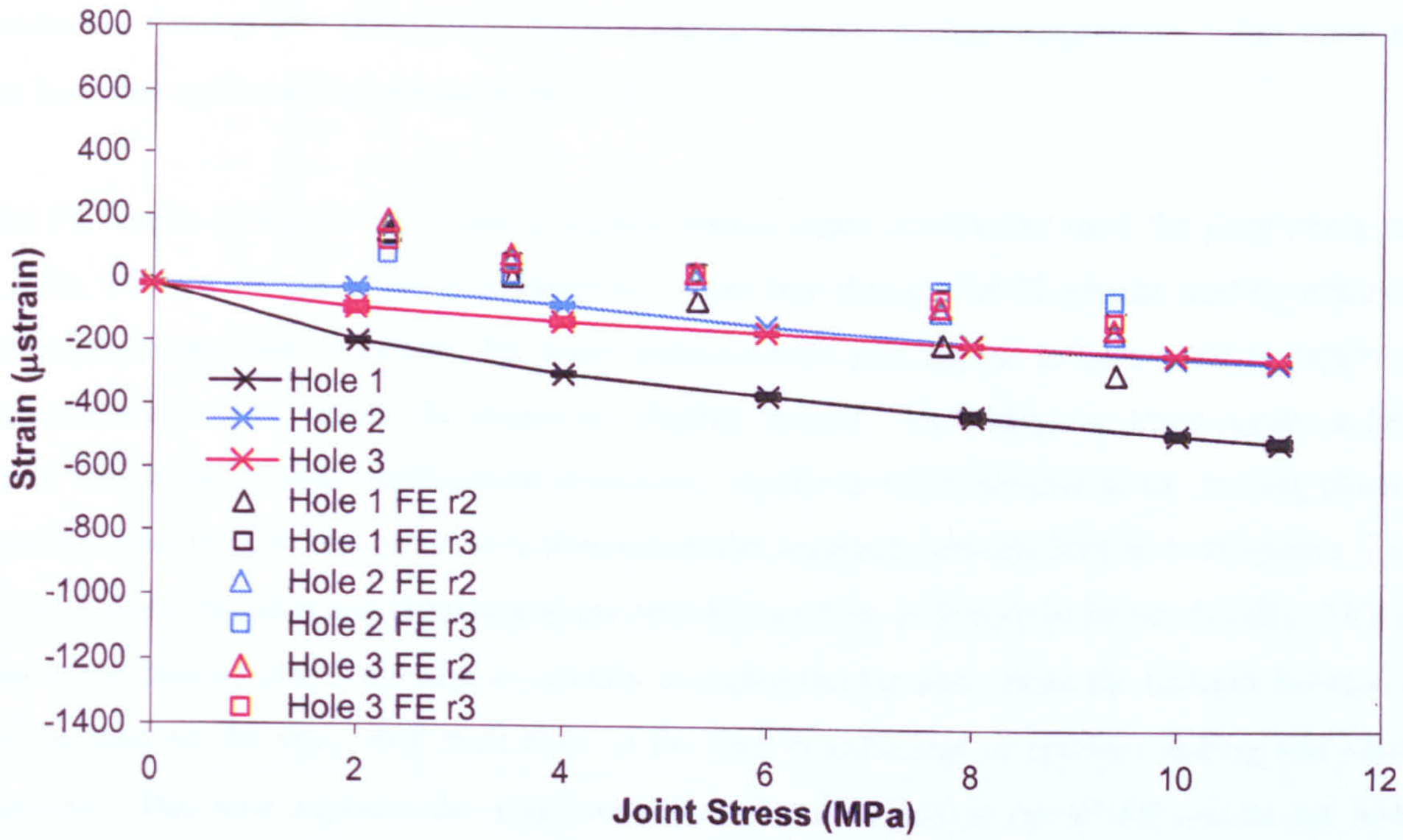

Figure 5.8. Joint stress versus radial strain at 45° (295K).

Table 5.4. Comparison of maximum radial strains at 45° (295K) at peak joint stresses.

	Hole 1 (μstrain)	Load Share	Hole 2 (μstrain)	Load Share	Hole 3 (μstrain)	Load Share
Experimental	**-505** ± 10	50%	-260 ± 5	26%	-250 ± 1	24%
FE r2	**-290**	48%	-167	28%	-150	24%
FE r3	-116	38%	-63	20%	**-126**	41%

Figure 5.8, gives evidence that the maximum experimental strain occurs at Hole 1, while the values of maximum strain at Hole 2 and Hole 3 are nearly identical. This appears to coincide with the behaviour at the bearing plane in that Hole 1 carries the greatest percentage of the maximum strain. The decrease in strain from Hole 2 to Hole 3 is less pronounced than at the bearing plane: 10μstrain at the 45° plane as compared to a decrease of 220μstrain at the bearing plane. The decrease in strain from Hole 1 to Hole 2 is greater at the 45° plane, with a difference of 245μstrain, compared to an 80μstrain decrease at the bearing plane. This is equivalent to Hole 1 bearing 50% of the maximum

total strain, Hole 2 having 26%, and Hole 3 carrying the remaining 24%, compared to 37%, 31%, and 32% at the bearing plane. That indicates that the bearing plane has a more even distribution of strain among all fasteners, and that the behaviour away from the bearing plane, although dependent on strain at 0°, is not linearly proportional. The radial strain at 45° is less compressive than at the bearing plane, because the degree of contact is less and the load is not applied directly at this point, unlike the force at 0°. This demonstrates a continuous decreasing compressive radial strain around the hole that agrees with previous work [70].

The FE results in Figure 5.8 reveal a slightly tensile strain at all holes until the joint stress reaches 5 MPa, where a change in slope is observed. After this change, the FE results tend to under-predict the experimental data; however, the outer radius results (r3) appear to have a slope similar to the experimental results. At r2, the slopes are slightly steeper. The change in slope occurs at the joint stress where the friction coefficient is overcome, similar to the behaviour at the bearing plane. The tensile strains prior to that point are a function of the assumed constant friction coefficients. Because of the friction, the skin and lap material are moving together, as shown in Figure 5.5 (b). This means that at the bearing plane, the skin is actually dragging the lap away from the fastener because of the tensile load on the skin, until such time as the load is sufficient to produce sliding and contact is induced. This also explains the small tensile strains observed at the 0° FE results for low joint stresses in Figure 5.3.

The behavioural trends of the experimental results and the FE results are very similar. At the start of the analysis, all hole strains are similar, with Hole 1 bearing the greatest strain. The experimental results show Hole 3 with slightly more strain than Hole 2, which is opposite to the FE results, but the values are almost identical and given the errors associated with both experimental results, especially at Hole 3, and FE model results, the agreement is good. At higher stresses, the strain at Hole 1 increases significantly in relation to the remaining two holes. This occurs in both FE and experimental data. As expected, the FE analysis shows the r2 results having higher strains than the r3 results. The results of increasing temperature to 373K are outlined in Figure 5.9, and the maximum strain comparisons in Table 5.5.

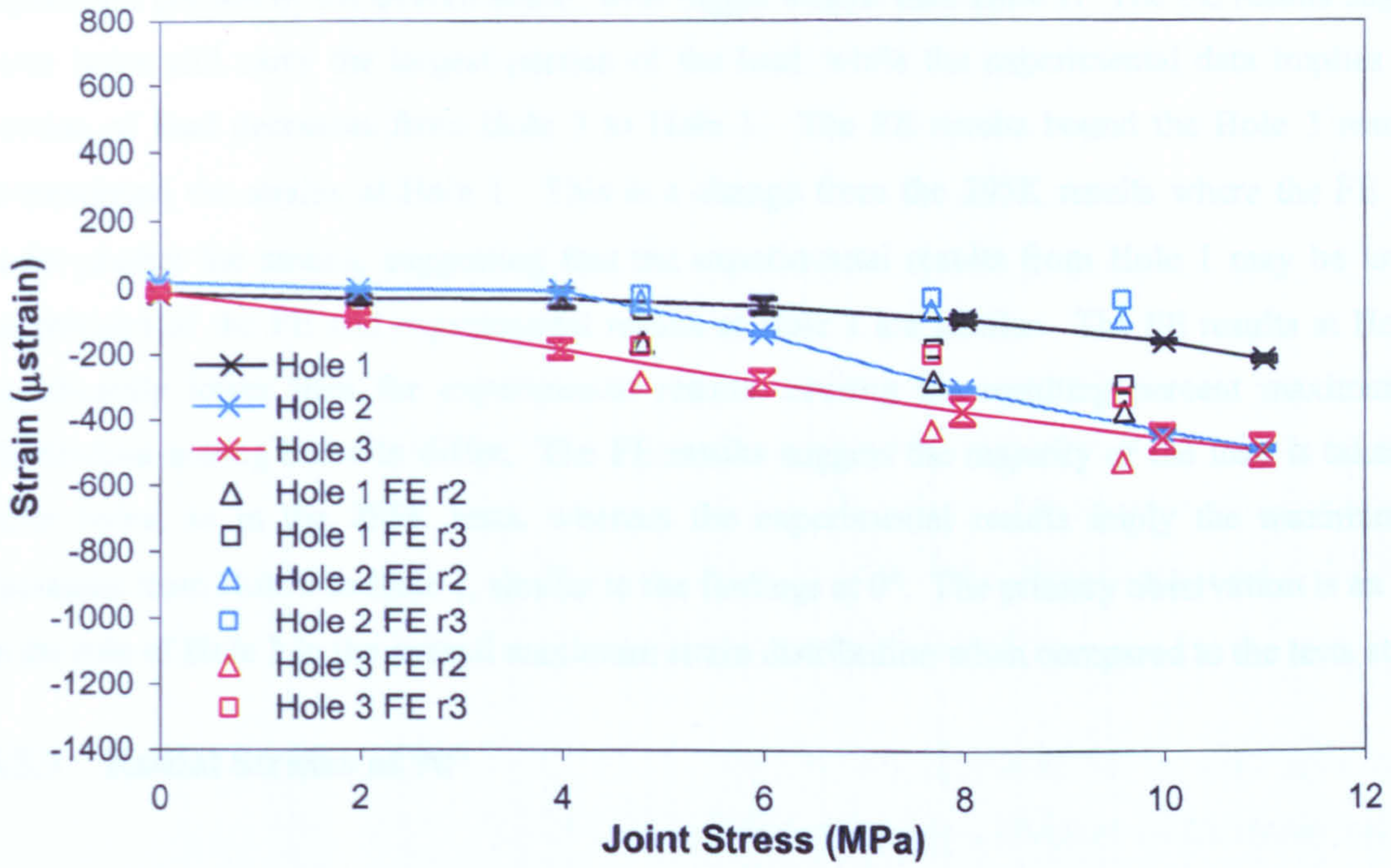

Figure 5.9. Joint stress versus radial strain at 45° (373K).

Table 5.5. Comparison of maximum radial strains at 45° (373K) at peak joint stresses.

	Hole 1 (μstrain)	Load Share	Hole 2 (μstrain)	Load Share	Hole 3 (μstrain)	Load Share
Experimental	-210 ± 6	18%	-492 ± 4	41%	**-494** ± 44	41%
FE r2	-375	38%	-91	9%	**-528**	53%
FE r3	-291	40%	-35	5%	**-392**	55%

The results from Figure 5.9 indicate trends similar to those at 295K, except that now Hole 3 carries the maximum strains rather than Hole 1. Experimentally, the maximum strain is reduced by 10 μstrain from that at 295K. Hole 2 has the lowest strains at low joint stresses, but there is a change in slope after 4 MPa, and it then behaves more like Hole 3. Hole 1 strains remain low throughout the test.

The FE results also show Hole 3 having the highest strains, with similar magnitudes. The slopes of the r2 results appear to match well with the experimental run. The maximum strain distribution at the remaining two holes is the greatest difference between FE and experimental results. The FE shows Hole 1 having the next greater strain, whereas experimentally, Hole 1 has the smallest strain of the three holes. Hole 2 in the FE results has negligible strain. Experimentally, Hole 2 carries a

significant portion of the overall strain, with bigger strains than Hole 1. The FE results suggest the outer holes still carry the largest portion of the load, while the experimental data implies that the portion of load decreases from Hole 3 to Hole 1. The FE results bound the Hole 3 results, and overestimate the strains at Hole 1. This is a change from the 295K results where the FE tends to under-predict the strains, suggesting that the experimental results from Hole 1 may be low. The magnitudes of the FE and experimental results at Hole 1 are similar. The FE results at Hole 2 are significantly lower than the experimental results, causing the resulting percent maximum strain distribution among holes to differ. The FE results suggest the majority of the load is taken by the outer holes, as in the 295K tests, whereas the experimental results imply the maximum strain decreases from Hole 3 to Hole 1, similar to the findings at 0°. The primary observation is an increase in the role of Hole 3 in the overall maximum strain distribution when compared to the tests at 295K.

5.2.3 Radial Strains at 90°

The final gauge is set at the net tension plane, 90°. Figure 5.10 illustrates the results for this plane at 295K, and Table 5.6 the comparison of maximum strains.

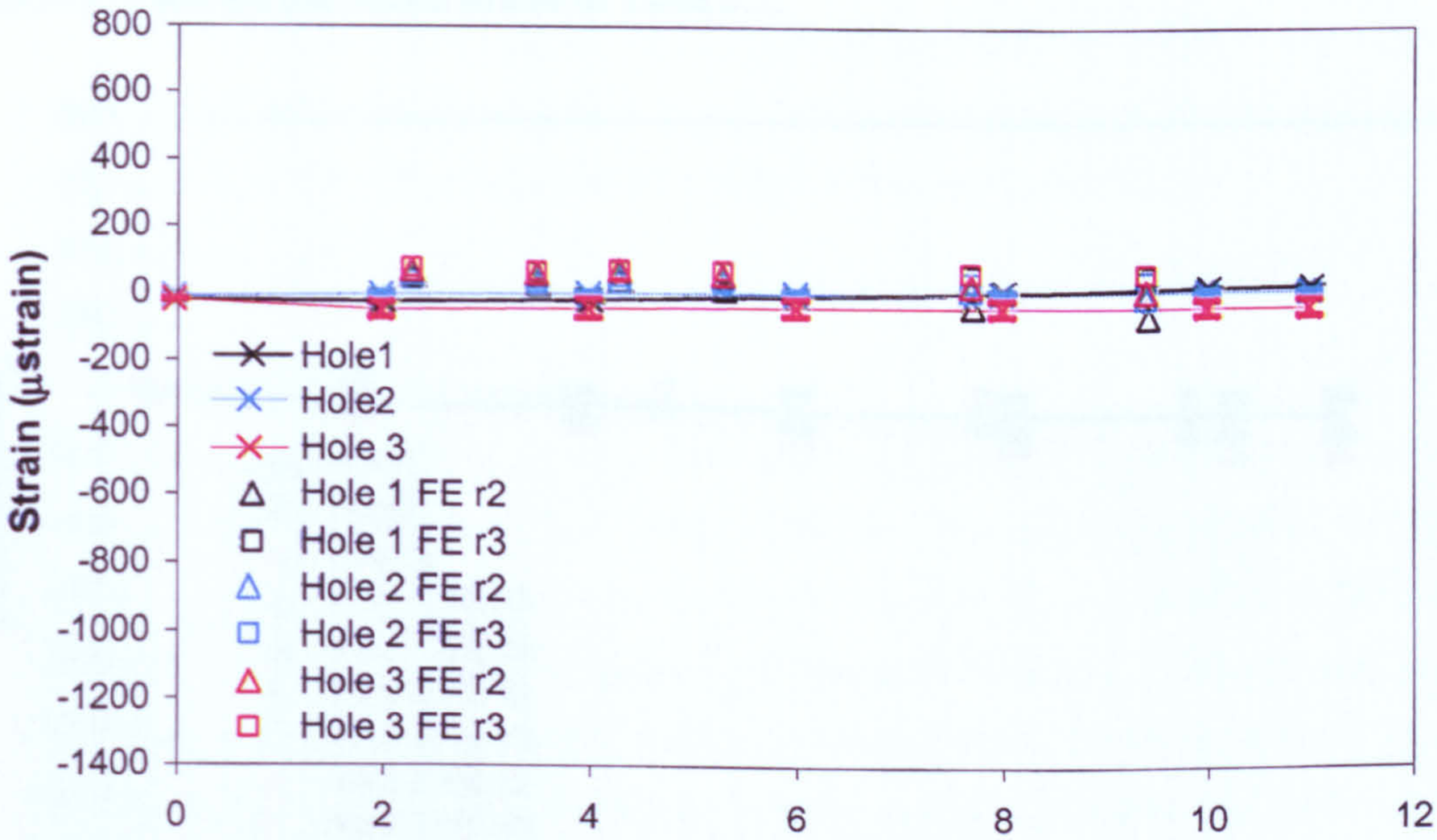

Figure 5.10. Joint stress versus radial strain at 90° (295K).

Table 5.6. Comparison of maximum radial strains at 90° (295K) at peak joint stresses.

	Hole 1 (μstrain)	Load Share	Hole 2 (μstrain)	Load Share	Hole 3 (μstrain)	Load Share
Experimental	25 ± 1	37%	7 ± 6	10%	**-35** ± 23	53%
FE r2	**-65**	78%	-10	12%	8	10%
FE r3	56	37%	36	23%	**61**	40%

Table 5.6 indicates that the radial strain at the net-tension plane is close to zero. All experimental values show little deviation from the initial strain. This is expected since the primary strain at 90° is primarily tangential rather than radial for tensile load conditions. The absence of radial strain is due to the fact that there is little or no contact at this region. Therefore, radial strains must originate from material motion, which is a secondary consideration to direct contact.

The FE analysis also shows negligible strain, implying that the model results show good agreement with the experimental data. The minor strains that exist are a function of the numerical analysis itself, and the discrepancies induced by the boundary conditions of the one-quarter model. The final run for the finger-tight specimen studies the 90° gauges at 373K. The results are shown in Figure 5.11 and the maximum strains in Table 5.7.

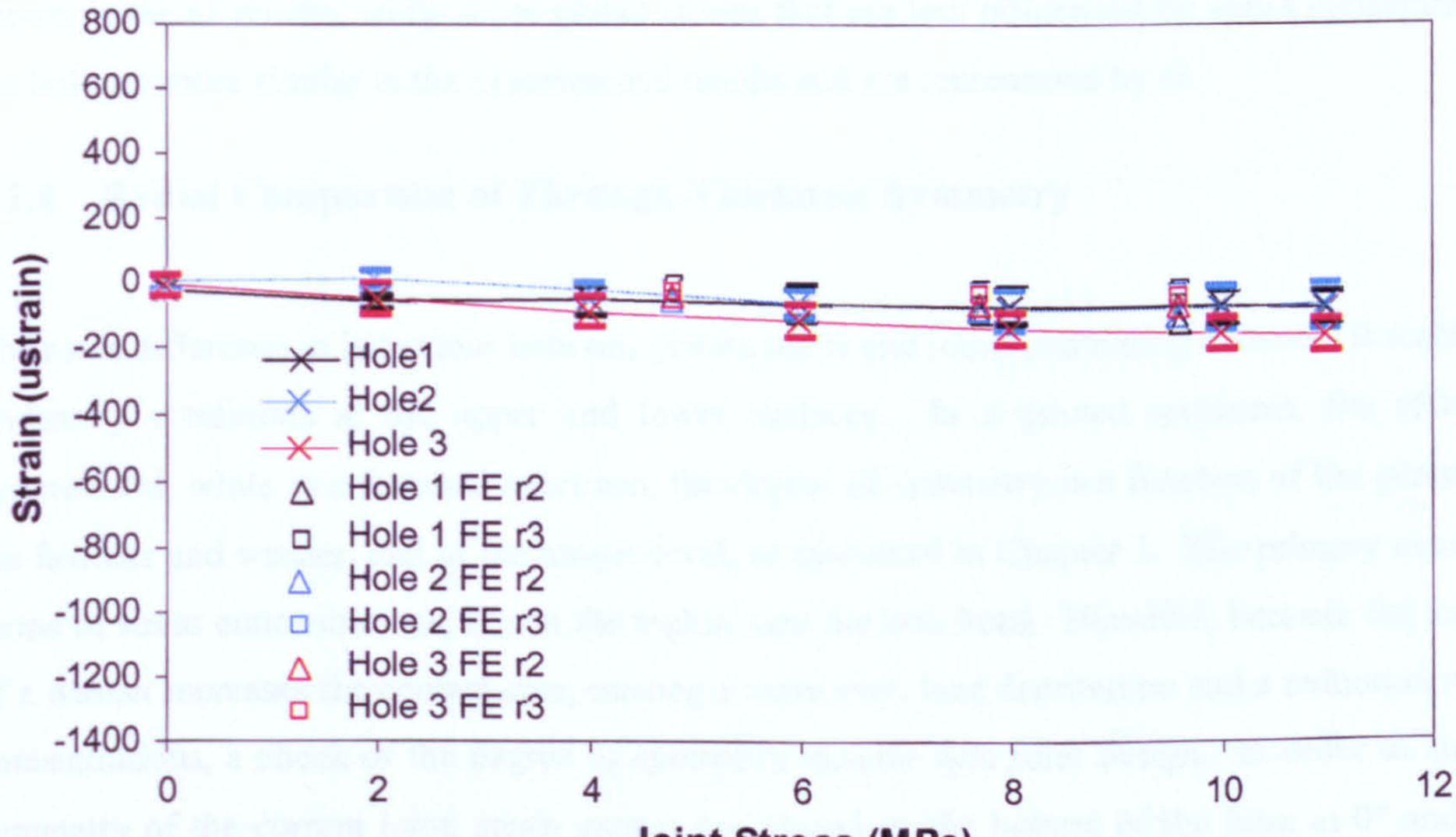

Figure 5.11. Joint stress versus radial strain at 90° (373K).

Table 5.7. Comparison of maximum radial strains at 90° (373K) at peak joint stresses.

	Hole 1 (μstrain)	Load Share	Hole 2 (μstrain)	Load Share	Hole 3 (μstrain)	Load Share
Experimental	-82 ± 52	26%	-72 ± 70	33%	-162 ± 48	51%
FE r2	-125	41%	-104	34%	-75	25%
FE r3	-16	19%	-30	34%	-41	47%

Figure 5.10 indicates that the strains are again very small. Experimentally, Hole 3 shows the greatest strain, with the strains at Holes 1 and 2 almost the same magnitude. All strains are slightly compressive at 373K. These minor strains are caused by the constraint at the mid-plane induced by the second column of fasteners. The CFRP expansion coefficient is less than aluminium, causing a small compression in the aluminium lap when heating occurs, and although the initial thermally induced strains are removed by re-zeroing, the aluminium continues to attempt to expand until such time as the tensile load overcomes the difference between the CFRP and aluminium, which explains why this effect is not detected at 295K.

The FE data shows similarly small strains. The FE results place the greatest strain at Hole 1 at r2, but this behaviour changes to Hole 3 at r3, while percent maximum strain at Hole 2 remains identical for both radii. The stress concentrations near the hole appear to cause a different strain distribution, shown in the r2 results, while more global strains that are less influenced by stress concentration at the hole are more similar to the experimental results and are represented by r3.

5.2.4 Radial Comparison of Through-Thickness Symmetry

The main difference in behaviour between pinned joints and joints containing fasteners is a change in symmetry conditions at the upper and lower surfaces. In a pinned specimen, the results are symmetrical, while in a fastened specimen, the degree of symmetry is a function of the geometry of the fastener and washer, and of the torque-level, as discussed in Chapter 1. The primary concern, in terms of stress concentrations, lies in the region near the bolt head. However, because the inclusion of a washer increases the contact area, causing a more even load distribution and a reduction in stress concentrations, a check of the degree of symmetry ensures safe joint design. In order to study the symmetry of the current joint, strain gauges are placed on the bottom of the joint at 0° and 90° at Hole 3, as described in the experimental procedure in Chapter 4, Figure 4.11. Figure 5.12 compares the top and bottom strain gauge results at 295K for the 0° gauges, while Figure 5.13 shows the results for the 90° gauges, at 295K.

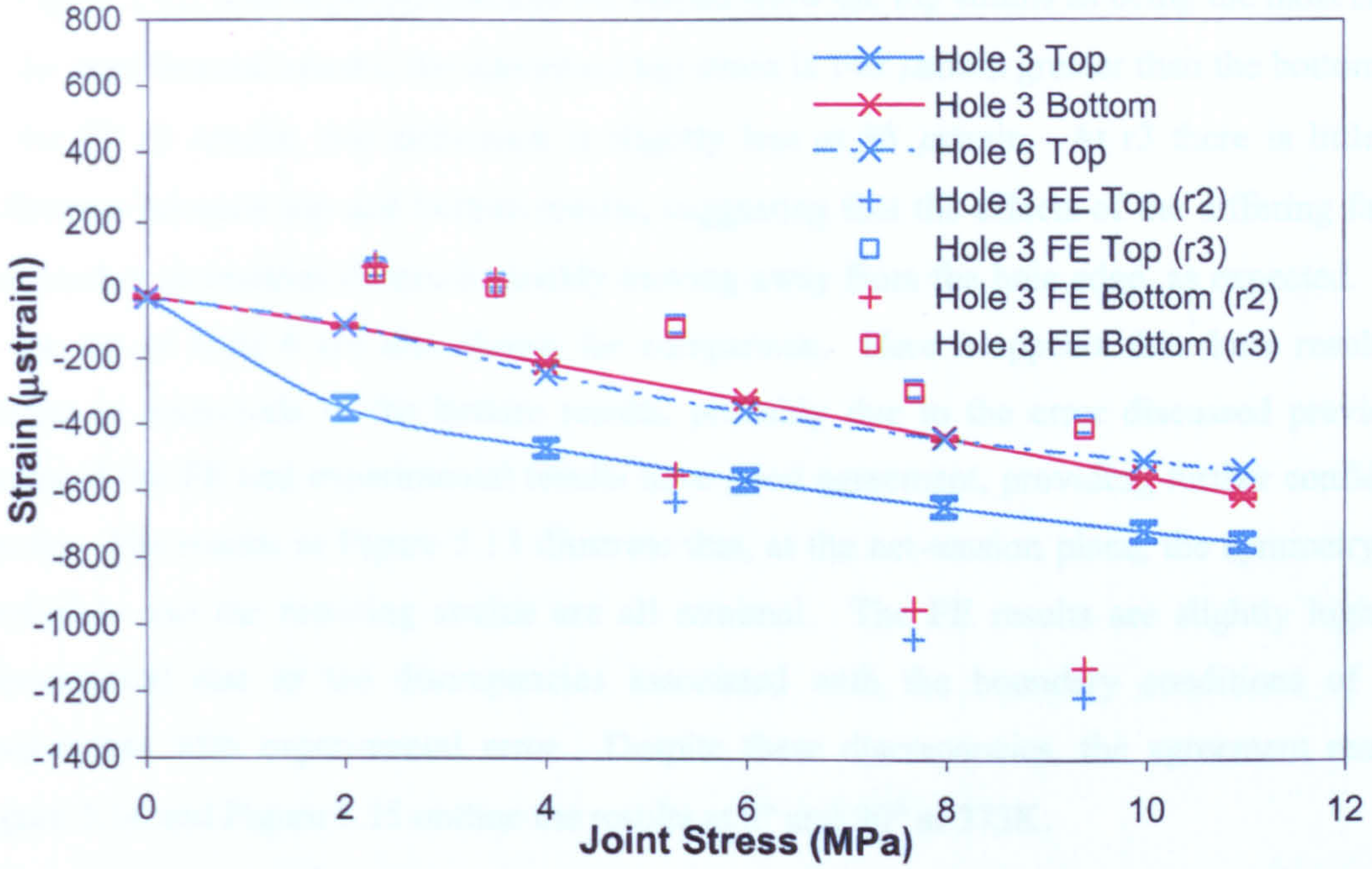

Figure 5.12. Symmetry comparison of top and bottom radial strain curves at 0° (295K).

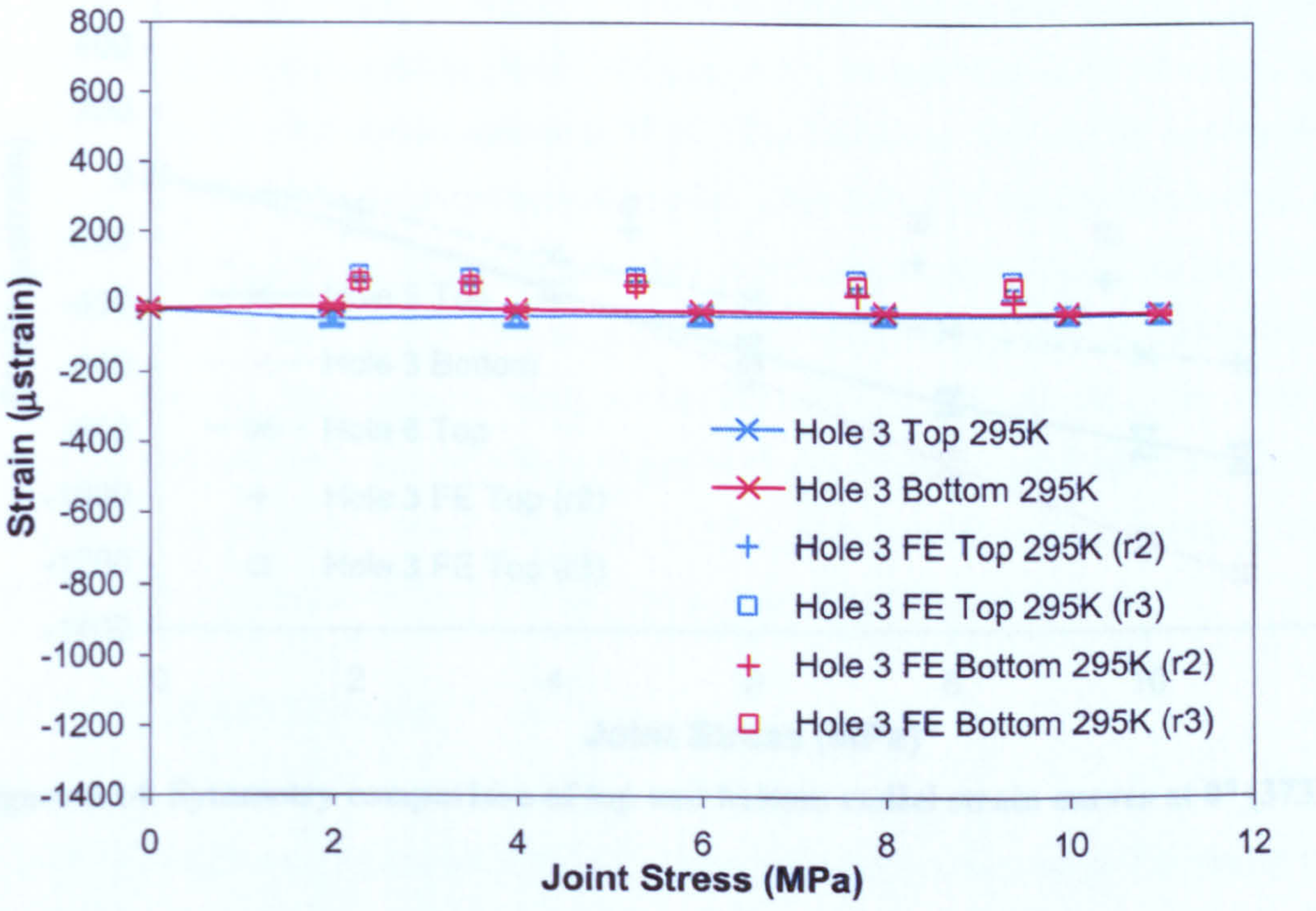

Figure 5.13. Symmetry comparison of top and bottom radial strain curves at 90° (295K).

In Figure 5.12, both experimental and FE results show the top strains as being the most compressive. In the experimental results, the maximum top strain is 140 μstrain greater than the bottom strain, and in the FE r2 results, this difference is slightly less at 88 μstrain. At r3 there is little noticeable difference between top and bottom results, suggesting that the effects of the differing fastener head and washer geometries diminish quickly moving away from the hole edge, as expected. The results at the top of Hole 6 are also shown for comparison. Here it appears that these results are more similar in magnitude to the bottom results, probably due to the error discussed previously. The trends of the FE and experimental results have good agreement, providing further confidence in the results. The results in Figure 5.13 illustrate that, at the net-tension plane, the symmetry effects are negligible and the resulting strains are all minimal. The FE results are slightly higher than the experimental due to the discrepancies associated with the boundary conditions of the FE, in conjunction with experimental error. Despite these discrepancies, the agreement remains good. Figure 5.14 and Figure 5.15 outline the results at 0° and 90° at 373K.

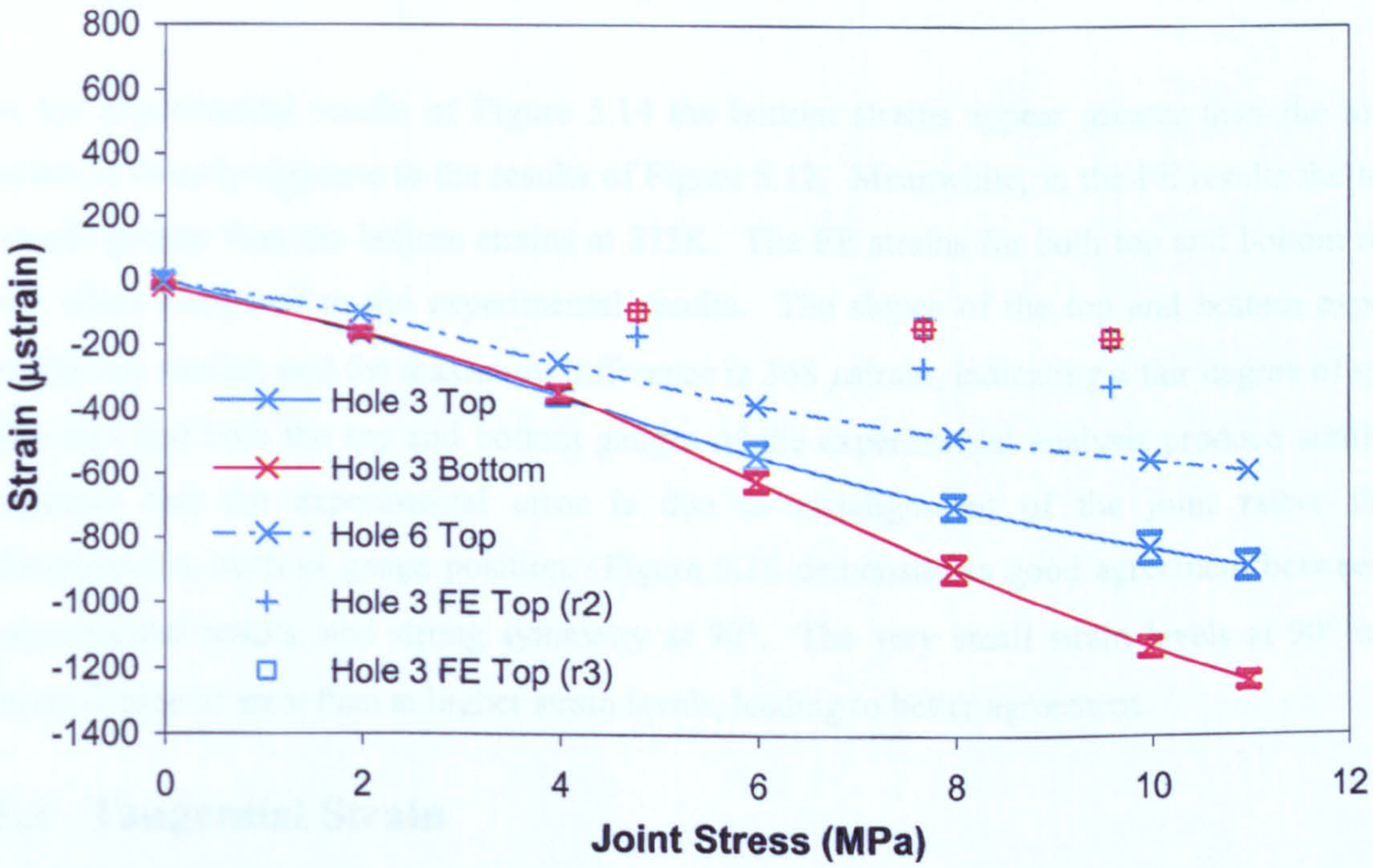

Figure 5.14. Symmetry comparison of top and bottom radial strain curves at 0° (373K).

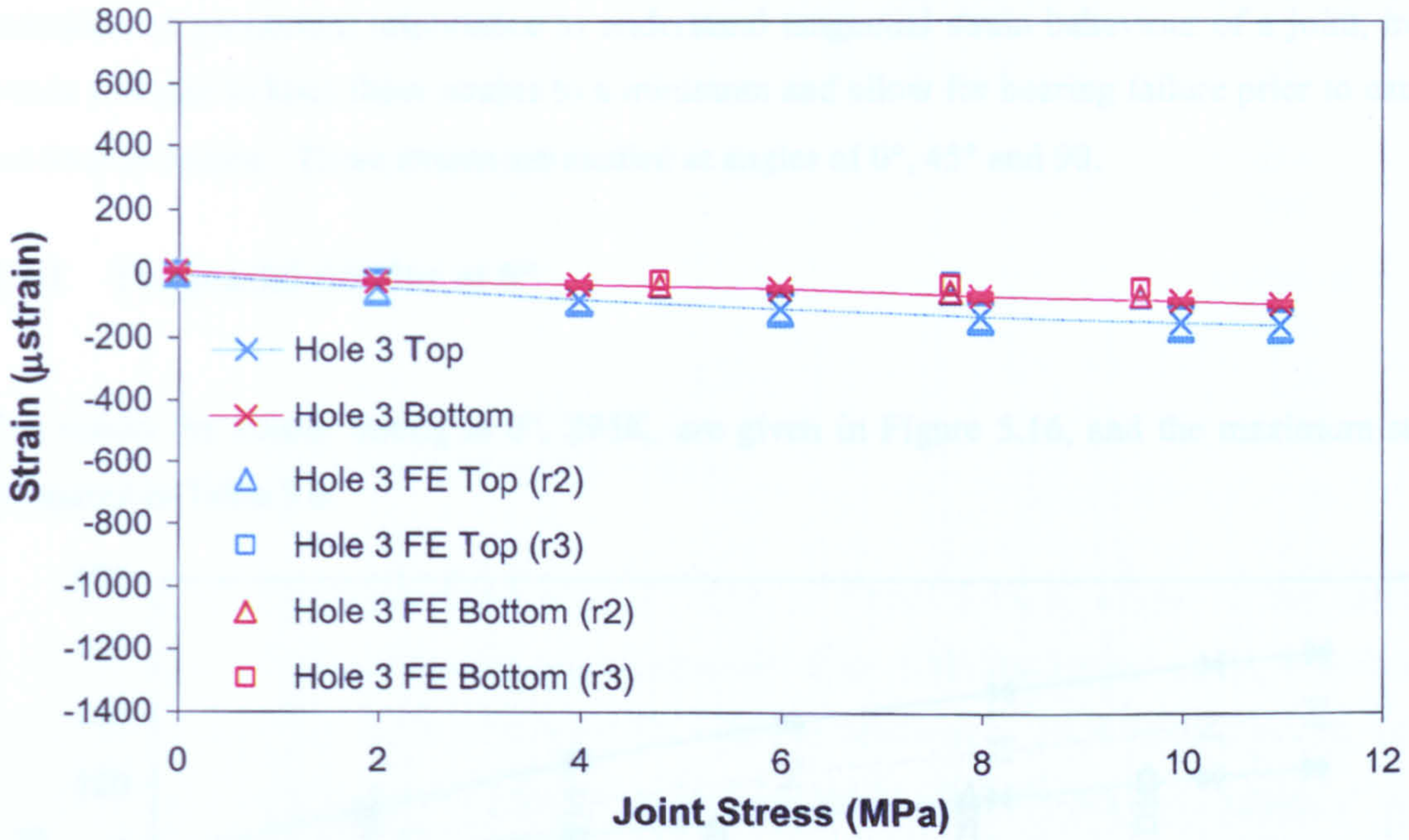

Figure 5.15. Symmetry comparison of top and bottom radial strain curves at 90° (373K).

In the experimental results of Figure 5.14 the bottom strains appear greater than the top strains, which is directly opposite to the results of Figure 5.12. Meanwhile, in the FE results the top strains remain greater than the bottom strains at 373K. The FE strains for both top and bottom results are low when compared to the experimental results. The slopes of the top and bottom experimental results are similar, and the maximum difference is 368 μstrain, indicating a fair degree of symmetry. The fact that both the top and bottom gauges of the experimental analysis produce similar results suggests that the experimental error is due to misalignment of the joint rather than local discrepancies, such as gauge position. Figure 5.15 demonstrates good agreement between FE and experimental results, and strong symmetry at 90°. The very small strain levels at 90° result in a lesser degree of error than at higher strain levels, leading to better agreement.

5.3 Tangential Strain

The study progresses from radial strains to tangential strains, since tangential strains play a role in determining overall joint strength and tend to dictate failure at the net-tension plane. Failure at the net-tension plane (90°) is generally catastrophic, meaning that complete joint failure occurs with no noticeable pre-failure damage, whereas failure at the bearing plane is generally considered a 'fail-safe' design, resulting in permanent, detectable damage to the joint before total joint failure. It is,

therefore, of paramount importance to understand tangential strain behaviour of a joint, in order to create a design to keep these strains to a minimum and allow for bearing failure prior to catastrophic net-tension failure. These strains are studied at angles of 0°, 45° and 90.

5.3.1 Tangential Strains at 0°

The results for tensile testing at 0°, 295K, are given in Figure 5.16, and the maximum strains are compared in Table 5.8.

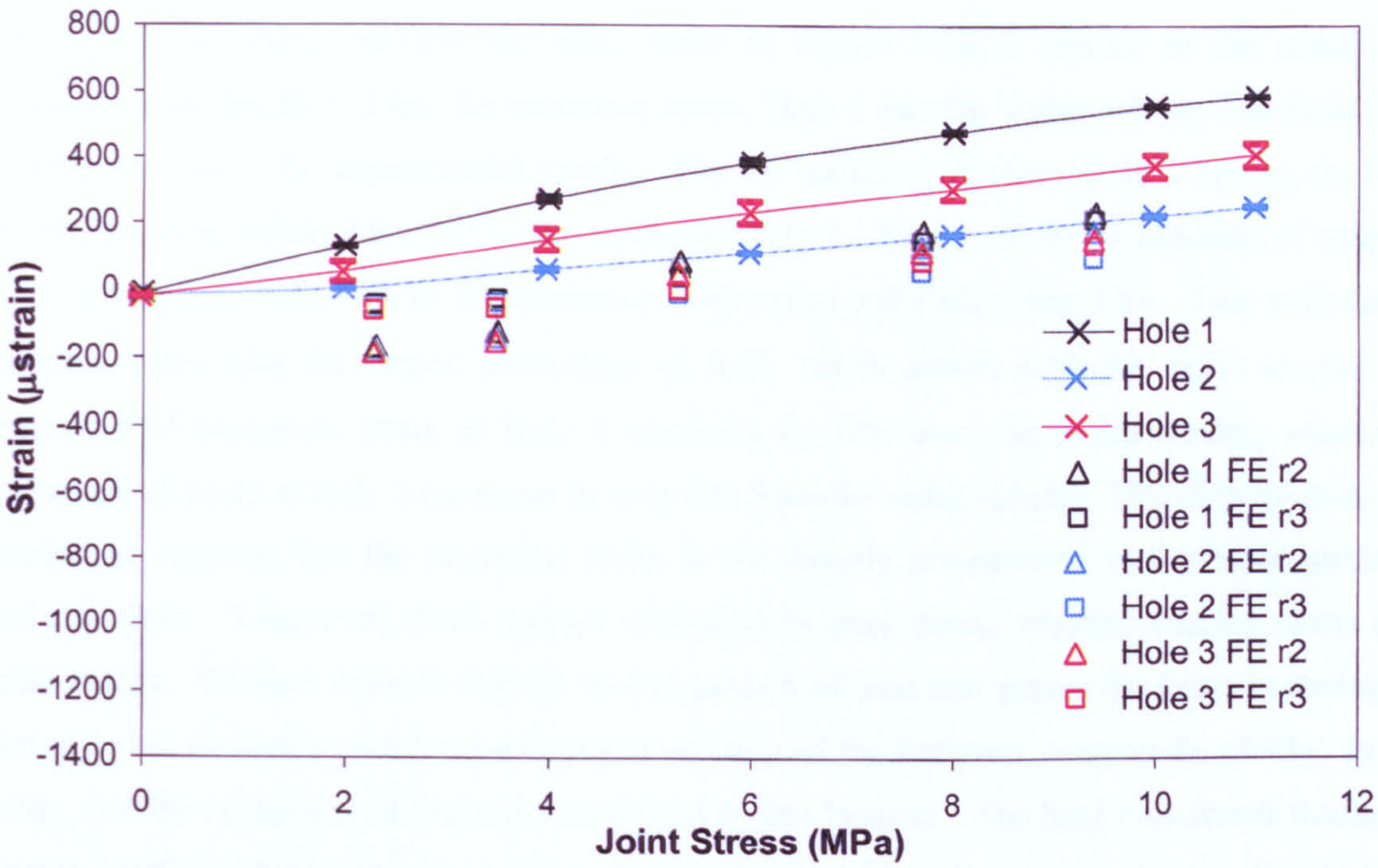

Figure 5.16. Joint stress versus tangential strain at 0° (295K).

Table 5.8. Comparison of maximum tangential strains at 0° (295K) at peak joint stresses.

	Hole 1 (μstrain)	Load Share	Hole 2 (μstrain)	Load Share	Hole 3 (μstrain)	Load Share
Experimental	**586** ± 1	47%	250 ± 2	20%	410 ± 36	33%
FE r2	**233**	41%	176	31%	154	28%
FE r3	**212**	48%	93	21%	135	40%

Examining Figure 5.16, the experimental tangential strain is positive, indicating a tensile strain or an expansion from the original element size at the bearing plane. This corresponds to the behaviour observed in the radial strain results. A radial compression is experienced at the 0° element. This

implies that the material being compressed in the radial direction tends to expand in the tangential direction, resulting in a positive tangential strain at the bearing plane, depicted in Figure 5.17.

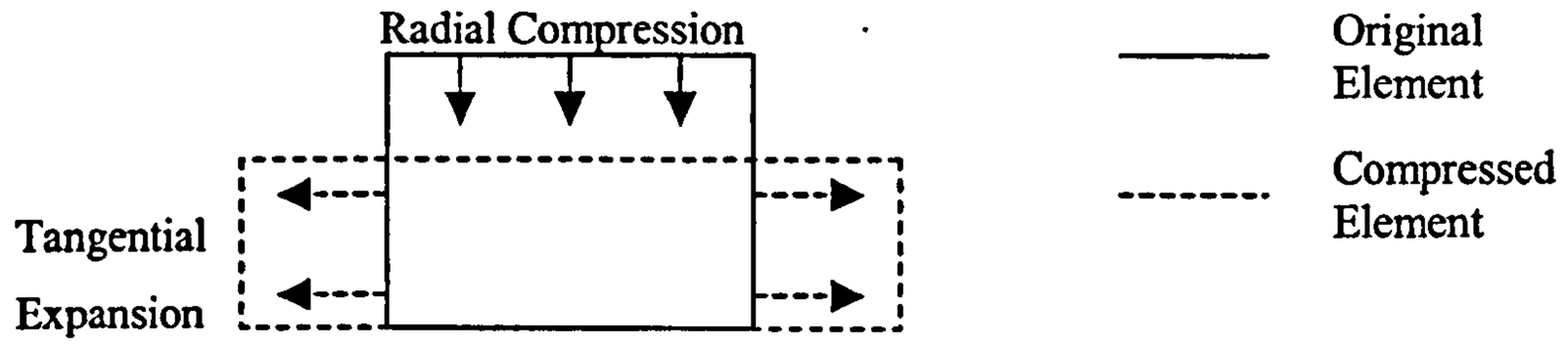

Figure 5.17. Description of element distortion.

The strain relationship between the three holes in Figure 5.16 is similar to the radial strain relationship, in that Hole 2 has the minimum strain, Hole 1 has the highest strain, and Hole 3 falls between the two in the experimental results. The FE results at r2 show Hole 3 having the lowest strains, but these values are close to the values of Hole 2. Hole 1 takes the majority of tangential strain distribution, with 47% of the maximum total strain, and Hole 3 has 33%. This indicates that the outer holes take the largest percentage of load, which agrees with the radial results. The percentage of maximum strain at Hole 1 increases by 10% over the radial results, whereas the percentage of strain at Hole 3 increases by only 1% from the radial results. This difference in strain distribution suggests that the tangential strain is not directly proportional to the radial strain at a particular hole. Tangential strain appears related to by-pass stress, whereas bearing stress drives radial strains. By-pass stress is defined as that portion of load that passes the fastener through the joint material, divided by the cross-sectional area between the fasteners, as given by (4-11). In other words, it is the remainder of load not transferred by the fastener. The load transferred through the fastener itself, divided by the cross-sectional contact area, defines bearing stress, according to (4-10). The current results imply that Hole 1 and Hole 3 have greater by-pass stress than Hole 2. The outer holes are expected to have higher strains at the net-tension, or by-pass region, as they are more directly influenced by the load application, unlike the middle fastener, which reacts only to the secondary motion or load induced by surrounding fasteners. The fact that the tangential strains do not correspond directly to the radial results demonstrates the complexity of the problem. The influence of other factors, in particular boundary conditions, is evident, since the tangential-radial relationship is clearly non-linear.

In this test, the slightly compressive strain observed at the beginning of the FE model results corresponds to the small tensile strain observed in the radial results. The tensile strain in the radial

direction causes element compression, and the corresponding compressive strains in the tangential direction. The FE results tend to under-predict the strains found experimentally. This discrepancy is a function of the friction coefficient in the FE analysis. The assumed coefficient appears to under-predict the sliding that occurs with the experimental specimen. Sliding of the joint material around the fastener induces tangential strains at the bearing plane as the element stretches and elongates around the fastener with increased load. In the FE model, the friction coefficient effectively reduces the sliding action, which in turn, reduces the induced tangential strains. Chordwise symmetry is examined next, to determine the load distribution between the two columns of fasteners. Figure 5.18 compares Holes 1 to 3 with Holes 4 to 6.

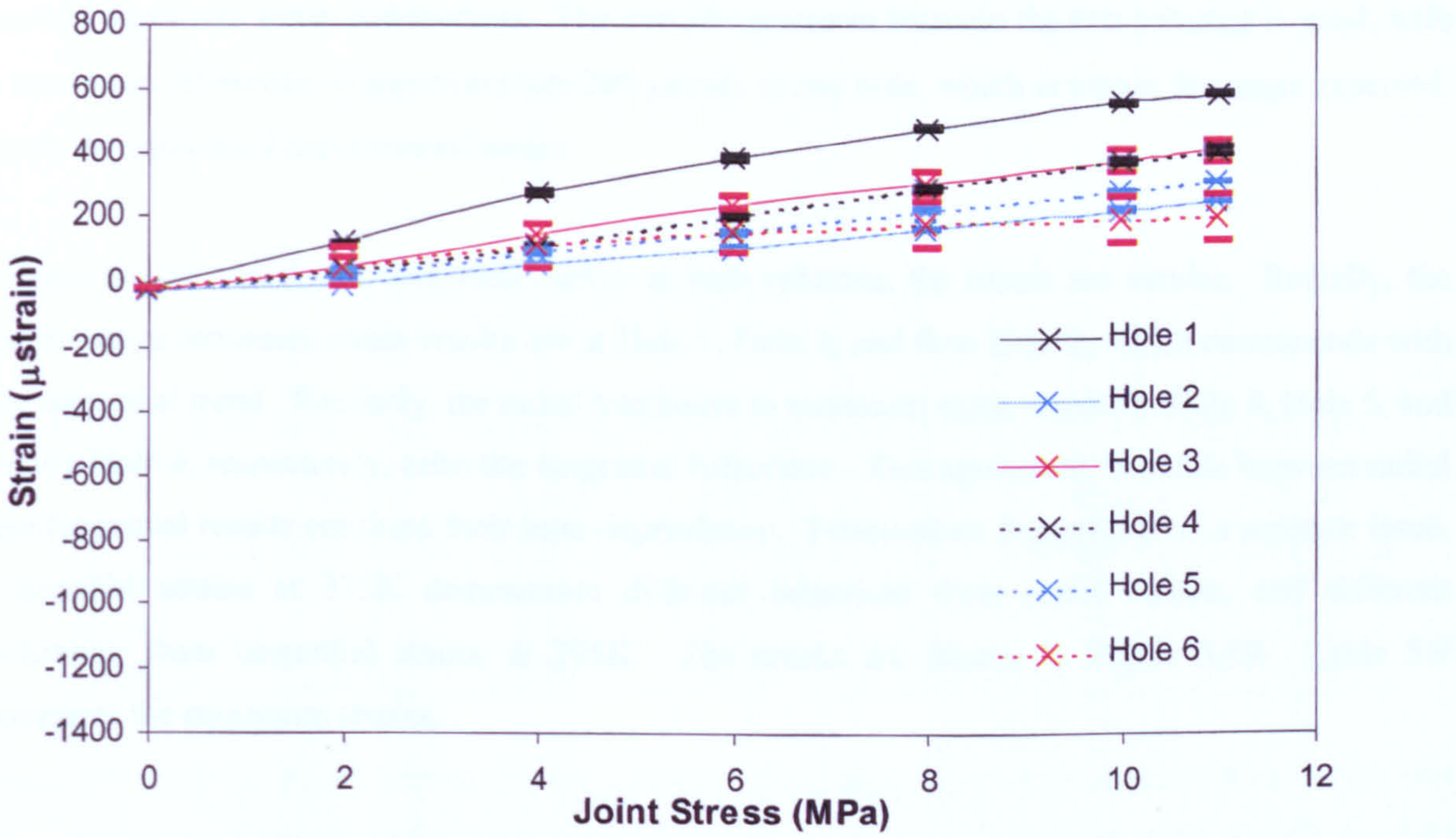

Figure 5.18. Comparison of tangential strain at Holes 1 to 3 with Holes 4 to 6 at 0° (295K).

From Figure 5.18, the strains at Holes 4 and 6 are less than those at Holes 1 and 3. However, the strain at Hole 5 is higher than at Hole 2, and the strains at Holes 4 to 6 are much closer in magnitude than those of Holes 1 to 3. The maximum strain in the second column is observed at Hole 4 with a tensile value of 407 ± 10 μstrain. The maximum strains at Holes 5 and 6 are 310 ± 2 μstrain and 205 ± 71 μstrain, respectively. This results in 44% of the maximum tangential strain at Hole 4, 34% at Hole 5, and 27% at Hole 6. The results are 3% lower than at Hole 1, 14% higher than at Hole 2, and 11% lower than at Hole 3, respectively. This shows a change in load distribution.

The greatest difference between the two columns, in terms of magnitude, occurs between Holes 3 and 6, with the maximum tangential strain at Hole 3 being twice that of Hole 6. The values at Hole 2 and 5 show fair agreement, and the results for Holes 1 and 4 show a similar profile and slope, despite the fact that the maximum strain at Hole 1 is double the maximum strain at Hole 4. The slope at Hole 6 appears to deviate from the slope at Hole 3, particularly after 5 MPa joint stress. This shift in percentage maximum strain location and the difference in magnitude between Hole 3 and Hole 6, are similar to the radial analysis, and are likely caused by misalignment during manufacture, or an error in the positioning of the gauge. The discrepancy between the columns in general, implies there is an error in load distribution between the two columns. Misalignment within the load cell itself is another possibility. Comparing the FE results, Holes 1 to 3 appear to be more similar, particularly in percent maximum strain distributions. The overall agreement between the two columns is good, with a maximum difference of approximately 200 μstrain at any hole, which is within the range expected, given the associated experimental errors.

Comparing the radial and tangential curves at both columns, the trends are similar. Radially, the maximum to minimum strain results are at Hole 1, Hole 3, and then Hole 2, which corresponds with the tangential trend. Similarly, the radial maximum to minimum strain results at Hole 4, Hole 5, and finally Hole 6, respectively, echo the tangential behaviour. This agreement in trends between radial and tangential results confirms their inter-dependency. Temperature dependence is a separate issue. Tangential strains at 373K demonstrate different behaviour from radial strains, and different behaviour from tangential strains at 295K. The results are shown in Figure 5.19. Table 5.9 compares the maximum strains.

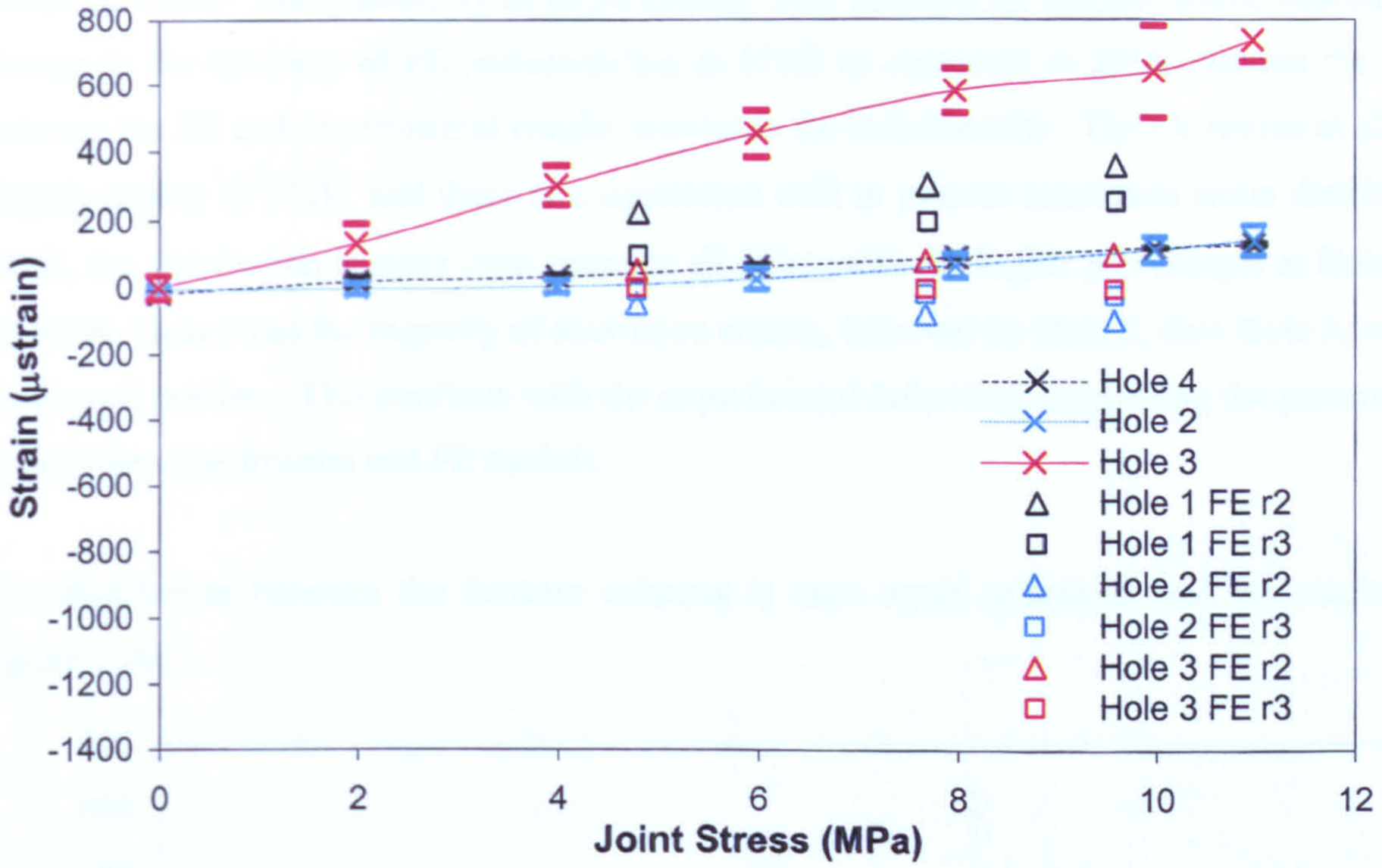

Figure 5.19. Joint stress versus tangential strain at 0° (373K).

Table 5.9. Comparison of maximum tangential strains at 0° (373K) at peak joint stresses.

	Hole 4 (μstrain)	**Load Share**	**Hole 2 (μstrain)**	**Load Share**	**Hole 3 (μstrain)**	**Load Share**
Experimental	11 ± 21	1%	136 ± 44	15%	**736** ± 65	83%
FE r2	**252**	89%	-26	9%	5	2%
FE r3	**358**	64%	-100	18%	98	18%

Since the gauge at Hole 1 became disengaged during heating, Figure 5.19 replaces Hole 1 data with Hole 4 results. Experimentally, Hole 4 appears to have negligible tangential strain, Hole 2 has little tangential strain, while Hole 3 exhibits the most significant strain. The maximum strain results at Hole 3 matches the radial results, where Hole 3 carries the greatest strain at 373K. The behaviour at Holes 1 and 2 correlates with the radial behaviour at elevated temperature in Figure 5.6, where Hole 1 has the smallest strain, and Hole 2 has low strain levels compared to Hole 3. Because the significant radial strain at Hole 1 is expected to cause associated tangential strains, therefore the results at Hole 1 are lower than expected.

The FE results show Hole 1 with the highest strains, followed by Hole 3, and then Hole 2, similar to FE radial strain behaviour. The FE again appears to have the outer holes carrying the larger portions of maximum strains. The results at Holes 2 and 3 underestimate the strains, correlating with the

trends at 295K. The possibility of experimental error induced by thermal loads, combined with a change in the accuracy of FE representation at 373K as compared to 295K reduces the agreement between the FE and experimental results, similar to the radial results. The FE strains at all holes are slightly higher at 373K, and there is a significant shift in percent maximum strain distribution. At 295K, the distribution is more even amongst all holes, with the higher percentages at Holes 1 and 3. At 373K, Hole 1 has the majority of maximum strains, followed by Hole 2, then Hole 3, which has a very small portion. This conflicts with the experimental behaviour, suggesting the presence of error in both the experimental and FE models.

The distribution between the fastener columns is once again examined, and the results given in Figure 5.20.

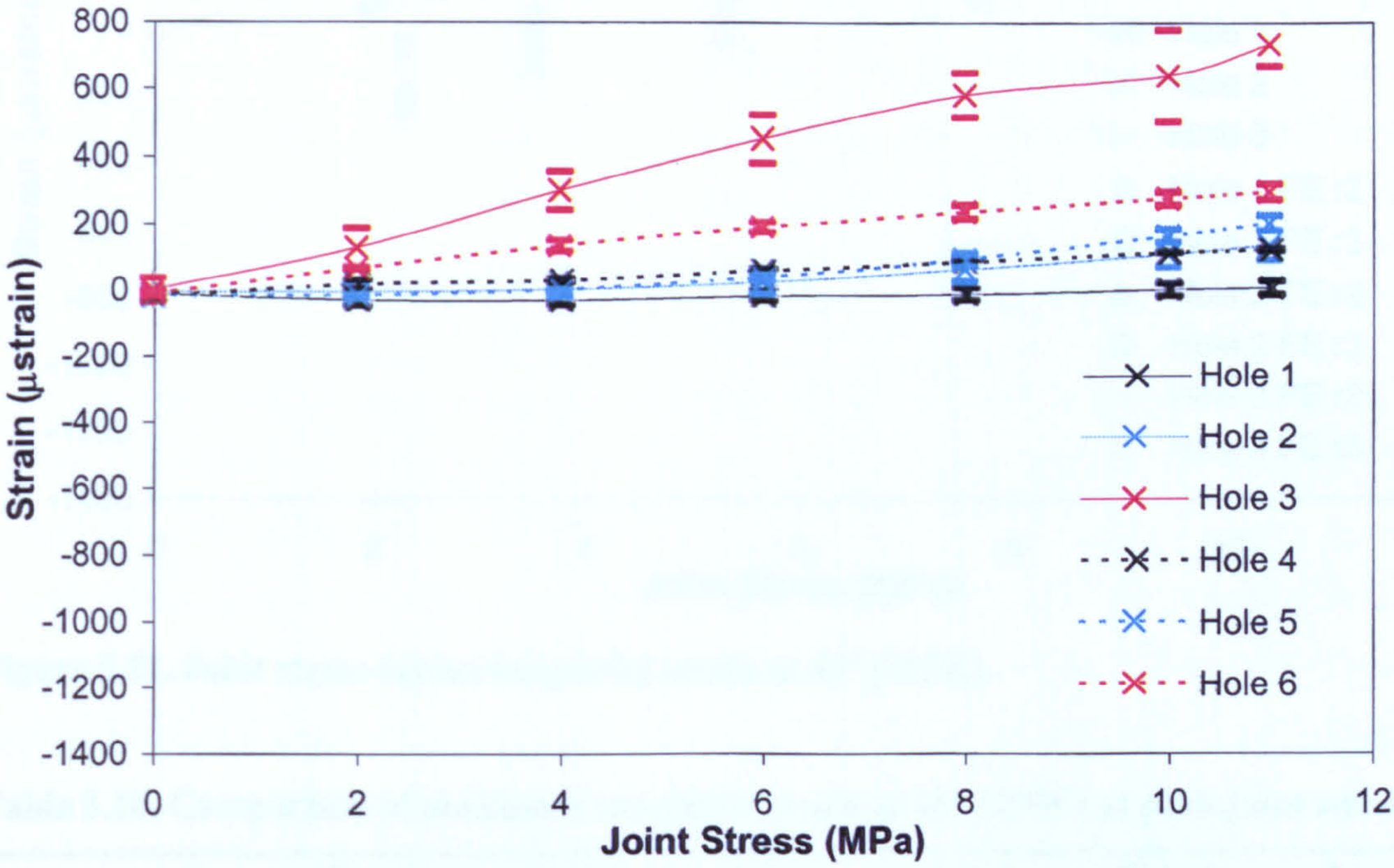

Figure 5.20. Comparison of tangential strains at Holes 1 to 3 with Holes 4 to 6 at 0° (373K).

Figure 5.20 shows the values of Hole 1 not deviating from initial strains because of the disengaugement of the gauge. Again the results show the greatest difference between the two columns at Holes 3 and 6, with the maximum value at Hole 3 being 440 μstrain greater than at Hole 6. This discrepancy confirms the possibility of misalignment, manufacturing error, or gauge placement error as suggested by the 295K results. Similar to results at 295K (Figure 5.19), Holes 2 and 5 show relatively good agreement, indicating a more even load distribution at this point, and

providing additional indication of individual error at Hole 3 or Hole 6. Hole 4 now demonstrates a tensile strain, agreeing with expected behaviour, given the compressive radial strains.

5.3.2 Tangential Strains at 45°

Moving away from the bearing plane, Figure 5.21 represents the tangential strain results for the 45° gauge at room temperature, with the maximum strain comparison given in Table 5.10.

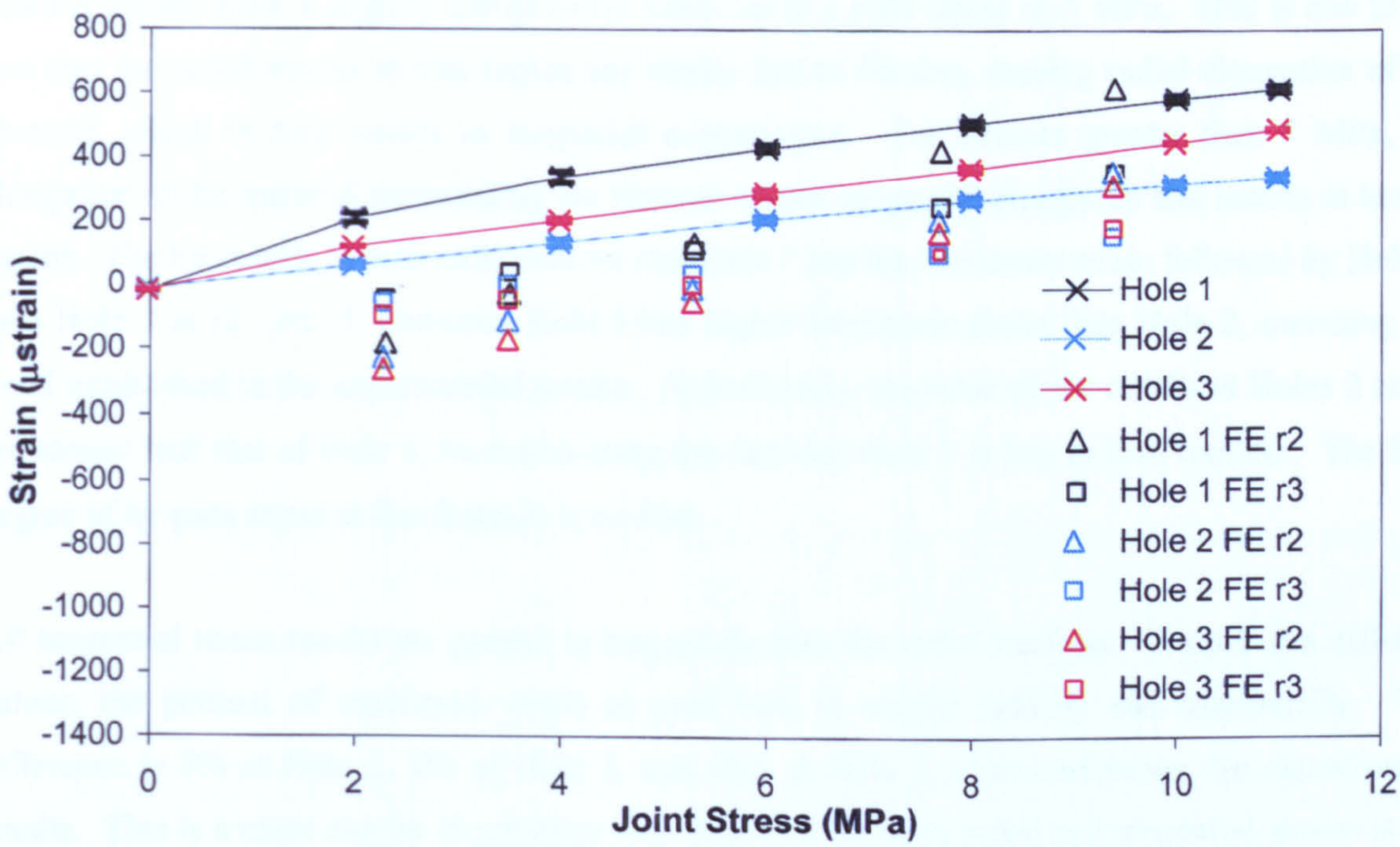

Figure 5.21. Joint stress versus tangential strain at 45° (295K).

Table 5.10. Comparison of maximum tangential strain at 45° (295K) at peak joint stresses.

	Hole 1 (µstrain)	Load Share	Hole 2 (µstrain)	Load Share	Hole 3 (µstrain)	Load Share
Experimental	**613** ± 11	42%	339 ± 11	24%	490 ± 2	34%
FE r2	**618**	48%	354	28%	314	24%
FE r3	**352**	51%	155	22%	182	27%

The results in Figure 5.21 show Hole 1 as having the experimental maximum strain, Hole 2 with the minimum strain, and Hole 3 falling in between. These results indicate Hole 1 and Hole 3 receive the greater portion of the by-pass stress, agreeing with results for radial behaviour in the same plane. The slopes of all three curves are very similar, suggesting that the tangential load distribution among

the fasteners remains comparable, regardless of joint stress. The 45° plane is less influenced by direct contact than the bearing plane, simplifying the change in conditions with increased joint stress. When compared to the strains at 0°, the tangential results at 45° are higher. The difference at all holes is less than 100 μstrain, and the percentages of maximum load remain similar to those at 0°. The increase in tangential strain is expected as the influence of by-pass stress increases as the net-tension plane is approached.

The FE results show a slightly compressive strain up to a joint stress of 5 MPa. This is due to the fact that the radial strains in this region are tensile due to friction, causing radial elongation of the element, which in turn results in tangential compression. For stresses greater than 5 MPa, the elongation of the material surrounding the fastener causes tangential elongation and results in tensile strains. The FE results at both radii indicate that Hole 1 has the maximum strain followed by Hole 2, then Hole 3 at r2. At r3, however, Hole 3 has higher maximum strain than Hole 2, matching the trend established in the experimental results. At both radii, the value of the results at Holes 2 and 3 are almost half that of Hole 1, re-emphasising the fact that Hole 1 is key to load transfer. The high degree of by-pass stress at this fastener is evident.

All tangential strain results are greater in magnitude than the radial readings. Despite the different values, the percent of maximum strain at each hole is similar radially and tangentially. The difference is 8% at Hole 1, 2% at Hole 2, and 10% at Hole 3 when comparing the experimental results. This is a more similar distribution than observed between radial and tangential strains at the bearing plane. The greatest difference between results at the 45° gauges and those at the bearing and net-tension planes is that the results at 45° are heavily influenced by both radial and tangential strains rather than dominated by one particular type of strain. This brings the maximum strain percentages closer together when comparing radial and tangential results. The results for the tensile tests at 373K are given in Figure 5.22. Table 5.11 depicts the maximum strains at each hole.

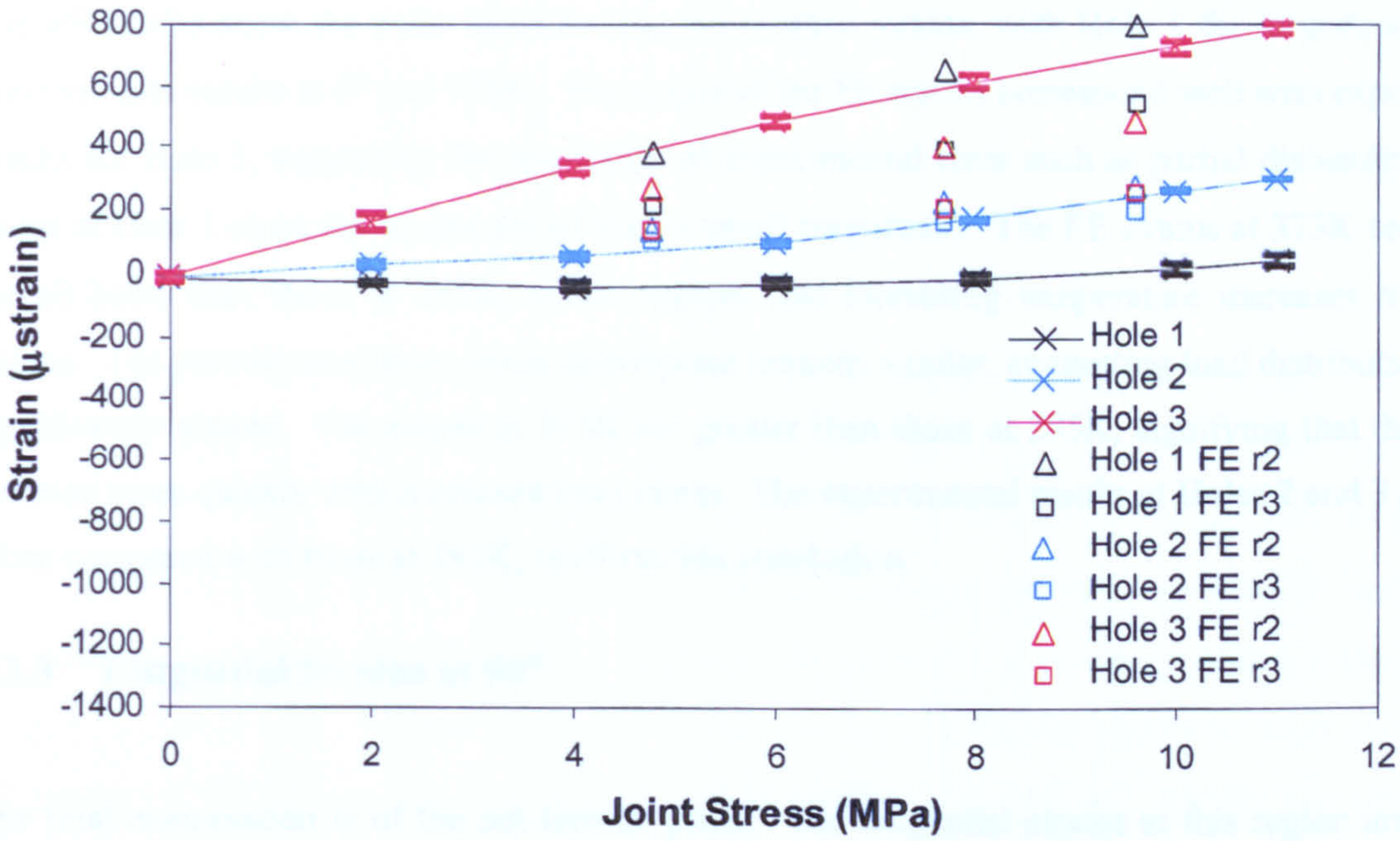

Figure 5.22. Joint stress versus tangential strain at 45° (373K).

Table 5.11. Comparison of maximum tangential strains at 45° (373K) at peak joint stresses.

	Hole 1 (μstrain)	Load Share	Hole 2 (μstrain)	Load Share	Hole 3 (μstrain)	Load Share
Experimental	41 ± 15	4%	296 ± 2	26%	**781** ± 18	70%
FE r2	**790**	51%	272	18%	481	31%
FE r3	**535**	54%	193	20%	252	26%

By comparing Figure 5.22 with Figure 5.21, it is easy to see a change in behaviour at the higher temperature. Experimentally, the maximum strain now occurs at Hole 3, with the strain at Hole 1 being negligible, and the maximum strain value at Hole 2 between the two. This behaviour is similar to that at 0°, 373K. At 45°, Hole 2 appears to take a greater portion of the load since the percent maximum strain has increased by 8% over that at 0°, and maximum strain has increased by 160 μstrain. The maximum strain at 45° increases by 45 μstrain over 0° results. Meanwhile, the percent at Hole 3 decreases 13% from the results at the bearing plane. Comparing these results to the results at 295K, the maximum tangential strains decrease by 572 μstrain at Hole 1, and 43 μstrain at Hole 2, but increase by 290 μstrain at Hole 3. This again emphasises that temperature change results in alteration in strain distribution.

The FE results show the outer holes having the greatest strains, with Hole 1 the largest, similar to previous data results at 0° and 373K. The slopes of the FE results correspond well with experimental results for Hole 3, suggesting the possibility of experimental error such as partial disbanding of the gauge at Hole 1 since the strains are of such a small magnitude. The FE strains at 373K are greater for all holes than those at 295K, which implies that increasing temperature increases maximum strains. The percent maximum strain distribution remains similar, suggesting load distribution is not significantly altered. The slopes at 373K are greater than those at 295K, signifying that the strains increase more quickly with increased joint stress. The experimental results at Holes 2 and 3 at 373K, when compared with those at 295K, reaffirm this conclusion.

5.3.3 Tangential Strains at 90°

The final examination is of the net tension plane. The tangential strains at this region are critical strains for joint design, as they dictate the occurrence of catastrophic net-tension failure. Figure 5.22 outlines the results at the 90° gauges at 295K, and Table 5.12 compares maximum strains.

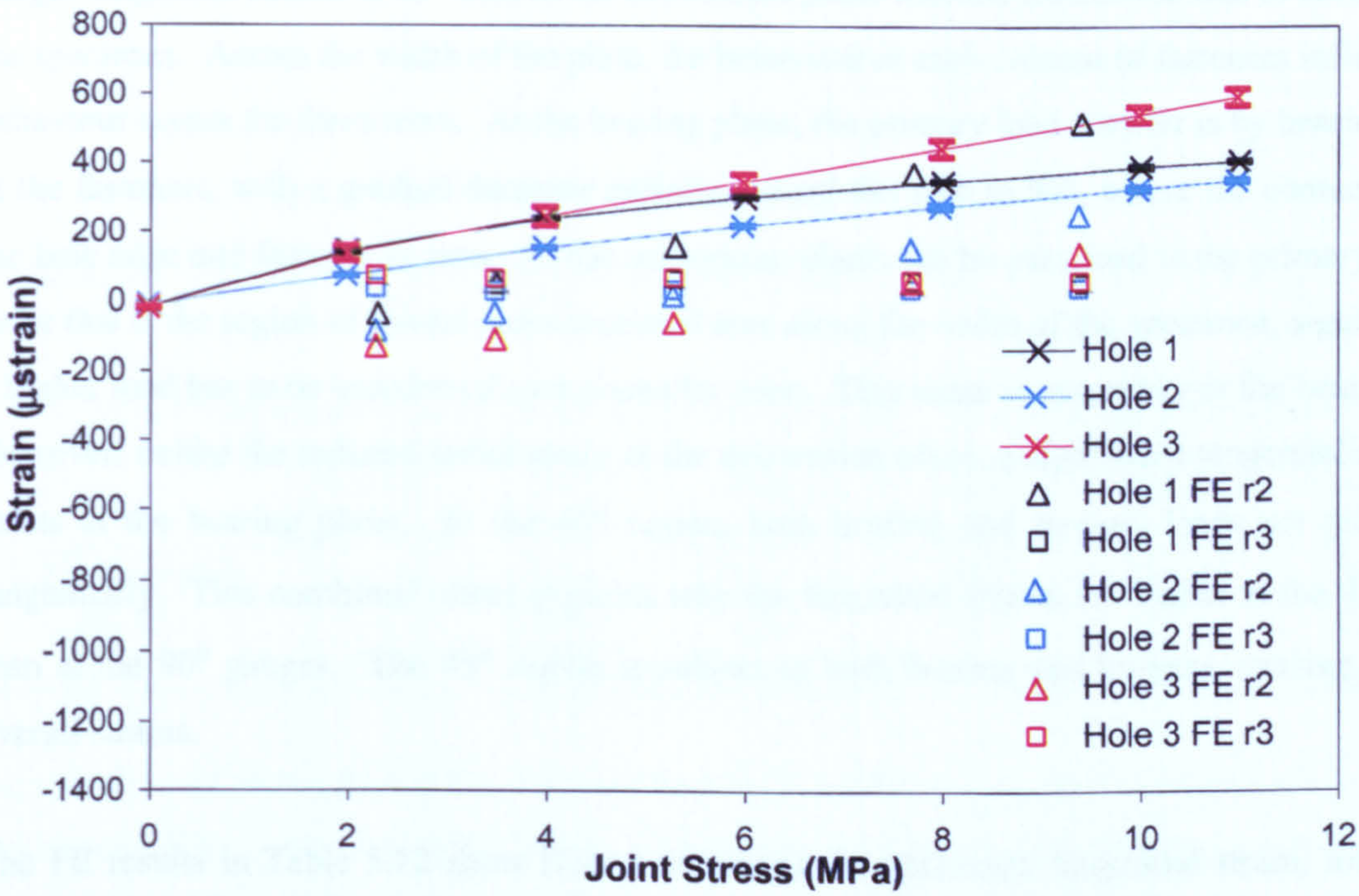

Figure 5.23. Joint stress versus tangential strain at 90° (295K).

Table 5.12. Comparison of maximum tangential strains at 90° (295K) at peak joint stresses.

	Hole 1 (μstrain)	Load Share	Hole 2 (μstrain)	Load Share	Hole 3 (μstrain)	Load Share
Experimental	406 ± 2	30%	346 ± 5	26%	592 ± 24	44%
FE r2	518	57%	248	27%	142	16%
FE r3	369	58%	152	24%	109	17%

The results of Figure 5.22 indicate that the experimental maximum tangential strain occurs at Hole 3, the smallest strain at Hole 2, with the strain at Hole 1 between the two. This behaviour differs from the 45° gauges, where Hole 1 has the greatest strain. This suggests that the by-pass load at Hole 3 is more significant than at Hole 1. The magnitudes of the strains are similar to those at 45°, and in fact, the maximum overall strain is 20 μstrain higher at 45°, although it occurs at Hole 1 rather than at Hole 3. A comparison of Figure 5.20 with Figure 5.22 reveals that the maximum tangential strains are greater at the 45° gauges than the 90°, by 107 μstrain at Hole 1, 7 μstrain at Hole 2, and 112 μstrain at Hole 3.

Larger tangential strains at 45° than at the net-tension plane indicate interaction due to constraints on the specimen. Across the width of the plate, the behaviour at each column of fasteners influences the behaviour across the three rows. At the bearing plane, the primary load transfer is by bearing contact at the fasteners, with a gradual decrease radially around the hole to 90°, where the contact between the hole edge and fastener is zero. At the net-tension plane, the by-pass load is the primary concern, since this is the region of lowest cross-sectional area along the width of the specimen, signifying that a higher load has to be transferred over a smaller zone. This strain is secondary at the bearing plane. However, unlike the reduced radial strain at the net-tension plane, a significant tangential strain still exists at the bearing plane. In the 45° region, both bearing and by-pass loads act radially and tangentially. This combined effect explains why the tangential strains are higher at the 45° gauges than at the 90° gauges. The 45° region is subject to both bearing and by-pass, causing increased overall strains.

The FE results in Table 5.12 show Hole 1 as having the maximum tangential strain, followed by Hole 2, then Hole 3 with the lowest strains. The percent maximum strain distribution also differs from the experimental results. This discrepancy is a function of error both in the experimental results, where manufacturing misalignment may shift load distribution, or gauge positioning may influence results, and in the FE results, where the assumption of certain boundary conditions may

influence the net-tension plane. In the FE analysis, the back portion of the model is constrained to move only in accordance with the behaviour of the CFRP skin, whereas experimentally, the mid-plane is influenced by the behaviour of the aluminium laps, as well as the CFRP skin. These differences are not evident in the radial results because the magnitude of the data is so small. Despite these discrepancies, the slopes of the FE and experimental results show acceptable agreement. The results for the 90° gauges at 373K are shown in Figure 5.24. The maximum strains are in Table 5.13.

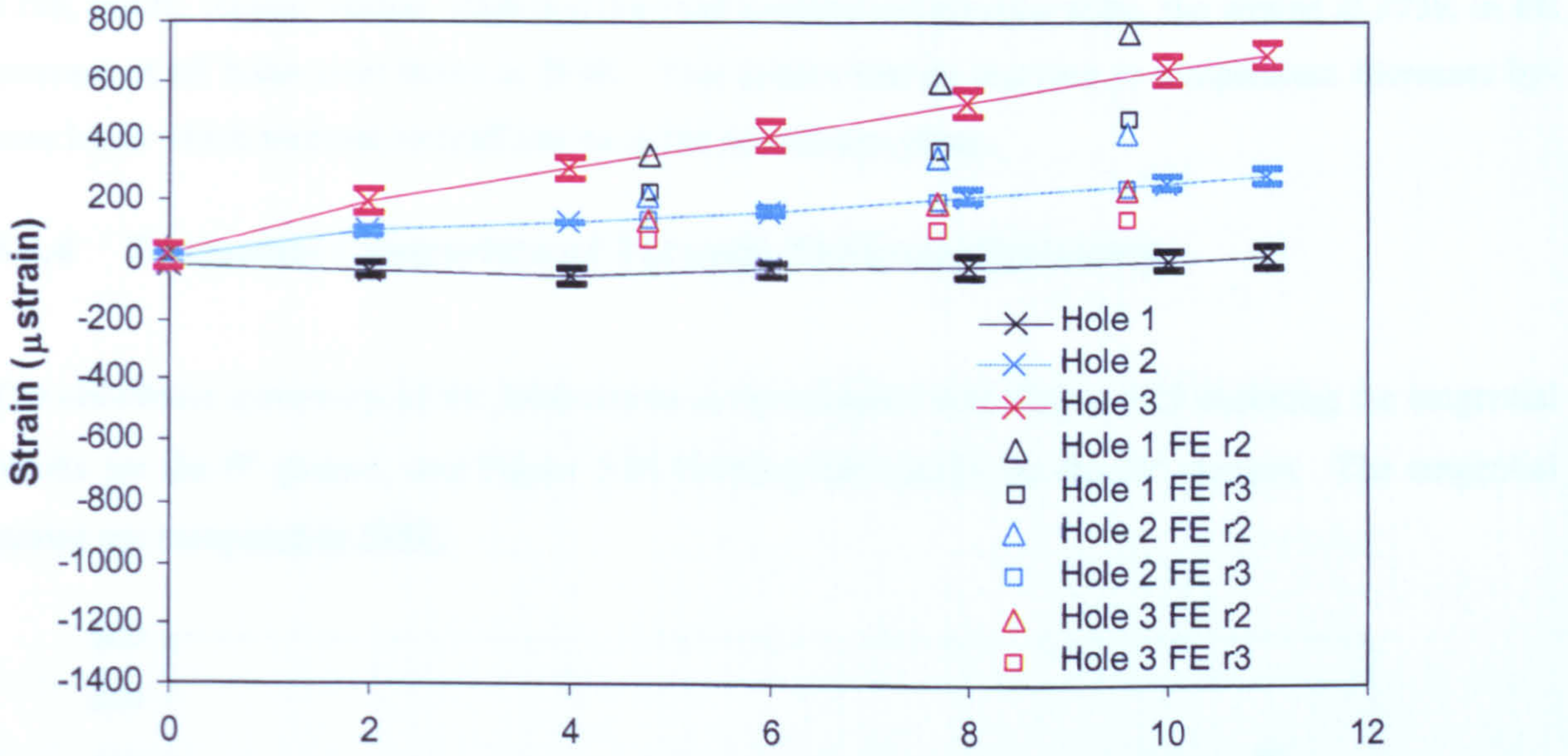

Figure 5.24. Joint stress versus tangential strain at 90° (373K).

Table 5.13. Comparison of maximum tangential strains at 90° (373K) at peak joint stresses.

	Hole 1 (μstrain)	Load Share	Hole 2 (μstrain)	Load Share	Hole 3 (μstrain)	Load Share
Experimental	17 ± 36	2%	282 ± 29	28%	**690** ± 43	70%
FE r2	**766**	54%	424	30%	237	16%
FE r3	**470**	55%	238	28%	139	17%

At the elevated temperature, the experimental maximum strain occurs at Hole 3, Hole 2 has less strain, and Hole 1 has negligible strain. This behaviour is very similar to that observed in Figure 5.21 at 45°, although the strains at 90° are lower by 91 μstrain at Hole 3, 14 μstrain at Hole 2, and 24 μstrain at Hole 1, respectively. As at 295K, the 45° plane has higher strains than the net-tension plane due to the constraints imposed by the second column of fasteners, as well as the interaction of the radial strains caused by the bearing load at the bearing (0°) plane and the tangential strains caused

by the by-pass loads at the net-tension (90°) plane. When compared with the 295K results, Hole 1 shows a decrease of 389 μstrain, and Hole 2 a decrease of 64 μstrain, but the strains at Hole 3 increase by 98 μstrain. The strain results at Hole 1 are lower than expected, since all holes should have some tangential strain at the net-tension plane due to the tensile load. This, coupled with the fact that the FE results show the strains at Hole 1 as the highest, suggests experimental error, again possibly gauge disbonding. Although the percent maximum strains between the 295K results and the 373K results remain similar, implying the load distribution remains alike, the strains at 373K in FE increase at all holes over those at 295K. This means that an increase in temperature increases by-pass loads which increase overall strains at the net-tension plane.

5.3.4 Tangential Comparison of Through-Thickness Symmetry

The chordwise symmetry of the joint strains is investigated with Figure 5.25 outlining the tangential results for the 0° gauges, and Figure 5.26 showing the results for the 90° gauges. The tangential strains are compared at 295K.

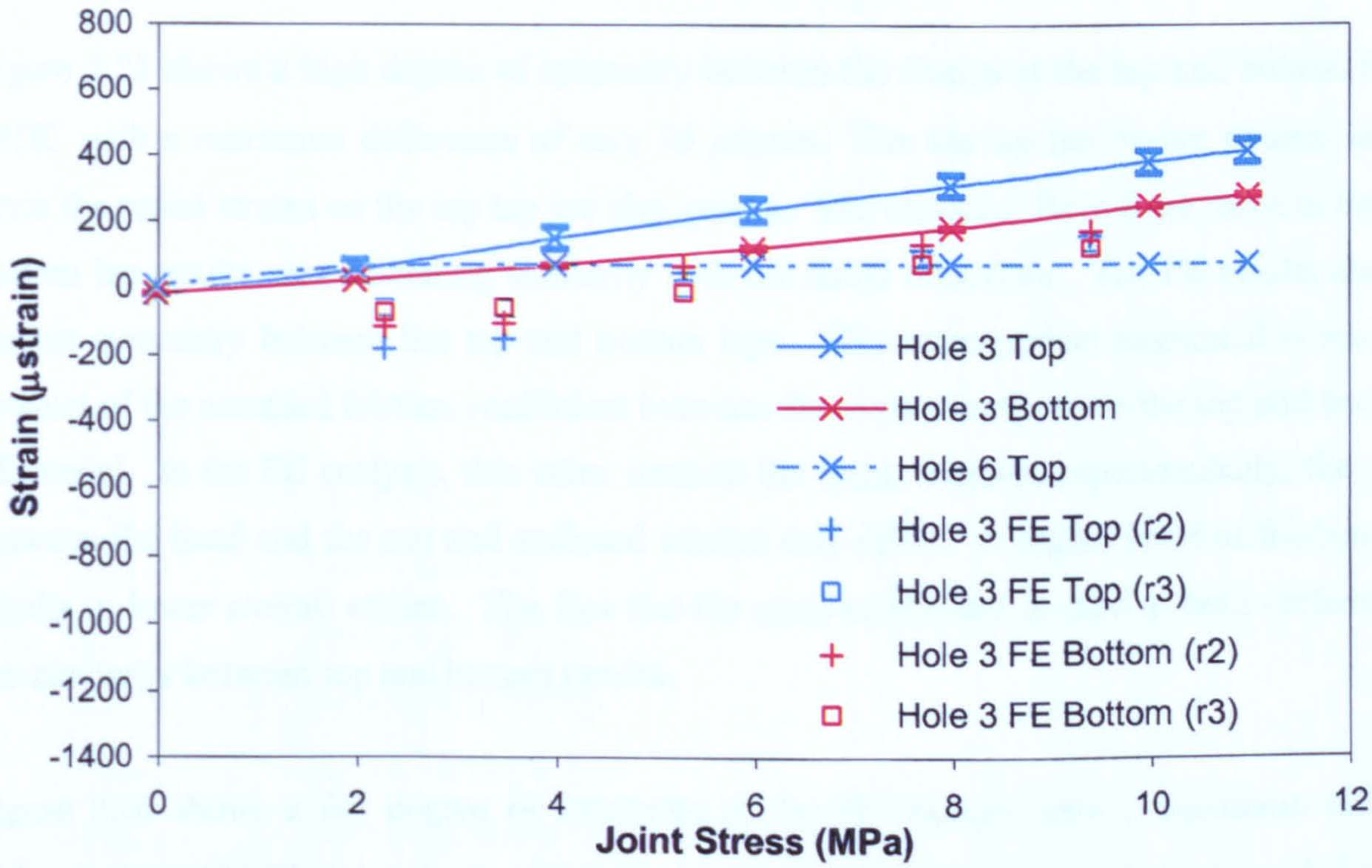

Figure 5.25. Symmetry comparison of top and bottom tangential strains at 0° (295K).

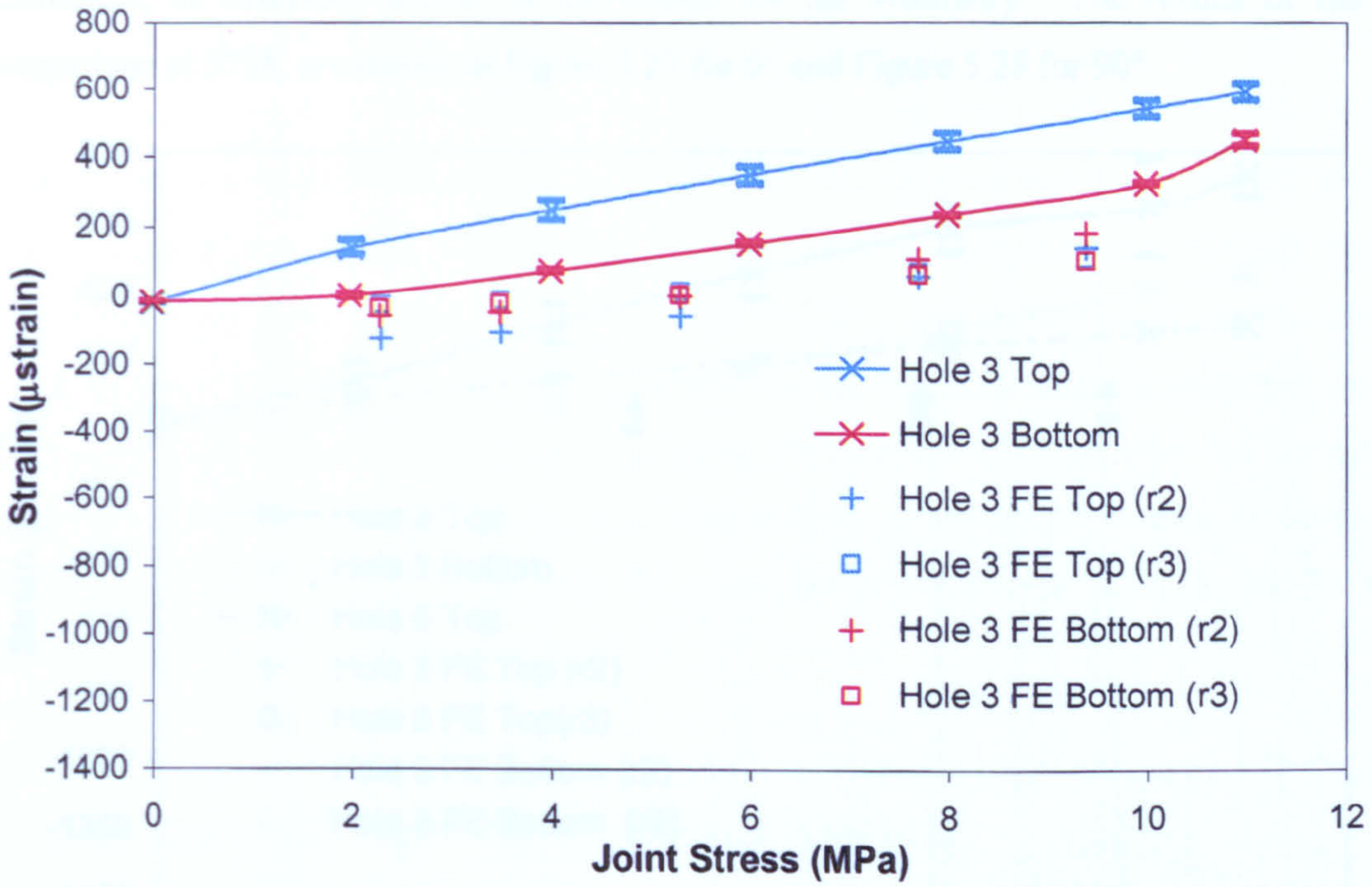

Figure 5.26. Symmetry comparison of top and bottom tangential strains at 90° (295K).

Figure 5.25 shows a high degree of symmetry between the strains at the top and bottom laps, at 0°, 295K, with a maximum difference of only 73 μstrain. The top lap has higher strains, as expected since the radial strains on the top lap are also greater. The results at Hole 6 are more in line with the bottom lap results, demonstrating similarity with the radial behaviour. The FE results show almost perfect symmetry between the top and bottom laps. This more perfect alignment is most likely a product of the assumed friction coefficient between the contact surfaces on the top and bottom of the FE model. In the FE analysis, this value remains the same, whereas experimentally, the coefficient between the head and the nut and enclosed washer may differ. A higher level of friction in the FE results in lower overall strains. The fact that the same coefficient is used at both surfaces explains the similarity between top and bottom results.

Figure 5.26 shows a fair degree of symmetry at the 90° gauges, with a maximum difference of 216 μstrain at 10 MPa joint stress. Again the top lap has the highest strains. In the radial results, the top lap appears to have slightly lower results than the bottom lap; however, the magnitude of the radial results is so small that there is insufficient evidence to draw any conclusions. The higher strain levels tangentially allow for a more accurate comparison of symmetry. Again the FE results show near perfect symmetry, with trends very similar to the 0° data, verifying the assumed friction

coefficient, as described above, as the reason for the symmetry. The results of the symmetry comparison at 373K are shown in Figure 5.27 for 0° and Figure 5.28 for 90°.

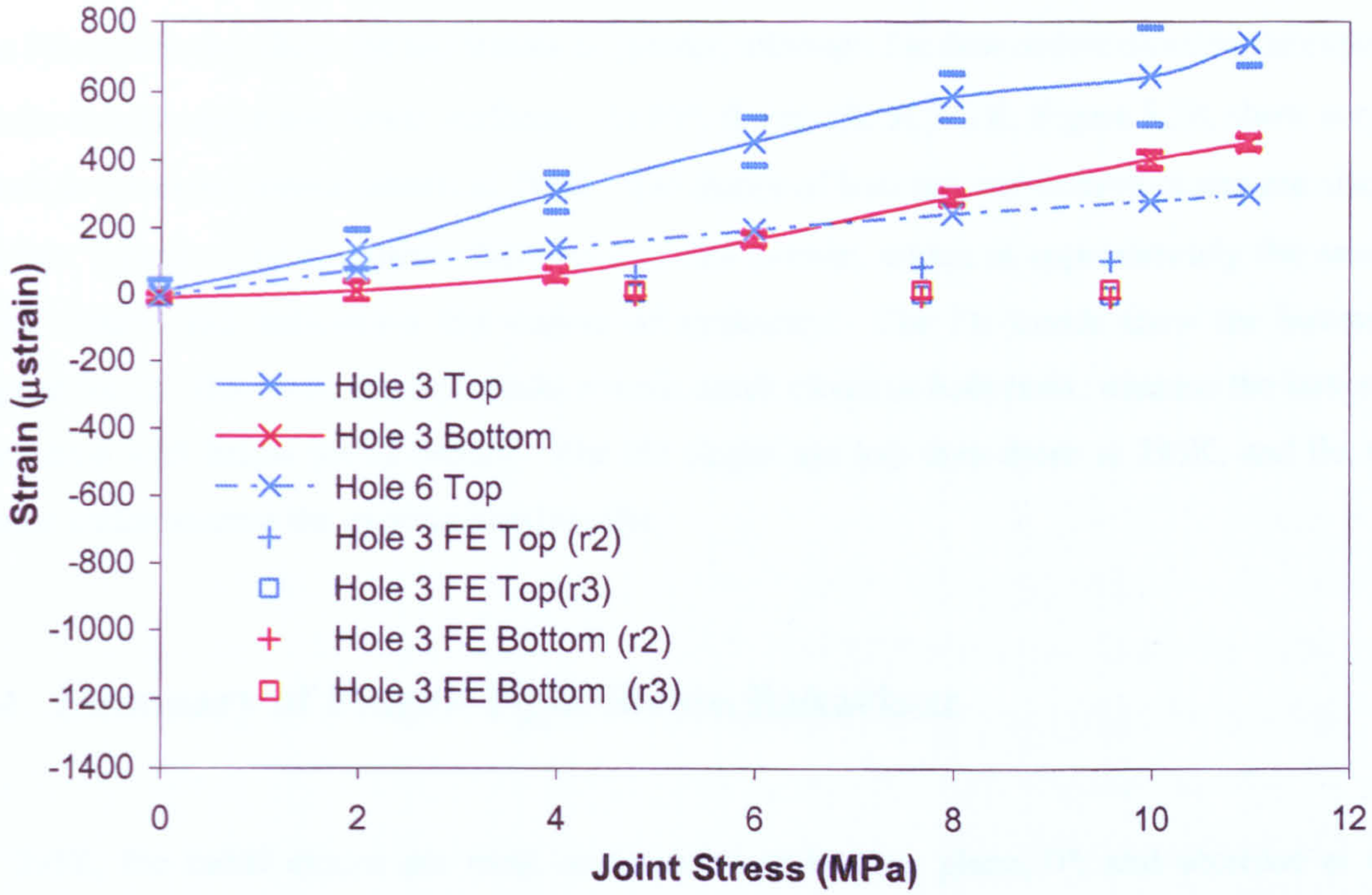

Figure 5.27. Symmetry comparison of top and bottom tangential strains at 0° (373K).

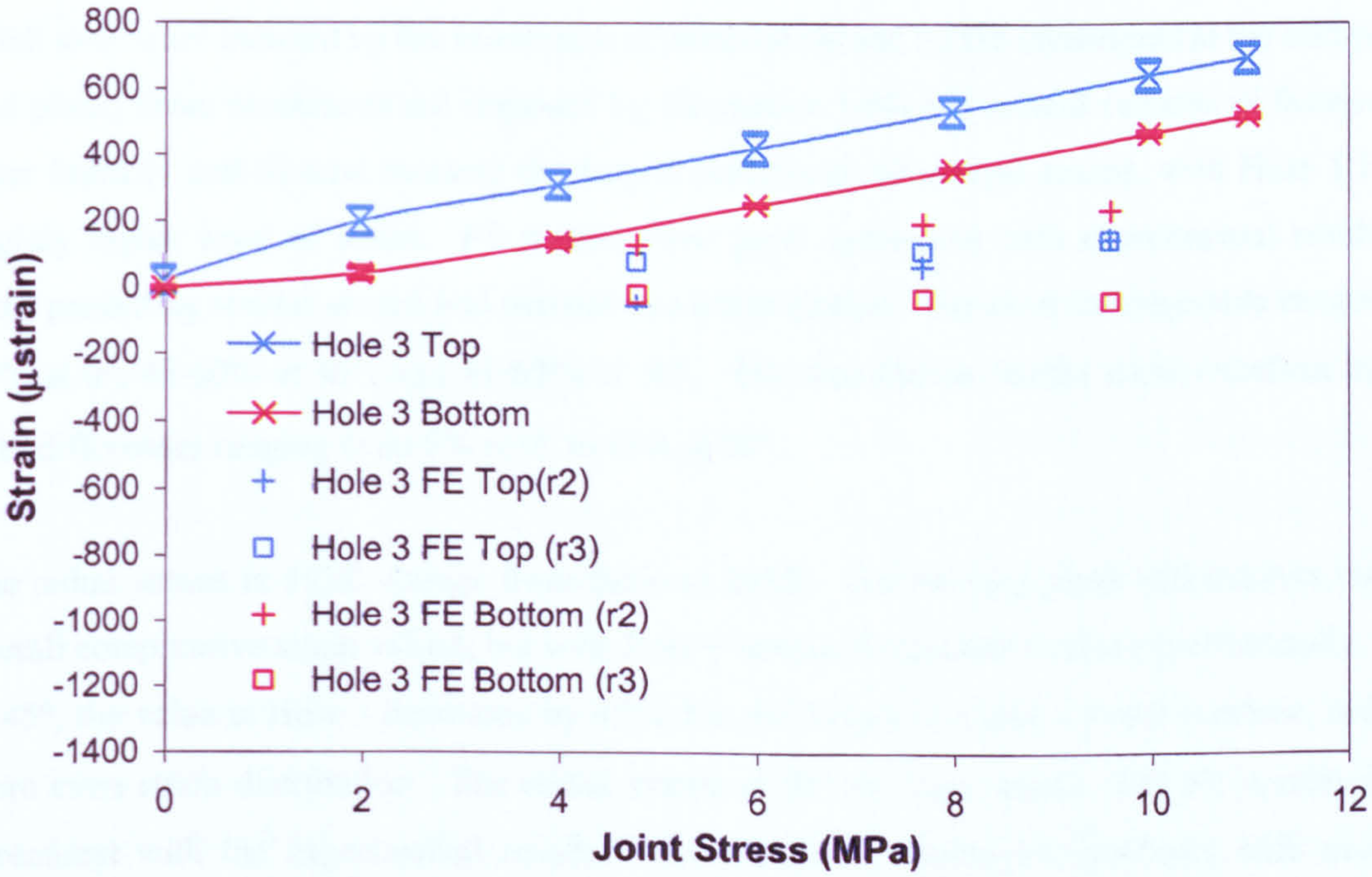

Figure 5.28. Symmetry comparison of top and bottom tangential strains at 90° (373K).

The experimental results in Figure 5.27 indicate that the top lap has higher strains, which is similar to behaviour at 295K. The degree of symmetry is fair since the maximum difference between the top and bottom strains is 330 μstrain. These results show a small improvement over radial symmetry. The FE results also show the top strains as greater, although the data underestimates the experimental results at both upper and lower surfaces. At 90°, the results at 373K, Figure 5.28, show very similar trends to the experimental results at 295K. The slopes of both top and bottom strains are also alike in the two figures. The maximum difference is 224 μstrain, which is approximately the same as the 295K results, and indicates a fair degree of symmetry. The FE trends show the bottom strains highest for r2. However, the top results remain much closer at both radii, whereas the bottom strains at r3 drop well below the r2 results. The FE slopes are less than those at 295K, and the resulting strains underestimate the experimental results.

5.4 Summary of Finger-Tight Strain Behaviour

At 295K, the radial strains are most compressive at bearing plane, 0°, and decrease at 45° with strains 35-56% lower than the values at the bearing plane. The radial strains at the net-tension plane, 90°, are very small since direct contact loading does not occur at this region. Therefore, the existing radial strains are induced by the movement of material caused by the constraints at the mid-plane. At mid-plane, these constraints are imposed by interaction with the second column of fasteners. The outer holes (1 and 3) tend to carry the largest percentage of overall strains, with Hole 1 bearing a slightly higher level of strain. FE results show good agreement with experimental results for all tests, predicting similar strains and percent maximum strains. The error in magnitude ranges from 7-10% at 0°, 45-60% at 45°, and 41-63% at 90°. The distribution results show excellent agreement with differences ranging from 5% at 0° to 15% at 90°.

The radial strains at 373K change from those at 295K. The bearing plane still exhibits the highest overall compressive strain values, but with Hole 3 having the greater strains experimentally. Moving to 45°, the value at Hole 3 decreases by 45%, but the values at Holes 1 and 2 increase, indicating a more even strain distribution. The radial strains at 90° are very small. The FE results show less agreement with the experimental results. The maximum strains are predicted with accuracy of 41-98%. The distribution agreement is only 40% at 0°, improving to 15% at 90°. The FE results indicate that the outer holes have higher strains. The FE results are similar to the experimental

results at Hole 3, but show an increase over the experimental strains at Hole 1, where the strains are small. This suggests possible experimental error, which is most likely due to error during gauge placement and particularly secondary effects associated with the experimental being performed at relatively low loads. Error in the FE representation at higher temperatures is another possibility. This misrepresentation can be induced by assumed boundary conditions during the heating process. This shows behaviour at 373K differing significantly from that at 295K. Overall, the results show a reduction in maximum strains at 373K over those at 295K, and a more even strain distribution across all holes. However, at 373K, the radial strains do not decrease at every hole when moving from the bearing plane to the net-tension plane, as is the case at 295K. The more even distribution means that some strains increase, despite the reduction in maximum overall strains.

The tangential strains at the net-tension plane are less severe in magnitude than the radial strains at the bearing plane. The radial strains then recede to nearly negligible magnitude at the net-tension plane; however, the tangential strains at the bearing plane are of a significant magnitude. The tangential strains are induced by compression of the material element radially, which causes expansion tangentially. The maximum tangential strains occur at 45° at both 295K and 373K. At 295K, the 45° strains are approximately 5% higher than those at 0° and 4% higher than those at 90°. The distribution shows the highest strains at the outermost holes (1 and 3), with a fairly even distribution across all holes. The FE results differ from the experimental maximum strains, particularly at 0°, where the FE results are 43% lower, and 90°, where they are 12% lower. The results at 45° are closer in comparison.

The maximum strains increase at 373K by 20% at 0°, 22% at 45°, and 14% at 90° from the maximums at 295K. The experimental results show the maximum tangential strains shifting from Hole 1 at 295K to Hole 3 at 373K. At the higher temperature, the experimental results show the strains at Hole 1 as negligible, implying an experimental error, such as disbanding of the gauge or misalignment of the specimen in the test machine, since radial strains alone are expected to induce significant tangential strains. The FE results at 373K show Hole 1 having the highest strains, with the overall strain split mainly between the outer holes. The FE model under-predicts the maximum strain at 0° (41%) and slightly over-predicts the results at 45° (16%) and 90° (11%). The greatest discrepancy lies in the strain distribution, where the experimental data shows Hole 3 taking the majority of the overall tangential strain, while the FE analysis results indicate a more even distribution over all holes, with Hole 1 having the greatest strains. This reinforces the possibility of

experimental error as suggested by the radial results, since tangential strains at Hole 1 are expected to be greater than those found experimentally. Despite this difference, the results give evidence that increasing the temperature increases maximum tangential strains and causes a change in strain distribution from a more even dispersing between outer holes to a shifting toward a single outer hole bearing more of the strain.

Top and bottom symmetry at Hole 3 examination reveal that radially, the top aluminium lap has higher strains at 90°, at both 295K and 373K, but at 0°, 373K, the bottom lap experiences greater strains. The symmetry distribution at 90° is not altered significantly with a change in temperature. The degree of symmetry at 0° also remains similar, despite the results showing the maximum strain moving from top to bottom lap. Tangentially, the top lap experiences the highest strains at both temperatures, as well as at all gauge positions. Again degree of symmetry is not greatly affected by change in temperature.

Chapter 6 Experimental Results - Effect of Increased Torque (35Nm)

Chapter 1 discussion suggests that torque, or clamp-up, significantly affects stress and strain distribution, which in turn, influences joint strength. To test these effects the experimental specimen is torque-tightened to 35Nm. This value of 35Nm is based on previous work by Ireman [68], [69] and Webber et al.[51], and the normal torque level of bolted joints for Airbus. The experiments are repeated to compare results at 295K and 373K with the finger-tight results.

Section 6.1 outlines load versus displacement results for the torque-tight specimen. Section 6.2 discusses radial strain results, with 6.2.1 covering the results at 0° or bearing plane, 6.2.2 covering 45°, and 6.2.3 covering 90° or net-tension plane. 6.2.4 highlights the through-thickness symmetry results. Tangential strains are covered in Section 6.3, which is subdivided into 6.3.1 for 0°, 6.3.2 for 45°, and 6.3.3 for 90°. The symmetry comparison is covered in 6.3.4. 6.4 is the summary.

6.1 Load versus Displacement

Radial strains are studied first and load versus displacement curves of the torque-tight specimen at 295K and 373K are compared. The trends, shown Figure 6.1, are very similar to those of the finger-tight specimen. Again #1 and #2 indicate the experimental test run number.

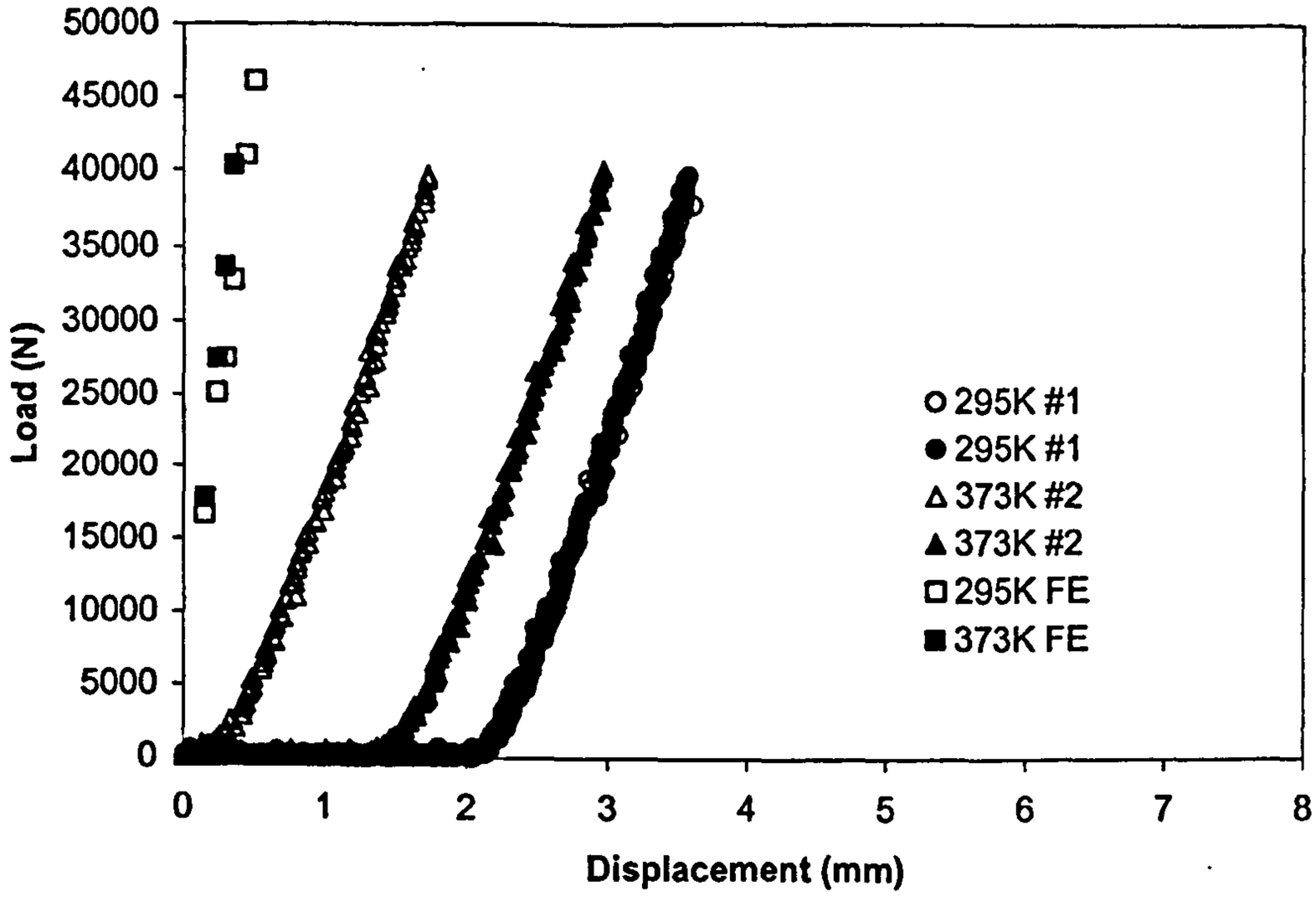

Figure 6.1. Load versus displacement curves at 295K and 373K.

The curves at room temperature (295K) demonstrate good agreement. Both commence loading at approximately 2mm displacement, with strong slope agreement (29500N/mm ±500N/mm). This slope is 16000N/mm greater than the finger-tight specimen. A visual comparison of Figure 6.1 and Figure 5.2 reveals this difference. The torque-tight specimen requires a much higher load than the finger-tight specimen to obtain a given displacement. The load is more evenly distributed amongst the fasteners, thereby reducing strains concentrations. In the finger-tight specimen, the 'play' associated with the looser fasteners allows for greater displacement before loading occurs; however, this leads to higher strains at the fastener edges. These findings agree with previous findings (Chapter 1) that suggest that torquing fasteners in a joint can greatly improve overall strength.

At 373K, the slope of the torque-tight specimen also shows fair agreement with the finger-tight specimen with a value of 27100N/mm ± 300N/mm. Again this value is higher than the finger-tight specimen, by approximately 14200N/mm, reaffirming the trend of improved joint strength due to torque. The trend of slope decrease with increased temperature follows the same pattern as the finger-tight results. The displacement starting point for loading is somewhat different between the 295K and 373K runs of the torque-tight specimen. The first run starts loading almost immediately, whereas the second run does not increase in load until approximately 1.5mm. This difference is most

likely the result of not fully releasing the thermally induced load before commencing the first tensile load. In the second run the load is released completely, promoting some slack in the specimen and allowing for greater displacement before loading is observed.

The effects of "low load" are less than in the finger tight specimen, occurring only in the 10-15% of the experimental load range. It is expected that the torque removes some of the secondary factors such as surface roughness, bolt tolerance and take-up due to the increased presence of clamp-up. As such, the low load results show less discrepancy than in the finger-tight specimen, however, the joint behaviour of primary still occur at higher loads, which are again discussed in greater detail than low load results.

Again, due to the boundary conditions, load onset in the FE model occurs sooner than in the experimental specimen, demonstrating a difference between ideal and actual conditions. As load onset in the experimental specimen occurs at earlier displacements due to the clamp-up force, this difference is less pronounced than in the finger-tight case.

6.2 Radial Strains

The first strains examined are the radial strains moving from the bearing plane (0°) to the net-tension plane (90°).

6.2.1 Radial Strain at 0°

The radial strains at the bearing plane for the tensile run at 295K are given in Figure 6.2. Table 6.1 shows the maximum strains.

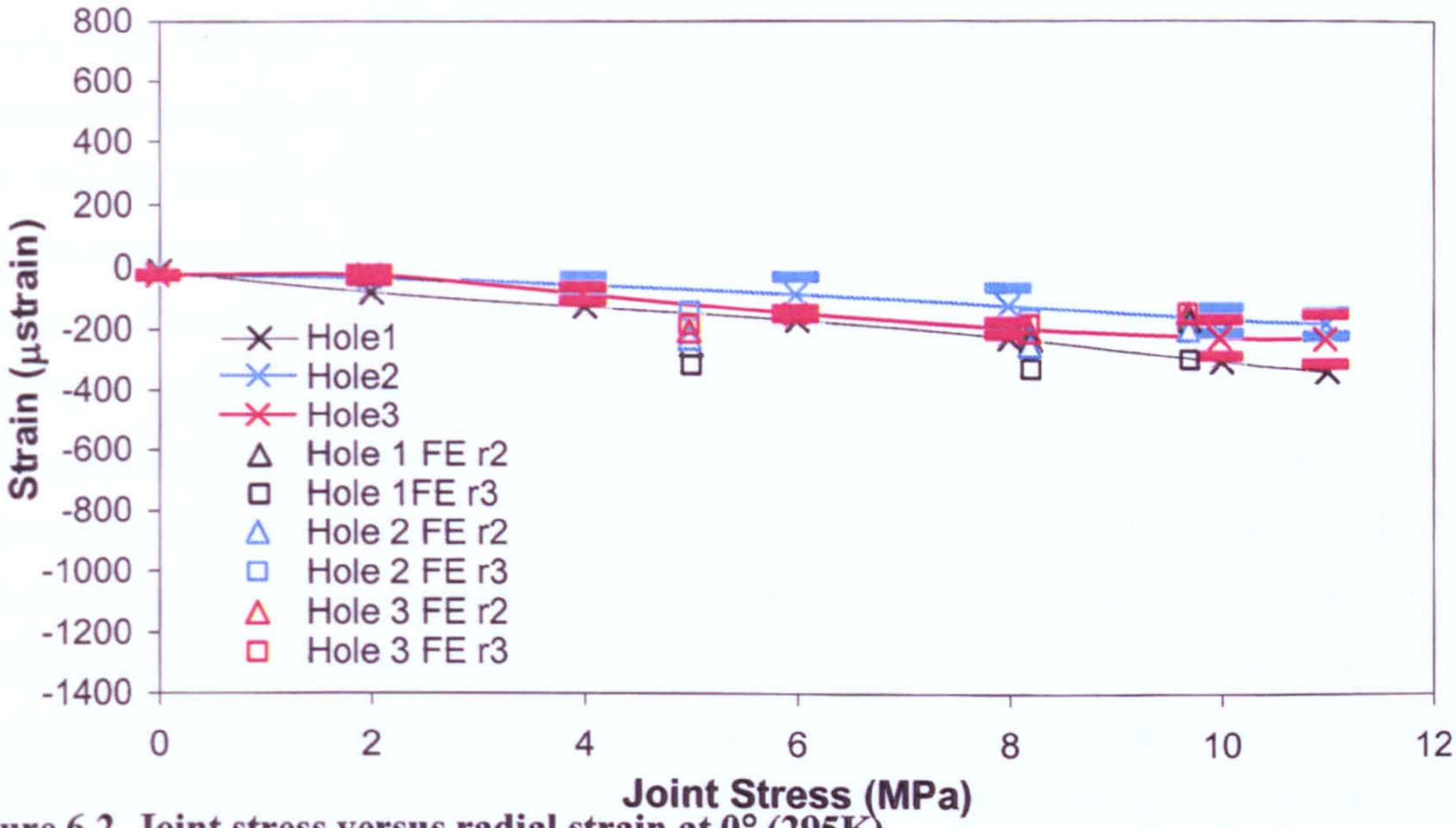

Figure 6.2. Joint stress versus radial strain at 0° (295K).

Table 6.1. Comparison of radial maximum strains at 0° (295K) at peak joint stresses.

	Hole 1 (μstrain)	Load Share	Hole 2 (μstrain)	Load Share	Hole 3 (μstrain)	Load Share
Experimental	**-341**	45%	-188 ± 39	25%	-234 ± 82	31%
FE r2	-170	33%	**-204**	39%	-146	28%
FE r3	**-298**	51%	-148	25%	-144	24%

Similar to results for the finger-tight specimen, Hole 1 assumes the greatest strain, with a maximum compressive value of 341 μstrain. The gauge functioned incorrectly in the second run. Therefore, a standard deviation is not available. The difference between the torque-tight specimen and the finger-tight specimen is found by comparing the magnitude of strain for similar joint stresses. The torque-tight specimen displays approximately 560 μstrain less strain than the finger-tight version. This is expected since increasing torque allows for more even strain distribution around the hole, thereby reducing strain concentrations. Other similarities observed between torque-tight, Figure 6.2, and finger-tight, Figure 5.3, are Hole 2 bearing the lowest strain and Hole 3 values falling between Holes 1 and 2. Again, these values are significantly lower than those of the finger-tight specimen, 562 μstrain and 523 μstrain, for Hole 2 and Hole 3, respectively. It is interesting to note that all strains are reduced by a similar magnitude, suggesting that torquing a specimen by a prescribed amount results in a uniform reduction in strain concentration without significantly altering strain and load patterns.

The FE results show a lower strain at r2 than at r3, where r2 is a distance of 5.1375mm (0.2in) from the hole edge, and at r3 is a distance of 7.1375mm (0.28in) from the hole edge, which bound the experimental gauge position of 6mm. These lower strains are due to the distribution of the torque load. Directly beneath the fastener head, the strains are significantly reduced (Chapter 1) because of the even compressive through-thickness pressure induced by the torque. Outside the radius of the fastener head, as at r3, this compressive force no longer exists, resulting in higher strain levels. However, r3 is some distance from the hole edge, meaning that the overall potential strains in this region are lower than the potential strains at the hole edge. The experimental percent maximum strains compare well with r3, as expected, since the experimental gauges are beyond the fastener head and the associated compressive through-thickness forces. The FE results show more compressive strains at lower joint stresses, that decrease as the joint stress increases. This discrepancy in behaviour between the FE results and the experimental results, which show increasing compressive strains, suggests the FE model is more heavily influenced by friction induced by the torque level than is the actual experimental model. Initial contact is induced at lower joint stresses due to the clamp-up which compresses elements in the through-thickness direction, causing initial radial expansion and reduced clearance, in turn resulting in more compressive strain results. As loading continues after initial contact, friction becomes more influential, similar to the description in Figure 5.5(b). This causes the aluminium lap, which is constrained, to move with the CFRP skin due to the frictional forces between plate surfaces. These effects are greater than those in the finger-tight specimen because the torque increases the interaction between plate surfaces. When the aluminium lap moves with the CFRP skin, it leads to lesser compressive strains in FE. In addition, the material beneath the fastener head is constrained by the through-thickness compression (clamp-up), further increasing tensile radial strains. Experimentally, the accuracy between torque-level measured by the torque wrench and the actual compressive force induced is again an issue, as discussed in Chapter 5. The friction coefficient between the plates is also a function of the applied compressive force via torque and the finish of the materials. This coefficient may differ from that assumed in FE, explaining the difference between the results. The strains from Holes 4 to 6 at the bearing plane are given in Figure 6.3, with the results for strains at Holes 1 to 3 included for comparison.

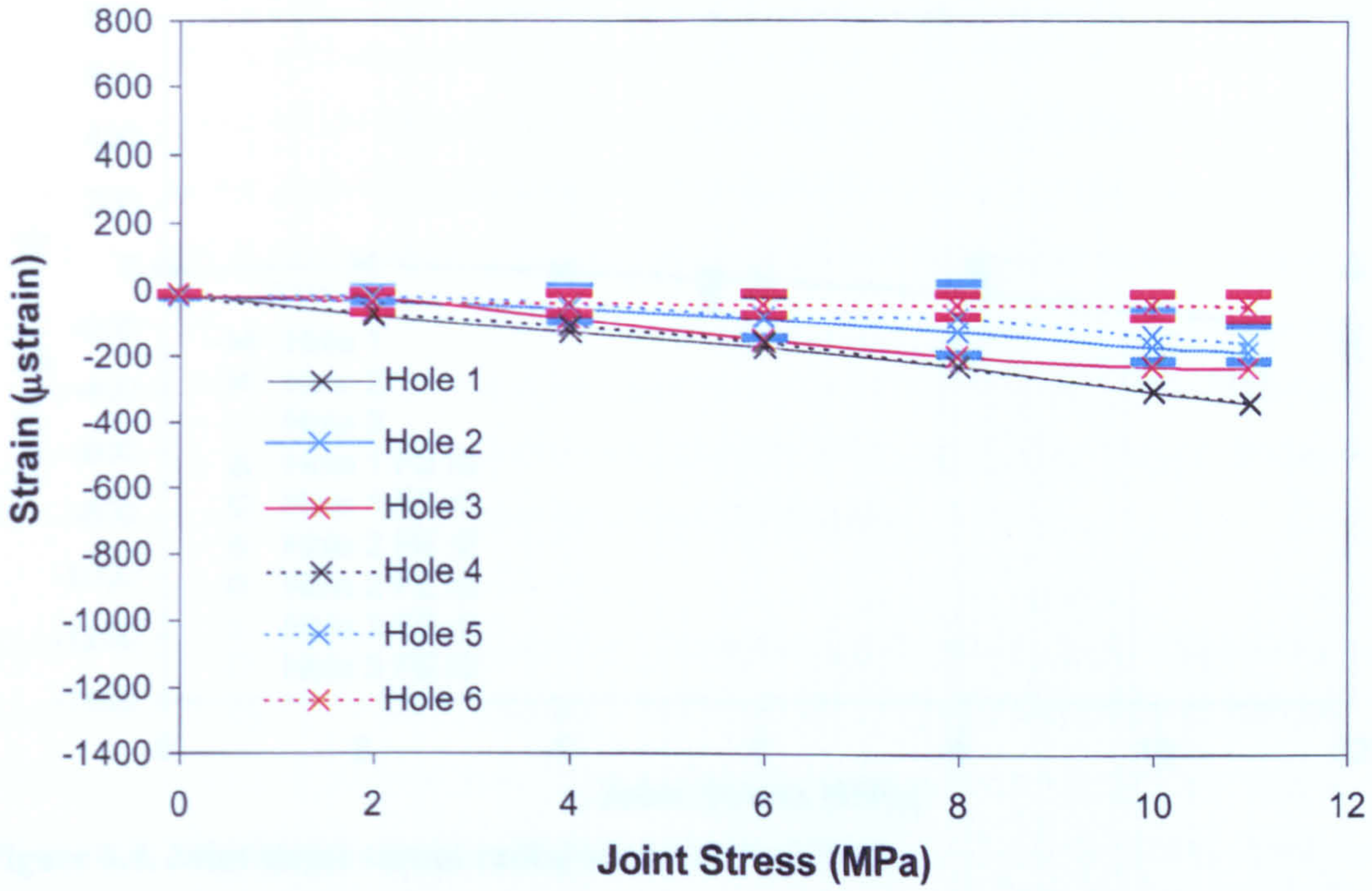

Figure 6.3. Comparison of radial strains at Holes 1 to 3 with Holes 4 to 6 (0° and 295K).

Figure 6.3 provides evidence of good agreement between both sides, for Holes 1 and 4, and Holes 2 and 5. The gauge at Hole 6 does not appear to have functioned correctly, thus limiting these results. However, given the accuracy between the first two holes, it is believed that both sides behaved similarly. The maximum difference between Hole 1 and Hole 4 is only 18 μstrain at a joint stress of 4 MPa, and between Hole 2 and Hole 5 is 38 μstrain at 8 MPa. This indicates an even load distribution between the two columns of fasteners. Compared with the results in Figure 5.4, load distribution is more even due to torque and its ability to promote improved strain distribution. The error observed in the finger-tight testing appears to have been alleviated with increased torque load. This implies that specimen misalignment is the most probable error. Increasing the torque distributes the contact evenly, eliminating the discrepancies seen in the finger-tight results. The slopes of the curves for the torque-tightened specimen are also smoother than those in the finger-tight analysis because of the improved contact conditions. The experiment is then repeated at 373K and the results outlined in Figure 6.4 and Table 6.2.

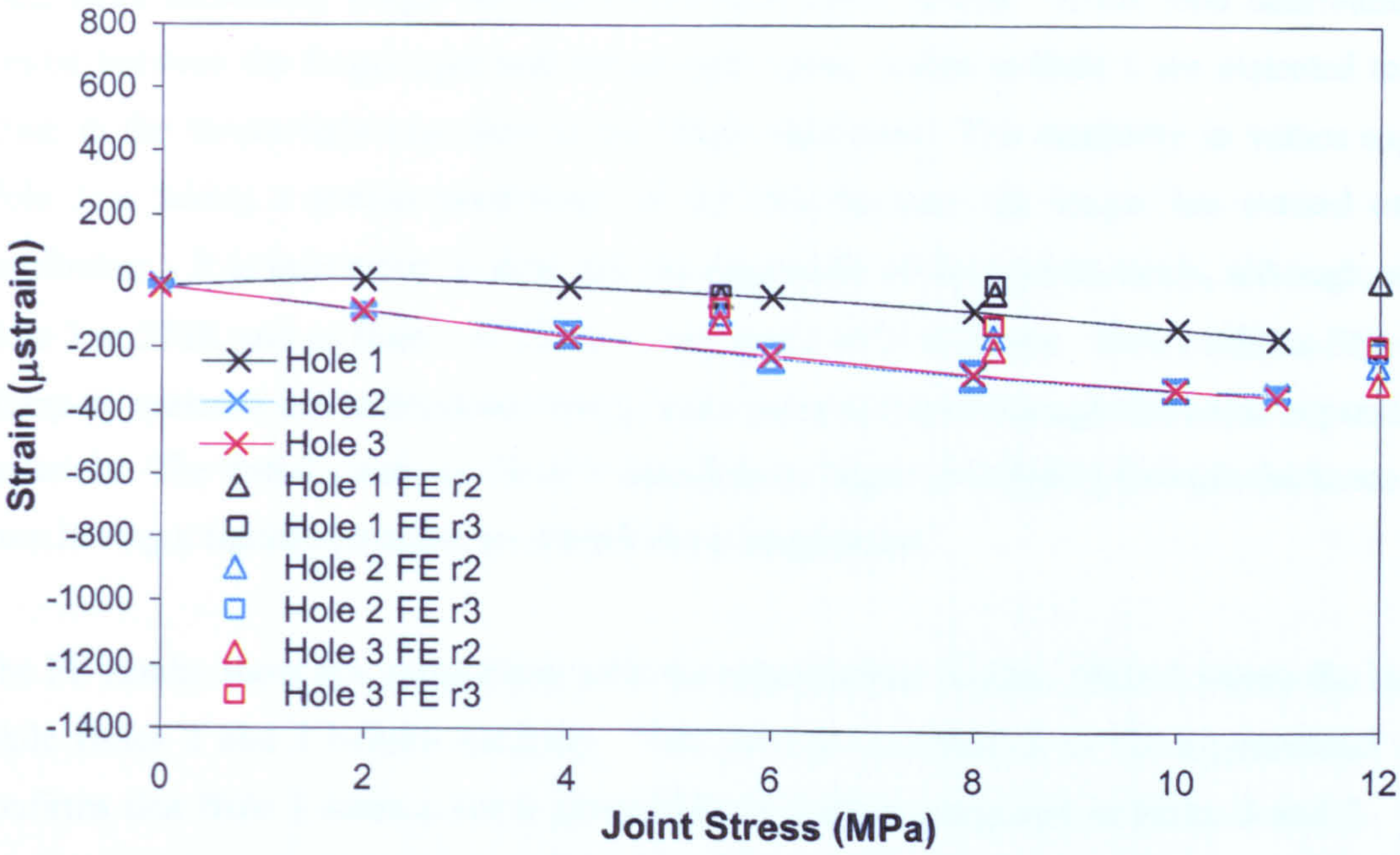

Figure 6.4. Joint stress versus radial strain at 0° (373K).

Table 6.2. Comparison of maximum radial strains at 0° (373K) at peak joint stresses.

	Hole 1 (μstrain)	Load Share	Hole 2 (μstrain)	Load Share	Hole 3 (μstrain)	Load Share
Experimental	-166	19%	-338 ± 18	39%	**-349**	41%
FE r2	101	16%	-251	38%	**-304**	46%
FE r3	-192	33%	**-208**	35%	-188	32%

Figure 6.4 gives evidence that behaviour at 373K differs from that at 295K. The experimental strains at Holes 2 and 3 are nearly identical, while that at Hole 1 is notably less. At 295K, as in the finger-tight case, Hole 1 has the highest strains, but at 373K, Hole 3 has the maximum compressive strain. Although all strain values for the torque-tight specimen are less than those for the finger-tight specimen, t at Hole 1 at 373K is lower by only 16 μstrain, and at Hole 2 by 18 μstrain. The difference at Hole 3 is considerably greater with a value of 539 μstrain. The most notable change between the two temperatures is the strain pattern. The loads change significantly from the first fastener to the third at 295K. At 373K the loading on Holes 2 and 3 is more evenly distributed, as their strain patterns are very similar. The fact that Hole 1 has a lesser value indicates the possibility of uneven loading or simply less reaction at Hole 1, because Holes 2 and 3 have already taken the majority of the load. The fact that maximum load at Hole 1 does not show a notable decrease from that of the finger-tight specimen indicates that Hole 1 is actually taking a greater percentage of the

load, since increasing torque decreases maximum strain values. If the load distribution remains similar between the finger-tight and torque-tight cases, results at Hole 1 are expected to show less strain in the torque-tight case than in the finger-tight case. The similarity in values suggests that Hole 1 is taking a greater percentage of the load because the torque has evened overall load distribution. It is interesting to note that the magnitude of the highest strain, although occurring at Hole 3 at 373K and at Hole 1 at 295K, is not appreciably different. This confirms little change in clamp-up pressure due to increased temperature and associated through-thickness expansion of joint materials. The initial clamp-up force is significantly larger, precluding through-thickness expansion from having a significant effect on overall strain magnitudes.

The FE results show fair comparison with the experimental results. Hole 1 shows the least strains, while Holes 2 and 3 behave similarly. This provides confidence in the experimental trends and confirms that Hole 1 takes a lower percentage of loading compared to Holes 2 and 3. FE under-predicts maximum strains, but compares well in percentage of maximum strain distribution, particularly at r2. Farther from the influence of clamp-up, r3 indicates a more even load distribution amongst all three fasteners. The results of comparison between the columns are illustrated in Figure 6.5.

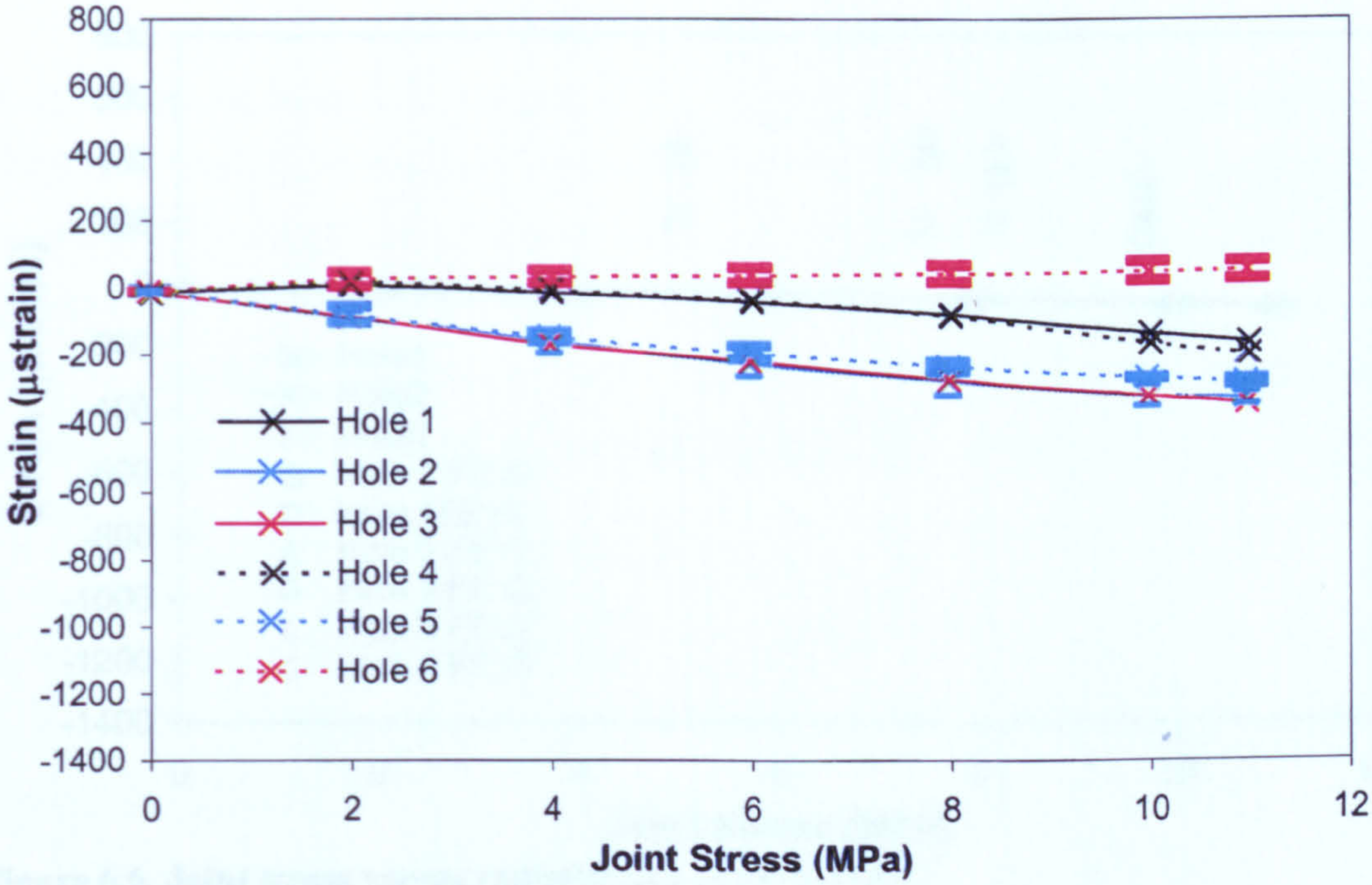

Figure 6.5. Comparison of radial strains at Holes 1 to 3 with Holes 4 to 6 (0° and 373K).

Figure 6.5 demonstrates that the distribution between the two columns is very even, particularly for Holes 1 and 4. This suggests the difference between strain values for Hole 1 and values for Holes 2 and 3 is due to the fact that only a smaller portion of the total joint stress is being reacted at Hole 1, with larger percentages being taken by the remaining two fasteners. It proves that there is no misalignment of the joint itself. The strain gauge at Hole 6 appears to have malfunctioned, as it did at 295K, resulting in no strain values for that particular hole. Given the accuracy at the other four holes, it can be concluded that the results for Hole 3 are an accurate representation of both columns of fasteners. A comparison of results of the torque-tight and finger-tight specimens verifies that additional clamp-up force improves load distribution among the columns. The maximum discrepancy is 297 μstrain between the two columns for the finger-tight specimen, and only 50 μstrain for the clamped-up specimen, emphasising the improvement in load distribution resulting from torque.

6.2.2 Radial Strains at 45°

Moving away from the bearing plane, Figure 6.6 shows radial strains at the 45° gauge. The maximum strains are given in Table 6.3.

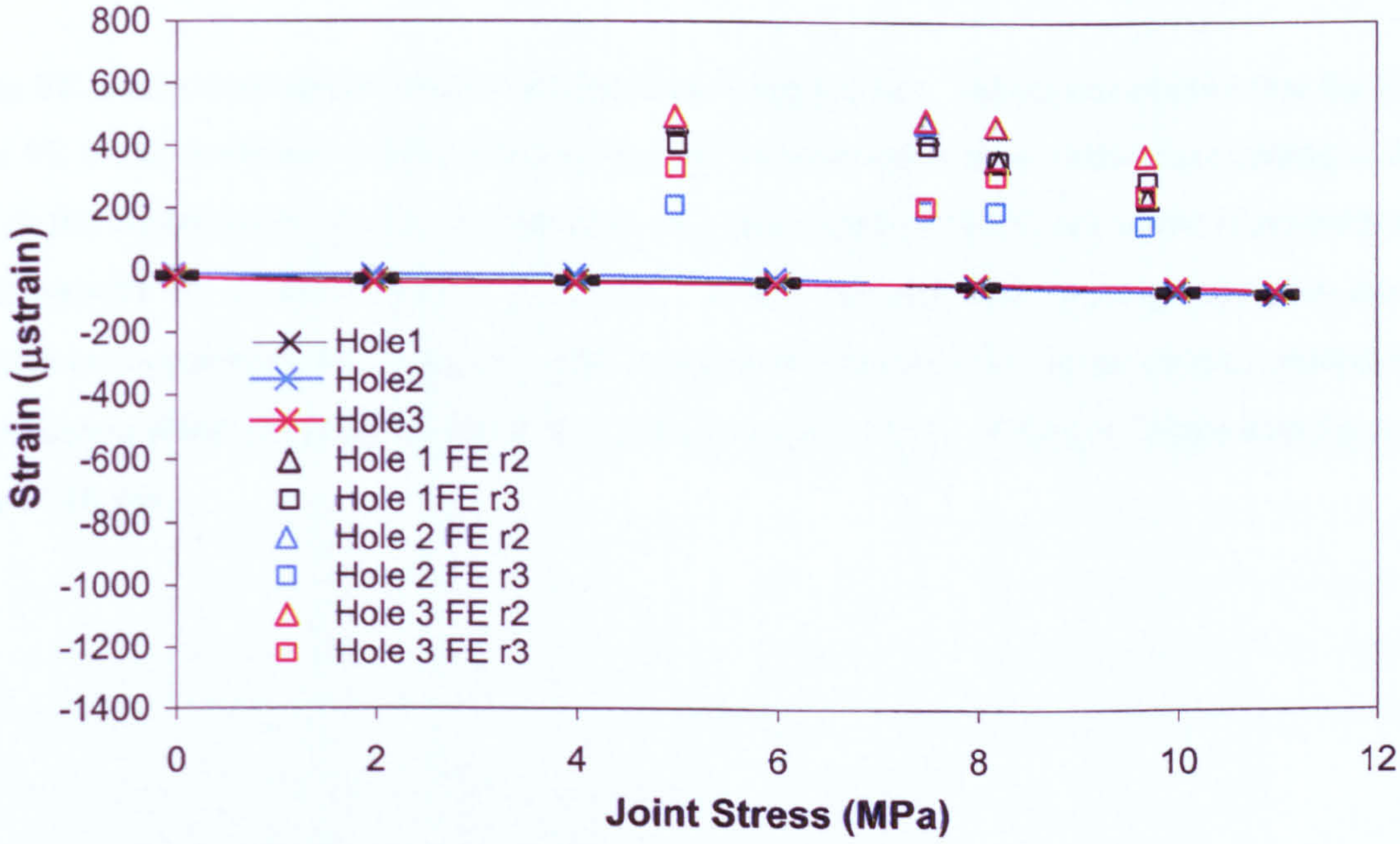

Figure 6.6. Joint stress versus radial strain at 45° (295K).

Table 6.3. Comparison of maximum radial strains at 45° (295K) at peak joint stresses.

	Hole 1 (μstrain)	Load Share	Hole 2 (μstrain)	Load Share	Hole 3 (μstrain)	Load Share
Experimental	-82 ± 1	34%	-86	36%	-72	30%
FE r2	232	24%	369	38%	368	38%
FE r3	285	43%	140	21%	238	36%

The resulting strains are small, with the maximums at all holes almost identical with an average of 79 ± 7 μstrain. This suggests that higher torque results in more even distribution. Comparing Figure 6.6 with Figure 5.7, the major difference is the magnitude of the resulting strains. The differences are 423 μstrain at Hole 1, 174 μstrain at Hole 2, and 178 μstrain at Hole 3. This implies that the torque greatly decreases maximum strains. The percent maximum strain distribution also differs from the finger-tight analysis. The torque-tight results show a very even strain distribution, whereas the finger-tight results indicate the majority of strain occurs at Hole 1, with Holes 2 and 3 sharing the remainder. Compared with the results at 0°, the radial strain decreases significantly and behaves similarly to the finger-tight specimen. The strains at Hole 1 are 259 μstrain less, at Hole 2, 102 μstrain less, and at Hole 3, 162 μstrain less than at 0°. The greatest reduction occurs at Hole 1, as the maximum strain distribution becomes more even across all holes, whereas at the bearing plane, Hole 1 carries 45% of the distribution.

The FE results show tensile strains similar to the bearing plane. Again this implies that the friction in the FE model promotes radial extension because of plate interaction, rather than sliding and contact as in the experimental results. The percent maximum strain distributions of the experimental results fall between the r2 and r3 results of the FE. At 45°, the strains at r2 are greater than those at r3, which are opposite to the 0° results. This suggests behaviour at 45° is not directly related to that at the bearing plane, the same results as in the finger-tight analysis. Figure 6.7 represents the results for the 373K run.

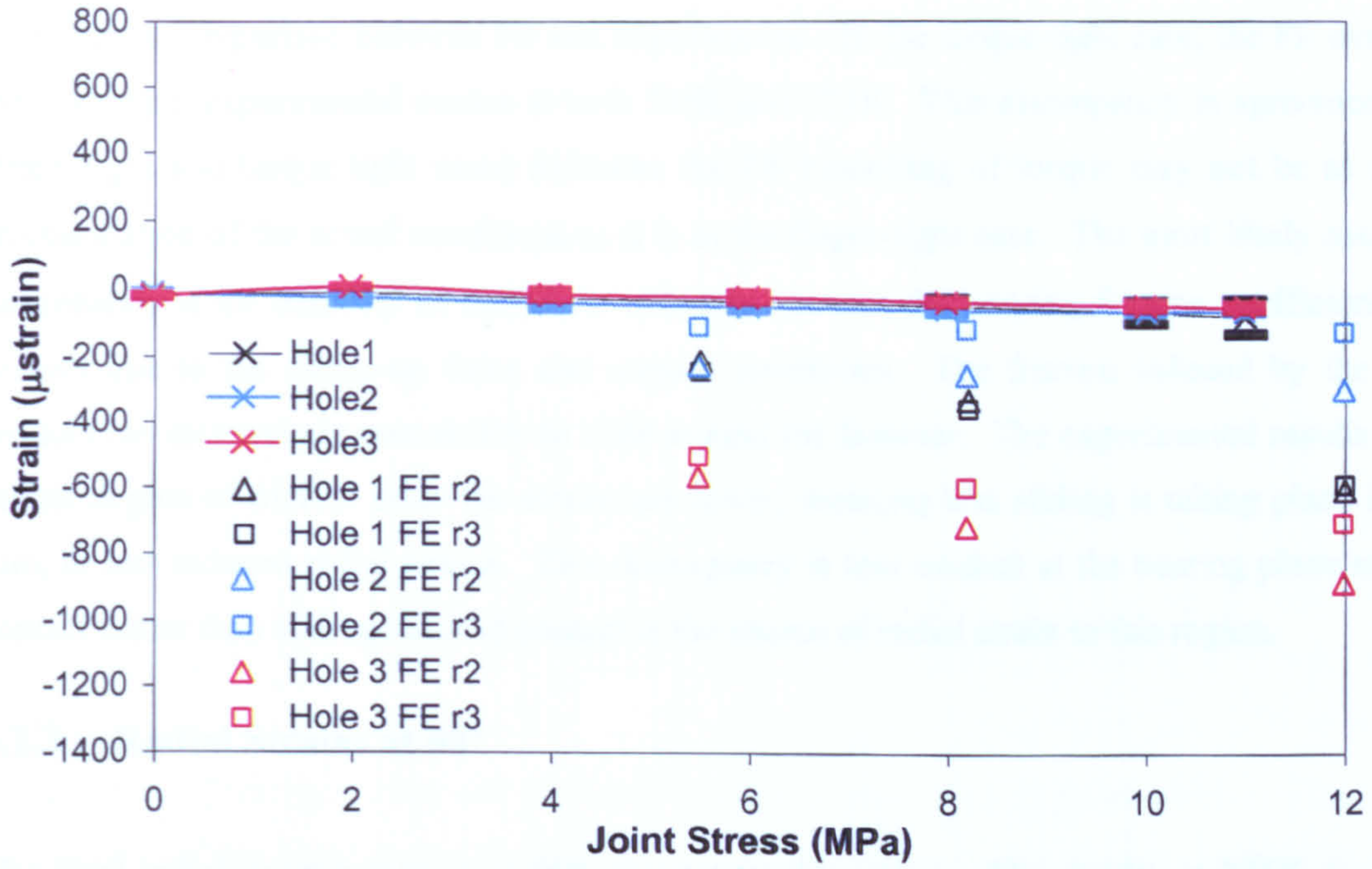

Figure 6.7. Joint stress versus radial strain at 45° (373K).

Table 6.4. Comparison of maximum radial strains at 45° (373K) at peak joint stresses.

	Hole 1 (μstrain)	Load Share	Hole 2 (μstrain)	Load Share	Hole 3 (μstrain)	Load Share
Experimental	**-82** ± 52	40%	-68 ± 4	33%	-54 ± 6	26%
FE r2	-610	33%	-306	17%	**-888**	49%
FE r3	-595	41%	-132	9%	**-710**	49%

Figure 6.7 again indicates that the experimental radial strains are negligible at 45°. This is a significant reduction from the values of the finger-tight case. The strains at Hole 1 are reduced by 120 μstrain, Hole 2 by 424 μstrain, and Hole 3 by 440 μstrain. As in the results at the bearing plane, Hole 1 is reduced by the least amount, indicating that it is now taking a larger portion of the load. This confirms that clamp-up evens load distribution. The magnitude of radial strains is less then the magnitude for these strains at the bearing plane, as expected since there is less direct contact between the hole edge and fastener. Hole 1 maximum strain is approximately half that of the bearing plane, while Hole 2 is 20% of the value at the bearing plane, and Hole 3, 15%. Experimentally, these results are similar to those at 295K.

The FE results show greater maximum strains, with Hole 3 having the greatest values at both r2 and r3, while Hole 1 has the highest maximum strain in the experimental results. The finger-tight values

show better comparison between FE and experimental. In the torque-tight case, the FE over-predicts the maximum experimental strains at both 295K and 373K. This discrepancy in agreement between finger-tight and torque-tight cases indicates the FE modelling of torque may not be as accurate a representation of the actual conditions as it is in the finger-tight case. The most likely cause for this discrepancy is the inability of the FE to take into account the varying friction coefficients that are present due to the clamp-up force and contact conditions. The friction induced by the clamp-up reduces the material element ability to slide around the fastener. The experimental results indicate a higher degree of friction since the strains are lower, meaning less sliding is taking place leading, in turn, to less induced radial strains. This discrepancy is less evident at the bearing plane since direct contact rather than sliding induced contact is the source of radial strain in this region.

6.2.3 Radial Strains at 90°

The final radial examination is at 90°, the net-tension plane. The results at 295K are shown in Figure 6.8, with the maximum strains in Table 6.5.

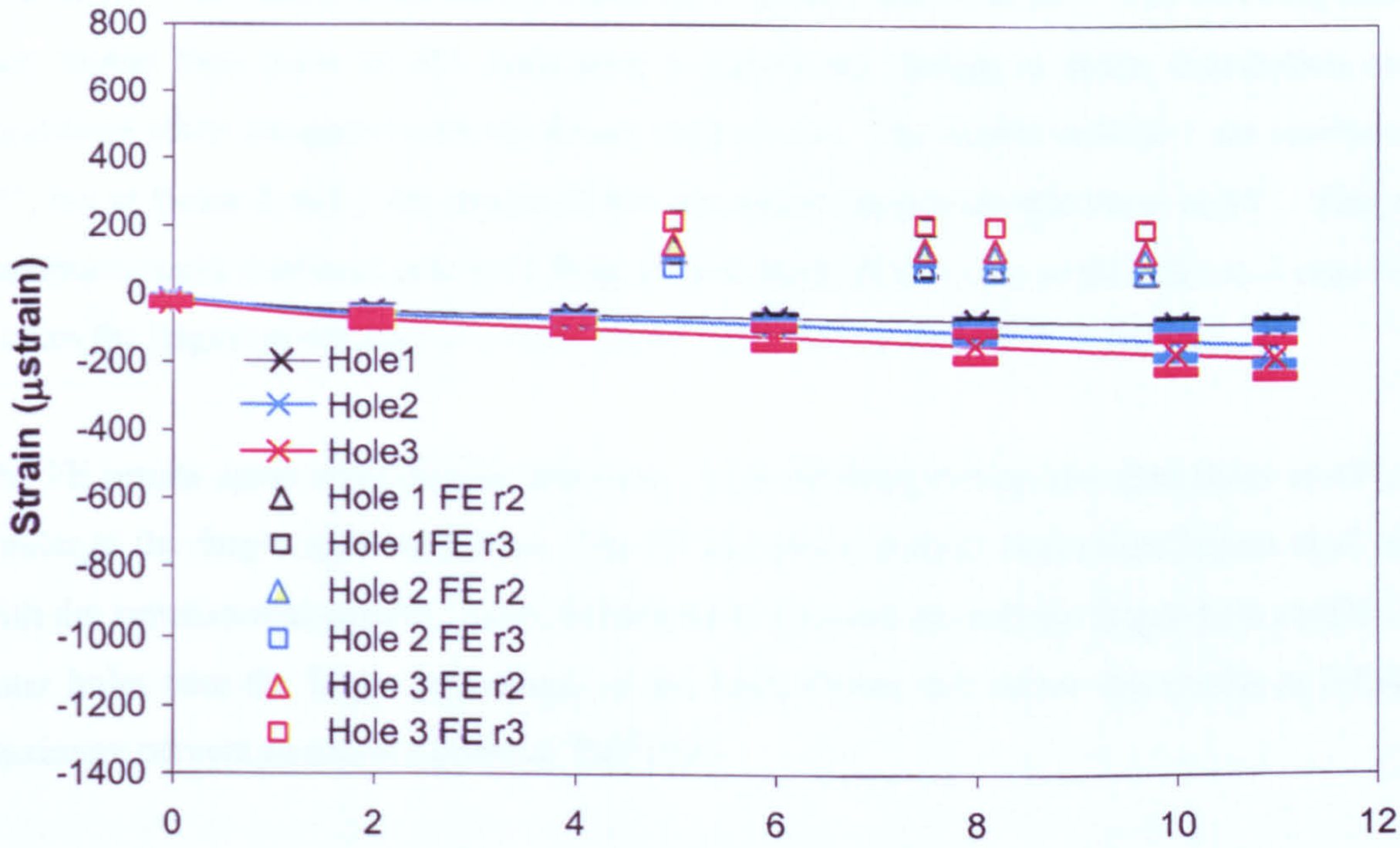

Figure 6.8. Joint stress versus radial strain at 90° (295K).

Table 6.5. Comparison of maximum radial strains at 90° (295K) at peak joint stresses.

	Hole 1 (μstrain)	Load Share	Hole 2 (μstrain)	Load Share	Hole 3 (μstrain)	Load Share
Experimental	-86 ± 8	21%	-148 ± 54	35%	-185 ± 52	44%
FE r2	62	22%	101	35%	125	43%
FE r3	191	43%	59	13%	192	43%

Figure 6.8 shows that all holes experience compressive strain, again due to clamp-up pressure holding the material beneath the fastener head in place. This causes the element to elongate tangentially under the tensile load, meaning that it must compress radially to maintain the same area. There is also the possibility of increased contact area because the clamp-up pressure holds the material next to the fastener. Hole 3 bears the maximum compression radially, followed by Hole 2, then Hole 1. The compressive strain at Hole 3 is similar to the behaviour of the finger-tight specimen; the difference being that the finger-tight specimen has negligible strains. Lack of clamp-up pressure in the finger-tight specimen results in uneven strain distribution around the hole, and translates into higher radial strain at the bearing plane and almost no strain at the net-tension plane. The torque evens strain distribution, resulting in greater strains at 90°. The resulting strains are, in fact, higher than those at 45°, indicating a significant change in strain distribution and contact conditions when compared with the finger-tight results. The results at Hole 1 are similar to those at 45°, but at Holes 2 and 3 the strains at 90° are approximately double those at 45°. This causes the maximum strain distribution to shift from almost equal distribution at all holes to a case where Hole 3 takes the largest percentage of overall strain, followed by Hole 2, then Hole 1.

The FE results again show tensile behaviour, with resulting strains less than those at 45°, and more similar to the finger-tight behaviour. The FE maximum percent strain distribution at r2 agrees well with the experimental results. At r3, behaviour tends more toward the finger-tight results, where the outer holes take the larger percentage of the load. Figure 6.9 shows the results at 373K, and the maximum percent strains are given in Table 6.6.

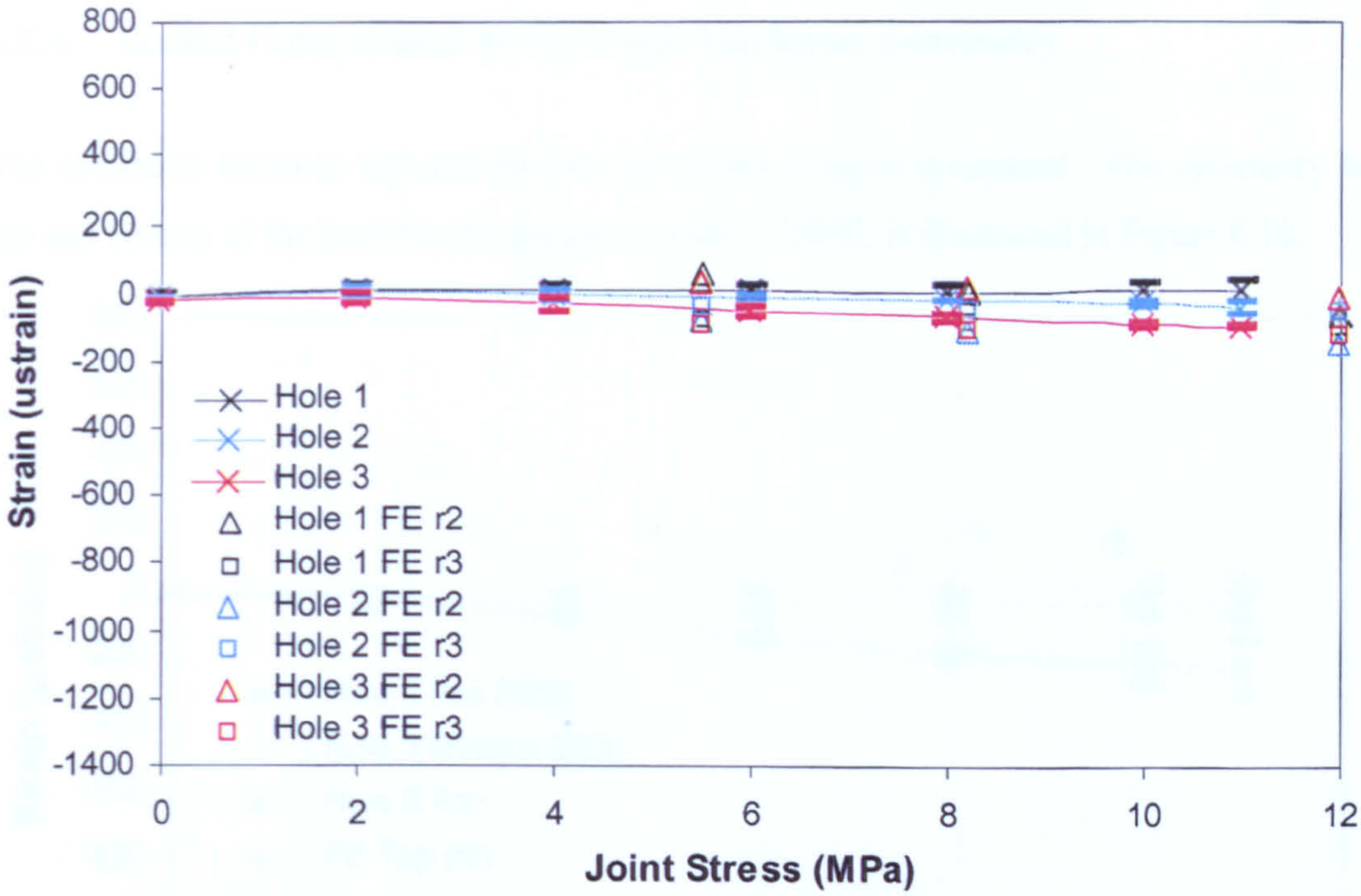

Figure 6.9. Joint stress versus radial strain at 90° (373K).

Table 6.6. Comparison of maximum radial strains at 90° (373K) at peak joint stresses.

	Hole 1 (μstrain)	Load Share	Hole 2 (μstrain)	Load Share	Hole 3 (μstrain)	Load Share
Experimental	11 ± 30	8%	-38 ± 18	27%	**-92**± 5	65%
FE r2	-66	29%	-150	67%	**-9**	4%
FE r3	-90	35%	-50	19%	**-115**	45%

The experimental trends demonstrated in Figure 6.9 are similar to those in Figure 6.8, with Hole 3 having the most compressive strain, but 90 μstrain less than at 295K. The finger-tight tests show Hole 3 having tensile strain at 373K. This increased tensile behaviour may explain the lower compressive strain observed in the 373K run of the torque-tight specimen. The similarity between Figure 6.8 and Figure 6.9 attest to the evenness of load distribution due to increased clamp-up. The strains in the torque-tight specimen are approximately half those in the finger-tight case. However, in both cases, the radial strains at the net-tension plane are very small. The FE results show good agreement in this case since all strains are small, due to lack of direct or sliding induced contact at this plane.

6.2.4 Radial Comparison of Through-Thickness Symmetry

The symmetry between top and bottom lap strains is again compared. The symmetry between the top and bottom of the joint for the gauges at Hole 3, 295K, is illustrated in Figure 6.10.

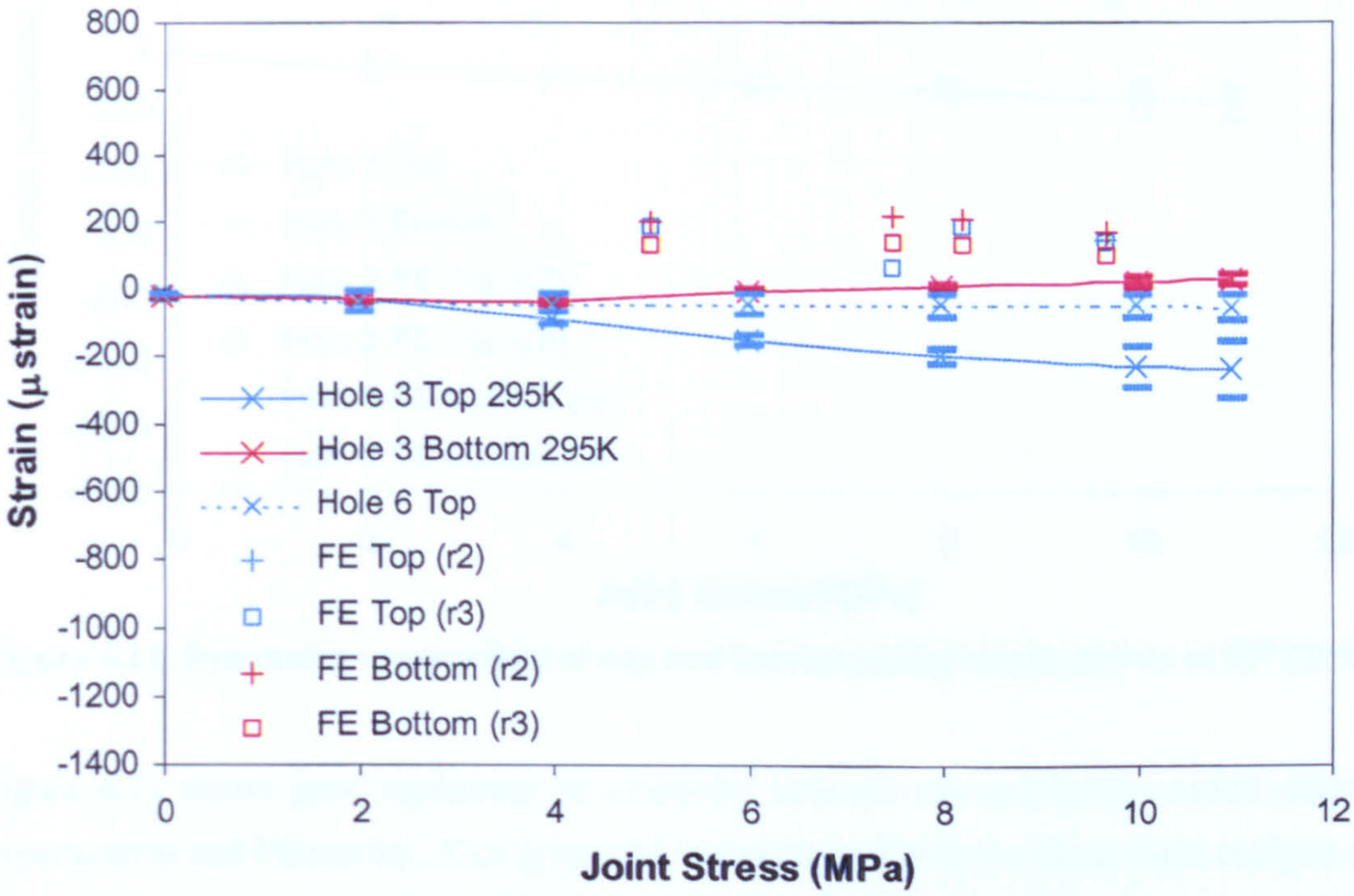

Figure 6.10. Symmetry comparison of top and bottom radial strain curves at 0° (295K).

Figure 6.10 shows almost zero strain on the bottom gauge. This differs from the top strains that are compressive. Hole 6 also shows almost zero strain. The FE results indicate positive or tensile strains, due to the differing effects of friction modelling as previously explained. The FE results demonstrate close symmetry between top and bottom strains. The experimental results suggest different conditions exist at the top and bottom of the laps that produce less symmetrical results. This requires further examination. The symmetry at the net-tension plane, 295K, is given in Figure 6.11.

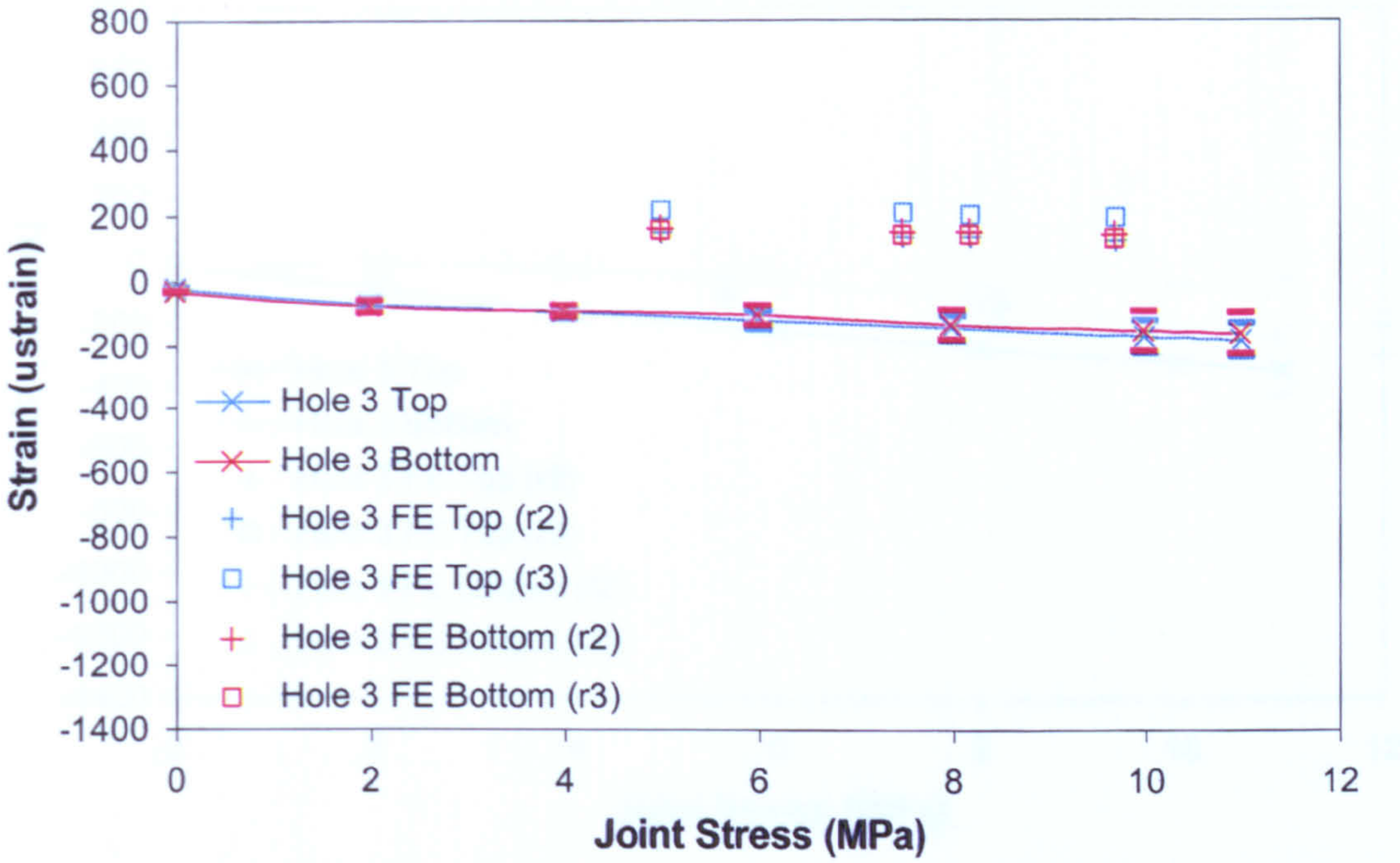

Figure 6.11. Symmetry comparison of top and bottom radial strain curves at 90° (295K).

Figure 6.11 shows good agreement in symmetry between top and bottom radial strains for both experimental and FE results. This symmetry is similar to that in the finger-tight analysis and greater than at the bearing plane. This higher degree of symmetry shown at the net tension plane is a function of lower radial strains, which minimize the potential for discrepancy. The results at 0°, 373K, are shown in Figure 6.12.

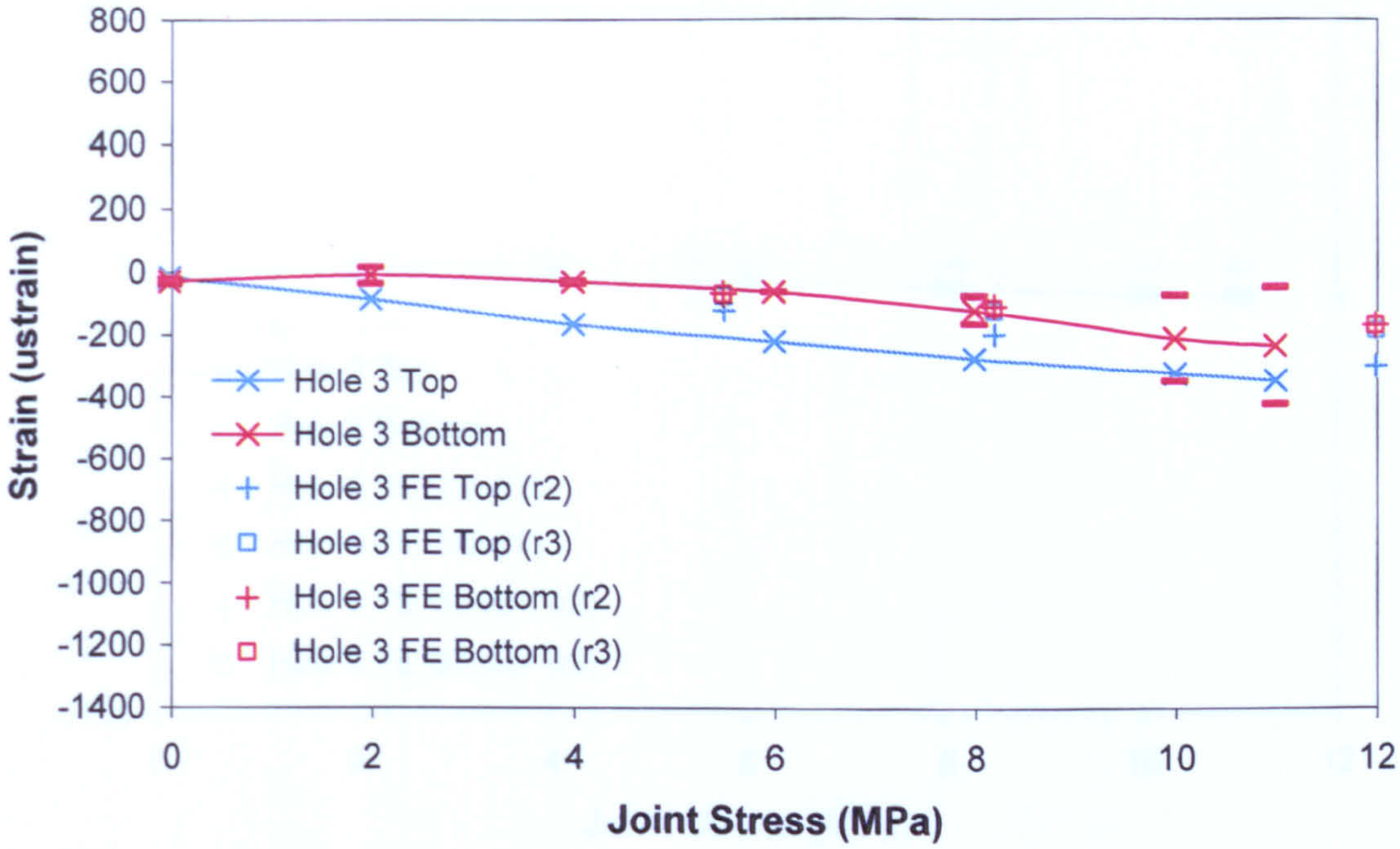

Figure 6.12. Symmetry comparison of top and bottom radial strain curves at 0° (373K).

Figure 6.12 shows approximately equal distribution between top and bottom strains and fair agreement between experimental and FE results. The behaviour of the top and bottom strains is more consistent than at 295K, Figure 6.10. But when compared with the finger-tight results, the position of the maximum strains is reversed. In finger-tight, the maximum radial strain occurs on the bottom lap, whereas in torque-tight, it occurs on the top lap. The torque-tight examination also shows similar results in magnitude between 295K and 373K. In the finger-tight specimen, the strains at 373K are significantly higher than those at 295K. This suggests that at a higher clamp-up force, torque is more influential in strain distribution than is temperature. The results at 90° and 373K are shown in Figure 6.13.

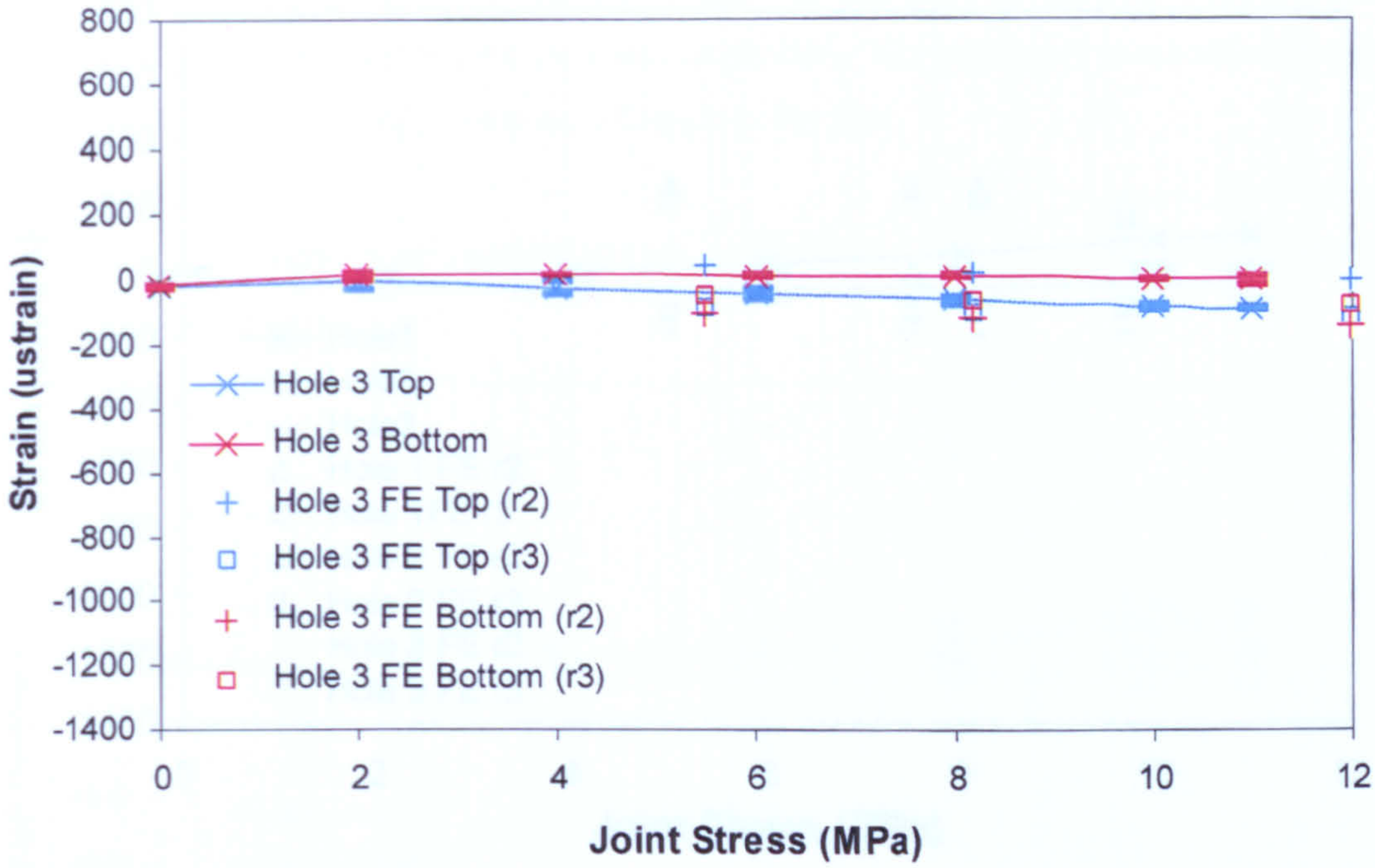

Figure 6.13. Symmetry comparison of top and bottom radial strain curves at 90° (373K).

Figure 6.13 results again show excellent symmetry between top and bottom. Overall, the degree of symmetry between top and bottom laps is greater in the torque-tight specimen than in the finger-tight case. This is expected since the increased clamp-up pressure allows a more even strain distribution, not only between fasteners but also through top and bottom laps. The increased through-thickness force reduces the effect of difference in geometry between the head of the fastener and the nut and washer, which in turn, improves through-thickness strain symmetry.

6.3 Tangential Strain

Similar to the radial strains, tangential strains are examined at 0°, 45°, and 90°, and the symmetry between the top and bottom laps as well as across the columns of fasteners is presented.

6.3.1 Tangential Strain at 0°

The effect of clamp-up on tangential strain distribution is also expected to be significant. Figure 6.14 shows the tangential strain results at the bearing plane for tensile testing at 295K. Table 6.7 shows the comparison of tangential strains at 295K.

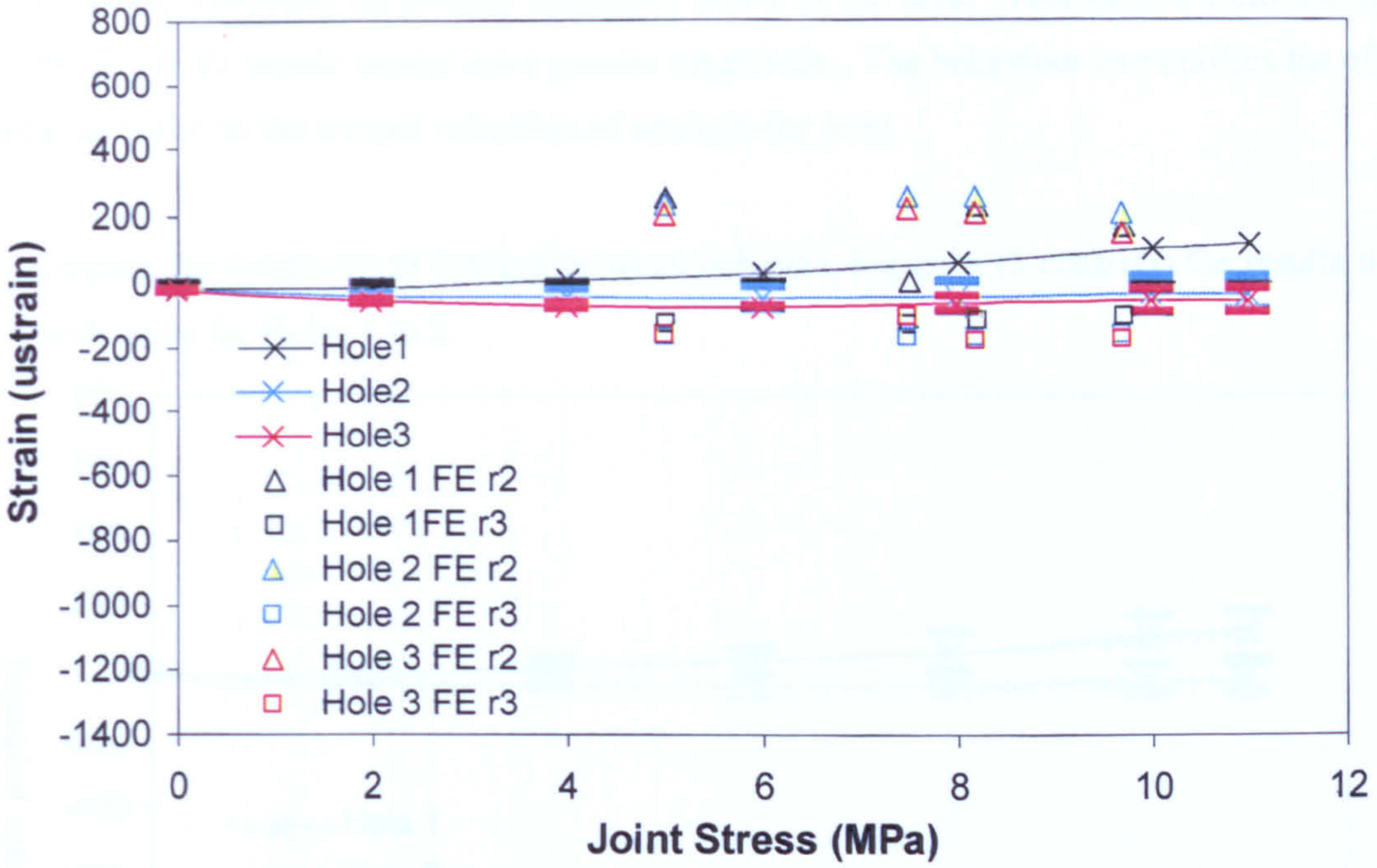

Figure 6.14. Joint stress versus tangential strain at 0° (295K).

Table 6.7. Comparison of maximum tangential strains at 0° (295K) at peak joint stresses.

	Hole 1 (μstrain)	Load Share	Hole 2 (μstrain)	Load Share	Hole 3 (μstrain)	Load Share
Experimental	**115**	55%	-38 ± 53	18%	-57 ± 37	27%
FE r2	170	33%	**204**	39%	146	28%
FE r3	-104	22%	-164	35%	**-172**	43%

There is a relatively small tangential strain at the bearing plane, as expected given that the majority of the load at this position is reacted radially. Experimentally, Hole 1 has a slight tensile strain, indicating that some of the load bypasses around the fastener. Hole 2 has a very small compressive strain, which suggests more bearing reaction and less load by-pass, and finally Hole 3 has a slightly compressive strain, since the load must be reacted as there are no more fasteners. All of these values are significantly lower than those of the finger-tight specimen. Hole 1 is 470 μstrain less, Hole 2 is 288 μstrain less, and Hole 3 is 467 μstrain less. These noticeable reductions in strain emphasise the effectiveness of the clamp-up in reducing stress concentrations.

The FE results verify negligible tangential strains at the bearing plane. The results bound the experimental values. At the inner radius, r2, the strains are tensile, while at r3 the strains are

compressive, indicating an overall negligible strain in the area. This differs from the finger-tight results, where all tensile strains are a greater magnitude. The behaviour exemplifies the effect of the clamp-up force on the overall reduction of strain in the joint.

To compare the symmetry of loading between columns, Figure 6.15 contrasts the results for Holes 4 to 6 with those for Holes 1 to 3.

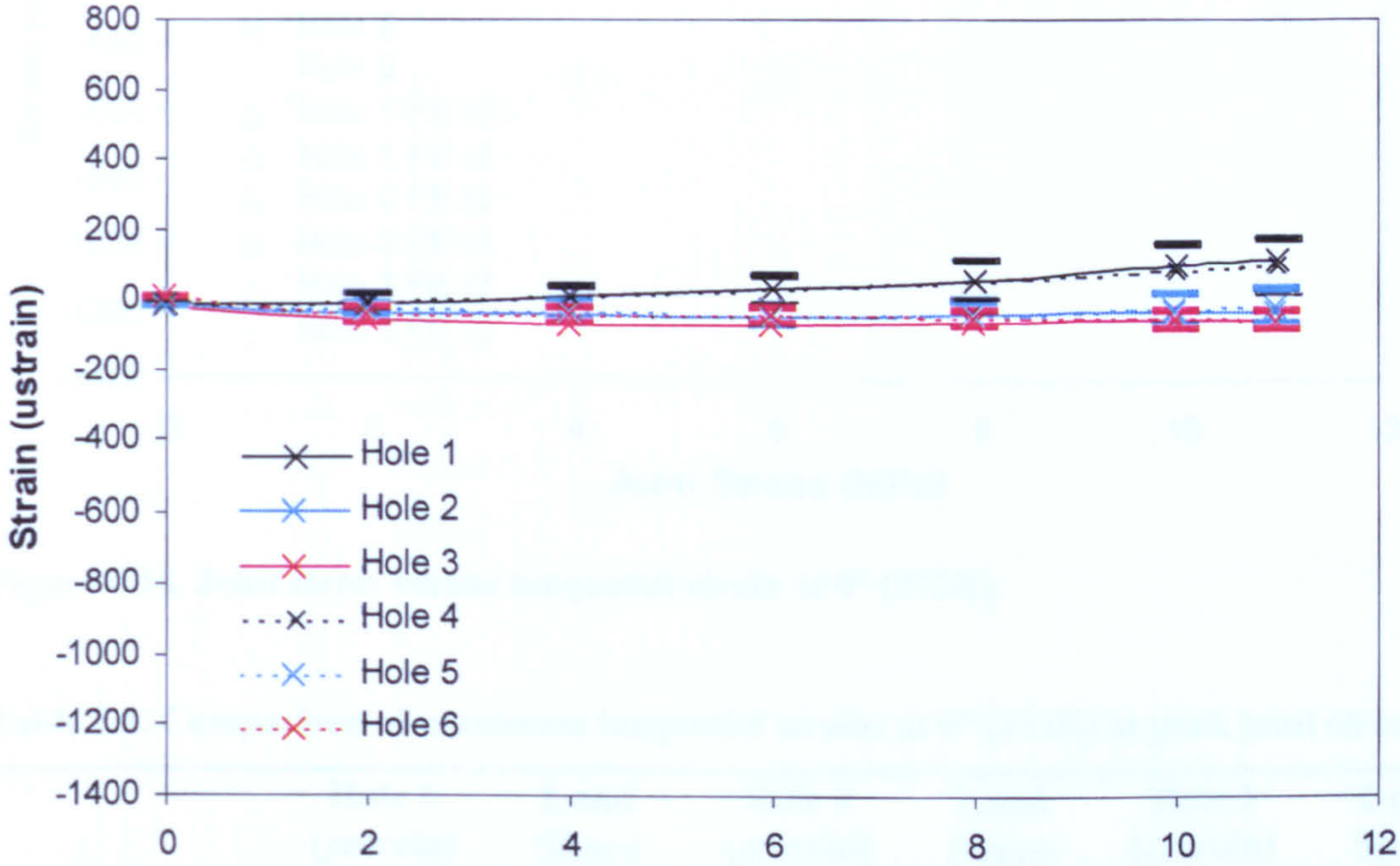

Figure 6.15. Comparison of tangential strains at Holes 1 to 3 with Holes 4 to 6 at 0° (295K).

There is good agreement in strains results for all holes. Recall from the previous chapter on finger-tight results that there are notable differences between the strains in the two columns; Holes 4 and 6 have a much lower strain than Holes 1 and 3, while Holes 2 and 5 behave in a similar manner. The improved agreement at all holes in the torque-tight results suggests that the clamp-up force evens the distribution between the two columns of fasteners. Figure 6.16 outlines the results of the torque-tightened specimen at 373K for Holes 1 to 3 and Table 6.8 the comparison of maximum strains at 373K, at 0°.

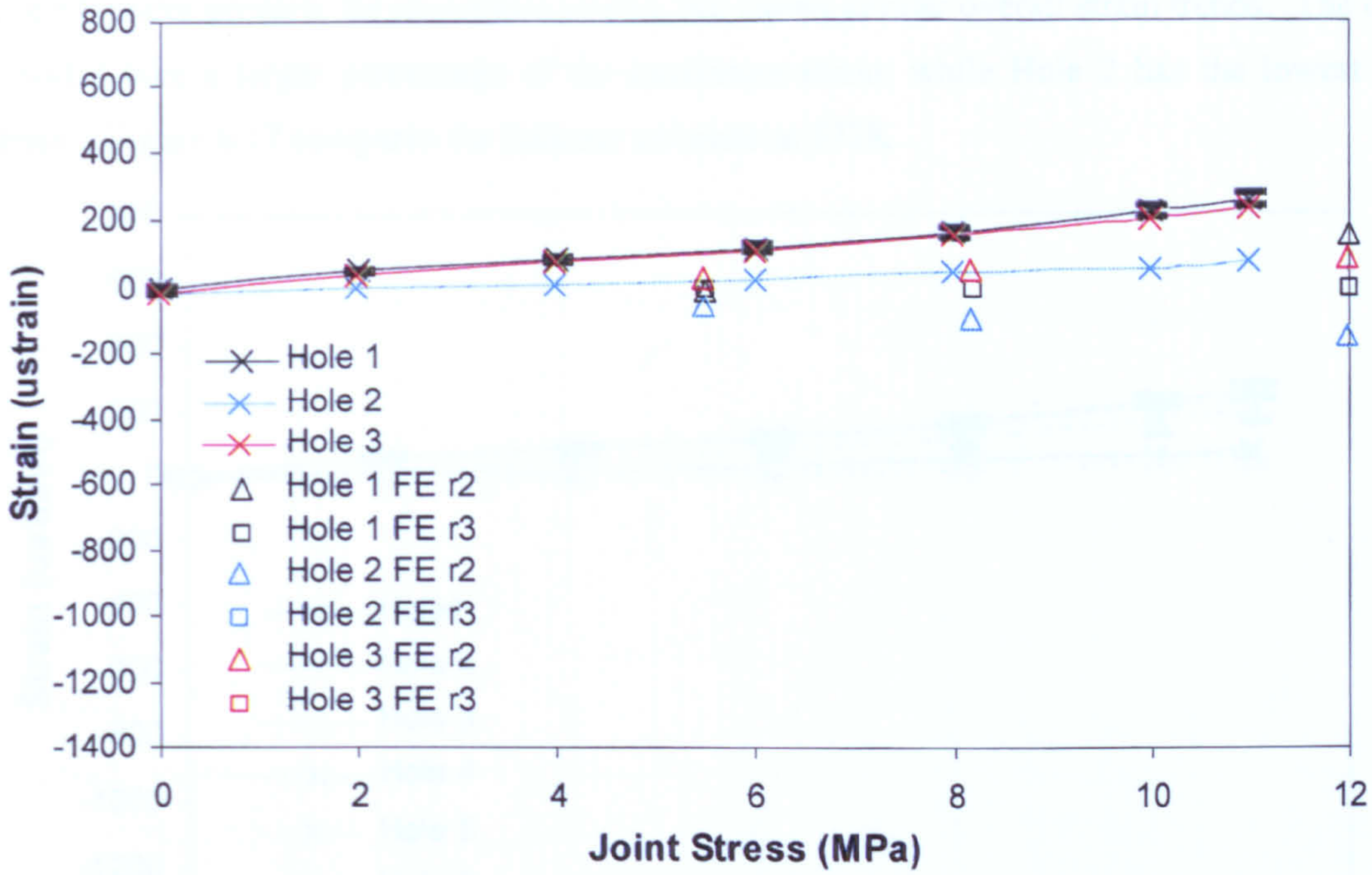

Figure 6.16. Joint stress versus tangential strain at 0° (373K).

Table 6.8. Comparison of maximum tangential strains at 0° (373K) at peak joint stresses.

	Hole 1 (μstrain)	Load Share	Hole 2 (μstrain)	Load Share	Hole 3 (μstrain)	Load Share
Experimental	**260** ± 20	46%	77	14%	231	40%
FE r2	**60**	50%	-39	32%	-21	18%
FE r3	**156**	40%	-147	38%	84	22%

From Figure 6.16, it appears that all strain values increase with an increase in temperature, demonstrating greater tensile strains. The behaviour at Holes 1 and 3 are very similar. Hole 2 has a lesser maximum strain. This is a change from the finger-tight results where Hole 1 (4) has a negligible strain and Hole 3 carries the majority of the load. Again, the torque evens load distribution, significantly reducing the maximum strain values at Holes 2 and 3, but increasing strain at Hole 1. Hole 1 increases by 250 μstrain, while Hole 2 is reduced by 60 μstrain, an approximate change of 50%, and Hole 3 is reduced by 505 μstrain, equivalent to approximately 30% of the finger-tight maximum tangential strain value. The greatest change in the torque-tight results from 295K to 373K is the resulting strains are more tensile. Hole 1 strains nearly double, while Hole 3 increases by approximately 80%. This implies that the aluminium elements are now elongating tangentially at all holes as they are compressed radially by contact at the bearing plane.

The FE under-predicts the maximum strains, but shows similar overall strain trends. The outer holes 1 and 3 take a larger percentage of the maximum strain, while Hole 2 has the lowest maximum strain. Figure 6.17 compares the fastener columns at 373K.

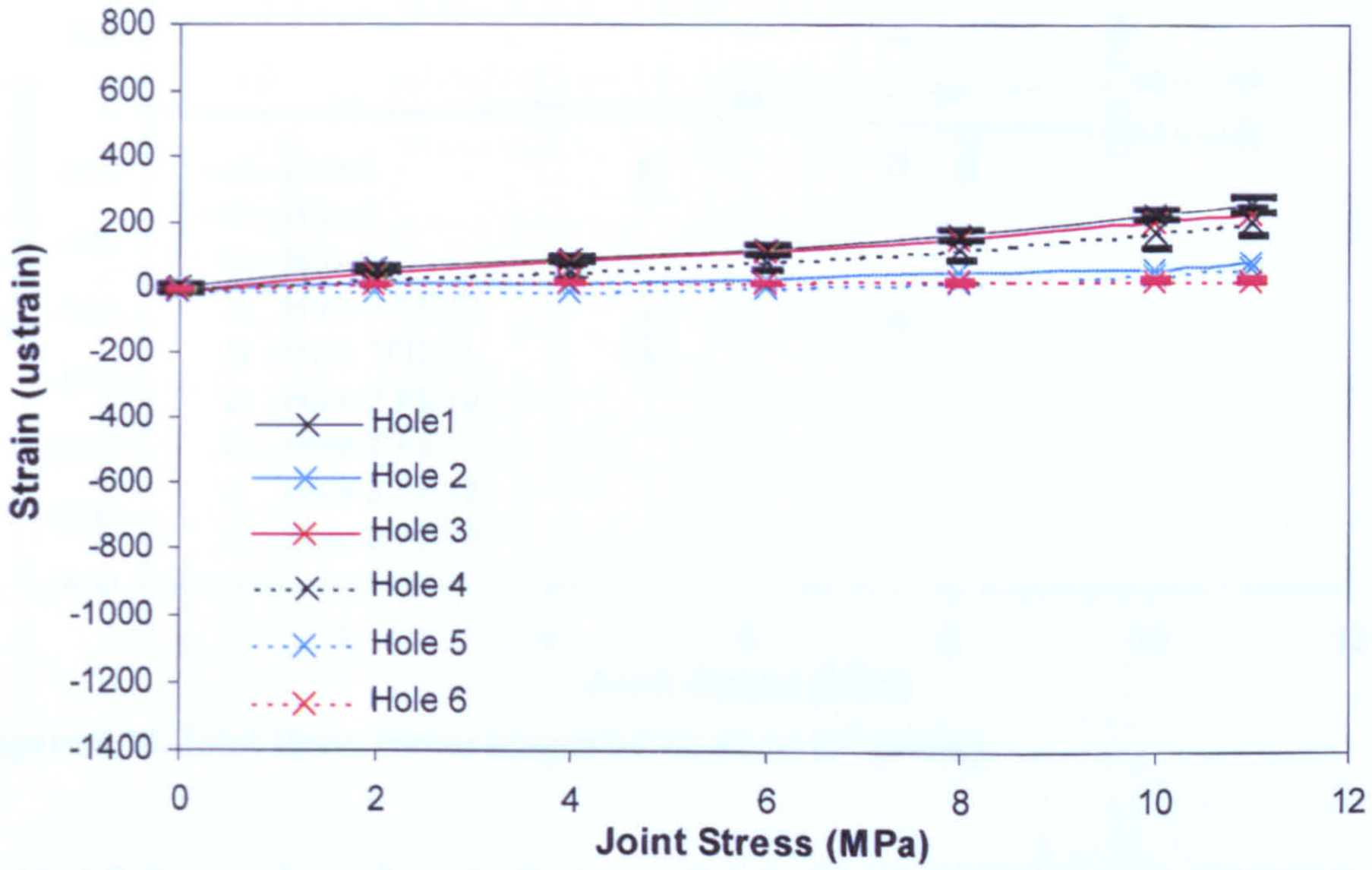

Figure 6.17. Comparison of tangential strains at Holes 1 to 3 with Holes 4 to 6 at 0° (373K).

Figure 6.17 shows the good agreement between fastener columns, particularly at Holes 1 and 2. It appears that the gauge at Hole 6 did not function, as the results remain at their initial level. However, given the accuracy in the other comparisons, it is reasonable to assume that the Hole 3 results are accurate. There is little change in the degree of symmetry between the two columns for 295K and 373K, which implies that temperature has little effect on symmetry at high torque levels. Finger-tight results show greater variation in strains between columns at different temperatures.

6.3.2 Tangential strains at 45°

Moving to 45° results, Figure 6.18 illustrates the tangential strains at 295K and Table 6.9 compares maximum tangential strains at 295K.

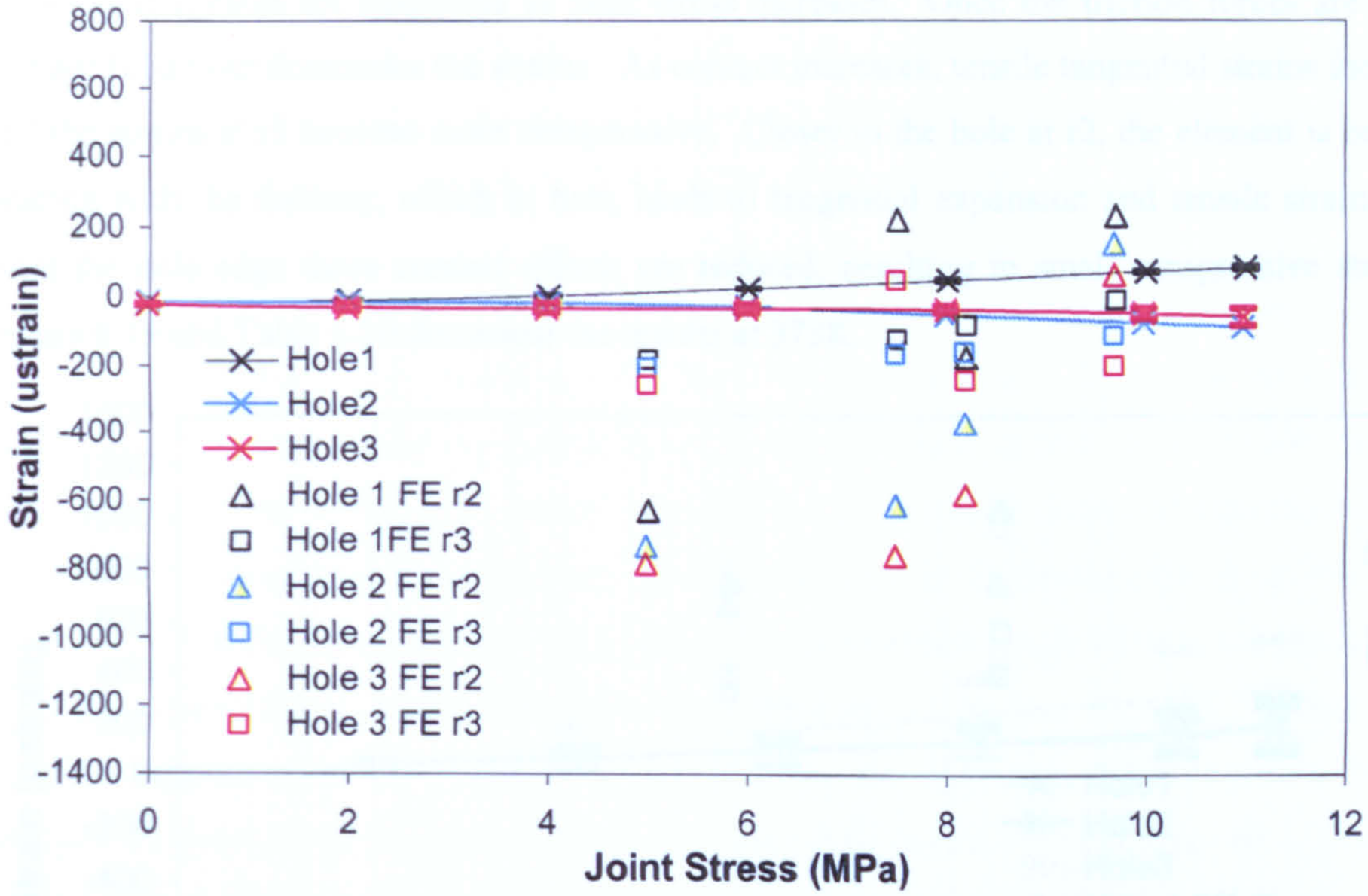

Figure 6.18. Joint stress versus tangential strain at 45° (295K).

Table 6.9. Comparison of maximum tangential strains at 45° (295K) at peak joint stresses.

	Hole 1 (μstrain)	Load Share	Hole 2 (μstrain)	Load Share	Hole 3 (μstrain)	Load Share
Experimental	**86** ± 3	38%	-86	38%	-54 ± 24	24%
FE r2	**232**	52%	152	34%	64	14%
FE r3	-9	3%	-112	35%	**-198**	62%

The experimental strains in the experimental results again appear quite small, with Hole 1 having a tensile maximum strain, and Hole 2 and Hole 3 having a more compressive maximum strain. The trend of Hole 1 bearing the most tensile strain with Hole 3 and Hole 2 having compressive strain similar to the trend results for finger-tight testing. The resulting values are lower due to improved distribution in the clamp-up specimen. The maximum difference is 527 μstrain at Hole 1, 425 μstrain at Hole 2, and 544 at Hole 3, verifying that all strains are significantly reduced.

The FE results show a greater deviance when compared with the radial and previous finger-tight results. The compressive strains at the lower joint stresses correspond to the tensile radial strains in the region. The results at the greatest joint stress show improved agreement with the experimental results, implying that the friction forces that cause plate interaction and alteration of strain patterns at

lower joint stresses are overcome as joint stress increases. Once the friction forces are overcome, contact behaviour dominates the strains. As contact increases, tensile tangential strains increase at r2 and the strains at r3 become more compressive. Closer to the hole at r2, the element is brought into bearing with the fastener, which in turn, leads to tangential expansion and tensile strains. Further from the hole edge these contact effects are reduced, resulting in small compressive strains at r3. Figure 6.19 and Table 6.10 document the results at 373K.

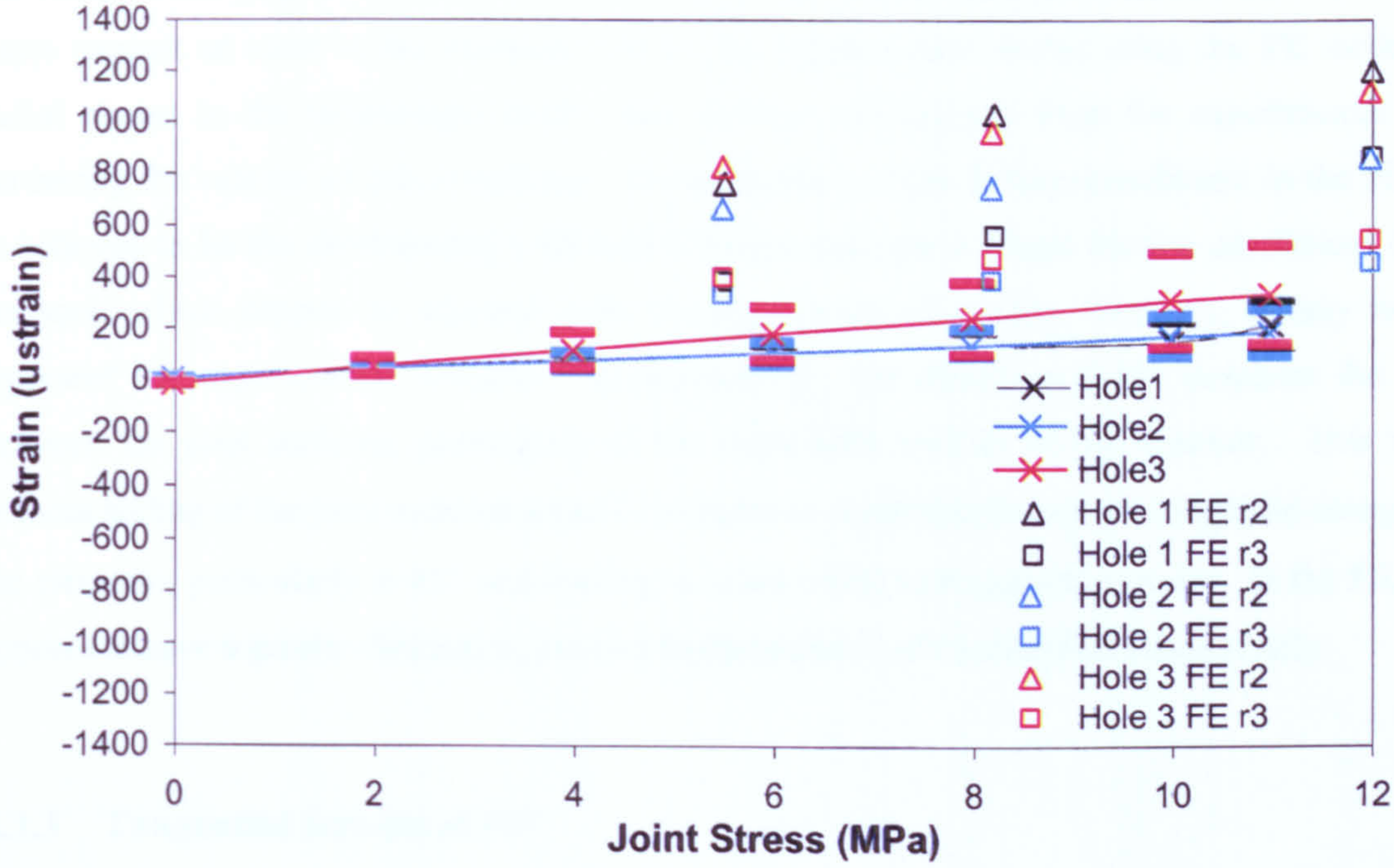

Figure 6.19. Joint stress versus tangential strain at 45° (373K). (*Note the change in the Strain axis scale.)

Table 6.10. Comparison of maximum tangential strains at 45° (373K) at peak joint stresses.

	Hole 1 (μstrain)	Load Share	Hole 2 (μstrain)	Load Share	Hole 3 (μstrain)	Load Share
Experimental	216 ± 91	29%	186 ± 91	25%	**338** ± 191	45%
FE r2	**1192**	55%	861	40%	1120	52%
FE r3	**868**	46%	460	24%	552	29%

At 373K, the experimental strains increase dramatically over those at 295K, with Hole 3 carrying the maximum tensile strain with an increase of 392 μstrain. Holes 1 and 2 also increase by 302 μstrain and 272 μstrain, respectively. These strains values are approximately three-times greater than the 295K values. This trend of Hole 3 becoming the most highly strained is also seen in the finger-tight

results to a greater extent. The torque reduces the maximum strains by 442 μstrain at Hole 3 and 110 μstrain at Hole 2, compared to finger-tight results. Hole 1 increases in strain by 175 μstrain due to the increase in bearing load brought about by the more even distribution resulting from torque. This increase in strain on Hole 1 reduces the strains at the other two holes.

The FE values are more than four-times greater than the experimental results, resulting in a change to the scale of this graph. The strains at 373K show less scatter than at 295K, but the values in both cases suggest an error in the representation of the experimental strains using the FE model. The radial strains in the torque-tight results also deviate substantially from the experimental values, furthering the validity of this hypothesis. Representation of the friction coefficient in the FE model is believed to be the shortcoming. ABAQUS allows for only a single friction coefficient between surfaces, which cannot be adjusted with the application of torque; therefore, it may not fully represent the experimental scenario. Experimentally, the clamp-up force increases the friction between the joint surfaces, particularly in the immediate vicinity of the fastener. This pressure reduces sliding of the joint material around the fastener, thereby reducing the tangential elongation of the elements, particularly at 45°, and leading to lower radial and tangential strains. In the FE, sliding appears to have a greater dimension, causing higher strains both radially and tangentially.

6.3.3 Tangential Strains at 90°

The strains at the 90° gauges are represented by Figure 6.20 for testing at 295K with a comparison of maximum tangential strains in Table 6.11.

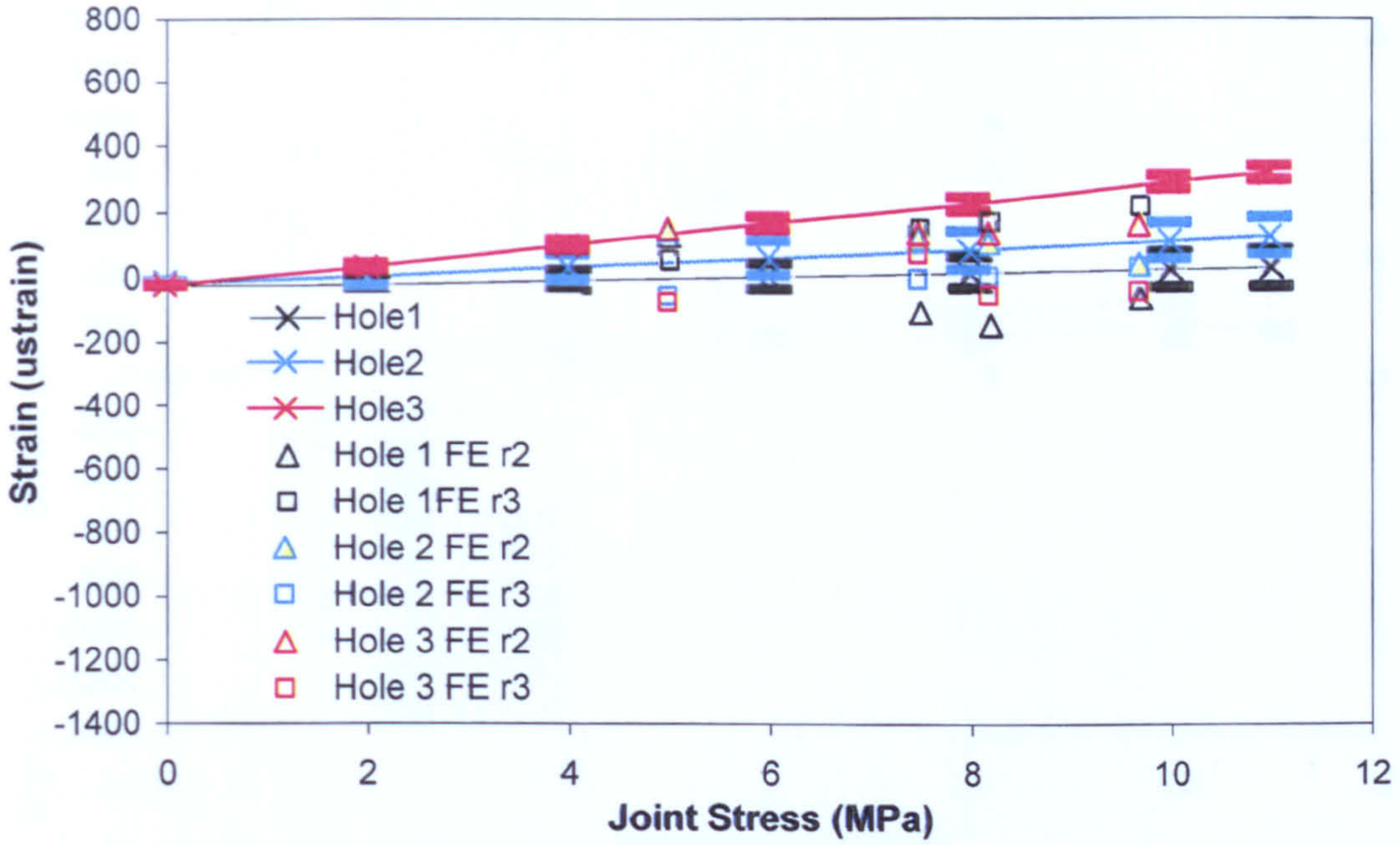

Figure 6.20. Joint stress versus tangential strain at 90° (295K).

Table 6.11. Comparison of maximum tangential strains at 90° (295K) at peak joint stresses.

	Hole 1 (μstrain)	Load Share	Hole 2 (μstrain)	Load Share	Hole 3 (μstrain)	Load Share
Experimental	30 ± 56	6%	115 ± 56	25%	**315** ± 20	68%
FE r2	-64	24%	37	14%	**161**	62%
FE r3	**217**	75%	28	10%	-42	15%

The trends remain the same as in the finger-tight tests with Hole 3 having the maximum tensile strain. Once again the values are lower because of clamp-up, and Hole 3 shows a decrease of 277 μstrain from the finger-tight results, Hole 2 a decrease of 220 μstrain, and Hole 1 strains are now negligible, a decrease of 405 μstrain.

The FE results show improved agreement over the 45° results, although the maximum values under-predict those of the experimental results. The values at r2 show better agreement with the experimental results, while the values at r3 show a reversal in maximum strain from Hole 3 to Hole 1. This again indicates that clamp-up has a significant effect on strains nearest the fastener head. This influence decreases as the distance from the hole edge increases. The results at 373K are given in Figure 6.21, and the comparison of strains in Table 6.12.

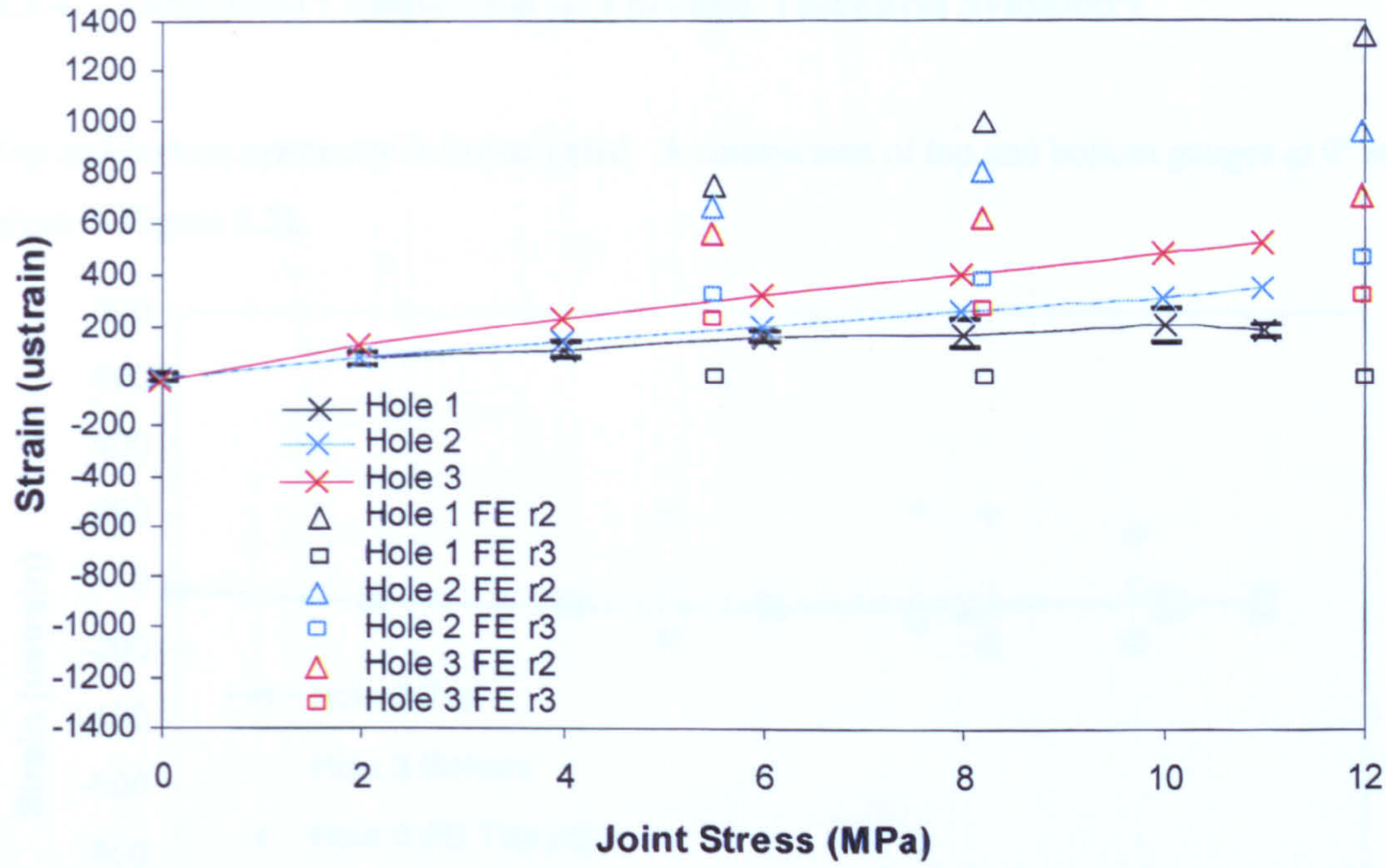

Figure 6.21. Joint stress versus tangential strain at 90° (373K). (*Note the change in the Strain axis scale.)

Table 6.12. Comparison of maximum tangential strains at 90° (373K) at peak joint stresses.

	Hole 1 (μstrain)	**Load Share**	**Hole 2 (μstrain)**	**Load Share**	**Hole 3 (μstrain)**	**Load Share**
Experimental	182 ± 28	17%	353 ± 132	33%	**527** ± 143	50%
FE r2	**1330**	44%	959	32%	704	24%
FE r3	**708**	47%	469	31%	321	22%

Although the trends remain similar, the experimental strains increase over those at 295K. Hole 1 increases by 85%, Hole 2 by 70%, and Hole 3 by 40%. This increase in tangential strain at the net-tension plane, caused by the increase in temperature, differs significantly from the radial strain behaviour at 90°, where at both temperatures the strains are minimal. When compared with the finger-tight results, the strains at Holes 1 and 2 are higher by 165 μstrain and 72 μstrain, respectively. By comparison, Hole 3 has reduced strain, 162 μstrain less. This is another example of re-distribution of stress reducing peak concentrations by more even load sharing amongst all fasteners.

The FE results again over-predict the maximum strains, resulting in a change in scale on the strain-axis of the graph. Sliding induced by a lower friction coefficient increases tangential strains over the experimental results, similar to behaviour at 45°.

6.3.4 Tangential Comparison of Through-Thickness Symmetry

Top and bottom symmetry is investigated. A comparison of top and bottom gauges at 0° and 295K is given in Figure 6.22.

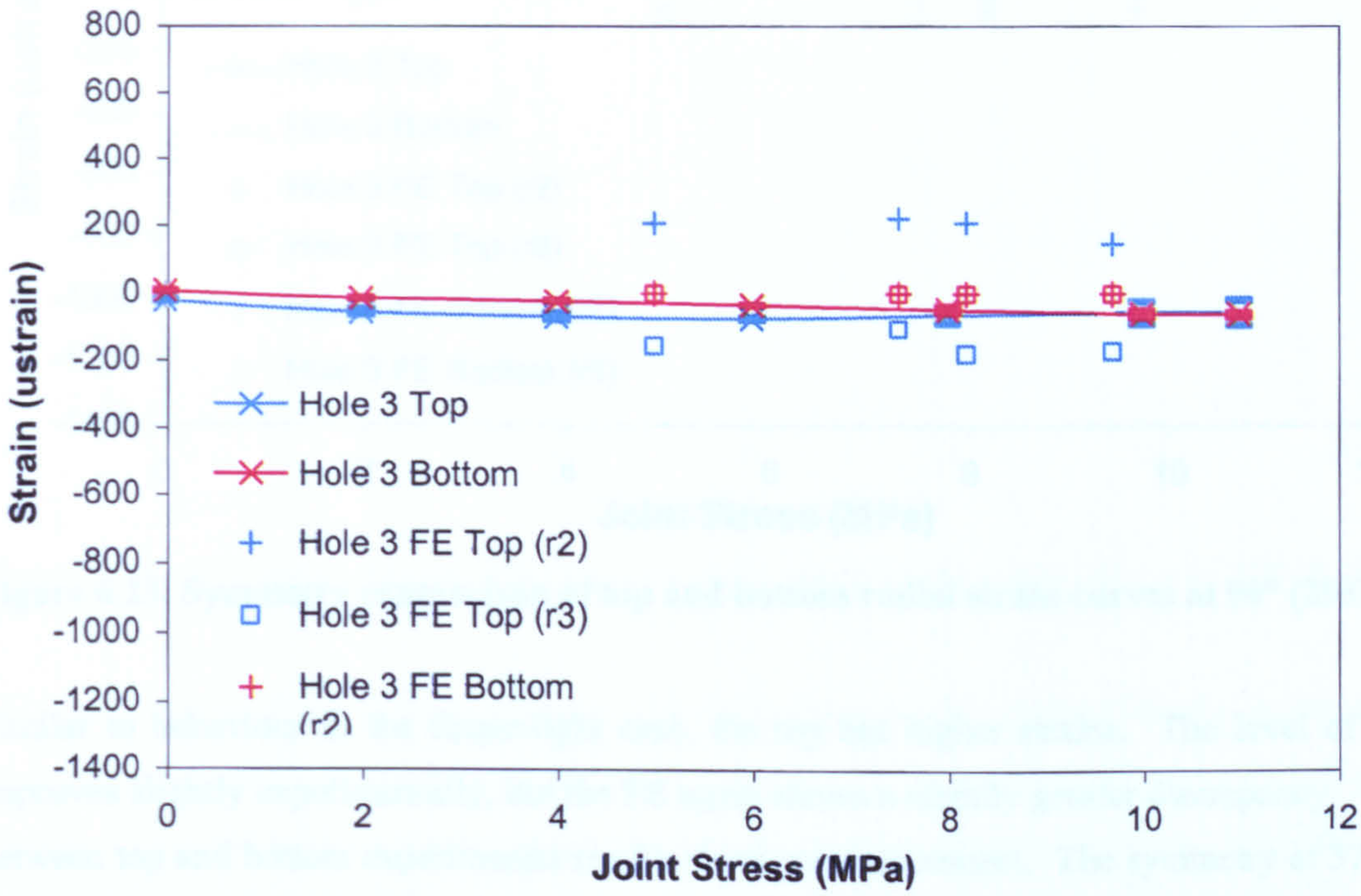

Figure 6.22. Symmetry comparison of top and bottom radial strain curves at 0° (295K).

Figure 6.22 reveals a high degree of symmetry between top and bottom results. The experimental symmetry shows improvement over the finger-tight results. The FE results, however, show a slightly lower degree of symmetry in comparison to the finger-tight results. The top FE results show a greater degree of variation between r2 and r3, suggesting the fastener head has a greater degree of influence than the washer and nut surfaces on the bottom lap. Figure 6.23 represents comparison at 90°.

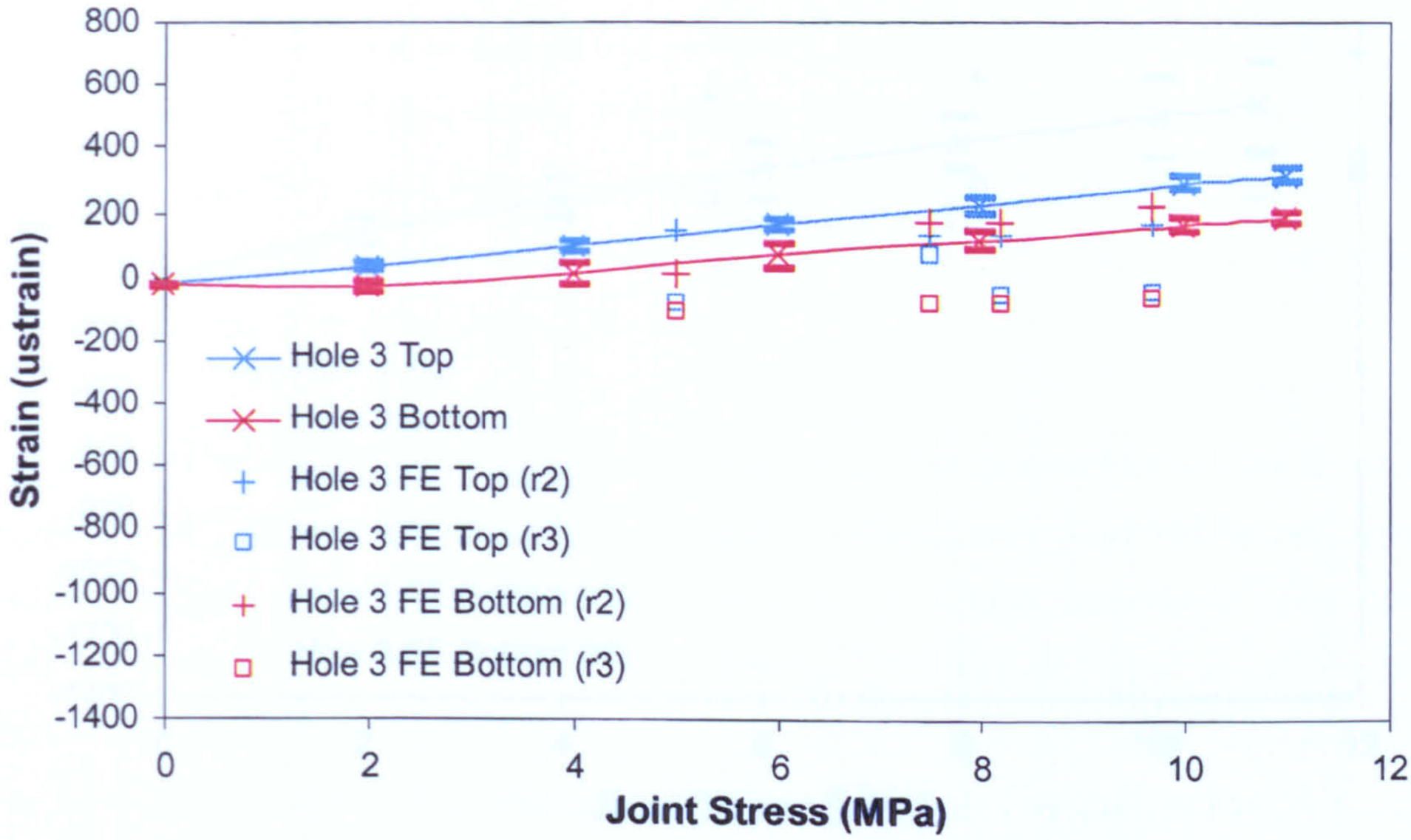

Figure 6.23. Symmetry comparison of top and bottom radial strain curves at 90° (295K).

Similar to behaviour in the finger-tight case, the top has higher strains. The level of symmetry improves slightly experimentally, but the FE again shows a slightly greater discrepancy. The trends between top and bottom experimental results show good agreement. The symmetry at 373K is also investigated. Figure 6.24 shows the results at 0°, while Figure 6.25 provides a comparison at 90°.

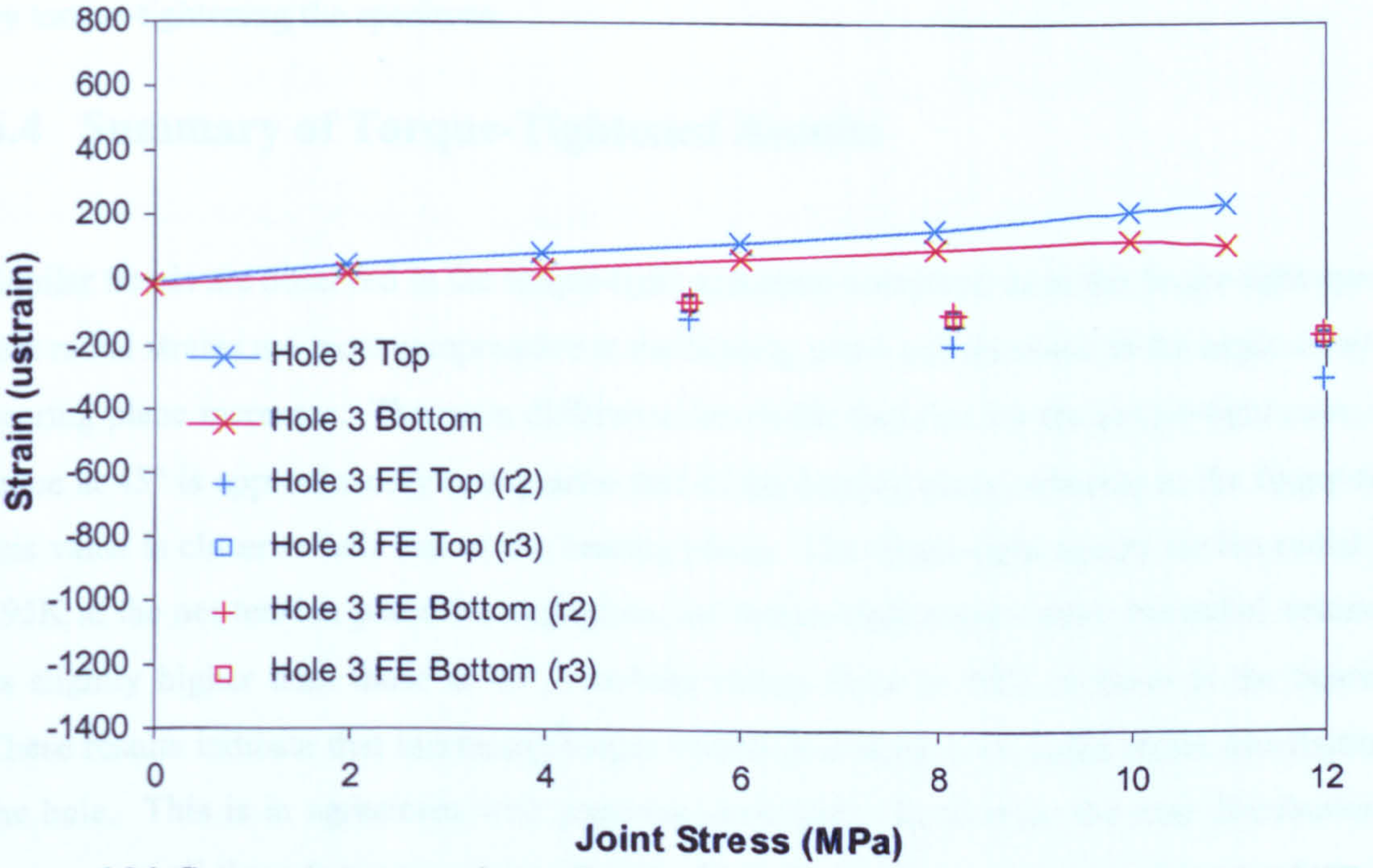

Figure 6.24. Symmetry comparison of top and bottom radial strain curves at 0° (373K).

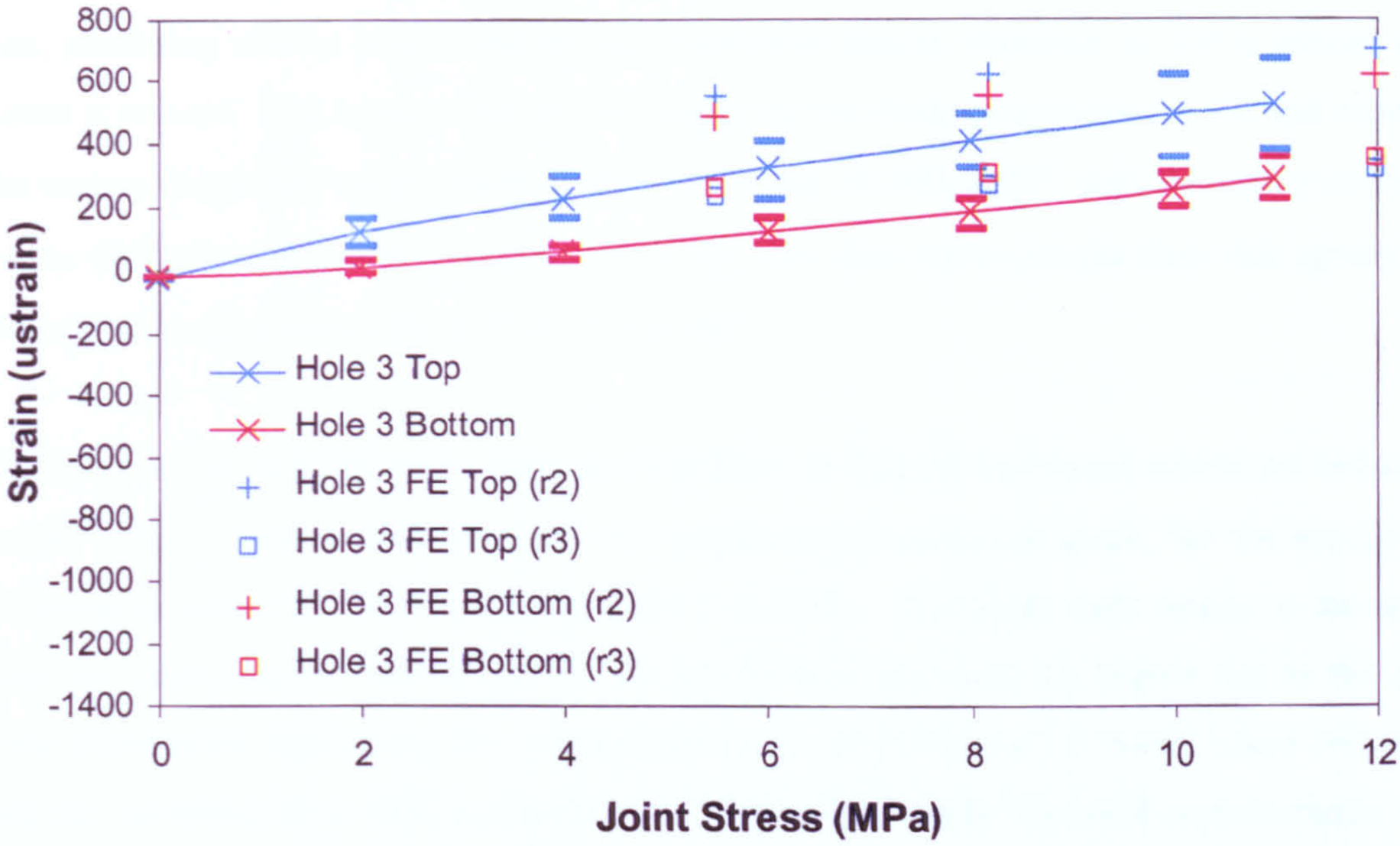

Figure 6.25. Symmetry comparison of top and bottom radial strain curves at 90° (373K).

The agreement in Figure 6.24 is good, an improvement over the finger-tight case, particularly in the experimental trends. At 90°, Figure 6.25 still demonstrates fair agreement, albeit to a slightly lesser extent. Comparing the tangential strain through-thickness symmetry of the finger-tight and torque-tight results, verifies that there is not a significant improvement in tangential strain symmetry gained by torque-tightening the specimen.

6.4 Summary of Torque-Tightened Results

Similar trends are observed in the torque-tight specimen compared as in the finger-tight specimen, in that radial strains are most compressive at the bearing plane and decrease as the angle away from the bearing plane increases. The main difference lies in the fact that for the torque-tight case, the strain value at 45° is approximately one-quarter that of the bearing plane, whereas in the finger-tight case, this value is closer to half that at the bearing plane. The finger-tight results for the radial strains at 295K at the net-tension plane are negligible, but torque-tight results show the radial strains at 295K as slightly higher than those at 45°, reaching values close to 50% of those at the bearing plane. These results indicate that increasing torque results in a more even radial strain distribution around the hole. This is in agreement with previous work [69]. In general, the load distribution is more even across all three fasteners compared with the finger-tight results, where the outer fasteners carry

the majority of the load. FE results show fair comparison with experimental results for 0° and 90° tests, predicting similar strains and percent maximum strains; however, at 45° a greater degree of scatter is present. The lower strain levels exaggerate the discrepancy between FE and experimental. The error in magnitude ranges from 45-61% at 0°, and 31-49% at 90°, with the scatter at 45° making it more difficult to determine the error (77-82%). The distribution results show fair agreement, with differences ranging from 12% at 0° to 25% at 90°.

The radial strains at 373K differ from those at 295K in that the maximum strains are reduced at 45° and 90°. At 0°, there is little change in the magnitude of maximum strain, but the maximum strain occurring at Hole 1 at 295K, occurs at Hole 3 at 373K. The finger-tight strains at the net-tension plane are negligible, but the strains for the torque-tight specimen are higher due to the change in strain distribution induced by the clamp-up pressure. At 373K, the FE results show less agreement with the experimental results, particularly at 45° and 90°, where frictional representation in the FE may not be an accurate representation of experimental conditions. The FE tends to over-predict the strain values by as much as 70% at 45° and 60% at 90°. The FE model's limitation in accounting for increased friction due to clamp-up results in lower perception of friction overall, which in turn, leads to a higher degree of sliding of material around the fastener. This changes the contact conditions, resulting in higher strain values than in the experimental results. In the experimental specimen, greater friction leads to a more even strain distribution around the fasteners. The FE maximum strains have a range of accuracy of 23-74%. The distribution agreement at 373K remains much the same as at 295K, with a 17% difference at 0°, and a greater discrepancy of 61% difference at 90°.

The tangential strains of the torque-tight specimen demonstrate a significant decrease in magnitude over the finger-tight results. At 295K, the greatest tangential strains for torque-tight occur at the net-tension plane, unlike the finger-tight results that show maximum strains at 45°. In fact, the tangential strains at 45° for the torque-tight are the lowest values, approximately 25% those at 90°. At 0°, the maximum strain is closer to 50% that at the net-tension plane. Despite these percentages, the overall maximum tangential strain is quite small at just over 300 μstrain. The FE results at 295K tend to bound the experimental curves. However, a high degree of scatter is again observed at 45°.

At 373K, the maximum strains show as increase of 56% at 0°, 75% at 45°, and 40% at 90° over the maximum values at 295K. The overall trends at 373K tend to be very similar to those at 295K,

suggesting that clamp-up pressure, rather than temperature, is the driving force behind strain distribution. The FE model under-predicts the maximum strain at 0° by 67%, but over-predicts the results at 45° and 90° by 71% and 60%, respectively. This again most likely results from the sliding of the material in the FE model due to the lower perceived friction coefficient, as compared with actual experimental conditions.

Examining the chordwise symmetry between the columns of fasteners, the torque-tight results show excellent agreement across columns. When compared with the finger-tight results, it is evident that increasing torque improves strain distribution between fastener columns, as well as along the row.

Examination of the top and bottom symmetry at Hole 3 reveals that the top aluminium lap generally bears the highest strains, radially and tangentially, at both temperatures. This is similar to the behaviour of the finger-tight specimen. The overall degree of radial symmetry improves over the finger-tight results, with the top and bottom results showing very strong agreement, while tangential strain symmetry shows little change. Increasing clamp-up allows for a more even strain distribution through the thickness and in-plane, reducing the geometry effects of the fastener head over the nut and washer. Again, temperature appears to have little effect on through-thickness symmetry.

Chapter 7 Conclusions

This research set out to gain an understanding of temperature effects on strain distribution in mechanically fastened CFRP/Aluminium double lap joints. The combination of these materials in multi-fastener joints under various thermal and mechanical loading conditions contributes to the originality of this work. Prior to examining strains in particular, the thermal environment of this double lap joint in a wingbox structure was examined. FE analysis was used to simulate three tank conditions: empty, full, and half-full, and provide an indication as to the effect of the three mechanisms of heat transfer: conduction, convection, and radiation. Analytical temperature prediction tools for single and multiple-layer 2D specimens were developed to account for finite geometry, with complex boundary conditions at both external surfaces. Following this temperature prediction work, the highest temperature results, namely the empty tank scenario, were used in a sequentially coupled thermal-stress analysis to prove that the CFRP skin side of the joint not only had the highest temperatures, but also the greatest resulting strains. With this conclusion, an experimental program was designed to further study the strains in this region subject to thermal and mechanical loading conditions. Increased temperature was found to alter the strain distribution among the joint fasteners, and in most cases decreased peak radial strains, but increase peak tangential strains. The effect of torque was also compared, and was shown to significantly reduce peak strains and even the strain distribution around individual fasteners as well as across the joint. Specific conclusions for the temperature profiling section are given in Section 7.1 and for the thermal-mechanical strain analyses in Section 7.2, which is broken down into 7.2.1 Finger-tight specimen and 7.2.2 Torque-tight specimen.

7.1 Temperature Profiles

FE analysis performed on thermal loading of a simplified wingbox structure at fuel tank levels of empty, full, and half-full, yields the following conclusions:

1. Radiation is the most influential heat transfer mechanism in the empty tank, providing 95% of the total resulting profile. Convection is the most influential heat transfer mechanism in the full tank, providing 99% of the total resulting profile.

2. To gain an accurate representation of the temperature, particularly for the empty and half-full tank scenarios, both radiation and convection must be modelled.

3. The highest temperatures occur in the CFRP skin side of the joint region for an empty tank on the top of the wingbox with a maximum of 374K when no titanium pins are present, and 378K when the pins are modelled. Titanium pins cause a small increase in the maximum temperature. All temperatures in the empty tank case are within 5 degrees.

4. The fuel acts as a heat sink; therefore, the full tank reaches a maximum temperature of 300K, only 12 degrees above the initial temperature. Titanium pins have no noticeable impact on temperatures.

5. The upper half of the half-full tank demonstrates behaviour similar to the empty tank, the lower portion of the half-full tank behaviour is similar to the full tank.

6. The skin away from the joint can be modelled analytically using the integral transform solution technique, accounting for fully transient convection and semi-transient radiation and combined convection-radiation boundary conditions at both surfaces.

7. The joint region can be modelled analytically using the separation of variables solution technique, accounting for fully transient convection and semi-transient radiation boundary conditions at both surfaces.

8. Sequentially coupled thermal-stress analysis confirms the CFRP skin side of the joint as having the greatest thermally induced stresses due to differing expansion coefficients.

7.2 Thermal and Mechanical Strain

Performing tensile testing at 295K and 373K in the elastic region of a double shear aluminium/CFRP/aluminium lap joint containing two columns of three fasteners generates the following conclusions:

7.2.1 Finger-Tight Specimen (1Nm)

1. At 295K, the highest radial strains are compressive strains occurring at the bearing plane. Radial strains decrease in magnitude from their maximum at 0° to almost negligible at 90°. The resulting strains at 45° are 35% to 56% lower than those at the bearing plane, indicating that this strain decrease is a non-linear relationship.

2. At 295K, the maximum tangential strains are tensile strains, occurring at 45°. The results at 45° are 3% higher than those at the net-tension plane (90°), and 5% greater than those at the bearing

plane. The maximum tangential strain results at 45° are due to a combination of bearing and by-pass loads at that position.

3. At 295K, the outer holes (Holes 1 and 3) take the majority of joint load, and therefore, have the highest strain distributions. Tangentially, Hole 1 percent maximum strains range from 30-47%, Hole 2 from 20-26%, and Hole 3 from 33-44%. Radially, percent maximum strains range from 37-50%, Hole 2 from 20-31%, and Hole 3 from 24-32%.

4. The FE model compares fairly with the experimental data at 295K for strain magnitude and overall strain distributions. The agreement for magnitude of strains between experimental results and the averaged FE results that bound the experimental gage position is 90-96% at 0°, 40-55% at 45°, and 47-59% at 90°. Strain distribution agreement between experimental and FE results is good, ranging from 5% difference at 0° to 15% at 90°.

5. At 373K, the bearing plane maintains the highest radial strains, approximately 45% greater than those at 45°. The radial strains at 90° are minimal.

6. At 373K, experimental results determine Hole 3 as having the largest radial strains, while FE results show the outer holes sharing the higher strains, with Hole 1 bearing the maximums.

7. At 373K, the FE model predicts maximum strains with an accuracy of between 41-98%, and includes discrepancies of 4-60% when predicting strain distributions.

8. The resulting maximum radial strains at 373K are lower than at 295K for 0° (1% less) and for 45° (3% less), but are higher at 90° by 21%. According to the FE results, the strain distribution is more even across all holes.

9. At 373K, the maximum tangential strains occur at 45°, similar to results at 295K. At 373K, the maximum strains increase by 20% at 0°, 22% at 45°, and 14% at 90° over the maximums at 295K.

10. At 373K, the tangential strains in the experimental results at Hole 1 are negligible implying experimental error, most likely due to the secondary factors of bolt tolerance and take-up because of the low-load operating range, since radial strains alone are expected to induce significant tangential strains, as there is no plastic deformation. Tangentially, Hole 1 percent maximum strains ranged from 1-4%, Hole 2 from 15-20%, and Hole 3 from 70-83%. Radially, the percent maximum strains ranged from 13-26% at Hole 1, 33-41% at Hole 2 and 41-62% at Hole 3.

11. At 373K, the FE model predicts a maximum tangential strain at 0° that is 41% lower than the experimental results, whereas maximum strains at 45° and 90° are greater than the experimental results by 16% and 11%, respectively. The accuracy of strain distribution is reduced, with discrepancies ranging from 50-75%.

12. Increasing temperature increases maximum tangential strains and causes a change in strain distribution from a more even dispersal between both outer holes to a greater strain at a single outer hole. Change in temperature has a larger effect on the magnitude of tangential strains than on radial strains.

13. Through-thickness symmetry shows the top lap having generally having greater strains and fairly similar values (i.e. good symmetry), and temperature is shown to have minimal impact on through-thickness symmetry.

14. The primary sources of error in the experimental results are the low-load operating region, gauge positioning error, and misapplication of torque to the specimen. The low-load operating region induces strain discrepancies due to effects such as surface roughness, load introduction and settling, bolt tolerance, and take-up, which are not observed at higher load levels; however, due to equipment limitations, results from this low-load region were used in the present study. Error in positioning of the strain gauges may be caused by not positioning the gauge perfectly perpendicular to the hole edge and/or positioning the gage at a different angle, both of which may skew strain results. Error associated with the application of torque through the use of a torque wrench, which may lead to reduced clamp-up levels caused by friction, may cause discrepancies in the load and strain distributions.

15. The primary sources of error in the FE analysis include: an assumed friction coefficient applied to all surfaces with no variation throughout the analysis, perfect application of compressive clamp-up load representing torque level, edge effects associated with the one-quarter scale of actual specimen geometry, and required boundary conditions. Error, in comparison to the experimental results, due to the assumed friction coefficient may be caused by the fact that no secondary motion and surface interactions are accounted for. The clamp-up force applied to the model may not be the actual force applied to the specimen due to the inherent error associated with the torque wrench, affecting direct comparisons. Finally, two boundary conditions, constraint boundary condition at mid-plane (back face) in which movement of joint is dictated only by CFRP behaviour, and symmetry boundary condition at mid-fastener plane (front face), preventing motion at this plane, were applied to allow the one-quarter model to simulate the entire specimen. These conditions are not able to account for edge effects and associated bolt interaction within the experimental specimen.

7.2.2 Torque-Tight Specimen (35Nm)

1. At 295K, the highest radial strains occur at the bearing plane, similar to the finger-tight behaviour. However, clamp-up force of the torque-tight specimen leads to a more even distribution over all fasteners. The magnitude of maximum strain at 45° is 25% that at 0°. At 90°, the strain magnitude is greater than at 45° with a value 54% that at 0°. This demonstrates the difference in behaviour between clamp-up and finger-tight, where radial strains were negligible at 90°.
2. At 295K, the maximum radial strain for the torque-tight specimen is only 37% that of the finger-tight specimen, demonstrating that clamp-up pressure reduces strain magnitudes.
3. At 295K, the maximum tangential strain occurs at the net-tension plane (90°) compared to at 45° in the finger-tight specimen. The bearing plane has the next highest tangential strains, 36% that at 90°, demonstrating a significant change in maximum strain location from the finger-tight specimen. In the finger-tight analysis, the 45° plane bears the highest strains, but in the torque-tight results, the 45° has the lowest magnitude at 28% that of the net-tension value.
4. At 295K, the greatest tangential strain magnitude of the torque-tight specimen is 62% that of the highest value in the finger-tight specimen.
5. At 295K, maximum tangential strain is 92% of maximum radial strain, an increase of more than 30% over the finger-tight values, and is directly attributed to clamp-up pressure induced distribution.
6. At 295K, the percent maximum strain distribution is more even across all three holes than in the finger-tight specimen, where the outer holes take the larger percentage of the load. Radially, the percent maximum strains range from 21-45% at Hole 1, 25-36% at Hole 2, and 31-44% at Hole 3. Tangentially, Hole 1 results range from 6-55%, Hole 2 from 18-38%, and Hole 3 from 27-68%.
7. At 295K, FE comparison does not show as strong an agreement as in the finger-tight results. The magnitude in the FE results shows an accuracy of approximately 69% at 0°, 25% at 45°, and 52% at 90°. A greater degree of scatter exists for the FE torque-tight results than in the finger-tight results. The percent maximum strain predictions differ by 12% at 0°, 15% at 45°, and 1% at 90°, demonstrating the prediction of overall load distribution is better than the strain magnitudes.
8. At 373K, the maximum radial strains again occur at the bearing plane, while the 45° and 90° results are significantly less in magnitude, at 23% of 0° and 26% of 0°, respectively. This distribution differs from finger-tight results in that a decrease in strain from the bearing to net-tension planes is no longer observed, and is a change in distribution from the 295K results in that 45° and

90° strains are more similar in magnitude. Rather, the bearing plane still carries the majority of the strain, but the remaining planes show a more even load distribution.

9. At 373K, Hole 3 tends to take the larger portion of load at 0° and 90°, while at 45°, there is a more even strain distribution. This trend differs from finger-tight results where the load is concentrated at the outer holes (Holes 1 and 3).

10. At 373K, the FE results again show discrepancy ranging from 93% at 45°, where scatter is observed, to 33% at 90°, and 30% at 0°. This discrepancy is greater than that of the finger-tight specimen. The percent maximum strains difference, when compared with the experimental results, is approximately 6% at 0°, 23% at 45°, and 61% at 90°, which suggests error in FE representation of torque, most likely due to the assumption of a constant coefficient of friction.

11. The magnitudes of maximum strains at 373K are within 5-50% those at 295K, showing a lesser variation than the finger-tight values. The percent maximum strain distributions show only minimal change from 295K distributions, unlike the finger-tight results that indicate a more uniform strain distribution.

12. At 373K, the maximum tangential strains occur at 90°, similar to results at 295K. The magnitude of strains increases by 66% at 0°, 75% at 45°, and 40% at 90° compared to the 295K results, much greater increases than those observed in the finger-tight specimen.

13. At 373K, the FE results under-predict the maximum strains by 27% at 0° and over-predict the maximum strains by 90% at 45° and 48% at 90°. This trend is similar to the finger-tight specimen, although higher in discrepancy, potentially caused by the error associated with representation of friction and torque. The strain distribution has a maximum difference of approximately 28%, an improvement over the finger-tight results.

14. Similar to finger-tight results, increasing the temperature increases maximum tangential strains and alters strain distribution. However, rather than the strain shifting only to the outer holes as in the finger-tight results, the middle hole (Hole 2) begins to carry a larger portion of load. The radial strains and distributions are much less affected by torque.

15. The experimental sources of error are essentially the same as in the finger-tight specimen, with the torque-induced error magnified by the higher torque requirement, and the low-load operating range continuing to induce discrepancy due to secondary loading effects.

16. The FE sources of error are also similar to those of the finger-tight model. However, the assuming of a constant friction coefficient magnifies the torque-induced friction over that of the experimental specimen. The results differ more significantly from the FE model than in the finger-tight case.

Chapter 8 Future Work Recommendations

The present work has two primary focuses: temperature prediction through a simplified wingbox structure and thermal strain analysis in a critical double lap aluminium/CFRP/aluminium joint region. To create a more accurate representation of an actual wingbox structure for temperature prediction, future work should look at geometry effects, including curvature and the influence of leading and trailing edges. Temperature prediction analysis should also incorporate internal heat generated from aircraft components. Different profiles incorporating moisture should be studied, including hot-wet, cold-dry, and cold-wet conditions. Fuel properties should be adapted to show effects of different fuels, and forced convection should be studied to represent fuel transfer between tanks. Externally, forced convection should model in-flight conditions, taking into account altitude and pressure-induced effects. In terms of joint materials, various lay-ups of CFRP and other composites with differing conduction and convection coefficients should be compared.

The results from this temperature prediction analysis should drive other strain investigations, either as a complete study or as individual studies formulated by adopting specific results from the current work. Any change in materials, or in the CFRP lay-up, results in different strain patterns. To provide confidence in the ability of any chosen CFRP lay-up, a sub-model of interlaminar strains should be studied. As information on bolted joints in hybrid structures is limited, a study should be conducted to provide information on joint design: variation in fastener pattern (linear or staggered), alteration of the number of fasteners, fastener pitch, fastener material, and fastener type, countersunk versus protruded head design.

To further the present work, different torque levels should be investigated to develop a performance prediction equation dependent on torque. A number of different temperatures, including greater heating and temperatures lower than 273K (0°C) should be studied to characterize the influence of temperature on a given joint design. Moisture effects need to be included. Compression testing should be performed as well. Experimentally, more gages should be used to study more planes and provide complete strain pattern prediction. Full-field strain investigation could be performed by using moiré interferometry or other optical technique. Shear strain investigation should also be performed, and using milled channels, the inclusion of strain gages on the CFRP itself is an option to characterise that behaviour independently. The microstructure behaviour of the CFRP in particular could be studied to allow for failure prediction and joint design optimisation.

In terms of FE modelling, the constraints of computing capability continue to be an issue for 3D analysis. However, various element patterns should be compared, and sub-models should be used to provide additional information. A different FE model should be written to include various friction effects, and then compared with experimental results to determine the accuracy of FE representation, thereby increasing the accuracy of torque-tight representation. With the development of different FE models, these models should be used to perform a parametric study to determine the most influential parameters in joint design: fastener type, torque level, skin thickness, friction coefficient, pitch, and fastener diameter. A combined experimental/FE approach could be adopted in order to perform failure analysis of a joint under various conditions, the results from which could then be used to optimise joint geometry.

This list of future work recommendations proves that study in this area of concern is still in its infancy. The present work provides a baseline for comparison for future investigation into both temperature prediction and thermal strain analysis in hybrid bolted joints.

Appendix 3A

Separation of Variables Method

Analytical methods are an important tool for understanding simple heat transfer problems. Several forms of analytical models exist. This work studies two methods: separation of variables and integral transform technique. The most common method of analytical solution is separation of variables. Many other solutions, including the integral transform technique, are derived from the basic principles outlined in this method. Therefore, it is important to understand this method of solution for eigenvalue problems. A basic, one dimensional, transient heat transfer problem is demonstrated in Figure 3A-1 and is described by equations (3A-1) to (3A-4), where (3A-1) represents a general form of the Fourier heat transfer equation, equations (3A-2) and (3A-3), the general boundary conditions, and equation (3A-4), the initial condition.

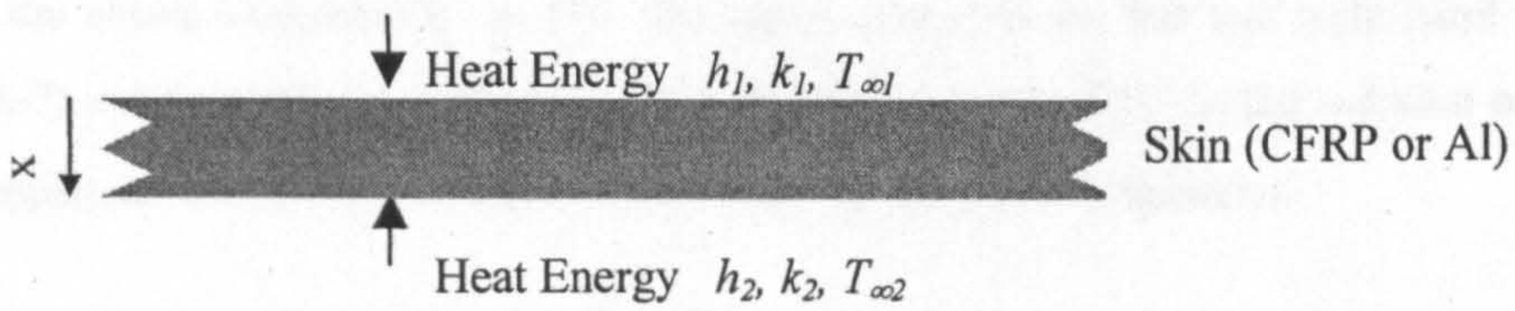

Figure 3A-1. Local model of heat transfer through the skin

$$\frac{\partial^2 T(x,t)}{\partial x^2} + \frac{g(x,t)}{k} = \frac{1}{\alpha}\frac{\partial T(x,t)}{\partial t} \qquad \text{in } 0 \le x \le L, t > 0 \qquad \text{(3A-1)}$$

$$-k_1(t)\frac{\partial T(x,t)}{\partial x} + h_1(t)T(x,t) = h_1(t)T_{\infty_1}(t) \qquad \text{at } x = 0 \qquad \text{(3A-2)}$$

$$k_2(t)\frac{\partial T(x,t)}{\partial x} + h_2(t)T(x,t) = h_2(t)T_{\infty 2}(t) \qquad \text{at } x = L \qquad \text{(3A-3)}$$

$$T(x,0) = T_i(x) \qquad \text{at } 0 \le x \le L, t = 0 \qquad \text{(3A-4)}$$

In order to use the above equations, it is assumed that the material has constant thermal properties and is homogeneous in the x-direction. In separation of variables, the space, $X(x)$, and time, $\Gamma(t)$, variables are separated such that the temperature with respect to both space and time, $T(x,t)$, can be written in the form:

$$T(x,t) = X(x) \cdot \Gamma(t) \tag{3A-5}$$

Using the homogeneous form of the boundary conditions (3A-2) and (3A-3), as given by:

$$-k(t)\frac{\partial T(x,t)}{\partial x} + h(t)T(x,t) = 0 \tag{3A-6}$$

Substituting equation (3A-5) into the homogeneous form of equation (3A-1), and assuming no internal heat generation term, $g(x,t)/k$, results in:

$$\frac{\nabla^2 X(x)}{X(x)} = \frac{1}{\alpha}\frac{\Gamma'(t)}{\Gamma(t)} \tag{3A-7}$$

In order for the above statement to be true, the ratios given on the left and right-hand sides of equation (3A-7) must equal some constant. It is standard practice [91] in the solution of partial differential equations to choose a constant value of $-\beta^2$ so that (3A-7) becomes:

$$\frac{\nabla^2 X(x)}{X(x)} = \frac{1}{\alpha}\frac{\Gamma'(t)}{\Gamma(t)} = -\beta^2 \tag{3A-8}$$

This implies that the separate equations of time and space can be represented by equations:

$$\Gamma'(t) + \alpha\beta^2\Gamma(t) = 0 \tag{3A-9}$$

$$\nabla^2 X(x) + \beta^2 X(x) = 0 \tag{3A-10}$$

The time variable has a solution of the form $\Gamma(t): Ae^{-\alpha\beta^2 t}$, where A is a proportionality constant obtained by applying the specified boundary conditions. This explains why a negative, squared constant is chosen. Physically, this means that since the value of β^2 in equation (3A-9) is always positive, as time increases, the temperature of the solid decreases. This is logical given that a solid dissipates heat from its surface to an environment of assumedly lower temperature by convection.

An eigenvalue problem is formed by combining equation (3A-10), also known as the Helmholtz equation [91], with its required homogeneous boundary conditions as described by:

$$-k_1\frac{dX(x)}{dx}+h_1X(x)=0 \quad \text{at } x=0 \tag{3A-11}$$

$$k_2\frac{dX(x)}{dx}+h_2X(x)=0 \quad \text{at } x=L \tag{3A-12}$$

For given eigenvalues, $\beta \equiv \beta_m$, there exists nontrivial solutions $X(\beta_m x) \equiv X_m(x)$, also known as eigenfunctions. In the case of Cartesian coordinates, the solution of the Helmholtz equation will be of the trigonometric form, $X(x)=B\cos\beta x+C\sin\beta x$, where B and C are constants. Since there are an infinite number, m, of eigenvalues, β_m, the final solution must be in the form of an infinite series:

$$T(x,t)=\sum_{m=1}^{\infty}X_m(x)\Gamma_m(t) \tag{3A-13}$$

Redefining A to represent its dependency on m, say c_m, and given the form of $\Gamma_m(t)$, the initial condition, equation (3A-4) can be rewritten as:

$$T(x,0)=\sum_{m=1}^{\infty}c_mX_m(x)\equiv F(x) \tag{3A-14}$$

The unknown coefficients, c_m, can be determined if the eigenfunctions, in this case $X(x)$, constitute an orthogonal set in the desired region. Provided that two real-valued functions, say $X_m(x)$ and $X_p(x)$, are defined in the desired region and the integral product of these two functions exists, orthogonality occurs when the integral of the product of these two functions is zero:

$$\int_R X_m(x)X_p(x)dx=\begin{cases}0 & \text{when } p\neq m\\ \text{Constant} & \text{when } p=m\end{cases} \tag{3A-15}$$

Basically, this implies that the solution domain of the two functions are independent of one another, such that no part of the domain of one function contains any part of the domain of the

second function, unless those functions are identical. The constant value occurs when the function has a nonzero Norm, as defined by [91]:

$$Norm = \sqrt{\int_R X_m^2(x)dx} \tag{3A-16}$$

The principle of orthogonality is important in series functions. It is recognised that any general function can be written in terms of a Fourier series, and has the form of $F(x)$ as shown in equation (3A-14). By multiplying both sides of equation (3A-14) by $X_p(x)$ and integrating over the region:

$$\int_R F(x)X_p(x) = \int_R \left(\sum_{m=1}^{\infty} c_m X_m(x)\right) X_p(x)dx = \sum_{m=1}^{\infty} c_m \int_R X_m(x)X_p(x) \tag{3A-17}$$

Because of orthogonality, the only non-zero integrals on the right hand side occur when $p=m$, implying that the right hand side becomes $\sum_{m=1}^{\infty} c_m Norm^2$. Defining a new variable, $N=Norm^2$, and rearranging equation (3A-17), the constant, c_m, is defined as:

$$c_m = \frac{\int_R X_m(x)F(x)dx}{N} \tag{3A-18}$$

Hence, a complete solution for the temperature under homogeneous boundary conditions combines the time solution $\Gamma(t)$, with the space solution $X(x)$, having found the arbitrary constant values represented by c_m by making use of the initial condition, and where B and C can be determined using the boundary conditions, to give:

$$T(x,t) = \sum_{m=1}^{\infty} \frac{e^{-\alpha\beta_m^2 t}}{N} X_m(x) \cdot \int_R X_m(x')F(x')dx' \tag{3A-19}$$

For simplicity, the eigenfunctions are often adjusted so that N in equation (3A-19) becomes unity. In this case, this is done by defining a normalised eigenfunction known as the kernel, $K(\beta_m,x)$ such that:

$$K(\beta_m,x) \equiv \frac{X_m(x)}{\sqrt{N}} \tag{3A-20}$$

Using this kernel, the solution equation (3A-19) then becomes:

$$T(x,t) = \sum_{m=1}^{\infty} e^{-\alpha\beta_m^2 t} K(\beta_m,x) \cdot \int_R K(\beta_m,x')F(x')dx' \tag{3A-21}$$

Separation of variables technique works very well for homogeneous problems. However, with more complex non-homogeneous boundary conditions, this method becomes extremely tedious, if not impossible, to use. Laplace transforms are a potential solution method. They remove the time variable from the partial differential equation. Integral transforms are another possibility, and they remove the space variable. Integral transforms have the advantage of defining the transform and inversion formula at the onset of the problem, whereas the Laplace transforms can have difficulties with the inversion due to complications of the time variable [1]. According to Ozisik [1], integral transforms are a more elegant and efficient method of handling transient heat problems.

Appendix 3B

Integral Transform Method

Integral transform removes the space variable from a partial differential equation, such as that in equation (3-1). The type of integral transform used is a function of the range of the space variable: infinite, semi-infinite, or finite, as well as the specific type of boundary conditions: first, second, or third-order, which is equivalent to constant temperature, constant flux, and convection heat transfer conditions, respectively. The total solution of an integral transform is based on two parts, the transform itself and the inversion formula, which are derived from the technique of rewriting the classical expansion of a function in two parts.

The initial steps in the integral transform method mimic those of the separation of variables method, with the inclusion of the non-homogeneous heat generation term in equation (3-2) and non-zero right-hand sides of boundary conditions (3-3) and (3-4). The development of the temperature profile equations rely on the following general form of the integral transform and inversion formula, respectively:

$$\overline{T}(\beta_m, t) = \int_{x'=0}^{L} K(\beta_m, x') \cdot T(x', t) \cdot dx' \tag{3B-1}$$

$$T(x,t) = \sum_{m=1}^{\infty} K(\beta_m, x) \cdot \overline{T}(\beta_m, t) \tag{3B-2}$$

Here, $K(\beta_m, x)$ is the kernel, as defined by (3A-20) in the previous eigenvalue problem, and $\overline{T}$ denotes the integral transform of equation (3-2). Equation (3B-1) removes the partial derivative with respect to space and reduces it to an ordinary differential equation, making an analytical solution possible. By substituting the transform solution of equation (3B-1) into the inversion formula equation (3B-2), after multiplying all terms by $K(\beta_m, x)$ and integrating over the region of heat transfer, a complete solution for the specified boundary value problem is obtained.

The transform equation (3B-1) is substituted into the general heat transfer equation (3-2) to give an integral equation:

$$\int_0^L K(\beta_m,x)\frac{\partial^2 T(x,t)}{\partial x^2}dx+\frac{1}{k}\int_0^L K(\beta_m,x)g(\beta_m,t)dx=\frac{1}{\alpha}\int_0^L K(\beta_m,x)\frac{\partial T(x,t)}{\partial t}dx \qquad (3B\text{-}3)$$

Rewriting equation (3B-3) using equation (3B-1) yields:

$$\int_0^L K(\beta_m,x)\frac{\partial^2 T(x,t)}{\partial x^2}dx+\frac{1}{k}\bar{g}(x,t)=\frac{1}{\alpha}\frac{d\bar{T}(\beta_m,x)}{dt} \qquad (3B\text{-}4)$$

Green's Second Theorem, as described in Appendix 3C, is used to rewrite the first term on the left-hand side of equation (3B-4) to give:

$$\int_0^L K(\beta_m,x)\frac{\partial^2 T(x,t)}{\partial x^2}dx=-\beta_m^2\bar{T}(\beta_m,x)+\left[\left.\frac{K(\beta_m,x)}{k_1}\right|_{x=0}\cdot f_1(t)+\left.\frac{K(\beta_m,x)}{k_2}\right|_{x=L}\cdot f_2(t)\right] \qquad (3B\text{-}5)$$

This stems from the general form of Green's Second Theorem:

$$\int_R\left(K(\beta_m,x)\frac{\partial^2 T(x,t)}{\partial x^2}-T(x,t)\frac{\partial^2 K(\beta_m,x)}{\partial x^2}\right)dx=\int_S\left(K(\beta_m,x)\frac{\partial T(x,t)}{\partial x}-T(x,t)\frac{\partial K(\beta_m,x)}{\partial x}\right)dx \qquad (3B\text{-}6)$$

Since $K(\beta_m,x)$ is a function of $X(x)$ as defined by equation (3A-20), the separation equation (3A-10) is multiplied by $T(x,t)$ and rewritten, such that the second term of the left hand side of equation (3B-6) is defined by:

$$\int_R T(x,t)\frac{\partial^2 K(\beta_m,x)}{\partial x^2}dx=-\beta_m^2\int_S K(\beta_m,x)T(x,t)dx=-\beta_m^2\bar{T}(\beta_m,t) \qquad (3B\text{-}7)$$

The right hand side of equation (3B-6) is solved by using the actual boundary conditions equations (3-3) and (3-4), and the homogeneous form of the eigenvalue boundary conditions (3A-11) and (3A-12). From equation (3A-11), it is evident that $k_i\frac{\partial K(\beta_m,x)}{\partial x}=h_i K(\beta_m,x)$, where i denotes a given surface. Multiplying this equation by $T(x,t)$, dividing both sides by

$K(\beta_m,x)$, and substituting into equation (3-3) results in $k_i\frac{\partial T(x,t)}{\partial x}+\frac{k_i T(x,t)}{K(\beta_m,x)}\frac{\partial K(\beta_m,x)}{\partial x}=f_i(t)$, where $f_i(t)=h_i T_{\infty i}(t)$. Manipulating this equation, the right hand side of equation (3B-6) becomes:

$$\left(K(\beta_m,x)\frac{\partial T(x,t)}{\partial x}-T(x,t)\frac{\partial K(\beta_m,x)}{\partial x}\right)=\frac{K(\beta_m,x)}{k_i}f_i(t) \qquad \text{(3B-8)}$$

Substituting equations (3B-7) and (3B-8), which must be summed over all surfaces, into equation (3B-6) produces equation (3B-5). In order to obtain a final transformed solution, equation (3B-5) is substituted into equation (3B-4), all integrals are removed, and the transformed solution becomes:

$$\frac{d\bar{T}(\beta_m,t)}{dt}+\alpha\beta_m^2\bar{T}(\beta_m,t)=A(\beta_m,t) \qquad \text{(3B-9)}$$

where,

$$A(\beta_m,t)=\frac{\alpha}{k}\bar{g}(\beta_m,t)+\alpha\left[\left.\frac{K(\beta_m,x)}{k_1}\right|_{x=0}\cdot f_1(t)+\left.\frac{K(\beta_m,x)}{k_2}\right|_{x=L}\cdot f_2(t)\right] \qquad \text{(3B-10)}$$

The initial conditions must also be transformed to fit the new problem given by equation (3B-9). Using the transform equation (3B-1) on equation (3-5), in combination with the definition of $F(x)$ given by equation (3A-14), the transformed initial condition is:

$$\bar{T}(\beta_m,0)=\int_{x'=0}^{L}K(\beta_m,x')F(x')\equiv\bar{F}(\beta_m) \qquad \text{(3B-11)}$$

Because equation (3B-9) is now an ordinary linear differential equation, and knowing the corresponding initial condition equation (3B-11), a standard solution [91] can be written as:

$$\bar{T}(\beta_m,t)=e^{-\alpha\beta_m^2 t}\left[\bar{F}(\beta_m)+\int_{t'=0}^{t}e^{\alpha\beta_m^2 t'}A(\beta_m,t')dt'\right] \qquad \text{(3B-12)}$$

The explanation behind the standard form of solution is derived in Appendix 3G. Substituting this transformed integral equation (3B-12) into the inversion formula (3B-2), a general solution to the heat conduction problem becomes:

$$T(x,t) = \sum_{m=1}^{\infty} e^{-\alpha\beta_m^2 t} K(\beta_m, x) \left[\overline{F}(\beta_m) + \int_{t'=0}^{t} e^{\alpha\beta_m^2 t'} A(\beta_m, t') dt' \right] \tag{3B-13}$$

In (3B-13) the coefficient $K(\beta_m,x)$ is determined in accordance with the desired boundary conditions, and $A(\beta_m t)$ and $\overline{F}(\beta_m)$ are given by equations (3B-10) and (3B-11), respectively. Ozisik [1] provides a table containing calculated $K(\beta_m,x)$ values for the nine potential combinations of first-, second-, and third-order boundary conditions. The first order boundary conditions, or Dirichlet problems, involve a prescribed temperature at the boundary. Second order boundary conditions, or Neumann problems, contain a first order directional derivative, i.e. $\partial T/\partial x$, a flux condition at the boundary, and third order, or mixed problems, are a combination of the two, such as convection conditions. In order to avoid difficulties within equation (3B-10), Ozisik [1] suggests that for first order conditions at a particular boundary surface, the following substitution can be made:

$$\left.\frac{K(\beta_m,x)}{k}\right|_{x=boundary} = \frac{1}{h}\left.\frac{dK(\beta_m,x)}{dx}\right|_{x=boundary} \tag{3B-14}$$

The applicability of these equations is restricted to linear boundary conditions. First, second, and third-order boundary conditions are examined, with prescribed temperature, constant flux, and convection to the environment corresponding to first, second and third, respectively.

Appendix 3C

Green's Theorem

All development stated herein is based on work in Kreyszig [91]. Green's Theorem is based on the idea that a volume integral can be represented by a surface integral by applying the divergence theorem to a harmonic function. Before delving into the explanation of this specific theorem, it is useful to first describe the physical interpretation of using a vector to represent the movement of heat through a given volume with respect to time. A vector is a directed line segment in a given co-ordinate system, say Cartesian. This vector $v(x,y,z)$, can be written in terms of its components in each direction in the co-ordinate system in terms of unit vectors i, j, and k on the x, y, and z axes, respectively:

$$v(x,y,z) = \upsilon_1(x,y,z)i + \upsilon_2(x,z,y)j + \upsilon_3(x,y,z)k \tag{3C-1}$$

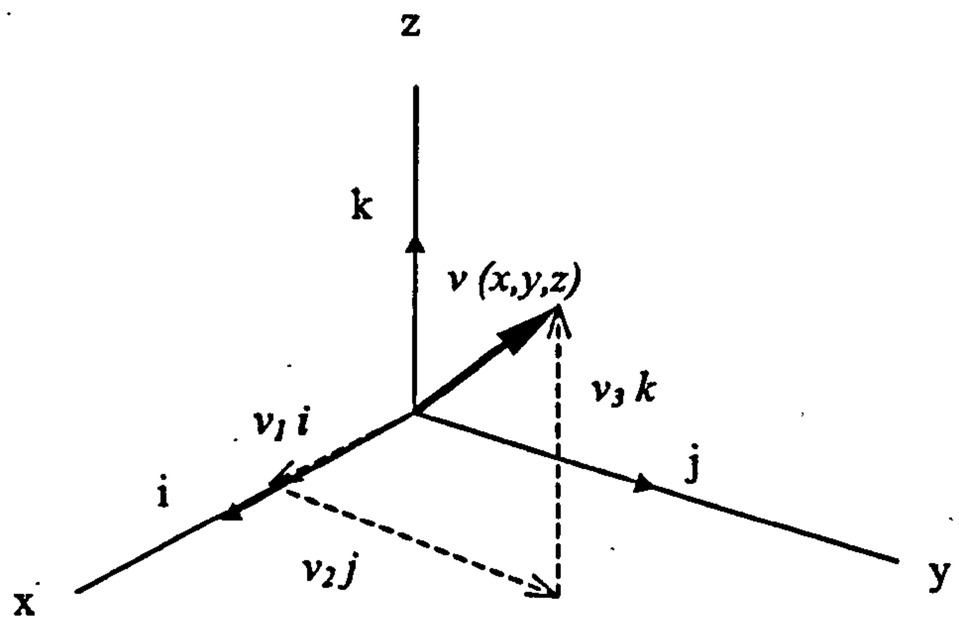

Figure 3C.1. Vector definition.

If a scalar function exists that can be represented by f, a directional derivative of this function can be used to describe the rate of change in a given direction for the function. A scalar function is dependent only on points in space, not on the particular co-ordinate system used. The directional derivative, also known as the gradient, allows a bridge between scalar and vector quantities. Representing the scalar function as $f(x,y,z)$ in the Cartesian system, a change in the function in any direction can be described by a combination of first-order partial derivatives multiplied by the unit vectors of the given co-ordinate system. This representation is known as the gradient of the scalar function, f, and is mathematically described by:

$$grad\ f = \nabla f = \frac{\partial f}{\partial x} i + \frac{\partial f}{\partial y} j + \frac{\partial f}{\partial z} k \tag{3C-2}$$

The gradient is an important tool in heat transfer because it allows temperature, a scalar quantity, to be represented in vector form for temperature variation throughout a body. The gradient can also be used to represent differentiation of the scalar function f, with respect to the outwards normal, n, of a given surface, as seen in:

$$\frac{df}{dn} = n \cdot grad\ f \tag{3C-3}$$

Another important function is divergence. Divergence describes the manner in which a vector field, given by the components v_1, v_2, and v_3 of $v(x,y,z)$, deviates from the Cartesian system. Partial derivatives of each of the components, in their respective directions, are used to describe the divergence of the vector field defined by v:

$$div\ v = \frac{\partial v_1}{\partial x} + \frac{\partial v_2}{\partial y} + \frac{\partial v_3}{\partial z} \tag{3C-4}$$

Since its value is not aligned with the particular co-ordinate system, divergence is a scalar function, whereas gradient is a vector quantity. Taking the divergence of a vector given by *grad f*, results in second-order partial derivatives, also known as the Laplacian operator, ∇^2:

$$div(grad\ f) = \nabla^2 f = \frac{\partial^2 f}{\partial x^2} + \frac{\partial^2 f}{\partial y^2} + \frac{\partial^2 f}{\partial z^2} \tag{3C-5}$$

Divergence provides a powerful method of equating surface and volume integrals, as described by the Divergence Theorem of Gauss:

$$\iiint_R div\ v \cdot dV = \iint_S v \cdot n \cdot dA \tag{3C-6}$$

In equation (3C-6), v is a vector in a 3D region R and n is the outward normal unit vector to surface S. By substituting equations (3C-4) and (3C-5) into equation (3C-6), and assuming that v is the gradient of some scalar function f, the equation can also be written as:

$$\iiint_R \nabla^2 f \cdot dV = \iint_S \frac{\partial f}{\partial n} \cdot dA \tag{3C-7}$$

Green describes two scalar functions, f and g such that $F = f\ grad\ g$. Using the divergence theorem:

$$div\ F = div\ (f\ grad\ g) = f\nabla^2 g + \nabla f \cdot \nabla g \tag{3C-8}$$

Using inner dot product, $F \cdot n = (f\nabla g) \cdot n = f(n \cdot \nabla g)$ and equation (3C-4), equation (3C-8) can be written in the form of the divergence theorem:

$$\iiint_R (f\nabla^2 g + grad\ f \cdot grad\ g) \cdot dV = \iint_S f \frac{\partial g}{\partial n} \cdot dA \tag{3C-9}$$

This is Green's first formula. Interchanging f and g gives a similar formula. Subtracting this formula from equation (3C-9), results in Green's second formula:

$$\iiint_R (f\nabla^2 g - g\nabla^2 f) \cdot dV = \iint_S \left(f \frac{\partial g}{\partial n} - g \frac{\partial f}{\partial n} \right) \cdot dA \tag{3C-10}$$

It is Green's second formula that is so useful in the integral transform technique.

Appendix 3D

Example of Fortran Program used for Single Layer (Integral Transform) Calculation with Combined Convection and Radiation Boundary Conditions

```
CCCCCCCCCCCCCCCCCCCCCCCCCCCCCCCCCCCCCCCCCCC
C
C SOLVES THE EIGENVALUES (BETA)
C
C VARIABLE DECLARATION
C
      real*8 L,k,betam,s,C
      integer p
      pi=4.0*atan(1.0)
      k=0.81
      hc=5
      a=.454e-7
      H1=(8+4*a*Ta1**3)/k
      H2=(2+4*a*Ta2**3)/k
      L=0.012
      alpha=6.16e-7
      time=3600
      To=288.
      Ta1=312
      Ta2=312
      B1=H1*L
      B2=H2*L
C
C
C LOOP FOR EACH BETA
C
      x=0.0048
      dx=0.0024
C LOOP FOR EACH POSITION X THRU THICK
C     do n=1,6
```

```
      T=0.
      s=0.38
C LOOP FOR SERIES
      do m=1,100
 101    C=s-(cos(s)/sin(s)-1/(B1+B2)*(s-B1*B2/s))/
     .  (-1-cos(s)**2/sin(s)**2-1/(B1+B2)-B1*B2/((B1+B2)*s**2))
C       write(6,*)C,abs(C-s)
        if(abs(C-s).lt.1e-14) then
C         write(6,*)C,abs(C-s)
          goto 111
        else
          s=C
C         write(6,*)s
          goto 101
        end if
C
 111    betam=C/L
        T=T+
     .  2/((betam**2+H1**2)*(L+(H2/(betam**2+H2**2)))+H1)*
     .  (betam*cos(betam*x)+H1*sin(betam*x))*
     .  (To*(sin(betam*L)-H1/betam*cos(betam*L)+H1/betam)*
     .  exp(-alpha*betam**2*time)+
     .  (1-exp(-alpha*betam**2*time))*
     .  (H1/betam+
     .  (H2/betam**2*
     .  (betam*cos(betam*L)+H1*sin(betam*L)))))
C
        if(m.eq.1) then
          s=C+2.8
        else
          s=C+pi
        end if
        write(6,*)T,s
        print*
      end do
C     x=x+dx
```

```
      write(6,*)T
C     end do
C     close(20)
C     close(21)
C
C END OF PROGRAM
      end
```

Appendix 3E

Example of Homogenisation of Boundary Conditions

A convection boundary condition existing at an external surface can be normalised as follows:

Boundary Condition

$$-k_1\frac{\partial T_1(x,t)}{\partial x}+h_1T_1(x,t)=h_1T_{\infty 1}(t) \tag{3E-1}$$

Normalisation Equation

$$\theta_i(x,t)=T_i(x,t)-q_i(x,t) \tag{3E-2}$$

$$q_1(x,t)=\frac{(x_2-x)^2h_1T_{\infty 1}(t)}{(x_2-x_1)(h_1x_2-h_1x_1+2k_1)} \text{ at surface } x=x_1 \tag{3E-3}$$

Procedure

Substituting the normalised equation into the boundary condition gives:

$$-k_1\frac{\partial}{\partial x}(\theta_1-q_1)+h_1[(\theta_1-q_1)-T_{\infty 1}]=0 \tag{3E-4}$$

Substituting for q:

$$k_1\left[\frac{\partial\theta_1}{\partial x}-\frac{2(x_2-x_1)h_1T_{\infty 1}}{(x_2-x_1)(h_1x_2-h_1x_1+2k_1)}\right]=h_1\left[\theta_1+\frac{(x_2-x_1)^2h_1T_{\infty 1}}{(x_2-x_1)(h_1x_2-h_1x_1+2k_1)}-T_{\infty 1}\right] \tag{3E-5}$$

Creating a common denominator and grouping like terms results in:

$$k_1\frac{\partial\theta_1}{\partial x}=h_1\theta_1+\frac{(x_2-x_1)h_1^2T_{\infty 1}-(h_1x_2-h_1x_1+2k_1)h_1T_{\infty 1}+2k_1h_1T_{\infty 1}}{(h_1x_2-h_1x_1+2k_1)} \tag{3E-6}$$

All parts of the right-most term cancel, leaving the desired normalised boundary condition:

$$k_1 \frac{\partial \theta_1}{\partial x} = h_1 \theta_1 \qquad \text{(3E-7)}$$

The internal boundary conditions are more straight forward, since at every internal surface $q_i(x,t)$ is zero, making the normalisation of these boundary conditions apparent.

$$
\begin{bmatrix}
h_1\cos\left(\frac{\beta_m x_1}{\sqrt{\alpha_1}}\right)+\frac{k_1\beta_m}{\sqrt{\alpha_1}}\sin\left(\frac{\beta_m x_1}{\sqrt{\alpha_1}}\right) & h_1\sin\left(\frac{\beta_m x_1}{\sqrt{\alpha_1}}\right)-\frac{k_1\beta_m}{\sqrt{\alpha_1}}\cos\left(\frac{\beta_m x_1}{\sqrt{\alpha_1}}\right) & 0 & 0 & 0 & 0 \\
\cos\left(\frac{\beta_m x_2}{\sqrt{\alpha_1}}\right) & \sin\left(\frac{\beta_m x_2}{\sqrt{\alpha_1}}\right) & -\cos\left(\frac{\beta_m x_2}{\sqrt{\alpha_2}}\right) & -\sin\left(\frac{\beta_m x_2}{\sqrt{\alpha_2}}\right) & 0 & 0 \\
-\frac{k_1\beta_m}{\sqrt{\alpha_1}}\sin\left(\frac{\beta_m x_2}{\sqrt{\alpha_1}}\right) & \frac{k_1\beta_m}{\sqrt{\alpha_1}}\cos\left(\frac{\beta_m x_2}{\sqrt{\alpha_1}}\right) & \frac{k_2\beta_m}{\sqrt{\alpha_2}}\sin\left(\frac{\beta_m x_2}{\sqrt{\alpha_2}}\right) & -\frac{k_2\beta_m}{\sqrt{\alpha_2}}\cos\left(\frac{\beta_m x_2}{\sqrt{\alpha_2}}\right) & 0 & 0 \\
0 & 0 & \cos\left(\frac{\beta_m x_3}{\sqrt{\alpha_2}}\right) & \sin\left(\frac{\beta_m x_3}{\sqrt{\alpha_2}}\right) & -\cos\left(\frac{\beta_m x_3}{\sqrt{\alpha_3}}\right) & -\sin\left(\frac{\beta_m x_3}{\sqrt{\alpha_3}}\right) \\
0 & 0 & -\frac{k_2\beta_m}{\sqrt{\alpha_2}}\sin\left(\frac{\beta_m x_3}{\sqrt{\alpha_2}}\right) & \frac{k_2\beta_m}{\sqrt{\alpha_2}}\cos\left(\frac{\beta_m x_3}{\sqrt{\alpha_2}}\right) & \frac{k_3\beta_m}{\sqrt{\alpha_3}}\sin\left(\frac{\beta_m x_3}{\sqrt{\alpha_3}}\right) & -\frac{k_3\beta_m}{\sqrt{\alpha_3}}\cos\left(\frac{\beta_m x_3}{\sqrt{\alpha_3}}\right) \\
0 & 0 & 0 & 0 & h_3\cos\left(\frac{\beta_m x_4}{\sqrt{\alpha_3}}\right)-\frac{k_3\beta_m}{\sqrt{\alpha_3}}\sin\left(\frac{\beta_m x_4}{\sqrt{\alpha_3}}\right) & h_3\sin\left(\frac{\beta_m x_3}{\sqrt{\alpha_3}}\right)+\frac{k_3\beta_m}{\sqrt{\alpha_3}}\cos\left(\frac{\beta_m x_3}{\sqrt{\alpha_3}}\right)
\end{bmatrix}
\begin{bmatrix} C_1 \\ D_1 \\ C_2 \\ D_2 \\ C_3 \\ D_3 \end{bmatrix}
= [0]
$$

Matrix form of boundary conditions for 3-layer slab with convection at both external surfaces.

Appendix 3G

Solution of Linear Differential Equations

The most general form of a first order linear differential equation is:

$$T' + p(t)T = r(t) \tag{3G-1}$$

If *r(t)* is zero, then becomes a homogeneous equation and can be solved effectively by separating the variables. When *r(t)* has a value, in other words, it is a non-homogeneous problem, the use of an integrating factor and exactness conditions are required before a separation of variables can occur. Here *T'* denotes differentiation with respect to *t*.

Homogeneous Problem

$$T' + p(t)T = 0 = \frac{d}{dt}(T) + p(t)T \tag{3G-2}$$

$$\frac{dT}{T} = -p(t)dt \Rightarrow \ln|T| = \int p(t)dt + c^* \tag{3G-3}$$

$$T(t) = ce^{-\int p(t)dt} \qquad \text{where } c = \pm e^{c^*} \tag{3G-4}$$

Non-homogeneous Problem

$$\frac{dT}{dt} + p(t)T = r(t) \Rightarrow dT + \big(p(t)T - r(t)\big)dt = 0 \tag{3G-5}$$

Let $P = p(t)T\text{-}r(t)$ and $Q = 1$ such that $QdT + Pdt = 0$. Then by using an integrating factor, F, define $FQdT + FPdt = 0$. By the condition of exactness, $\frac{\partial M}{\partial x} = \frac{\partial N}{\partial y}$, where in this case this implies:

$$\frac{\partial}{\partial T}(FP) = -\frac{\partial}{\partial t}(FQ) \tag{3G-6}$$

Assuming that F depends on only one variable, say t, equation (3G-6) can be rewritten as $F\frac{\partial P}{\partial T} = \frac{\partial F}{\partial t}Q + F\frac{\partial Q}{dt}$ and dividing by FQ gives:

$$\frac{1}{F}\frac{\partial F}{\partial t} = -\frac{1}{Q}\left(\frac{\partial P}{\partial T} - \frac{\partial Q}{dt}\right) \qquad \text{(3G-7)}$$

Evaluating the right hand side of equation (3G-7), according to the definitions of P and Q, proves that $\frac{1}{F}\frac{\partial F}{\partial t} = p(t)$. Thus, a separation of variables solution can now be obtained:

$$\frac{dF}{F} = -p(t)dt \Rightarrow \ln|F| = \int p(t)dt \Rightarrow F(t) = e^{h(t)} \text{ where } h(t) = \int p(t)dt \qquad \text{(3G-8)}$$

This implies that $h(t)'=p(t)$. Multiplying equation (3G-1) by $F=e^{h(t)}$ gives:

$$e^{h(t)}(T' + h(t)'T) = e^{h(t)}r(t) \qquad \text{(3G-9)}$$

Expanding the first term according to the product rule, $e^{h(t)}\cdot T' = (e^{h(t)}T)' = e^{h(t)}T' + e^{h(t)}h(t)'T$, which gives $(e^{h(t)}T)' = e^{h(t)}r(t)$ when compared with (3G-9). Integrating this equation, $e^{h(t)}T = \int e^{h(t)}r(t)dt + c$, and dividing both sides by $e^{h(t)}$ produces the desired solution:

$$T(t) = e^{-h(t)}\left[\int e^{h(t)}r(t)dt + c\right] \text{ where } h(t) = \int p(t)dt \qquad \text{(3G-10)}$$

Appendix 3H

Example of Fortran Program used in Multi-Layer Calculation (Separation of Variables) with Convection Boundary Conditions and Transient Sink Temperatures

```
CCCCCCCCCCCCCCCCCCCCCCCCCCCCCCCCCCCCCCCCCC
C
C SOLVES THE EIGENVALUES (BETA)
C
C VARIABLE DECLARATION
C
      real betam,s,s1,so1,s2,so,Cfin,Clast
      real L,z1,z2,z3,p,To1,To2,To3,t,to
      real h1,h3,alpha1,alpha2,alpha3
      real x1,x2,x3,x4,y,Cs
      real part1,part2,part3,part4,part5,part6
      real c1,c2,c3,d1,d2,d3,xx1,xx2,xx3
      real intX1,intX2,intX3,intX
      real intXsq1,intXsq1c,intXsq1cd,intXsq1d
      real intXsq2,intXsq2c,intXsq2cd,intXsq2d
      real intXsq3,intXsq3c,intXsq3cd,intXsq3d
      real intXXsq1c,intXXsq1d,intXXsq3c,intXXsq3d
      real intXXsq1,intXXsq3,intXXsq,vntop1a,vntop2a
      real Norm1,Norm2,Norm,fntop1a,fntop1b,fntop1,fntop2,fn
      real vntop1,vntop2,vn,vnpoly1,vnpoly2,vnpoly1a,vnpoly1b
      real intop1,intop2,in,inpoly1,inpoly2,inpoly1a,inpoly1b
      real intop3,inpoly3,fntop3,vntop3,vnpoly3,Norm3
      real inpoly1ba,inpoly1bb
      real t4e,t3e,t2e,t1e,t0e
      real aa1,bb1,cc1,dd1,ee1,ff1,Tsink1,Tsink1o
      real aa2,bb2,cc2,dd2,ee2,ff2,Tsink2,Tsink2o
      real Theta1a,Theta2a,Theta3a,Theta1,Theta2,Theta3
      real xpos1,xpos2,xpos3,q1,q2,q3,T1,T2,T3
      integer i,j,ifail,n,k,q
      integer aamax,ia,np,nmax
```

```
      parameter (np=12)
      parameter (nt=1)
      parameter (n=6)
      integer nin,nout
      parameter (nin=5,nout=6)
C
      real det,det1,det2
      dimension b(np,np),b1(np,np),b2(np,np),indx(np)
      dimension a(np,np),a1(np,np),a2(np,np),ab(np,np)
      dimension bfin(np,np),cd(n)
C
      pi=4.0*atan(1.0)
C MATERIAL PROPERTIES
      z1=164.
      z2=0.81
      z3=164.
      h1=8.
      h3=2.
      alpha1=6.66e-5
      alpha2=6.16e-7
      alpha3=6.66e-5
      x1=0.003
      x2=0.009
      x3=0.015
      x4=0.018
C Tsink POLYNOMIALS(1=air T's, 2=internal T's)
      aa1=5.89924952e-17
      bb1=-7.39323069e-12
      cc1=2.3621898e-7
      dd1=-7.35621475e-4
      ee1=16.2249722
C
      aa2=8.49528667e-17
      bb2=-1.2717039e-11
      cc2=4.3674752e-7
      dd2=-1.3199566e-3
```

```
      ee2=16.3859082
C
C INITAL CONDITIONS
      To1=15.
      To2=15.
      To3=15.
C TIME
      t=3600.
      to=0.
C Tsink1
      Tsink1=aa1*t**4+bb1*t**3+cc1*t**2+dd1*t+ee1
      Tsink1o=ee1
C Tsink2
      Tsink2=aa2*t**4+bb2*t**3+cc2*t**2+dd2*t+ee2
      Tsink2o=ee2
C
C POSITIONS THROUGH x WHERE TEMPERATURES ARE DESIRED
C (x1<=xpos1<=x2 & x2<=xpos2<=x3)
      xpos1=x1
      xpos2=x2
      xpos3=x3
C
C LOOP FOR EACH BETA
      T1=0.
      T2=0.
      s=.05
      so=s
      s1=0.
      s2=0.
      q=0.
      p=0.
C LOOP FOR SERIES
      do m=1,3
C CHOOSES AN ORIGINAL VALUE OF BETAM(s) THEN BOUNDS IT TO FIND
MAX/MIN VALUES
 91   if(m.eq.1) then
```

```
          y=0.04
        else y=0.05
          end if
          s1=s-y
          s2=s+y
C
 101        q=q+1
          write(6,*)'s1,s2 ',s1,s2
          betam=s1
          call MATRIX(betam,z1,z2,z3,alpha3,h1,h3,alpha1,alpha2,
     .    x1,x2,x3,x4,np,a1)
C WRITES ALL VALUES IN MATRIX A1 TO A SEPARATE, DESTROYABLE MATRIX
B1
          do j=1,n
          do i=1,n
           b1(i,j)=a1(i,j)
          enddo
          enddo
          call LUDCMP(b1,n,np,indx,det1)
          do j=1,n
            det1=det1*b1(j,j)
          end do
C
          betam=s2
          call MATRIX(betam,z1,z2,z3,alpha3,h1,h3,alpha1,alpha2,
     .    x1,x2,x3,x4,np,a2)
          do j=1,n
          do i=1,n
           b2(i,j)=a2(i,j)
          enddo
          enddo
          call LUDCMP(b2,n,np,indx,det2)
          do j=1,n
            det2=det2*b2(j,j)
          end do
C
```

```
C CHECKS IF BOTH VALUES OF THE DETERMINANT ARE +'VE or -'VE, MEANING
PROBLEM
C NOT BOUNDED, THEN TAKES NEW BETA VALUES AND TRIES AGAIN TO FIND
BOUNDS
      if(q.eq.1) then
        if(det1.lt.0 .and. det2.lt.0) then
          s=s-0.00005
C           write(6,*)'betam too low s=',s
          goto 121
        end if
        if(det1.gt.0 .and. det2.gt.0) then
          s=s+0.00005
C           write(6,*)'betam too high s=',s
          goto 121
        end if
      end if
C IF THE ONE OF THE DETERMINANTS IS CLOSE ENOUGH TO ZERO (IE. 1), THAT IS
THE
C DESIRED BETA VALUE, IF NOT, THE BOUNDING REGION IS DIVIDED IN HALF
      if(abs(det1).lt.1.e-1) then
        Cfin=s1
        goto 111
      else if(abs(det2).lt.1.e-1) then
        Cfin=s2
        goto 111
C SECOND DETERMINANT IS -'VE, THEN BETA1 BECOMES THE HIGH VALUE
(BETA2),
C BETA2 MOVES DOWN TO THE MIDDLE VALUE (BETAo), AND BETAo HOLDS THE
OLD BETA1
        else if(det2.lt.0) then
          so1=s1
          s1=s2
          s2=so
          so=so1
        write(6,*)'det<0 ',s1,s2
        goto 101
```

```
C SECOND DETERMINANT IS +'VE, THEN BETA1 REMAINS AT THE LOWEST VALUE,
BETA2,
C MOVES DOWN TO BECOME THE NEW HALF POINT, AND BETAo HOLDS THE OLD
BETA2
                else
                 s1=s1
                 so=s2
                 s2=(s1+s2)/2
                 goto 101
C               end if
C            end if
        end if
C
 121  q=0
      write(6,*)'m= ',m
      goto 91
C CHECKS IF THE NEW BETA VALUE IS SAME AS OLD VALUE, IF YES, THEN START
POINT
C so IS INCREASED
 111    Cs=Cfin-Clast
        if(abs(Cs).lt.5.0e-3) then
          p=p+0.05
          s=s+p
          so=s
          write(6,*)'s,p ',s,p
          q=0
C           pause
          goto 91
        else
          betam=Cfin
          write(6,*)'betam ',betam
          write(6,*)'m ',m
          print*
C
C BOUNDARY CONDITION CONSTANTS
        call MATRIX(betam,z1,z2,z3,alpha3,h1,h3,alpha1,alpha2,
```

```
     x1,x2,x3,x4,np,ab)
     part1=ab(2,1)-ab(3,1)-ab(2,2)*ab(1,1)/ab(1,2)+
     ab(3,2)*ab(1,1)/ab(1,2)-(ab(2,4)-ab(3,4))*
     (ab(2,1)-ab(3,1)-ab(2,2)*ab(1,1)/ab(1,2)+
     ab(3,2)*ab(1,1)/ab(1,2))/
     (ab(2,4)-ab(3,4)-ab(4,4)+ab(5,4))
     part2a=(ab(2,3)-ab(3,3))
     part2b=
     (ab(2,4)-ab(3,4))*
     (ab(4,3)-ab(5,3)-ab(2,3)+ab(3,3))/
     (ab(2,4)-ab(3,4)-ab(4,4)+ab(5,4))
     part2=part2a+part2b
     write(6,*)'part2',part2a,part2b,part2
     part3=(ab(2,4)-ab(3,4))*(ab(4,5)-ab(5,5)-
     ab(4,6)*ab(6,5)/ab(6,6)+ab(5,6)*ab(6,5)/ab(6,6))/
     (ab(2,4)-ab(3,4)-ab(4,4)+ab(5,4))
     part4a=ab(4,3)-ab(5,3)
     part4b=
     (ab(4,4)-ab(5,4))*
     (ab(4,3)-ab(5,3)-ab(2,3)+ab(3,3))/
     (ab(2,4)-ab(3,4)-ab(4,4)+ab(5,4))
     part4=part4a+part4b
     write(6,*)'part4',part4a,part4b,part4
     part5=(ab(4,4)-ab(5,4))*(ab(2,1)-ab(3,1)-
     ab(2,2)*ab(1,1)/ab(1,2)+ab(3,2)*ab(1,1)/ab(1,2))/
     (ab(2,4)-ab(3,4)-ab(4,4)+ab(5,4))
     part6=ab(4,5)-ab(5,5)-ab(4,6)*ab(6,5)/ab(6,6)+
     ab(5,6)*ab(6,5)/ab(6,6)+(ab(4,4)-ab(5,4))*
     (ab(4,5)-ab(5,5)-ab(4,6)*ab(6,5)/ab(6,6)+
     ab(5,6)*ab(6,5)/ab(6,6))/
     (ab(2,4)-ab(3,4)-ab(4,4)+ab(5,4))
C
     c1=1.
     d1=-c1*ab(1,1)/ab(1,2)
     c3=c1*(part1+part5+(part2*(-part5-part1)-
     part4*(-part5-part1))/(part2-part4))/
```

```
     .   (part6-part3+(part4*(part6-part3)-
     .   part2*(part6-part3))/(part2-part4))
         d3=-c3*ab(6,5)/ab(6,6)
         c2=((-part5-part1)*c1+(part6-part3)*c3)/(part2-part4)
         d2=c2*((ab(4,3)-ab(5,3)-ab(2,3)+ab(3,3))+
     .   c3*(ab(4,5)-ab(5,5)-ab(4,6)*ab(6,5)/ab(6,6)+
     .   ab(5,6)*ab(6,5)/ab(6,6))-
     .   c1*(ab(2,1)-ab(3,1)-ab(2,2)*ab(1,1)/ab(1,2)+
     .   ab(3,2)*ab(1,1)/ab(1,2)))/
     .   (ab(2,4)-ab(3,4)-ab(4,4)+ab(5,4))
         write(6,*)'c1,d1,c2,d2,c3,d3',c1,d1,c2,d2,c3,d3
         print*
C
C INTEGRAL OF X
         intX1=sqrt(alpha1)/(betam*1.)*
     .   (c1*(sin(betam*x2/sqrt(alpha1))-
     .   sin(betam*x1/sqrt(alpha1)))-
     .   d1*(cos(betam*x2/sqrt(alpha1))-
     .   cos(betam*x1/sqrt(alpha1))))
         intX2=sqrt(alpha2)/(betam*1.)*
     .   (c2*(sin(betam*x3/sqrt(alpha2))-
     .   sin(betam*x2/sqrt(alpha2)))-
     .   d2*(cos(betam*x3/sqrt(alpha2))-
     .   cos(betam*x2/sqrt(alpha2))))
         intX3=sqrt(alpha3)/(betam*1.)*
     .   (c3*(sin(betam*x4/sqrt(alpha3))-
     .   sin(betam*x3/sqrt(alpha3)))-
     .   d3*(cos(betam*x4/sqrt(alpha3))-
     .   cos(betam*x3/sqrt(alpha3))))
C
C INTEGRAL OF X^2
         intXsq1c=c1**2*((x2-x1)/2+sqrt(alpha1)/(4*betam*1.)*
     .   (sin(2*betam*x2/sqrt(alpha1))-
     .   sin(2*betam*x1/sqrt(alpha1))))
         intXsq1cd=2*c1*d1*sqrt(alpha1)/(4*betam*1.)*
     .   (cos(2*betam*x1/sqrt(alpha1))-
```

```
     .   cos(2*betam*x2/sqrt(alpha1)))
         intXsq1d=d1**2*((x2-x1)/2+sqrt(alpha1)/(4*betam*1.)*
     .   (sin(2*betam*x1/sqrt(alpha1))-
     .   sin(2*betam*x2/sqrt(alpha1))))
         intXsq1=intXsq1c+intXsq1cd+intXsq1d
C
         intXsq2c=c2**2*((x3-x2)/2+sqrt(alpha2)/(4*betam*1.)*
     .   (sin(2*betam*x3/sqrt(alpha2))-
     .   sin(2*betam*x2/sqrt(alpha2))))
         intXsq2cd=2*c2*d2*sqrt(alpha2)/(4*betam*1.)*
     .   (cos(2*betam*x2/sqrt(alpha2))-
     .   cos(2*betam*x3/sqrt(alpha2)))
         intXsq2d=d2**2*((x3-x2)/2+sqrt(alpha2)/(4*betam*1.)*
     .   (sin(2*betam*x2/sqrt(alpha2))-
     .   sin(2*betam*x3/sqrt(alpha2))))
         intXsq2=intXsq2c+intXsq2cd+intXsq2d
         write(6,*)'intXsq',intXsq2
C
         intXsq3c=c3**2*((x4-x3)/2+sqrt(alpha3)/(4*betam*1.)*
     .   (sin(2*betam*x4/sqrt(alpha3))-
     .   sin(2*betam*x3/sqrt(alpha3))))
         intXsq3cd=2*c3*d3*sqrt(alpha3)/(4*betam*1.)*
     .   (cos(2*betam*x3/sqrt(alpha3))-
     .   cos(2*betam*x4/sqrt(alpha3)))
         intXsq3d=d3**2*((x4-x3)/2+sqrt(alpha3)/(4*betam*1.)*
     .   (sin(2*betam*x3/sqrt(alpha3))-
     .   sin(2*betam*x4/sqrt(alpha3))))
         intXsq3=intXsq3c+intXsq3cd+intXsq3d
C
C
C INTEGRAL OF (x - xi)^2 * X
         intXXsq1c=-c1*sqrt(alpha1)/(betam*1.)*
     .   (-1*(x2-x1)**2*sin(betam*x1/sqrt(alpha1))-
     .   2*(x1-x2)*sqrt(alpha1)/(betam*1.)*
     .   cos(betam*x1/sqrt(alpha1))-
     .   2*alpha1/(betam*1.)**2*
```

```
     .    (sin(betam*x2/sqrt(alpha1))-sin(betam*x1/sqrt(alpha1))))
          intXXsq1d=-d1*sqrt(alpha1)/(betam*1.)*
     .    ((x2-x1)**2*cos(betam*x1/sqrt(alpha1))-
     .    2*(x1-x2)*sqrt(alpha1)/(betam*1.)*
     .    sin(betam*x1/sqrt(alpha1))+
     .    2*alpha1/(betam*1.)**2*
     .    (cos(betam*x2/sqrt(alpha1))-cos(betam*x1/sqrt(alpha1))))
C         write(6,*)intXXsq1c,intXXsq1d
          intXXsq1=intXXsq1c+intXXsq1d
C
          intXXsq3c=-c3*sqrt(alpha3)/(betam*1.)*
     .    ((x4-x3)**2*sin(betam*x4/sqrt(alpha3))+
     .    2*(x4-x3)*sqrt(alpha3)/(betam*1.)*
     .    cos(betam*x4/sqrt(alpha3))-
     .    2*alpha3/(betam*1.)**2*
     .    (sin(betam*x4/sqrt(alpha3))-sin(betam*x3/sqrt(alpha3))))
          intXXsq3d=-d3*sqrt(alpha3)/(betam*1.)*
     .    (-1*(x4-x3)**2*cos(betam*x4/sqrt(alpha3))+
     .    2*(x4-x3)*sqrt(alpha3)/(betam*1.)*
     .    sin(betam*x4/sqrt(alpha3))+
     .    2*alpha3/(betam*1.)**2*
     .    (cos(betam*x4/sqrt(alpha3))-cos(betam*x3/sqrt(alpha3))))
C         write(6,*)'betams',-betam**2,-1*betam**2
          intXXsq3=intXXsq3c+intXXsq3d
C
          t4e=1/betam**2*(t**4-4*t**3/betam**2+4*3*t**2/betam**4-
     .    4*3*2*t/betam**6+4*3*2*1/betam**8)-
     .    exp(-betam**2*t)/betam**2*(4*3*2*1/betam**8)
          t3e=1/betam**2*(t**3-3*t**2/betam**2+3*2*t/betam**4-
     .    3*2*1/betam**6)-
     .    exp(-betam**2*t)/betam**2*(-3*2*1/betam**6)
          t2e=1/betam**2*(t**2-2*t/betam**2+2/betam**4)-
     .    exp(-betam**2*t)/betam**2*(2/betam**4)
          t1e=1/betam**2*(t-1/betam**2)-
     .    exp(-betam**2*t)/betam**2*(-1/betam**2)
          t0e=1/betam**2*(1-exp(-betam**2*t))
```

```
C
C NORMAL Nn
      Norm1=z1/alpha1*intXsq1
      Norm2=z2/alpha2*intXsq2
      Norm3=z3/alpha3*intXsq3
      Norm=Norm1+Norm2+Norm3
      write(6,*)'norm',Norm1,Norm2,Norm3,Norm
C
C fn*
      fntop1=z1/alpha1*((To1*intX1)+h1*Tsink1o*intXXsq1
     .  /((x2-x1)*(h1*x2-h1*x1+2*z1)))
      fntop2=z2/alpha2*(To2*intX2)
      fntop3=z3/alpha3*((To3*intX3)+h3*Tsink3o*intXXsq3
     .  /((x4-x3)*(h3*x4-h3*x3+2*z3)))
      fn=(fntop1+fntop2+fntop3)*exp(-betam**2*t)/Norm
      write(6,*)'fn',fntop1,fntop2,fn
C
C Vn* (CONTAINS BOTH EXP TERMS)
C int{d/dt(q)* exp}  POLYNOMIAL RESULTS (fr. FINAL EXPRESSION FOR THETA)
      vnpoly1=4*aa1*t3e+3*bb1*t2e+2*cc1*t1e+dd1*t0e
C
      vnpoly3=4*aa2*t3e+3*bb2*t2e+2*cc2*t1e+dd2*t0e
C
C Vntop
      vntop1a=h1*vnpoly1*intXXsq1/
     .  ((x2-x1)*(h1*x2-h1*x1+2*z1))
      vntop1=z1*vntop1a/alpha1
      vntop2=0.
      vntop3a=h3*vnpoly3*intXXsq3/
     .  ((x4-x3)*(h3*x4-h3*x3+2*z3))
      vntop3=z3*vntop3a/alpha3
      Vn=(vntop1+vntop2+vntop3)/Norm
      write(6,*)'vn',vntop1,vntop3,vn
C
C In* (CONTAINS BOTH EXP TERMS)
C int{Tsink poly * exp} POLYNOMIAL RESULTS (fr. FINAL THETA EXPRESSION)
```

```
      inpoly1=aa1*t4e+bb1*t3e+cc1*t2e+dd1*t1e+ee1*t0e
C
      inpoly3=aa2*t4e+bb2*t3e+cc2*t2e+dd2*t1e+ee2*t0e
C
C Intop
      intop1=z1*2*h1*intX1*inpoly1/((x2-x1)*(h1*x2-h1*x1+2*z1))
      intop2=0.
      intop3=z3*2*h3*intX3*inpoly3/((x4-x3)*(h3*x4-h3*x3+2*z3))
      In=(intop1+intop2+intop3)/Norm
      write(6,*)'in',intop1,intop3,in
C
C FINAL THETA EXPRESSION
      xx1=(c1*cos(betam*xpos1/sqrt(alpha1))+
     .  d1*sin(betam*xpos1/sqrt(alpha1)))
      Theta1a=xx1*(in-vn+fn)
      xx2=(c2*cos(betam*xpos2/sqrt(alpha2))+
     .  d2*sin(betam*xpos2/sqrt(alpha2)))
      Theta2a=xx2*fn
      xx3=(c3*cos(betam*xpos3/sqrt(alpha3))+
     .  d3*sin(betam*xpos3/sqrt(alpha3)))
      Theta3a=xx3*(in-vn+fn)
C
      print*
      write(6,*)'X1,X2,X3',xx1,xx2,xx3
      write(6,*)'Theta1a,Theta2a,Theta3a',Theta1a,Theta2a,Theta3a
C SERIES SOLUTION
      Theta1=Theta1+Theta1a
      Theta2=Theta2+Theta2a
      Theta3=Theta3+Theta3a
      write(6,*)'Theta1,Theta2,Theta3',Theta1,Theta2,Theta3
       pause
       q=0
       p=0
C
       s=Cfin+0.4
       so=s
```

```
      Clast=Cfin
     end if
    end do
C ACTUAL VALUE OF TEMPERATURES (AT GIVEN x positions)
    q1=(x2-xpos1)**2*h1*Tsink1/((x2-x1)*(h1*x2-h1*x1+2*z1))
    q2=0.
    q3=(xpos3-x3)**2*h3*Tsink3/((x4-x3)*(h3*x4-h3*x3+2*z3))
    T1=Theta1+q1
    T2=Theta2+q2
    T3=Theta3+q3
    write(6,*)'q1,q2,q3',q1,q2,q3
   write(6,*)'T1,T2,T3',T1,T2,T3
C
C END OF PROGRAM
C
    end
C
    SUBROUTINE MATRIX(betam,z1,z2,z3,alpha3,h1,h3,alpha1,alpha2,
   .    x1,x2,x3,x4,np,a)
    dimension a(np,np)
      a(1,1)=h1*cos(betam*x1/sqrt(alpha1))+
   .    z1*betam/sqrt(alpha1)*sin(betam*x1/sqrt(alpha1))
      a(1,2)=h1*sin(betam*x1/sqrt(alpha1))-
   .    z1*betam/sqrt(alpha1)*cos(betam*x1/sqrt(alpha1))
      a(1,3)=0.
      a(1,4)=0.
      a(1,5)=0.
      a(1,6)=0.
      a(2,1)=cos(betam*x2/sqrt(alpha1))
      a(2,2)=sin(betam*x2/sqrt(alpha1))
      a(2,3)=-cos(betam*x2/sqrt(alpha2))
      a(2,4)=-sin(betam*x2/sqrt(alpha2))
      a(2,5)=0.
      a(2,6)=0.
      a(3,1)=-z1*betam/sqrt(alpha1)*sin(betam*x2/sqrt(alpha1))
      a(3,2)=z1*betam/sqrt(alpha1)*cos(betam*x2/sqrt(alpha1))
```

```
a(3,3)=z2*betam/sqrt(alpha2)*sin(betam*x2/sqrt(alpha2))
a(3,4)=-z2*betam/sqrt(alpha2)*cos(betam*x2/sqrt(alpha2))
a(3,5)=0.
a(3,6)=0.
a(4,1)=0.
a(4,2)=0.
a(4,3)=cos(betam*x3/sqrt(alpha2))
a(4,4)=sin(betam*x3/sqrt(alpha2))
a(4,5)=-cos(betam*x3/sqrt(alpha3))
a(4,6)=-sin(betam*x3/sqrt(alpha3))
a(5,1)=0.
a(5,2)=0.
a(5,3)=-z2*betam/sqrt(alpha2)*sin(betam*x3/sqrt(alpha2))
a(5,4)=z2*betam/sqrt(alpha2)*cos(betam*x3/sqrt(alpha2))
a(5,5)=z3*betam/sqrt(alpha3)*sin(betam*x3/sqrt(alpha3))
a(5,6)=-z3*betam/sqrt(alpha3)*cos(betam*x3/sqrt(alpha3))
a(6,1)=0.
a(6,2)=0.
a(6,3)=0.
a(6,4)=0.
a(6,5)=h3*cos(betam*x4/sqrt(alpha3))-
  z3*betam/sqrt(alpha3)*sin(betam*x4/sqrt(alpha3))
a(6,6)=h3*sin(betam*x4/sqrt(alpha3))+
  z3*betam/sqrt(alpha3)*cos(betam*x4/sqrt(alpha3))
return
end
C
C
  SUBROUTINE LUDCMP(b,n,np,indx,det)
  PARAMETER (nmax=100,tiny=1.0e-20)
  DIMENSION B(np,np),indx(n),VV(nmax)
  det=1.
  print*
  do i=1,n
    aamax=0.
    do j=1,n
```

```
      if (abs(b(i,j)).gt.aamax) then
        aamax=abs(b(i,j))
      end if
    end do
    if (aamax.eq.0) pause 'singular matrix.'
    VV(i)=1./aamax
  end do
  do j=1,n
    do i=1,j-1
      sum=b(i,j)
      do k=1,i-1
        sum=sum-b(i,k)*b(k,j)
      end do
      b(i,j)=sum
    end do
    aamax=0.
    do i=j,n
      sum=b(i,j)
      do k=1,j-1
        sum=sum-b(i,k)*b(k,j)
      end do
      b(i,j)=sum
      dum=vv(i)*abs(sum)
      if(dum.ge.aamax) then
      imax=i
      aamax=dum
      end if
    end do
    if(j.ne.imax) then
      do k=1,n
        dum=b(imax,k)
        b(imax,k)=b(j,k)
        b(j,k)=dum
      end do
      det=-det
      vv(imax)=vv(j)
```

```
    end if
    indx(j)=imax
    if(b(j,j).eq.0.) b(j,j)=tiny
    if(j.ne.n) then
      dum=1./b(j,j)
      do i=j+1,n
        b(i,j)=b(i,j)*dum
      end do
    end if
  end do
  return
  end
```

Appendix 4A

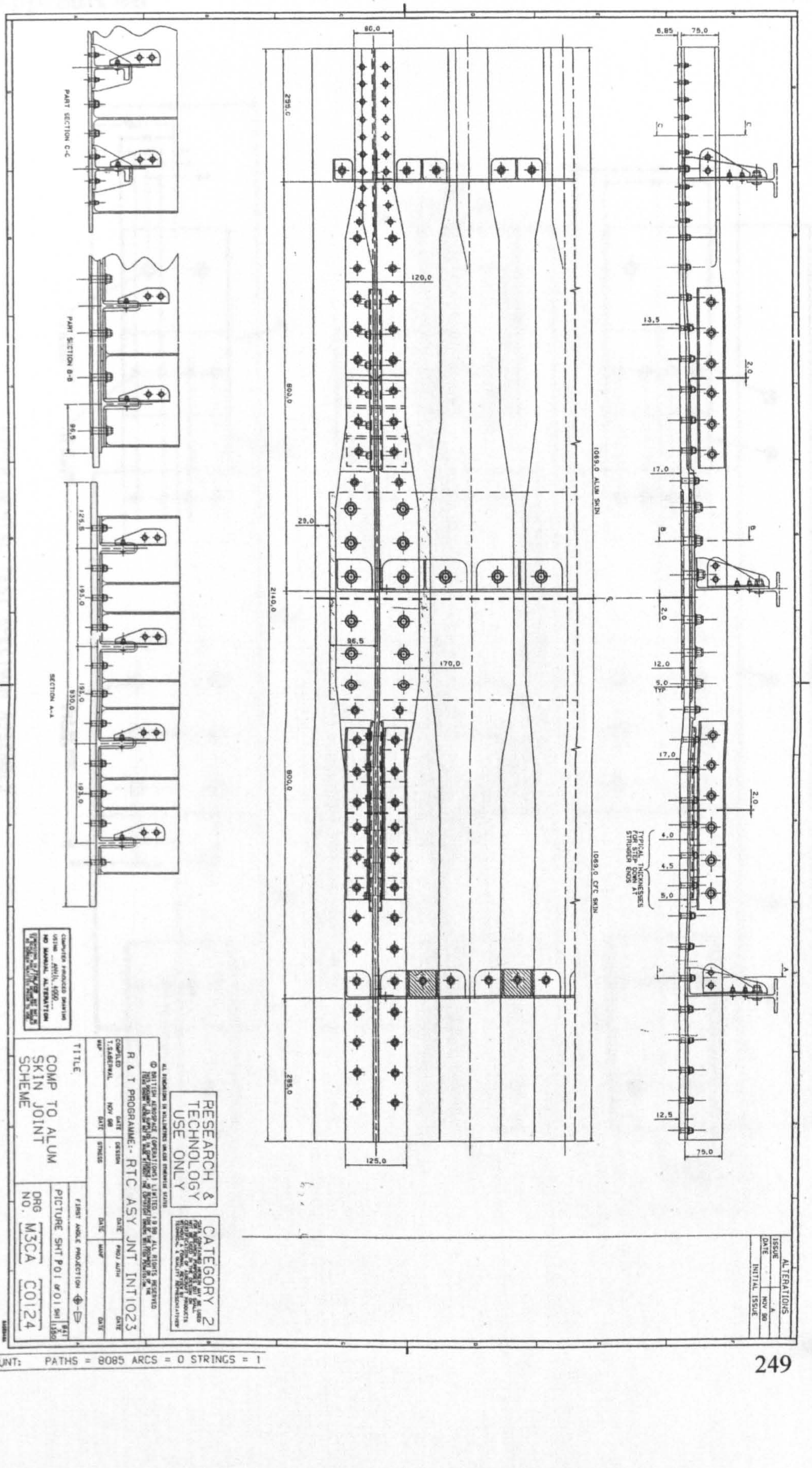

Preliminary Airbus Joint Design

Appendix 4B

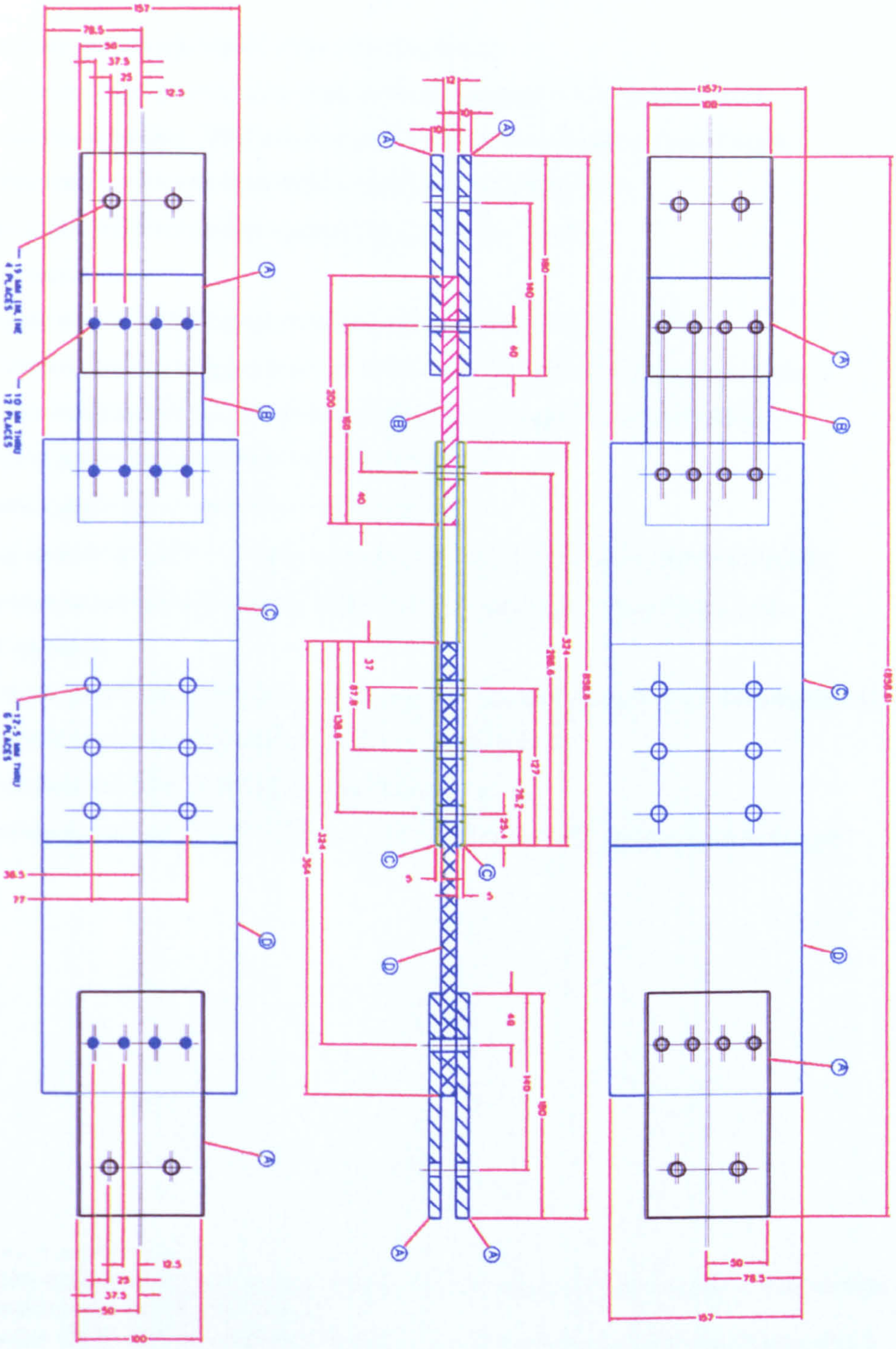
EXPERIMENTAL TEST SPECIMAN ASSEMBLY
157
78.5
50
37.5
25
12.5
19 MM DIA HOLE 4 PLACES
10 MM THRU 12 PLACES
12.5 MM THRU 6 PLACES
100
12
10
10
180
140
40
200
150
40
324
298.8
37
97.8
136.8
42
76.2
23.4
344
5
5
40
140
180
50
78.5
157

Appendix 4D

Experimental Procedure

1. Insert specimen into Zwick Model 1466 oven attachment.
2. Insert eight strain gage wires into the eight available channels of the data recorder.
3. Position thermocouple into CFRP block and insert block into chamber at mid-height.
4. Insert thermocouple wire into hand-held temperature recording device.
5. Zero strain gages and record room temperature (generally ~22°C).
6. Commence tensile test:
    a. Apply tensile load at rate of 0.1mm/s and record data at a rate of 1pt/s.
    b. Continue loading to approximately 40kN, as given on load displacement curve.
    c. Upon reaching 40kN, unload manually at a rate of 2mm/s to a load of 0kN.
7. Re-zero strain gages and recommence tensile testing.
8. Re-zero strain gages and prepare oven for heating.
9. Set heating element to 100°C*, set data recording rate to 1pt/min, and commence heating.
10. When thermocouple reading† reaches 100°C, wait 10 minutes to ensure temperature saturation of specimen.
11. Re-zero strain gages‡, change data recording rate to 1pt/s, and proceed as per first tensile test.
12. Repeat second tensile test procedures as per room temperature.
13. Open oven door and allow cooling to room temperature.
14. When thermocouple temperature indicates 22°C, wait 10 minutes, and proceed with next experiment.

---

* It is not possible to control oven heating rate. Heating element applies maximum amount of heat to reach desired temperature in the least amount of time.
† The oven reaches 100°C much more quickly than the thermocouple, but the thermocouple temperature is the critical temperature.
‡ Re-zeroing the gages at this point allows for a direct comparison between the strains under mechanical loading at room temperature versus mechanical loading at elevated temperature.

Appendix 5A

Example of FE Program

```
*HEADING
*NODE, SYSTEM=R,nset=allnd
    10001, 7.8979039E+01,-4.1422654E+01, 1.1550000E+02
    10002, 8.4479039E+01,-4.1422654E+01, 1.1550000E+02
    10003, 7.8719060E+01,-4.1422654E+01, 1.1286336E+02
    10004, 8.4113142E+01,-4.1422654E+01, 1.1178918E+02
    10005, 7.7949330E+01,-4.1422654E+01, 1.1032875E+02
    10006, 8.3029818E+01,-4.1422654E+01, 1.0822194E+02
    10007, 7.6701383E+01,-4.1422654E+01, 1.0799607E+02
                          .
                          .
                          .
    54151, 5.7979058E+01,-4.9352661E+01, 1.1550000E+02
    54152, 5.7979058E+01,-5.1652659E+01, 1.1550000E+02
    54153, 5.7979058E+01,-4.3252662E+01, 1.1550000E+02
    54154, 5.6979060E+01,-4.4752661E+01, 1.1550000E+02
    54155, 5.7979058E+01,-4.1422650E+01, 1.1550000E+02
    80001, 0.1000000E+01, 0.0000000E+01, 0.0000000E+01
    80002, 0.1000000E+01, 0.1000000E+01, 0.0000000E+01
    80003, 0.1000000E+01, 0.1000000E+01, 0.1000000E+01
*ELEMENT,TYPE=C3D8  ,ELSET=laps
 10001, 10001, 10002, 10004, 10003, 10370, 10373, 10379, 10376
 10002, 10370, 10373, 10379, 10376, 10371, 10374, 10380, 10377
 10003, 10371, 10374, 10380, 10377, 10372, 10375, 10381, 10378
 10004, 10003, 10004, 10006, 10005, 10376, 10379, 10385, 10382
 10005, 10376, 10379, 10385, 10382, 10377, 10380, 10386, 10383
 10006, 10377, 10380, 10386, 10383, 10378, 10381, 10387, 10384
                          .
                          .
                          .
 20921, 21460, 21463, 21475, 21472, 21461, 21464, 21476, 21473
 20922, 20365, 20060, 20058, 20369, 21462, 20547, 20541, 21474
 20923, 21462, 20547, 20541, 21474, 21463, 20548, 20542, 21475
 20924, 21463, 20548, 20542, 21475, 21464, 20549, 20543, 21476
*ELEMENT,TYPE=C3D8  ,ELSET=cfrp
 30001, 30103, 30086, 30087, 30104, 30994, 30892, 30898, 31000
 30002, 30994, 30892, 30898, 31000, 30995, 30893, 30899, 31001
 30003, 30995, 30893, 30899, 31001, 30996, 30894, 30900, 31002
 30004, 30996, 30894, 30900, 31002, 30997, 30895, 30901, 31003
                          .
                          .
                          .
 31906, 32622, 32628, 32664, 32658, 32623, 32629, 32665, 32659
 31907, 32623, 32629, 32665, 32659, 32624, 32630, 32666, 32660
 31908, 32624, 32630, 32666, 32660, 32625, 32631, 32667, 32661
```

```
*ELEMENT,TYPE=C3D6  ,ELSET=blt1
 50060, 50064, 50063, 50141, 50068, 50067, 50144
 50065, 50024, 50023, 50111, 50028, 50027, 50114
 50064, 50020, 50019, 50108, 50024, 50023, 50111
 50063, 50016, 50015, 50105, 50020, 50019, 50108
                      .
                      .
                      .
51204, 51657, 51744, 51817, 51661, 51747, 51820
 51742, 52329, 52332, 52362, 52402, 52405, 52435
 51272, 51661, 51820, 51893, 51665, 51823, 51896
*ELEMENT,TYPE=C3D8  ,ELSET=blt2
 50001, 50044, 50090, 50163, 50126, 50040, 50089, 50162, 50123
 50003, 50042, 50043, 50125, 50124, 50038, 50039, 50122, 50121
 50004, 50040, 50089, 50162, 50123, 50036, 50088, 50161, 50120
 50005, 50039, 50040, 50123, 50122, 50035, 50036, 50120, 50119
                      .
                      .
                      .
  50953, 51485, 51468, 51541, 51558, 51487, 51469, 51542, 51560
  51609, 52270, 52307, 52380, 52343, 52267, 52306, 52379, 52340
  52088, 52754, 52815, 52888, 52827, 52751, 52819, 52892, 52824
*elset,elset=blts
blt1,blt2
*ORIENTATION,NAME=O0000001,SYSTEM=RECTANGULAR
 0.1000E+01, 0.0000E+00, 0.0000E+00, 0.0000E+00, 0.1000E+01, 0.0000E+00
2, 0.0000E+00
*SOLID SECTION,ELSET=blts,MATERIAL=titanium,ORIENTATION=O0000001
*SOLID SECTION,ELSET=laps,MATERIAL=aluminium,ORIENTATION=O0000001
*SOLID SECTION,ELSET=cfrp,MATERIAL=cfrp,ORIENTATION=O0000001
*MATERIAL,NAME=titanium
*conductivity,type=isotropic
21.6e-3
*specific heat
528.
*density
4500.e-9
*elastic,type=isotropic
103.e3,.29,298.
*expansion,type=iso
9.e-6,298.
**
*material,name=aluminium
*conductivity,type=isotropic
164.e-3
*specific heat
883.
*density
2787.e-9
*elastic,type=isotropic
71.7e3,.3,298.
```

```
*expansion,type=iso
23.e-6,298.
**
*material,name=cfrp
*conductivity,type=ortho
8.58e-3,0.81e-3,8.58e-3,270
11.99e-3,1.37e-3,11.99e-3,500
*specific heat
848.,270
1485.,500
*density
1550.e-9
*elastic,type=engineering constants
75.2e3,9.5e3,36.2e3,.2,.39,.02,17.4e3,4.9e3
17.4e3,298.
*expansion,type=ortho
8.56e-7,2.8e-5,4.98e-6,298.
**
*nset, nset =.....
*elset, elset = ....
**
*surface,name=b1lp1
b1lp1b,s2
*surface,name=lp1b1
lp1b1b,s1
*contact pair,interaction=topnut1,adjust=0.2
b1lp1,lp1b1
*surface interaction,name=topnut1
*friction
0.4
                    .
                    .
                    .
**
*surface,name=prts1
pret1,s2
*surface,name=prts2
pret2,s2
*surface,name=prts3
pret3,s2
**
*pre-tension section, surface=prts1,node=80001
*pre-tension section, surface=prts2,node=80002
*pre-tension section, surface=prts3,node=80003
**
**
*file format, zero increment
**
*initial conditions, type=temperature
 allnd, 295.0000
**
```

```
*equation
2
bknds,3,-1,32630,3,1
**
********Step1***********
*Step,inc=500
*Static
200,10000
*output,field,frequency=0,variable=all
*cload
80001,1,787.
*cload
80002,1,787.
*cload
80003,1,787.
*boundary
lsnds,pinned
*boundary
rscp,pinned
*boundary
frnds,zsymm
*boundary
30360,ysymm
*end step
**
********Step2***********
*STEP,inc=500, amplitude=ramp
*STATIC
20,10000
**
**
*output,field,frequency=0,variable=all
**
*boundary,op=new
*boundary,fixed,op=new
80001,1,1
*boundary,fixed,op=new
80002,1,1
*boundary,fixed,op=new
80003,1,1
*boundary,op=new
lsnds,xsymm
*boundary,op=new
frnds,zsymm
*boundary,op=new
30360,ysymm
*boundary,op=new,type=displacement
rscp,1,,0.05
**
*el print,elset=l2b351,position=averaged at nodes,frequency=15
E
```

```
*el print,elset=l2b353,position=averaged at nodes,frequency=15
E
**
*node print,nset=rscp,frequency=15
U,RF
*node print,nset=cpb1b2, frequency=15
U,RF
*node print,nset=cpb2b3, frequency=15
U,RF
**
                    .
                    .
                    .
*end step
                    .
                    .
                    .
********Step N***********
*STEP,inc=500, amplitude=ramp
*STATIC
20,10000
**
**
*output,field,frequency=0,variable=all
**
*boundary,op=new
*boundary,fixed,op=new
80001,1,1
*boundary,fixed,op=new
80002,1,1
*boundary,fixed,op=new
80003,1,1
*boundary,op=new
lsnds,xsymm
*boundary,op=new
frnds,zsymm
*boundary,op=new
30360,ysymm
*boundary,op=new,type=displacement
rscp,1,,x
*end step
```

References

1. Ozisik MN. Boundary value problems of heat conduction, Scranton, Pennsylvania: International Textbook Co.; 1968.
2. Holman JP. Heat transfer. 7th ed. London: McGraw-Hill; 1992.
3. Lorente S, Petit M, Javelas R. Simplified analytical model of thermal transfer in vertical hollow brick. Energy and buildings 1996;24:95-103.
4. Globe S and Dropkin D. Natural-convection heat transfer in liquids confined by two horizontal plates and heated from below. Trans. ASME, J. Heat Trans 1959 Feb:24-28.
5. Catton I and Edwards DK. Effect of side walls on natural convection between horizontal plates heated from below. J. Heat Transfer 1967 Nov:295-99.
6. Jakob M. Free heat convection through enclosed plane gas layers. Transactions of the A.S.M.E. (Heat Transfer Division) 1946;189-94.
7. Jaluria Y. Natural convection heat and mass transfer. Oxford, England: Permagon Press Ltd.; 1980.
8. Elsayed MM, Al-Najem NM, El-Refaee MM and Noor AA. Numerical study of natural convection in fully open tilted cavities. Heat Trans. Eng. 1999;20(3):73-85.
9. Pessoa-Filho JB and Thynell ST. An approximate solution to radiative transfer in two-dimensional rectangular enclosures. Trans. ASME., J. Heat Trans. 1997 Nov;738-45.
10. Dickenson RD. Thermal analysis of composite wings using the ABAQUS finite element code. British Aerospace Airbus, Report No. AM8623/compwing/R001; 1999 Nov.
11. Epifanie A. Composite wing programme fuel support fuel tank temperature profiles. British Aerospace Airbus Technical Report DET/2003/1999/0293; 1999.
12. Eckert ERG and Drake RM. Analysis of heat and mass transfer. London: Hemisphere Publishing Corporation 1987.
13. Schnieder PJ. Conduction heat transfer. Reading: Addison-Wesley Publishing Co. 1955.
14. Carslaw HS. Introduction to the mathematical theory of the conduction of heat in solids. London: Macmillan & Co. 1921.
15. De Monte F. Transient heat conduction in one-dimensional composite slab. A 'natural' analytic approach. Int. J. Heat Mass Trans. 2000;43:3607-19.
16. Antonopoulos KA and Tzivanidis C. Analytical solution of boundary value problems of heat conduction in composite regions with arbitrary convection boundary conditions. Acta Mechanica 1996;118:65-78.
17. Boley BA and Weiner JH. Theory of thermal stresses. New York: John Wiley & Sons Inc.; 1960.

18. Zerkle RD and Sunderland JE. The transient temperature distribution in a slab subject to thermal radiation. ASME J. Heat Trans. 1965;87:117-32.
19. Mantelli MBH and Yavanovich MM. Compact analytical model for overall thermal resistance of bolted joints. Int. J. Heat Mass Transfer 1998;41(10):1255-66.
20. Mantelli MBH and Yavanovich MM. Parametric heat transfer study of bolted joints. J. Thermophysics & Heat Trans. 1998;12(3):382-90.
21. Airbus-F, Presentation of Results - Experimental Validation of Composite Structures Thermal Modelling, CoC Structures ESA-NT, 22/11/2001.
22. Barzelay ME and Boison JC. Investigation of stresses due to thermal gradients in typical aircraft structures. NACA Research Memorandum 51K06, 1952 Jan.
23. Hart-Smith LJ. Bonded-bolted composite joints. J. Aircraft 1985 Nov;22(11):993-1000.
24. Nelson WD, Bunin BL, and Hart-Smith LJ. Critical joints in large composite aircraft structure, NASA Contract Report 3710, under contract NAS1-16857; 1983.
25. Hart-Smith LJ. Analysis methods for bolted composite joints subject to in-plane shear loads, fastened joints for advanced composites, McDonnell Douglas Paper Presented in 1996;553-574.
26. Oplinger DW. On the structural behavior of mechanically fastened joints in composite structures. In: Lencoe, EM, Oplinger, DW, Burke, JJ, editors. Fibrous composites in structural design. New York: Plenum Press 1980;575-602.
27. Madenci E and Ireli L. Analytical determination of contact stresses in mechanically fastened composite laminates with finite boundaries. Int. J. Solids Struc. 1993;30(18):469-84.
28. Chang FK, Scott RA and Springer GS. Design of composite laminates containing pin loaded holes. J. Composite Materials 1984;18:279-89.
29. Blackie AP and Chutima S. Stress distributions in multi-fastened composite plates. Composite Struc. 1996;34:427-36.
30. Eriksson IL. Contact stresses in bolted joints of composite laminates. Composite Struc. 1986;6:57-75.
31. Chang FK, Scott RA and Springer GS. Failure of composite laminates containing pin-loaded holes - method of solution. J. Composite Materials 1984;18:255-75.
32. Pagano NJ and Pipes RB. The influence of stacking sequence on laminate strength. J. Composite Materials 1971;5:50-7.
33. Quinn WJ and Matthews FL. The effect of stacking sequence on laminate strength in glass fibre reinforced plastic. J. Composite Materials 1977;11:139-45.

34. Whitney JM and Kim RY. Effect of stacking sequence on the notched strength of laminated composites. Composite Materials: Testing and Design (4th Conference) ASTM STP 617; 1977;229-42.
35. Daniel IM, Rowlands RE and Whiteside JB. Effects of material and stacking sequence on the behavior of composite plates with holes. Exp. Mech. 1974;1-9.
36. Rybicke EF and Schmueser DW. Effect of stacking and lay-up angle on free edge stresses around a hole in a laminated plate under tension. J. Composite Materials 1978;12:300-13.
37. Roberts N. Three-dimensional finite element analysis of a carbon fibre composite bolted joint, Airbus UK Technical Report TCC/5012/2001/0106; 2001.
38. Petrossian Z. Initial stress investigations of thermally induced loads in hybrid structures for temperatures encountered during manufacture and in-service. British Aerospace Airbus Technical Report MC/RPT/BD/0000/3146, British Aerospace (Operations) Ltd. 1998.
39. Chen WH, Lee SS, and Yeh JT. Three-dimensional contact stress analysis of a composite laminate with bolted joint. Composite Struc. 1995;30:287-97.
40. Smith PA, Pascow KJ, Polak C and Stroud DO. The behaviour of single-lap bolted joints in CFRP laminates. Composite Struc. 1986;6:41-55.
41. Shokrieh MM and Lessard LB. Effects of material nonlinearity on the tree-dimensional stress state of pin-loaded composite laminates. J. Composite Materials 1996;30(7):839-61.
42. Hassan NK, Mohamedien MA and Rizkalla SH. Finite element analysis of bolted connections for PFRP composites. Composites: Part B 1996;27B:339-49.
43. Naik RA and Crews Jr. JH. Stress analysis method for clearance-fit joints with bearing-bypass loads. AIAA Journal 1991 Jan;29(1):89-95.
44. Wang HS, Hung CL, and Chang FK. Bearing failure of bolted composite joints. Part I: Experimental Characterization. J. Composite Materials 1996;30(12):1284-1358.
45. Hung CL and Chang FK. Bearing failure of bolted composite joints. Part II: Model and Verification. J. Composite Materials 1996;30(12):1359-1400.
46. Tsai MY and Morton J. Stress and failure analysis of a pin-loaded composite plate: an experimental study. J. Composite Materials 1990 Oct;24:1101-21.
47. Chen WH and Lee SS. Numerical and experimental failure analysis of composite laminates with bolted joints under bending loads. J. Composite Materials 1995;29(1):15-36.
48. Crews Jr. JH and Naik RA. Combined bearing and bypass loading on a graphite/epoxy laminate. Composite Struc. 1980;6:21-40.

49. Yan Y, Wen WD, Chang FK, and Shyprykevich P. Experimental study on clamping effects on the tensile strength of composite plates with a bolt-filled hole. Composites: Part A 1999;30A:1215-29.
50. Lin CC and Lin CH. Stress and strength analysis of composite joints using direct boundary element method. Composite Struc. 1993;25:209-15.
51. Webber JPH, Graham U, and Wisnom MR. Strain distributions around fasteners in laminated plates under biaxial in-plane loading. J. of Strain Analysis 1997 March;32(3):167-74.
52. Chang FK, Scott RA, and Springer GS. Strength of mechanically fastened composite joints. J. Composite Materials 1982 Nov;16:470-93.
53. Garbo SP and Ogonowski JM. Effect of variances and manufacturing tolerances on the design strength and life of mechanically fastened composite joints. Flight Dynamics Laboratory, Air Force Wright Aeronautical Laboratories, Technical Report AFWAL-TR-31-3041, 1981 Apr.
54. Daniel IM, Rowlands RE, and Whiteside JB. Effects of material and stacking sequence on behavior of composite plates with holes. Exp. Mech. 1974 Jan;1-9.
55. Wong CMS and Matthews FL. A finite element analysis of single and two-hole bolted joints in fibre reinforced plastic. J. Composite Materials 1982;16:481-91.
56. Hyer MW, Klang EC, and Cooper DE. The effects of pin elasticity, clearance and friction on the stresses in a pin-loaded orthotropic plate. J. Composite Materials 1987 Mar;21:190-206.
57. Dano ML, Gendron G and Picard A. Stress and failure analysis of mechanically fastened joints in composite laminates. Composite Struc. 2000;50:287-96.
58. Hyer MW and Lui D. Stresses in a quasi-isotropic pin-loaded connector using photoelasticity. Exp. Mech. 1984;23(3):249-56.
59. Camanho PP and Matthews FL. Delamination onset prediction in mechanically fastened joints in composite laminates. J. Composite Materials 1999;33(10):906-27.
60. Camanho PP and Matthews FL. A progressive damage model for mechanically fastened joints in composite laminates. J. Composite Materials 1999;33(24):2248-80.
61. Waszczak JP and Cruse TA. Failure mode and strength predictions of anisotropic bolt bearing specimens. J. Composite Materials 1971;5:421-25.
62. De Jong T. Stresses around pin-loaded holes in elastically orthotropic or isotropic plates. J. Composite Materials 1977;11:313-31.
63. Marshall IH, Arnold WS, Wood J and Mousley RF. Observations on bolted connections in composite structures. Composite Struc. 1989;6:133-51.

64. Postupka S, Duhweg A and Arendts FJ. Determination of the bolt flexibility of CFRP-joints. ECCM-8; 2000;61-68.
65. Matthews FL, Wong CM and Chryssafitis S. Stress distribution around a single bolt in fibre-reinforced plastic. Composites 1982 Jul;316-22.
66. Ireman T, Nyman T and Hellbom K. On design methods for bolted joints in composite aircraft structures. Composite Struc. 1993;25:567-78.
67. Ireman T and Eriksson I. Strength of composite laminates containing holes and subject to complex loading conditions. J. Composite Materials 1997;31:1214-48.
68. Ireman T, Ranvik T and Eriksson I. On damage development in mechanically fastened composite laminates. Composites: Part B 2000 June;49:151-71.
69. Ireman T. Three-dimensional stress analysis of bolted single-lap joints. Composites: Part B 1998 Nov;43:195-216.
70. Ireman T and Purin P. Evaluation of factors affecting the design of bolted composite laminates. IMechE Conference Transactions "Joining and Repair of Plastics and Composites" 16-17 1999 Mar.
71. Hunter WG, Hunter JS, and Title. Wiley series in probability and mathematical statistics. John Wiley & Sons, Inc. 1978.
72. Parvatareddy H, Wang JZ, Dillar DA and Ward TC. Environmental aging of high-performance polymeric composites: effects on durability. Composites Sci. & Tech. 1995;53:399-409.
73. Motavalli M, Terrasi GP, and Meier U. On the behaviour of hybrid aluminium/CFRP box beams at low temperatures. Composites: Part A 1997;28A:121-29.
74. Scarponi C, Marini G and Montanari P. The importance of the temperature and lateral pressure on the CFRP joints' strength under uniaxial loading. J. Reinforced Plastics and Composites 1997;16(9):825-47.
75. Eriksson, I., On the bearing strength of bolted graphite/epoxy laminates. J. Composite Materials 1990 Dec;24:1246-69.
76. Peterson D, Rolfes R and Zimmermann R. Thermo-mechanical design aspects for primary composite structures of large transport aircraft. Aerosp. Sci. Techno. 2001;5:135-46.
77. Kim RY and Whitney JM. Effect of temperature and moisture on pin bearing strength of composite laminates. J. Composite Mat. 1976;15:481-91.
78. Chen WH and Lee YJ. Failure process and pin-bearing strength of laminated composites at elevated temperature. J. Reinforced Plastics and Composites 1992;11:743-71.
79. Bolz RE and Tuve GL. CRC handbook of tables for applied engineering science, 2nd ed. Cleveland, Ohio: The Chemical Rubber Co.; 1973.

80. Singh SN, Birkebak RC, and Drake RM. Laminar free convection heat transfer from downward-facing horizontal surfaces of finite dimension. Prog. Heat Mass Trans. 1969;2:87-98.
81. Hibbitt, Karlsson, and Sorenson Inc. ABAQUS users manual, Version 5.8; 1999.
82. Hollands KGT, Raithby GD, and Konicek L. Correlation equations for free convection heat transfer in horizontal layers of air and water. Int. J. Heat Mass Trans. 1975;18:879-84.
83. Goldstein RJ and Chu TY. Thermal convection in a horizontal layer of air. Prog. Heat Mass Trans. 1969;2:55-74.
84. Vliet GC. Natural convection local heat transfer on constant-heat-flux inclined surfaces. Trans. ASME, J. Heat Trans. 1969 Nov;511-516.
85. Fujii T and Imura H. Natural-convection heat transfer from a plate with arbitrary inclination. Int J. Heat Mass Trans. 1972;15:755-67.
86. Eckert ERG and Drake RM. Analysis of heat and mass transfer. London: Hemisphere Publishing Corporation; 1987.
87. Schneider PJ. Conduction heat transfer. Reading: Addison-Wesley Publishing Co.; 1955.
88. Chapman AJ. Heat transfer. New York: The Macmillan Co.; 1960;108-21.
89. Jakob M. Heat transfer. New York: John Wiley & Sons Inc.; 1949. Volume I:270-91, 411-20.
90. Jaeger JC. Conduction of heat in a solid with a power law of heat transfer at its surface. Proc. Cambridge Phil. Soc. 1950;46:634-41.
91. Kreyszig E. Advanced engineering mathematics. New York: John Wiley & Sons Inc.; 1988.
92. Tittle WC and Robinson VL. Analytical solution of conduction problems in composite media. ASME 1965; paper 65-WA-HT.
93. Miller JR, and Weaver PM. Temperature distribution in a CFRP box structure subject to transient heat fluxes. Transactions of 42nd AIAA/ASME/ASCE/AHS/ASC Structures, Structural Dynamics, and Materials Conf & Exhibit. Seattle, WA: 2001 Apr; Paper 2001-1451.
94. McGraw-Hill Book Co. Inc. McGraw-Hill publications in Aeronautical Science - thermal stresses. York, PA: The Maple Press Company; 1957.
95. Miller JR and Weaver PM. Literature review on thermal properties and strength prediction in mechanically fastened composite and metallic joints. University of Bristol Report #AEROSA 5349, 2000 Jan.
96. T. Saberwal, Comp to Alum Skin Joint Scheme Drg No. M3CA C0123, R&T Prog: RTC Asy Jnt Int1023, British Aerospace (Operations) Limited; 1998 Nov.

97. T. Saberwal, CFC Element Assembly Drg No. M3CA C0121, R&T Prog: CWP-LCWI, British Aerospace (Operations) Limited. 1998 Aug.
98. Farrow IR, Lee J, and Kong CD. Flexural testing of composite laminates for drilling trial assessment. Advanced Composite Letters 2000;9(4).
99. Persson E, Eriksson I, and Zackrisson L. Effects of hole machining defects on strength and fatigue life of composite laminates. Composites: Part A 1997;28A.
100. Pegra JJ and Wook RE. Influence of hole quality on graphite epoxy composite laminates. Collective Technical Paper AIAA, ASME, AHS, 21st Structural Dynamics Materials Conference 1980;AIAA Paper 80-0777:687-90.
101. Airbus Design Handbook - A320 & Subs Aircraft 2000. ALN 50 Issue 1& ALN 51 Issue 1, Airbus UK Ltd.
102. Canadian Institute for Non-Destructive Examination, www.csndt.org.
103. Techni Measure Ltd. UK manufactured by Sokkikenkyujo Co. Ltd. Japan.